ΕΘΝΙΚΟ ΚΑΙ ΚΑΠΟΔΙΣΤΡΙΑΚΟ ΠΑΝΕΠΙΣΤΗΜΙΟ ΑΘΗΝΩΝ

ΣΧΟΛΗ ΘΕΤΙΚΩΝ ΕΠΙΣΤΗΜΩΝ

ΤΜΗΜΑ ΧΗΜΕΙΑΣ

ΔΙΔΑΚΤΟΡΙΚΗ ΔΙΑΤΡΙΒΗ

Ανάπτυξη Ανόργανων και Υβριδικών Περοσβσκιτικών Υλικών και Εφαρμογή τους σε Φωτοβολταϊκές Διατάξεις

MOHAMED MAHMOUD TAHA ELSENETY

ΧΗΜΙΚΟΣ

ΑΘΗΝΑ

Ιανουάριος 2021

NATIONAL AND KAPODISTRIAN UNIVERSITY OF ATHENS

SCHOOL OF SCIENCES

Department of Chemistry

DOCTORAL THESIS

Development of Inorganic and Hybrid Perovskite Materials and their Application in Photovoltaic Devices

MOHAMED MAHMOUD TAHA ELSENETY

CHEMIST

ATHENS

January 2021

ΔΙΔΑΚΤΟΡΙΚΗ ΔΙΑΤΡΙΒΗ

Ανάπτυξη Ανόργανων και Υβριδικών Περοσβσκιτικών Υλικών και Εφαρμογή τους σε Φωτοβολταϊκές Διατάξεις

MOHAMED MAHMOUD TAHA ELSENETY

Α.Μ.: 001613

ΕΠΙΒΛΕΠΩΝ ΚΑΘΗΓΗΤΗΣ:

Αθανάσιος Φιλιππόπουλος, Επίκουρος Καθηγητής Τμήματος Χημείας ΕΚΠΑ

ΤΡΙΜΕΛΗΣ ΕΠΙΤΡΟΠΗ ΠΑΡΑΚΟΛΟΥΘΗΣΗΣ:

Χριστίνα-Άννα Μητσοπούλου, Καθηγήτρια Τμήματος Χημείας ΕΚΠΑ

Πολύκαρπος Φαλάρας, Ερευνητής Α' Βαθμίδας, ΙΝΝ, ΕΚΕΦΕ Δημόκριτος

Αθανάσιος Φιλιππόπουλος, Επίκουρος Καθηγητής Τμήματος Χημείας ΕΚΠΑ

ΕΠΤΑΜΕΛΗΣ ΕΞΕΤΑΣΤΙΚΗ ΕΠΙΤΡΟΠΗ

Χριστίνα-Άννα Μητσοπούλου, Καθηγήτρια Τμήματος Χημείας ΕΚΠΑ

Παναγιώτης Κυρίτσης, Καθηγητής Τμήματος Χημείας ΕΚΠΑ

Κωνσταντίνος Μεθενίτης, Αναπληρωτής Καθηγητής Τμήματος Χημείας ΕΚΠΑ

Αθανάσιος Κόντος, Αναπληρωτής Καθηγητής ΣΕΜΦΕ, ΕΜΠ

Ανδρέας Καλτζόγλου, Ερευνητής Γ' Βαθμίδας, ΙΘΦΧ , Εθνικό Ιδρυμα Ερευνών

Πολύκαρπος Φαλάρας, Ερευνητής Α' Βαθμίδας , ΙΝΝ, ΕΚΕΦΕ Δημόκριτος

Αθανάσιος Φιλιππόπουλος, Επίκουρος Καθηγητής Τμήματος Χημείας ΕΚΠΑ

ΗΜΕΡΟΜΗΝΙΑ ΕΞΕΤΑΣΗΣ 12/01/2021

Περίληψη

Τα ηλιακά κελιά με αλογονούχους περοβσκίτες έχουν προσελκύσει μεγάλο ενδιαφέρον στη φωτοβολταϊκή κοινότητα τα τελευταία πέντε χρόνια, καθώς η απόδοση τους στη μετατροπή της φωτεινής ισχύος σε ηλεκτρική έχει φτάσει σε τιμές που ξεπερνούν το 25 %. Τα περοβσκιτικά ηλιακά κελιά (PSCs) εξελίχθηκαν από τα στερεάς κατάστασης-φωτοευαισθητοποιημένα ηλιακά κελιά (DSSCs) αντικαθιστώντας τη χρωστική ουσία με έναν περοβσκίτη του τύπου ABX_3, όπου A ένα ανόργανο ή οργανικό κατιόν (π.χ. Cs^+, $(CH_3NH_3)^+$, $(HC(NH_2)_2)^+$), B ένα μεταλλικό κατιόν (π.χ. Pb^{2+}, Sn^{2+}), και X ένα κατιόν αλογόνου (Cl^-, Br^-, I^-). Παρά τις υψηλές αποδόσεις, αυτή η κατηγορία χημικών ενώσεων παρουσιάζει αστάθεια σε μακροχρόνια χρήση στον αέρα, λόγω των υγροσκοπικών αμινικών κατιόντων και επίσης παρουσιάζει τοξικότητα λόγω του μολύβδου.

Σκοπός της διατριβής:

Ο στόχος μου είναι να επεκτείνω τη μέχρι στιγμής περιορισμένη ποικιλία οργανικών κατιόντων μελετώντας νέα θειούχα κατιόντα όπως το τριμεθυλοσουλφώνιο $((CH_3)_3S)^+$ ως σταθερά οργανικά κατιόντα, τα οποία μπορούν να ενσωματωθούν σε ηλιακά κελιά για: (α) αύξηση της απόδοσης μετατροπής ισχύος, (β) αύξηση της σταθερότητας ως προς την υγρασία, (γ) μείωση της τοξικότητας σε περοβσκιτικές ενώσεις χωρίς μόλυβδο.

Παρακάτω παρατίθεται η κεντρική ιδέα κάθε κεφαλαίου:

Κεφάλαιο (1)

Εδώ συζητούνται λεπτομερώς οι αρχές των ηλιακών κελιών. Επίσης, αναλύεται το υπόβαθρο και το κίνητρο για νέες τεχνολογίες σε ηλιακά κελιά, ιδιαίτερα για την κατασκευή και τις προσκλήσεις των DSSCs και PSCs.

Κεφάλαιο (2)

Τα υλικά, οι τεχνικές σύνθεσης και οι μέθοδοι χαρακτηρισμού αναλύονται σε αυτό το κεφάλαιο.

Κεφάλαιο (3)

Εδώ παρουσιάζεται η σύνθεση, η κρυσταλλική δομή, οι οπτοηλεκτρονικές ιδιότητες και οι θεωρητικοί υπολογισμοί τύπου ab-initio DFT (density functional theory) για τις σταθερές χημικές ενώσεις των περοβσκιτών $(CH_3)_3SPbI_{3-x}Br_x$ και $(CH_3)_3SPbI_{3-x}Cl_x$ (x = 0, 1, 2, 3).

Κεφάλαιο (4)

Η σύνθεση, ο χαρακτηρισμός και τα πολυ-θερμοκρασιακά φάσματα Raman του νέου 1D $(CH_3)_3SSnI_3$ περοβσκίτη μελετώνται σε αυτό το κεφάλαιο.

Κεφάλαια (5,6)

Μια νέα σειρά ενώσεων του Sn^{4+} με δομή 'κενού' (defect) περοβσκίτη και σύσταση $((CH_3)_3S)_2SnX_6$ (X = Cl, Br, I), $((CH_3)_3S)_2SnI_{6-n}Cl_n$ και $((CH_3)_3S)_2SnI_{6-n}Br_n$ (n=1, 2) παρασκευάσθηκαν και χαρακτηρίσθηκαν με κρυσταλλογραφικές και φασματοσκοπικές μεθόδους. Επίσης, οι ενώσεις αυτές του Sn^{4+} χρησιμοποιήθηκαν με επιτυχία ως υλικά μεταφοράς οπών (hole transporting materials - HTMs) σε DSSCs.

Κεφάλαιο (7)

Εδώ παρουσιάζεται η προσέγγιση της διαστασιμότητας στην αρχιτεκτονική διπλής στοιβάδας $(FA/MA/Cs)PbI_{3-x}Br_x/(CH_3)_3SPbI_3$ (3D/1D) περοβσκιτών. Αυτή η διπλή στοιβάδα 3D/1D κατασκευάστηκε εξ ολοκλήρου με τεχνικές διαλύματος και βελτιστοποιεί την αντίστοιχη διεπιφάνεια προσροφητή και στοιβάδας μεταφοράς οπών στα PSCs. Το 1D $(CH_3)_3SPbI_3$ οδηγεί σε σημαντική βελτίωση της σταθερότητας των μη-στεγανοποιημένων ηλιακών κελιών, τόσο κάτω από ατμοσφαιρικές συνθήκες όσο και υπό έντονη ακτινοβόληση (light stress).

Κεφάλαιο (8)

Εδώ αναπτύσσεται η βελτίωση της διεπιφάνειας με τη χρήση του οργανικού χρωμοφόρου (E)-3-(5-(4-(bis(2',4'-dibutoxy-[1,1'-biphenyl]-4-yl)amino)phenyl)thiophen-2-yl)-2-cyanoacrylic acid (D35) ως ενδιάμεση στοιβάδα ανάμεσα στο περοβσκιτικό απορροφητή και το υλικό μεταφοράς οπών σε μεσοπορώδη PSCs. Αυτά τα οργανικά ηλιακά κελιά βασισμένα σε D-π-A παρουσιάζουν σημαντική σταθερότητα καθώς διατηρούν το 83% της αρχικής τους απόδοσης μετά από 37 ημέρες αποθήκευσης στο σκοτάδι και σε συνθήκες ανοιχτού κυκλώματος.

Κεφάλαιο (9)

Περίληψη των σημαντικότερων ερευνητικών αποτελεσμάτων, συμπερασμάτων και προοπτικής της παρούσας διατριβής.

Κεφάλαιο (10)

Βιβλιογραφικές αναφορές

SUMMARY

Halide perovskite solar devices have attracted much attention in the photovoltaic community, due to their efficiency in converting solar energy into electricity, which has reached values over 25.2% in the last five years. Perovskite solar cells (PSCs) evolved from the solid-state, dye-sensitized solar cells (DSSCs) by replacing the dye absorber with an ABX_3 type perovskite material where A is an inorganic or/and organic cation (Cs^+, $(CH_3NH_3)^+$, $(HC(NH_2)_2)^+$), B is a metal cation (e.g Pb^{2+}, Sn^{2+}), and X is a halogen anion (Cl^-, Br^-, I^-). Despite high efficiencies, this class of compounds suffers from long-term instability in ambient air due to the hygroscopic amine cations and from the toxicity of lead.

Aim of the work:

My aim is to expand the, so far, limited variety of organic cations by exploring sulfur-based analogues using trimethyl sulfonium cation $((CH_3)_3S)^+$ as stable organic moiety, that could ultimately be incorporated in solar cells for: (a) enhance power conversion efficiency , (b) increase stability against humidity, (c) decrease toxicity in lead-free perovskite.

Below, I summarized the main idea of each chapter:

Chapter (1)

Fundamental of photovoltaic solar cells devices were discussed widely. Also, the background and motivation of a new technology of solar cells specially Dye-sensitized solar cells (DSSC) and Perovskites solar cells (PSCs), including fabrication processes, promises and challenges.

Chapter (2)

The materials, synthesis techniques, and characterization analysis were recorded in this chapter.

Chapter (3)

I present the synthesis, crystal structures, optoelectronic properties, and first principles theoretical ab-initio DFT calculations of a novel chemically stable $(CH_3)_3SPbI_{3-x}Br_x$ and $(CH_3)_3SPbI_{3-x}Cl_x$ (x = 0, 1, 2, 3) perovskites.

Chapter (4)

The synthesis, characterization, optoelectronic properties and multi-temperature Raman of a novel lead-free $(CH_3)_3SSnI_3$ 1-D perovskite were discussed.

Chapters (5,6)

A novel series of Sn^{4+} halide lead-free defect perovskites $((CH_3)_3S)_2SnX_6$ (X = Cl, Br, I), $((CH_3)_3S)_2SnI_{6-n}Cl_n$ and $((CH_3)_3S)_2SnI_{6-n}Br_n$ (n=1, 2) were synthesized and characterized using different spectroscopic techniques. Moreover, the lead-free Sn(IV)-based compounds were successfully incorporated as hole transporting materials (HTMs) in Dye-sensitized solar cells (DSCs)

Chapter (7)

Dimensionality engineering approach consisting of a (FA/MA/Cs) $PbI_{3-x}Br_x/(CH_3)_3SPbI_3$ (3D/1D) perovskite bilayer architecture, fabricated exclusively with solution processes have been discussed. The 3D/1D bilayer structure further optimizes the corresponding absorber/hole transporting layer (HTL) interface of the PSCs. The 1D $(CH_3)_3SPbI_3$ lead to significant stability improvement for non-sealed devices both under ambient conditions and light stress

Chapter (8)

Interface engineering approach involving the utilization of the organic chromophore (E)-3-(5-(4-(bis(2',4'-dibutoxy-[1,1'-biphenyl]-4-yl)amino)phenyl)thiophen-2-yl)-2-cyanoacrylic acid (D35) as an interlayer between the perovskite absorber and the hole transporter (HTM) of mesoporous PSCs. The organic D-π-A -based solar cells present superior stability since they preserved 83% of their initial efficiency after 37 days of storage under dark and open circuit conditions.

Chapter (9)

I summarized the main findings, conclusions and perspective.

Chapter (10)

References

PUBLICATIONS

(1) Elsenety, M. M.; Stergiou, A.; Sygellou, L.; Tagmatarchis, N.; Balis, N.; Falaras, P. Boosting Perovskite Nanomorphology and Charge Transport Properties via a Functional D–π-A Organic Layer at the Absorber/Hole Transporter Interface. *Nanoscale* **2020**, *12* (28), 15137–15149.

(2) Elsenety, M. M.; Antoniadou, M.; Balis, N.; Kaltzoglou, A.; Sygellou, L.; Stergiou, A.; Tagmatarchis, N.; Falaras, P. Stability Improvement and Performance Reproducibility Enhancement of Perovskite Solar Cells Following (FA/MA/Cs)$PbI_{3-x}Br_x$/$(CH_3)_3SPbI_3$ Dimensionality Engineering. *ACS Appl. Energy Mater.* **2020**, *3* (3), 2465–2477.

(3) Elsenety, M. M.; Antoniadou, M.; Kaltzoglou, A.; Kontos, A. G.; Philippopoulos, A. I.; Mitsopoulou, C. A.; Falaras, P. Synthesis, Characterization of $((CH_3)_3S)_2SnI_{6-n}Cl_n$ and $((CH_3)_3S)_2SnI_{6-n}Br_n$ (n=1, 2) Perovskites and Use in Dye-Sensitized Solar Cells. *Mater. Chem. Phys.* **2020**, *239*, 122310-122318.

(4) Kaltzoglou, A.; Manolis, G. K.; Elsenety, M. M.; Koutselas, I.; Psycharis, V.; Kontos, A. G.; Falaras, P. Synthesis and Characterization of Lead-Free $(CH_3)_3SSnI_3$ 1-D Perovskite. *J. Electron. Mater.* **2019**, *48* (11), 7533–7538.

(5) Elsenety, M. M.; Kaltzoglou, A.; Antoniadou, M.; Koutselas, I.; Kontos, A. G.; Falaras, P. Synthesis, Characterization and Use of Highly Stable Trimethyl Sulfonium Tin(IV) Halide Defect Perovskites in Dye Sensitized Solar Cells. *Polyhedron* **2018**, *150*, 83–91.

(6) Kaltzoglou, A.; Elsenety, M. M.; Koutselas, I.; Kontos, A. G.; Papadopoulos, K.; Psycharis, V.; Raptopoulou, C. P.; Perganti, D.; Stergiopoulos, T.; Falaras, P. Synthesis, Characterization and Optoelectronic Properties of Chemically Stable $(CH_3)_3SPbI_{3-x}Br_x$ and $(CH_3)_3SPbI_{3-x}Cl_x$ (x = 0, 1, 2, 3) Perovskites. *Polyhedron* **2018**, *140*, 67–73.

(7) Elsenety M. M.; Belesiotis G.; Kaltzoglou, A.; Antoniadou, M.; G., K. A.; Falaras, P. Hole Transporting Behavior of Tin (IV) Hybrid Defect Perovskites Combining $(CH_3)_3S^+$ Cation and Halide Anions. In *Proceedings EG0372*; The 12th Panhellenic Scientific Conference of Chemical Engineering (NTUA): Athens, 2019; pp 29–31.

ACKNOWLEDGMENTS

First, my thanks to the Education Ministry of Egypt (Missions Sector) and the Greek Ministry of Foreign Affairs, for my Ph.D. scholarship and financial support. Also, I would like to thank the chemistry department, faculty of science, Al-Azhar University, Cairo, Egypt for the agreement and support.

Second, my warm thank to the Institute of Nanoscience and Nanotechnology (INN) NCSR "Demokritos" for the opportunity and hosting me during the whole period of the PhD.

My gratitude goes to my supervisor, Dr. Polycarpos Falaras, for the guidance, he gave me during these years, the keenness to train me in a lot of techniques, and the help in accomplishing this challenging, life-changing step in the kindest way possible. My heartfelt thanks to my supervision committee Ass. Prof. A. Philippopoulos and Prof. C. Mitsopoulou for the encouragement and help that I got during these years.

I would like to thank Dr. P. Falaras's group members, from whom I gained a great amount of knowledge, for their kindness and willingness to help, in particular Prof. A. Kontos, Prof. T. Stergiopoulos Dr. A. Kaltzoglou, Dr. M. Antoniadou, Dr. N. Balis, Dr. I. Koutselas, Dr. V. Psycharis, Dr. G. Manolis, Dr. K. Papadopoulos, Dr. M. Vasilopoulou, D. Perganti, I. Ibrahim, A. Zaky, E. Christopoulos, M. K. Arfanis, L. Givalou, K. Gkini, G. Belessiotis, ……etc

I am particularly grateful to the most important men and women of my life, my dad, mom, wife, uncles, aunts, brother, sisters, and relatives for being always on my side, and for supporting me even during my stressed moods.

Warm thanks also to my Egyptian supervisor, Dr. Badr A. Elsayed, all professors and the staff of the chemistry department, faculty of science, Al-Azhar University, Cairo, Egypt, and my colleagues and friends there for the help and support.

M.Elsenety

CONTENTS

CONTENTS

CONTENTS

LIST OF FIGURES

LIST OF FIGURES

LIST OF FIGURES

LIST OF FIGURES

LIST OF FIGURES

LIST OF FIGURES

LIST OF FIGURES

LIST OF FIGURES

LIST OF FIGURES

LIST OF TABLES

LIST OF TABLES

LIST OF TABLES

LIST OF ABBREVIATIONS

PV: Photovoltaic

PCE: Power conversion efficiency

V_{OC}: Open-circuit voltage

J_{SC}: Short-circuit current density

FF: Fill factor

MPP: Maximum power point

DSSC: dye-sensitized solar cell

PSCs: Perovskite solar cells

ETL: Electron-transporting layer

HTL: Hole-transporting layer

HTM: Hole-transporting material

MA: Methylammonium

FA: Formamidinium

FTO: Fluorine-doped tin oxide

FWHM: Full width at half maximum

PL: Photoluminescence

LED: Light-emitting diode

DMF: N, N-dimethylformamide

DMSO: Dimethyl sulfoxide

CB: Conduction band

VB: Valence band

EF: Fermi level

E_g: Bandgap

T: Temperature

Z: Impedance

XRPD: X-ray powder diffraction

AFM: Atomic force microscopy

XPS: X-ray photoelectron spectroscopy

R_s: Series resistance

R_{ch}: Charge transfer resistance

R_{rec}: Recombination resistance

W/m^2: Watt per square meter

DFT: Density functional theory

D-π-A: Donor-pi-acceptor

TPES: Total primary energy supply

TCO: Transparent conductive oxide

AM: Air Mass

ASTM: American Society for Testing and Materials

Hν: photon energy

SRH: Shockley–Read–Hall

ESP: Electrostatic potential

HOMO: Highest occupied molecule orbital

LUMO: lowest un-occupied molecular orbital

DOS: Density of states

PDOS: Partial density of states

S.O.F: Site occupancy factor

CHAPTER (1)

"Introduction & literature review"

CHAPTER 1: Introduction & Literature Review

1.1 Background and motivation

The global energy consumption in 2018 increased at nearly twice the average rate of growth since 2010, driven by a robust global economy and higher heating and cooling needs in some parts of the world. Thus, tremendous environmental impacts have been generated from oil fossil fuel use. Environmental developments have been noted to pose risks to our health and environmental stability. Specifically, carbon dioxide (CO_2, a greenhouse gas) emissions lead to an increase in temperature and climate change.[1] **Figure 1-1**(a, b) illustrate the Global total primary energy supply (TPES) by source, in the period of 1990-2017 and the recent global carbon dioxide emissions across main energy sources, respectively.[2] As a result of higher energy consumption, CO_2 emissions rose 1.7% last year.

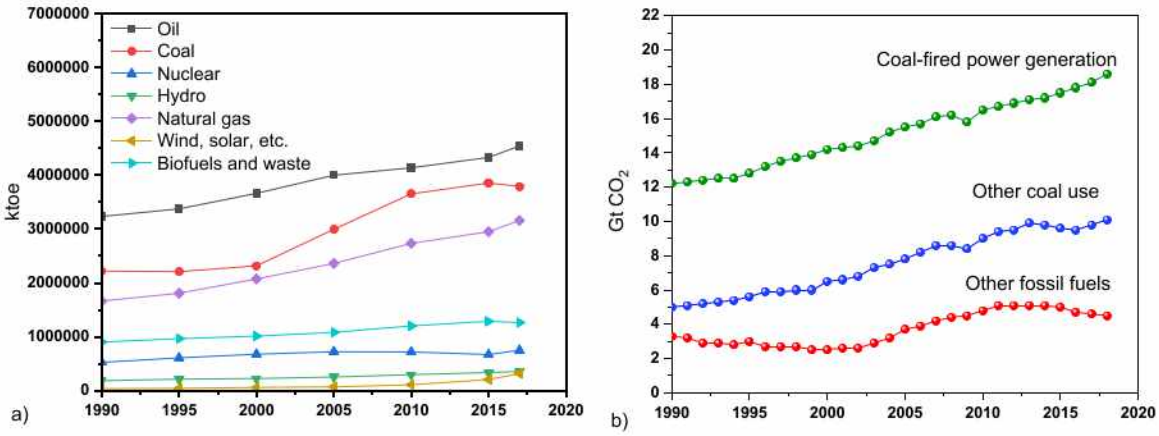

Figure 1-1: Global total primary energy supply (a); Global carbon dioxide emissions across main energy sources (b).

The rapid consumption and major changes in environmental conditions of the limited fossil fuels due to population growth indicate the urgent need for modern, sustainable, renewable and clean energy resources. Therefore, the need for an energy source that is abundant, does not produce carbon dioxide, and that can supply a large fraction of the world's needs is of the utmost importance if society is to continue its current energy consumption.

Figure 1-2, shows that all candidates as renewable energy sources include wind power, solar power, geothermal power, tidal power and hydropower.

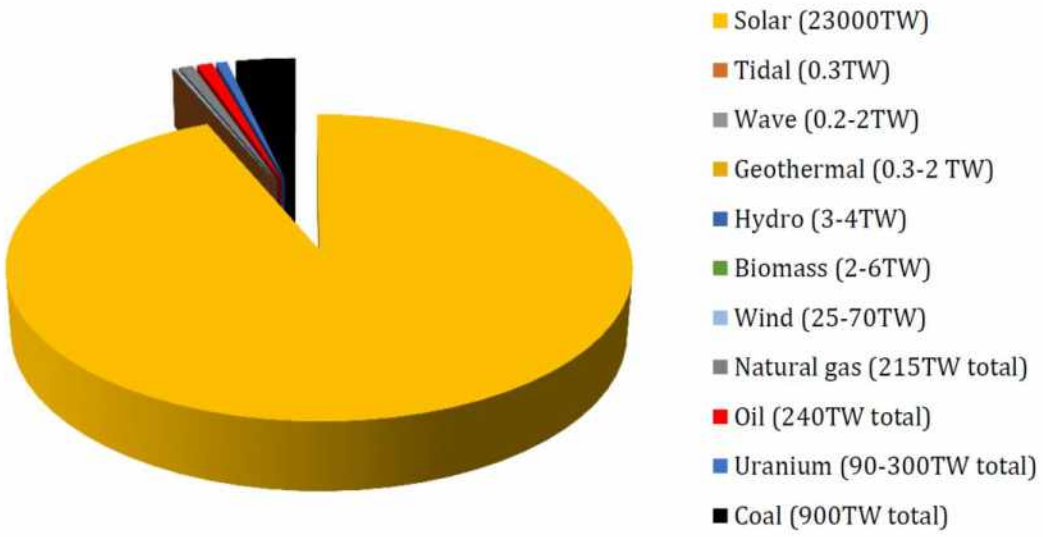

Figure 1-2: The potential for finite and renewable energy sources. [3]

A first major step towards reducing the greenhouse gas was taken in 1997 by 192 countries (including the EU) that signed the Kyoto Protocol.[4] Further adjustments were made in 2015 when 195 countries signed the Paris Agreement, which aims to reduce the impacts of climate change and restrict the global warming below 2°C on average before the end of this century.[5] Additionally, the governments decided to reach more optimistic goals every 5 years.

In 2018, there was an even greater global clean energy investment which more internationally, especially in China, Europe, and the United States. In recent years, renewable energy systems have developed rapidly mainly because of substantial cost savings in photovoltaic solar cells and wind power fields.

Solar photovoltaic devices have proven to be the most significant development leading to creating effective solutions for renewable energy. It was reported that the total annual capacity for solar irradiation is 6000 times global annual energy consumption.[6] In addition, the production of PV is flexible and scalable PV itself can be used for broad solar parks from mobile and home installations needing a minimum of maintenance and guaranteed 90% of its output for 25 years. There are several solar photovoltaic systems, but silicone cells are the most appropriate commodity on the market, accounting 95% of the overall PV output in 2019.[7] Silicon is commonly used in both crystalline and polycrystalline forms. However, the most efficient Silicon crystalline wafer produces up to 26.7% in December 2019.[8] While the

earth is rich in silicon (in the form of quartzite), but there are constraints, including costly processes of purification and non-favorable physicochemical properties of indirect bandgap and low absorption coefficient. Thus, new interest innovations have emerged, including thin-film technologies Cadmium telluride, Copper indium gallium selenide, Gallium arsenide, single/Multijunction cells, Dye-sensitized cells, organic cells, inorganic, perovskite cells, Quantum dot cells. Some of these have achieved or exceed the performance of the silicone devices. Despite high efficiencies, but the stability challenge remains under researching and development. **Figure 1-3** shows the record efficiencies of the main PV technologies that have emerged and developed until 2020.[9]

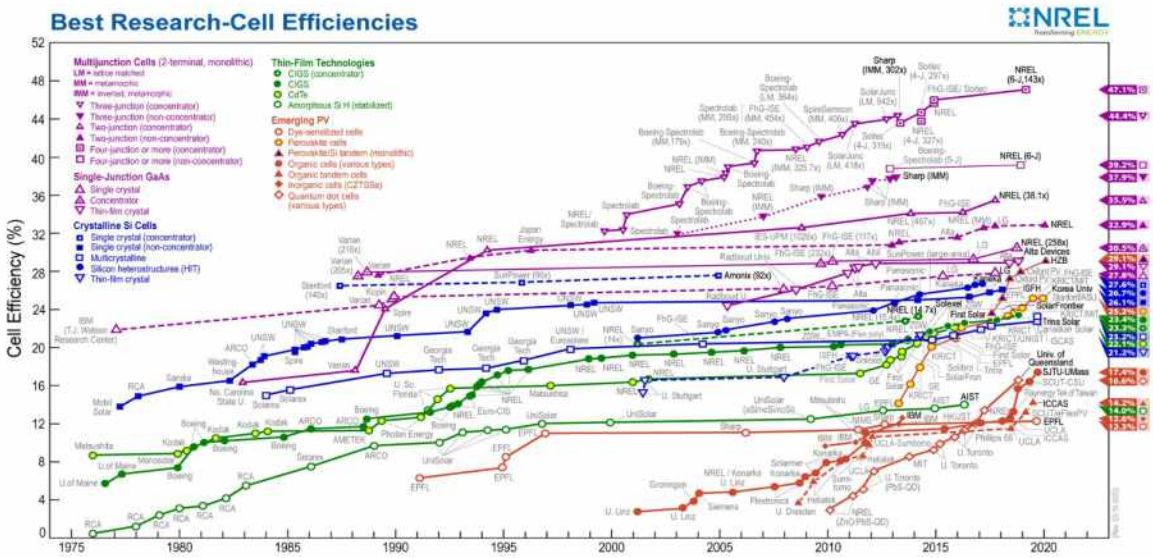

Figure 1-3: The record efficiencies of the main PV technologies.[9]

Thus, PV will continue to produce power indefinitely (as long as the sun shines). Photovoltaic are truly a sustainable and environmentally friendly method of producing energy. Not only this but it's for free, so why shall we not utilize it.[10] PV technology provide the dramatic achievements in the field of photochemical and photovoltaic conversion of solar energy into electricity. The selection of PV technology base on different criteria such as efficiency, cost of production, stability, etc.

Today a range of PV cell technologies are available on the market, PV solar cell technologies are usually classified into three generations (**Figure 1-4**), depending on the basic material used and the commercial level.

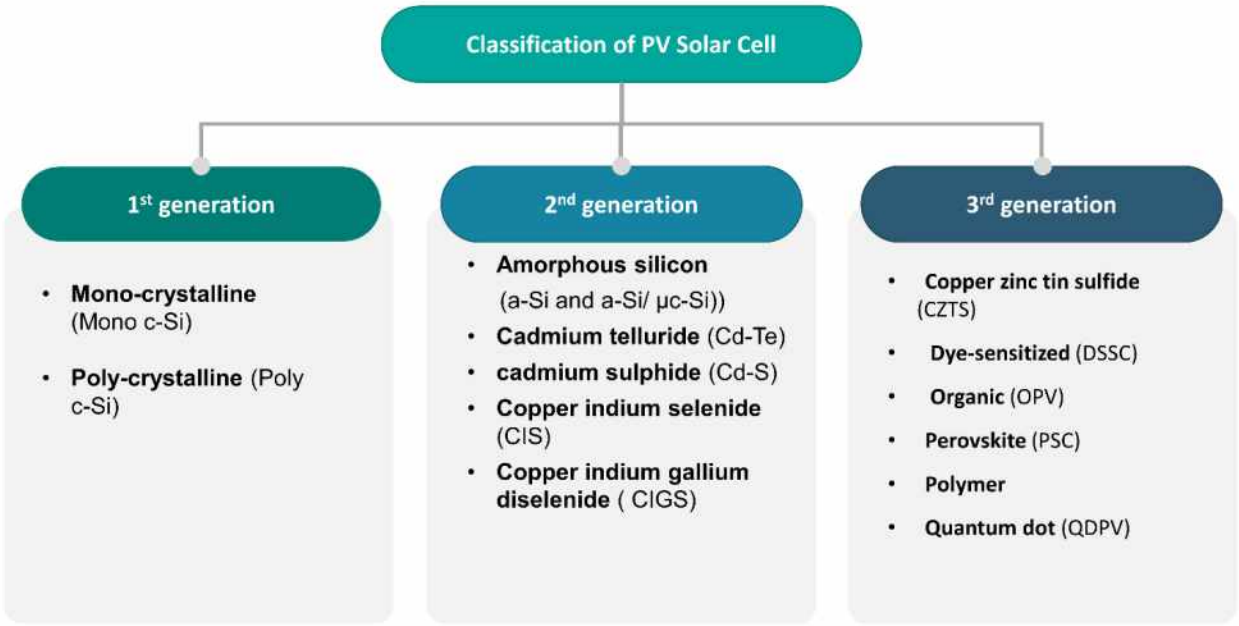

Figure 1-4: Classification of PV cells.

Recently, extensive efforts have been made to address the problems by designing new practical materials. Since the energy conversion processes in different technologies are different, the functional materials used in these technologies require rather different materials properties.

Among the new materials of photovoltaic technologies, DSCC and perovskite devices have shown impressive results and attracted much attention in the photovoltaic community due to low cost production and their efficiency in converting solar energy into electricity. Moreover, perovskite solar cells (PSCs) have reached power conversion efficiency (PCE) values over 25% in less than ten years, achieving device performances that are very close of those accomplished by Silicon.[8,9]

1.2 Dye-sensitized solar cells (DSSC)

A typical DSSC is composed of a porous layer of transparent titanium dioxide (TiO_2) nanoparticles, coated with a molecular dye that absorbs sunlight, such as metal organic (Z907, N719) and organic (MK2, D35) dyes or like the chlorophyll in green leaves.[11] The transpar-

ent TiO_2 electrodes (as an anode) is sensitized by immersion into dye solutions (as an electrolyte) for some hours, above which is a platinum-based catalyst counter electrode (as a cathode). Sunlight passes through the transparent photoanode (TiO_2) into the photosensitive dye layer where it can excite electrons that then flow into the anode. The electrons flow toward the photoanode where they are collected for powering a load. After flowing through the external circuit, they are reintroduced into the cell on a counter electrode on the back, flowing into the electrolyte. The electrolyte then transports the electrons back to the dye molecules, by oxidation reduction process, as shown in **Figure 1-5**.

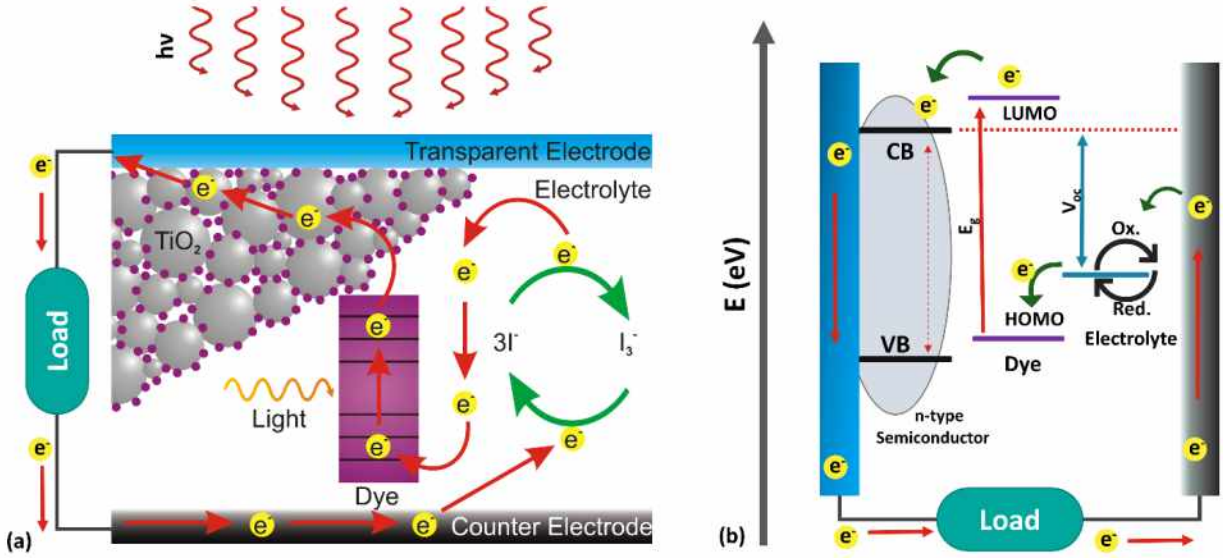

Figure 1-5: (a) Principle of operation and (b) energy level diagram of a typical DSSC. (figure (a) has been modified and taken from reference [12])

1.3 Perovskite solar cells

A perovskite is any material with the same type of crystal structure as calcium titanium oxide ($CaTiO_3$), known as the perovskite structure. Perovskites take their name from the mineral, which was first discovered in the Ural mountains of Russia by Gustav Rose in 1839 and is named after Russian mineralogist L. A. Perovski (1792–1856).[13,14]

1.3.1 Structure of perovskite

Oxide-perovskites and their derivatives ABO_3 (where A and B are large electropositive cations) have been widely reported and exhibit several other attractive magnetic and dielectric

properties including (e.g. superconductivity, ferroelectricity, magnetoresistance, ionic conductivity, piezoelectricity, etc.), which can be used in all these technologies, reflecting their multipurpose properties.[15–20] The ideal oxide perovskite structure is a cubic phase with a high symmetry of $Pm\bar{3}m$ space group (No.221), which usually observed at high temperatures above 1000 K.[21] In fact, cubic perovskites undergo octahedral rotations along thier symmetry axes ([100], [010], [001]) and change to lower symmetry phases at low temperature (e.g., orthorhombic, tetragonal, rhombohedral, etc.).[22–24]

Recently, halide perovskites have attracted global interest in photovoltaic applications due to their superior photovoltaic properties such as extremely high optical absorption coefficient, super long carrier diffusion length and low-temperature solution processability.[25–27]

Perovskite solar cells (PSCs) evolved from the solid-state, dye-sensitized solar cells (DSSCs)[28,29] by replacing the dye absorber with an ABX_3 type.

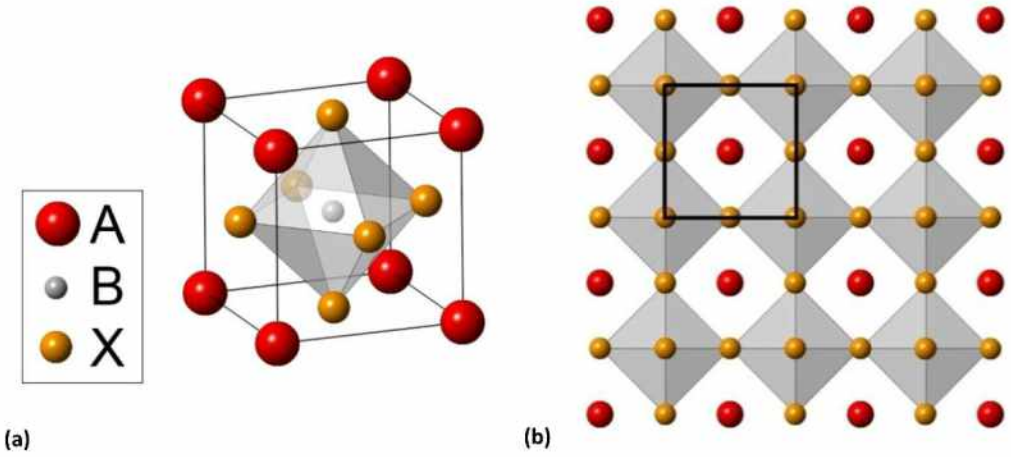

Figure 1-6: Crystal structure of ABX_3-type metal halide perovskites (a); View along one crystallographic axis of a greater number of unit cells, with the unit cell black (b).[30]

Halide perovskite architecture contains a wide variety of crystalline materials with the stoichiometry of ABX_3, where A is a monovalent organic cation (e.g. methylammonium ($CH_3NH_3^+$, MA^+), formamidinium ($CH(NH_2)_2^+$, FA^+)) or an inorganic cation (e.g. K^+, Rb^+, Cs^+), B = (Pb^{+2}, Sn^{+2}), and X = Cl^-, Br^-, I^-. The efficiency of PSCs has increased within only a few years of development and researchers elaborate intensively on their optimization. **Figure 1-6** shows the optimal form of perovskite material, it's a cubic crystal structure collected

from corner-sharing [BX_6] octahedral to form a three dimensional (3D) network, whereby *A* cations are occupying the resulting holes with cuboctahedra symmetry (12-fold) sites.[30]

In addition, most perovskites are distorted and do not have the ideal cubic structure. Glazer has shown that, based on possible distortions of the octahedron [BX_6] with respect to its neighboring octahedra, the perovskite structure can have 15 different space-group symmetries in the case of spherically symmetric groups of monovalent cations (eg. Rb^+, Cs^+).[22] However, in the case of non-spherically symmetric groups such as organic methylammonium, $CH_3NH_3^+$, additional space-group symmetries exist, and more complete classification of perovskite structured symmetries was presented by Alexandrov et al.[31]

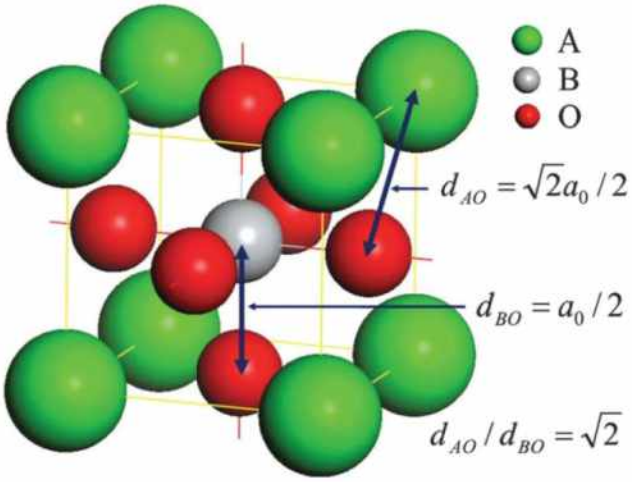

Figure 1-7: Schematics of the ideal lattice of perovskites and the relation between structure parameters.[32]

The ideal structure of perovskites, as shown in **Figure 1-7**, is a cubic lattice in which the A–O distance (d_{AO}) is $\sqrt{2}$ times larger than the B–O distance (d_{BO}).[32] Although most perovskites have slight or large distortions tending to lower the symmetry and stabilize the lattice. Thus, the size of perovskite (ABX_3) and their derivatives are usually associated with a geometrical misfit of the relative ionic dimensions. In the ideal cubic case the cell axis, a, is geometrically related to the ionic radii r_A, r_B, and r_X of A, B, and X respectively, and it can be calculated through the *Eq. 1*.[33,34]

$$a = \sqrt{2}\,(r_A + r_X) = 2\,(r_B + r_X) \qquad \textit{Eq. 1.1}$$

The ratio of the two expressions for the cell length is called the Goldschmidt's tolerance factor *t* and allows us to estimate the degree of distortion and predicting stability of the geometric ratio. It is based on ionic radii (i.e. purely ionic bonding is assumed) but can be regarded as an indication for compounds with a high degree of ionic bonding; Goldschmidt tolerance factor, *t*, is described in *Eq. 1.2* .[33–35]

$$t = \frac{r_A + r_X}{\sqrt{2(r_B + r_X)}} \qquad \textit{Eq. 1.2}$$

Where r_A, r_B and r_X are the ionic radii of 'A', 'B' and 'X', respectively. The tolerance factor calculates whether the A site cation in the BX_3 system will fit inside the cavities. A tolerance factor of 1 implies a great fit; in the range $0.8 \le t \le 1$ perovskites generally do form. Moreover, if tolerance factor more than 1, this indicates the A site cation is too large and generally prevents formation of a 3D perovskite framework, and if tolerance factor less than 0.8, the A cation is too small, again often leading to alternative structures depending on thermodynamically stability. Also, the octahedral factor (μ) of [BX_6] octahedron has an importance of its own and responsible for the favored symmetry, which defined in *Eq. 1.3*.

$$\mu = r_B \,.\, r_X \qquad \textit{Eq. 1.3}$$

Empirical structure maps of $t-\mu$ show that the formation window of a perovskite is limited to $0.8<t<1$ and $\mu>0.4$ for oxide perovskites and $0.85<t<1.1$ and $\mu>0.4$ for halide-perovskites.[36,37] Therefore, the Goldschmidt tolerance factor and octahedral factor have attracted considerable attention recently to predict novel perovskite compounds for photovoltaic applications based on the ionic radii of the involved ions, and **Table 1-1** shows the effective ionic radius (r) of commonly used ions in ABX_3-type.[26,38–43]

Besides *t* and μ which describe the interatomic spacing of A, B, and X in the unit cell of perovskite crystal system, the ionic charge (the formal oxidation state at each lattice point) also affects the formation energy.

Table 1-1: Effective ionic radii of organic molecular cations and Shannon ionic radii of inorganic cations as well as effective ionic radii of various anion.

A	*r A*,eff/pm	B	*r B*,eff/pm	B	*r B*,eff/pm	X	*r X*,eff/pm
Ammonium, $[NH_4]^+$	146	Pb^{2+}	119	Te^{4+}	97	F^-	129
Hydroxylammonium, $[NH_3OH]^+$	216	Sn^{2+}	110	La^{3+}	103	Cl^-	181
Methylammonium, $[CH_3NH_3]^+$	217	Sn^{4+}	69	Ce^{3+}	101	Br^-	196
Hydrazinium, $[NH_3NH_2]^+$	217	Ge^{2+}	73	Pr^{3+}	99	I^-	220
Azetidinium, $[(CH_2)_3NH_2]^+$	250	Mg^{2+}	72	Nd^{3+}	98	$HCOO^-$	136
Formamidinium, $[CH(NH_2)_2]^+$	253	Ca^{2+}	100	Sm^{3+}	96		
Imidazolium, $[C_3N_2H_5]^+$	258	Sr^{2+}	118	Eu^{3+}	95		
Dimethylammonium, $[(CH_3)_2NH_2]^+$	272	Ba^{2+}	135	Gd^{3+}	94		
Ethylammonium, $[(CH_3CH_2)NH_3]^+$	274	Cu^{2+}	73	Dy^{3+}	91		
Guanidinium, $[(NH_2)_3C]^+$	278	Fe^{2+}	78	Er^{3+}	89		
Tetramethylammonium, $[(CH_3)_4N]^+$	292	Pd^{2+}	86	Tm^{3+}	88		
Thiazolium, $[C_3H_4NS]^+$	320	Eu^{2+}	117	Lu^{3+}	86		
3-Pyrrolinium, $[NC_4H_8]^+$	272	Tm^{2+}	103	Pu^{3+}	100		
K^+	164	Yb^{2+}	102	Am^{3+}	98		
Rb^+	172	Tl^+	150	Bk^{3+}	96		
Cs^+	188	Au^+	137	Sb^{3+}	76		
trimethylsulfonium $(CH_3)_3S^+$	244	Au^{3+}	85	Bi^{3+}	103		

Table 1-2 shows formation energies and site potentials (Madelung potentials) for perovskites with different formal oxidation states in each site.

Table 1-2: Electrostatic lattice energy ($E_{lattice}$) and site Madelung potentials (V_i) where (I = A, B, X) for a range of ABX_3 perovskite structures (cubic lattice, a = 6.00 Å) assuming the formal oxidation state of each species

Stoichiometry		$E_{lattice}$ (eV/cell)	V_A (V)	V_B (V)	V_X (V)
Oxides & chalcogenides	I–V–II_3	−140.48	−8.04	−34.59	16.66
	II–IV–II_3	−118.82	−12.93	−29.71	15.49
	III–III–II_3	−106.92	−17.81	−24.82	14.33
Halides	I–II–I_3	−29.71	−6.46	−14.85	7.75

The halide perovskites, [I]-[II]-$(I)_3$, have exceptionally lower formation energy values, compared to those with divalent X anions.

1.3.2 Dimensionality of hybrid perovskites

Typically, 3D hybrid perovskites adopt a cubic structure formed from corner-sharing $[BX_6]^{4-}$ octahedra (**Figure 1-6**). Notably, the A cation (such as FA, MA, Cs, Rb) must be small enough to fit within the voids of the octahedral units to preserve the structural integrity of the 3D lattice.

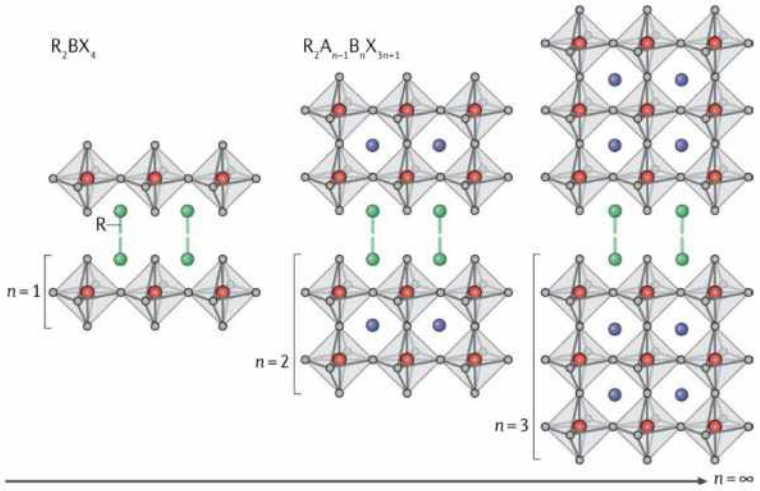

Figure 1-8: Illustration of the structures of low-dimensional perovskites with different numbers of perovskite layers (n). The pure 2D perovskite (n = 1) has a R_2BX_4 structure, where R is a bulky organic cation. For n > 1, the quasi-2D perovskites arrange into a $R_2A_{n-1}B_nX_{3n+1}$, structure.

The maximum dimensions of the organic cations are empirically determined by the so-called Goldschmidt tolerance factor, which limits the radius of the A cation to 2.6 Å. Thus, only a few organic cations have suitable dimensions to insert into the structure and form a stable 3D lattice.[44] Another class of materials gaining significance are the two-dimensional (2D) perovskites (**Figure 1-8**) -a blend of perovskites with layered crystal structure- (Ruddlesden-Popper type) offer a greater synthetic versatility and allow for more specialized device implementation due to the directional nature of the crystal structure.

1.3.3 Fabrication processes of perovskite devices

The quality of perovskite layer is critical for the device performance. The deposition of the perovskite films is mainly based on the reaction of the organic halide (e.g. MAX/FAX) or Inorganic halide (e.g. CsX/RbX) with lead/Tin halide components, where X= I, Cl, Br. Until now, several deposition processes for Lead/Tin halide perovskite films have been investigated which, in the form of solution processes, vapor processes and combinations, are mainly classifiable as a single-step or two-step processes. Generally, both methods configure device architecture of TCE/ETL/Perovskite/HTL/Ag. However, continuous improvements in device layers and architecture, perovskite growth techniques and mixed halide perovskite with enhanced electronic properties have been achieved to enhance photovoltaic performance.

In particular, PSCs configuration can be classified into two major groups: a) regular n-i-p PSCs, in which electron transporting layer (ETL) is spin-cast onto transparent conductive oxide electrode (TCO), and b) inverted p-i-n PSCs, in which hole transporting layer (HTL) is spin-cast onto TCO. Therefore, each type of PSCs can be determined by the arrangement of deposited layers.

- **One-step process**

In one step process, organic and inorganic precursors are co-deposited through a solution or a vapor process. Generally, a mixed solution of Lead/Tin halide and Organic/Inorganic halide in polar solvents (DMSO, DMF, GBL) should prepared in inert gas condition. Then, perovskite films were deposited by spin-coating, followed by thermal annealing. However, many reports studied the effect of different stoichiometric ratio of perovskite precursors or solvents,[45,46] crystallization,[47] using additives.[48] Moreover, Seok et al. developed a solvent engineering technique to improve the film quality (extremely uniform, dense perovskite layers

and better covered than the pristine films), by using nonpolar solvent of toluene dripping while spin-coating of the perovskite precursor in the mixture of GBL and DMSO.[49]

- **Two-step process**

In one step process, organic and inorganic precursors are co-deposited through a solution or a vapor process. Two-step methods, or sequential methods, are based on the formation of PbX_2 layer, by spin-coating, and their subsequent transformation into perovskite films. The transformation process of the PbX_2 films can be done in deferent ways, (a) dipping in a MA/FA/Cs halide solution,[50,51] (b) spin-coating of MA/FA/Cs halide solution on top of the PbX_2 layer,[52,53] or (c)evaporating MA/FA/Cs halide powder at elevated temperature and exposing the PbX_2,[54] as shown in Figure 1-9.

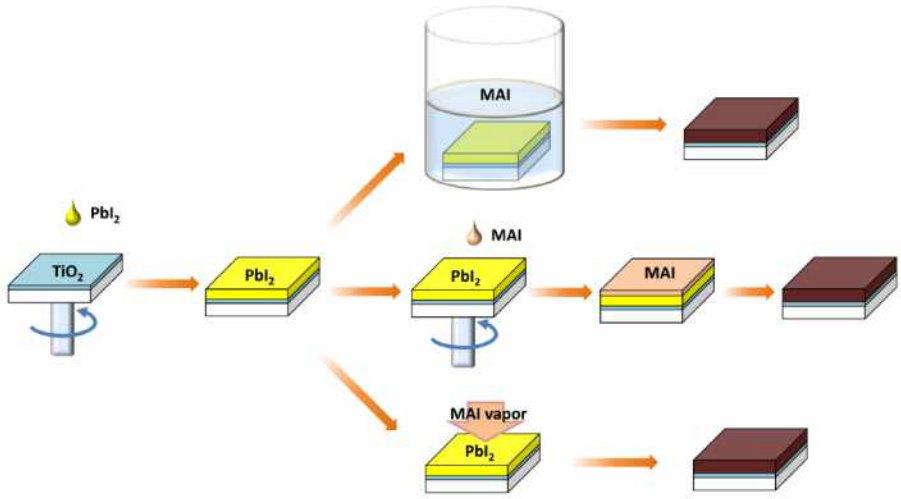

Figure 1-9: Schematic diagram of two-step methods for perovskite film preparation.

1.3.4 Significant Promises and Challenges

The unique characteristics of perovskite materials drew greater interest in the field of photovoltaic applications, that has propelled enormous work done in a short span of ten years. Significant features of these perovskites such as low energy tunable bandgap, high absorption coefficient, high charge carrier diffusion length, low exciton binding energy, balanced electron–hole transport, shallow defects, and easy low-cost solution processing, which makes it highly desirable as a promising photovoltaic material.

Although perovskite solar cells have demonstrated numerous extraordinary properties and their potential to replace silicon based solar cell, with low cost fabrication and high device efficiency, some issues (e.g. hysteresis, stability and toxicity) still need to be addressed before to their widespread application. Apart from those issues, the practical technological issues (stability) is a major bottleneck in achieving its high potential, which mainly due to the presence of highly hydrophilic organic cations (methyl ammonium-MA or formamidinium-FA).[55] Moreover, these perovskite devices are highly sensitive to moisture in ambient air. Moisture leads to a domino effect of decomposition of perovskite film causing material degradation, thus losing photovoltaic properties.

Furthermore, the use of toxic lead in perovskite is a matter of environmental concern. Lead compounds are very hazardous, and the impact of lead-based perovskite devices is a big concern for their large-scale application. As a good alternative to lead perovskites, less toxic tin-based analogues were developed but the long-term performance of the corresponding devices is seriously affected by the progressive oxidation of Sn^{2+} to Sn^{4+}.[56,57]

Another crucial issue, which has been studied and discussed widely, is hysteresis in perovskite devices. However, various approaches have been implemented to reduce the hysteresis behavior in these devices.

1.4 Fundamentals of solar cells

1.4.1 Solar irradiance

Solar radiation is the power generated by the Sun's nuclear fusion reactions per unit area (W/m^2), in the form of electromagnetic radiation, which reaches Earth with an intensity of 1367 W/m^2. However, this is reduced by atmospheric absorption and dispersion and is dependent on Earth's latitude as shown in **Figure 1-10** of global horizontal radiation map.[58] The solar cell will absorb a range of energy that reflects the spectrum of solar radiation above and at the surface of the Earth that equals ~1000 W/m^2 (after atmosphere attenuation), with an incline of 37° comparable to the equator.

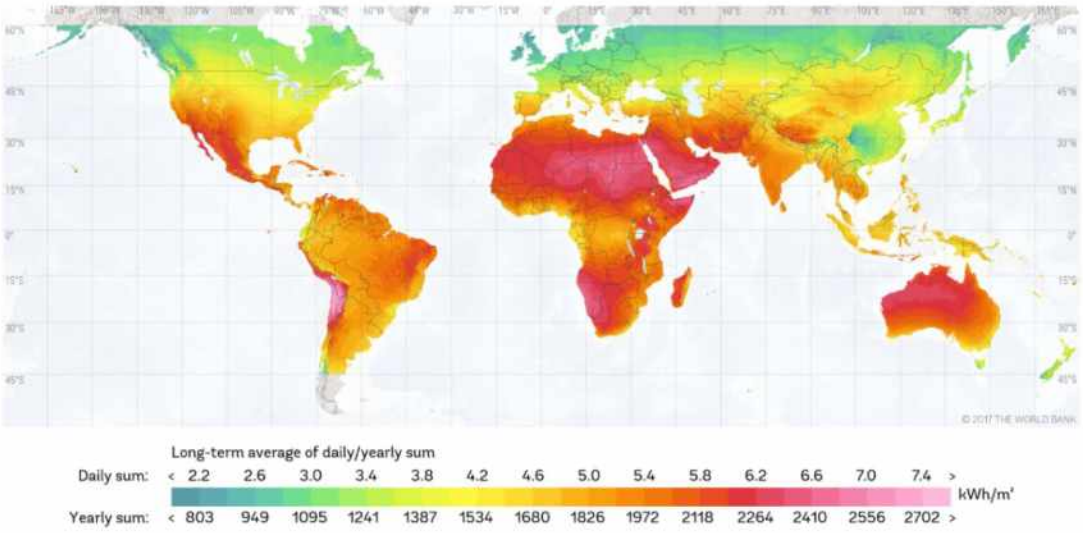

Figure 1-10: Global Map of Global Horizontal Radiation.[58]

The evaluation of solar cell devices has been therefore standardized using the AM1.5 irradiance spectrum, where AM is the air mass coefficient defines the direct optical path length through the Earth's atmosphere, expressed as a ratio relative to the path length vertically upwards).[10,59]

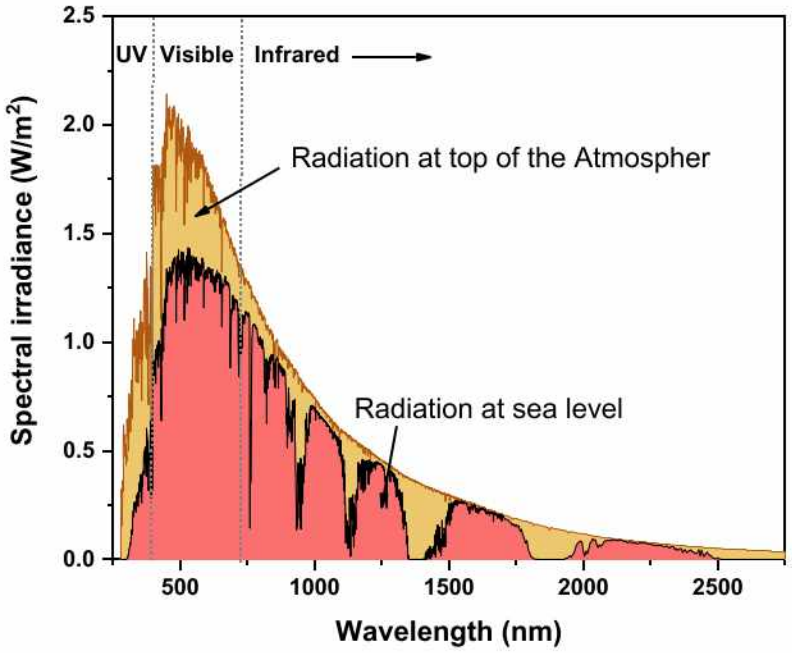

Figure 1-11: Solar irradiance spectrum above atmosphere and at surface, plotted using the ASTM G137-03 reference spectra.[9]

The solar irradiance spectrum has a wide range (100nm up to 1mm) of electromagnetic radiation. But as **Figure 1-11** shows most of the irradiance occurs between 250nm- 2500nm with the maximum in the visible region of light (300-800nm), which ensures that solar cells will strive to absorb as much of the sunlight in the visible region.[10] Whereas at low wavelengths (< 300 nm) absorption is caused by oxygen, ozone and nitrogen, while water and carbon dioxide molecules cause absorption at high wavelengths in the infrared region.

1.4.2 The photovoltaic effect

The photovoltaic effect is the phenomenon that converts sunlight into electrical energy. When a photon hits a solar cell, one of three things can happen:

- The photon can pass straight through the absorbing layer — this (generally) happens for lower energy photons.
- The photon can reflect off the surface.
- The photon can be absorbed by the absorbing layer if the photon energy is higher than the absorber band gap value.

If A photon is absorbed by a medium, this generates an electron-hole pair and sometimes heat depending on the band structure. It differs from the photoelectric effect in which an electron is ejected out of the material into the vacuum, whereas in the photovoltaic effect the electron is excited from the ground state S_0 (valence band / HOMO) to the excited state S_1 (conduction band / LUMO) of a semiconductors or dyes, as shown in Jablonski Diagrams (**Figure 1-12**), where (S = singlet state, T= triplet state, IC= internal conversion, ISC= inter-system crossing, R= relaxation, F= fluorescence, P= phosphoresces). The photon is absorbed in the material only if the photon energy ($h\nu$) ≥ energy bandgap (E_g). Photo-excited electrons in higher excited state (S_n) with $h\nu > E_g$, quickly relax to the conduction band (S_1) and lose their surplus energy by Internal Conversion (IC) processes. On the contrary, photons with $h\nu < E_g$ are not absorbed and are therefore transmitted by the material.

Moreover, the bandgap of a semiconductor can either be described as direct or indirect, which refers to whether there must be a transfer of phonon (crystal lattice vibration) momentum involved in an absorption or emission process. The material is said to be a direct

bandgap, if no momentum transfer required. In contrast, it is said to be an indirect gap material, if momentum transfer required. Phonon momentum is described in *k*-space, related to the Fourier transform of the periodicity of the lattice in real space. In a direct bandgap material, the CB minimum and VB maximum have the same value of *k*, in an indirect bandgap material they differ, as shown in **Figure 1-12**.

In traditional Si-solar cell, after light absorption, normally the silicon acts as both the source of photoelectrons, as well as providing the electric field to separate the charges (electron/hole pairs) and create a current. The generated charges must reach the depletion region in order to avoid recombination.

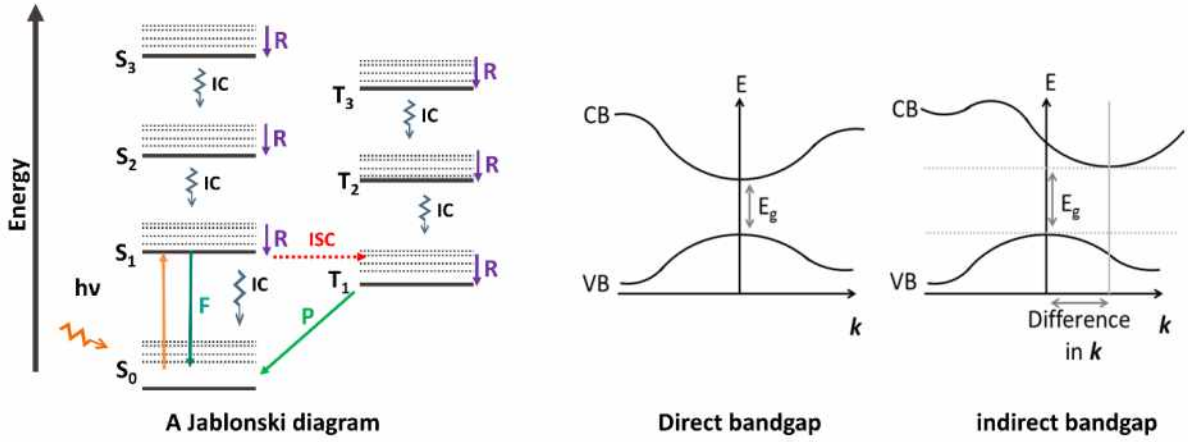

Figure 1-12: A Jablonski diagram and Diagram of direct and indirect bandgap materials, represented in k-space.

Due to the presence of the electric field, these e-/h+ pairs are separated and drift: the electrons toward the n-part and the holes toward the p-part of the Si-cell. By connecting the device to an external circuit, the electron flow will produce electric current. However, in the DSSC and perovskite cells separate the two functions provided by Si-cell. In the DSSC and perovskite cells, the n-type semiconductor (electron transport layer -ETL) is used only for charge transport, the photoelectrons are provided from a absorbing layer (perovskite / photosensitive dye). Charge separation occurs at the surfaces between the absorbing layer and ETL in the front side of the cell, and between the absorbing layer and hole transport layer (HTL)/ electrolyte for perovskite/ DSSC, respectively.

1.4.3 Current-Voltage I-V characteristics

1.4.3.1 Equivalent circuit of a solar cell

To understand the electronic behavior of a solar cell, it is useful to create a model which is electrically equivalent and is based on discrete ideal electrical components whose behavior is well defined. A schematic representation of an ideal solar cell modelled by a current source in parallel with a diode shown in circuit diagrams of **Figure 1-13**; in practice no solar cell is ideal, so a shunt resistance and a series resistance component are added to the model. Both models are designed by a diode (I_D) and a current generator (I_L), however the real solar cell contains parasitic series (R_S) and shunt resistances (R_{SH}).

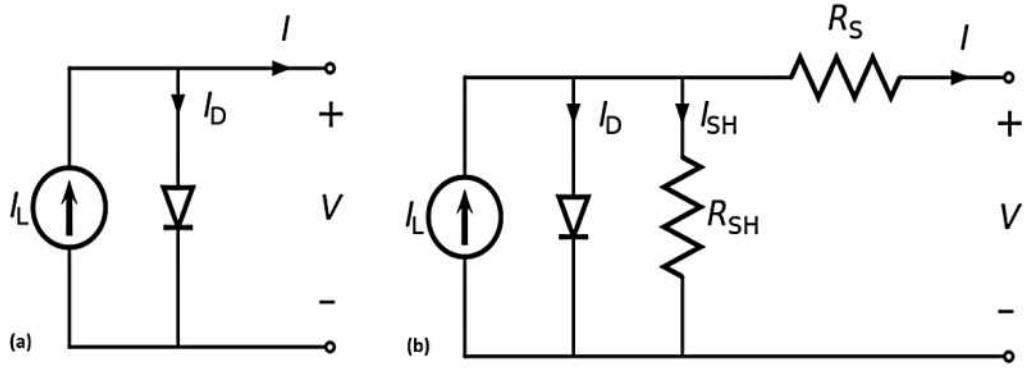

Figure 1-13: Equivalent circuit of an ideal cell (a); and a real solar cell (b).

The p-n junction can be represented under dark conditions with a single diode, the current density – voltage (J – V) response is provided by the Shockley diode equation, (Eq. 1.4), where current density (J = I/area) in an ideal diode.

$$J = J_0\left(e^{\frac{eV}{nk_BT}} - 1\right) \qquad \textit{Eq. 1.4}$$

where: J is the current diverted through the diode, J_0 is the reverse saturation current, V is the voltage across the diode, k_B is the Boltzmann's constant, T is absolute temperature and n is the diode ideality factor (a parameter which indicates how close the diode follows the ideal diode equation). The ideality factor is strictly related to the quality of the solar cell material and the recombination processes (1 for an ideal diode). However real solar cell model, the diode is connected in parallel to a current source (light) and hence the *J-V* response is:

$$J = J_0\left(e^{\frac{eV}{nk_BT}} - 1\right) - J_L \qquad \textit{Eq. 1.5}$$

where: J_L is the light generated current. Moreover, both shunt (R_{SH}) and series resistances (R_S), which should be taken into consideration of the *J-V* response in the real model as a following equation:

$$J = J_0\left(e^{\frac{e(V-AJR_S)}{nk_BT}} - 1\right) - J_L + \frac{V-AJR_S}{R_{SH}} \qquad \textit{Eq. 1.6}$$

Where R_{SH} = shunt resistance (Ω), shunt current density $J_{SH} = [(V\text{-}AJR_S)/R_{SH}]$ *and A* is the active area of the solar cell.[60–62]

1.4.3.2 Performance parameters

A typical J-V (**Figure 1-14**)characterization is carried out by illuminated solar cells that provide short-circuit current density (J_{SC}), current maximum PowerPoint density (J_{MPP}), open-circuit voltage (V_{OC}), voltage maximum PowerPoint (V_{MPP}), and fill factor (FF). These values are significant for calculate the power conversion efficiency (PCE %) of the solar cell.

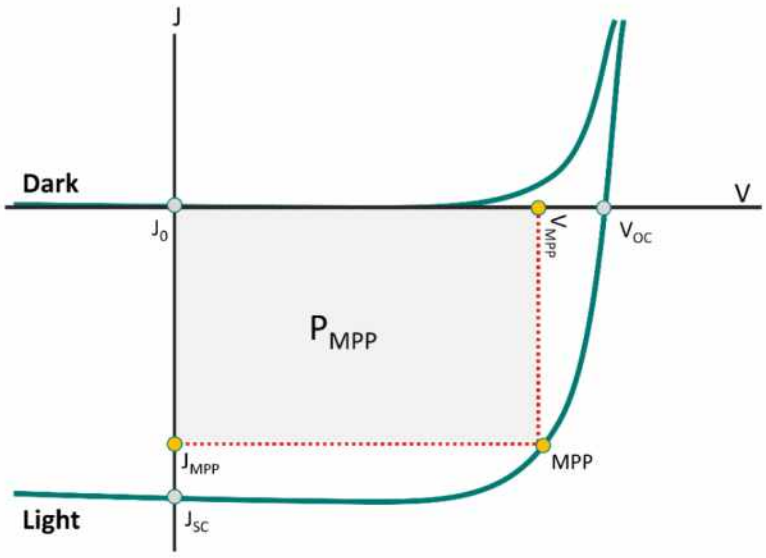

Figure 1-14: A typical J-V curve of a solar cell device under dark and light conditions.

The main parameters for the illuminated *J-V* curve are described as follows:

- Short circuit current density (J_{SC}): is the current density flowing in the external circuit when the voltage is zero (when the cell is operated at open circuit).
- Open circuit voltage (V_{OC}): it's referred to the maximum voltage available for the solar cell, when the current is zero (no current can flow J = 0).
- J_{MPP} and V_{MPP} are the maximum current and voltage output of the device, respectively.
- Maximum power point (MPP), it's corresponds to the maximum power output of the device and it can be calculated using the following equation:

$$P_m = J_{MPP} \,.\, V_{MPP} \qquad \textit{Eq. 1.7}$$

- Fill factor (FF) This parameter defines the 'squareness' of the J-V curve and corresponds to the ratio of the maximum power density (P_m at MPP) and the $V_{OC} \cdot J_{SC}$ product, as shown in the following equation.

$$FF = \frac{P_m}{J_{sc} \cdot V_{oc}} = \frac{J_{MPP} \,.V_{MPP}}{J_{sc} \cdot V_{oc}} \qquad \textit{Eq. 1.8}$$

- Power conversion efficiency (PCE): it is defined as the ratio of the output power (P_{out}) and the input power (P_{in}) at AM1.5 which equal 1000 W/m^2 as shown in the following equation:

$$PCE\ (\%) = \frac{P_{out}}{P_{in}} \,.\, 100 = \frac{J_{MPP} \,.V_{MPP}}{P_{in}} \,.\, 100 = \frac{J_{sc} \cdot V_{oc} \cdot FF}{P_{in}} \,.\, 100 \qquad \textit{Eq. 1.9}$$

1.4.3.3 Shockley-Queisser limit (SQ Limit)

The maximum theoretical efficiency of a single p-n junction solar cell is determined by the SQ Limit, which collect power from the cell where the only loss mechanism is radiative recombination in the solar cell.[63,64] Thus, SQ Limit is a function of the band gap (E_g) and the incident spectrum. Since the incident spectrum is standardized (AM1.5), the power conversion efficiency (*PCE%*) is depend only by the E_g, as presented in **Figure 1-15a**.

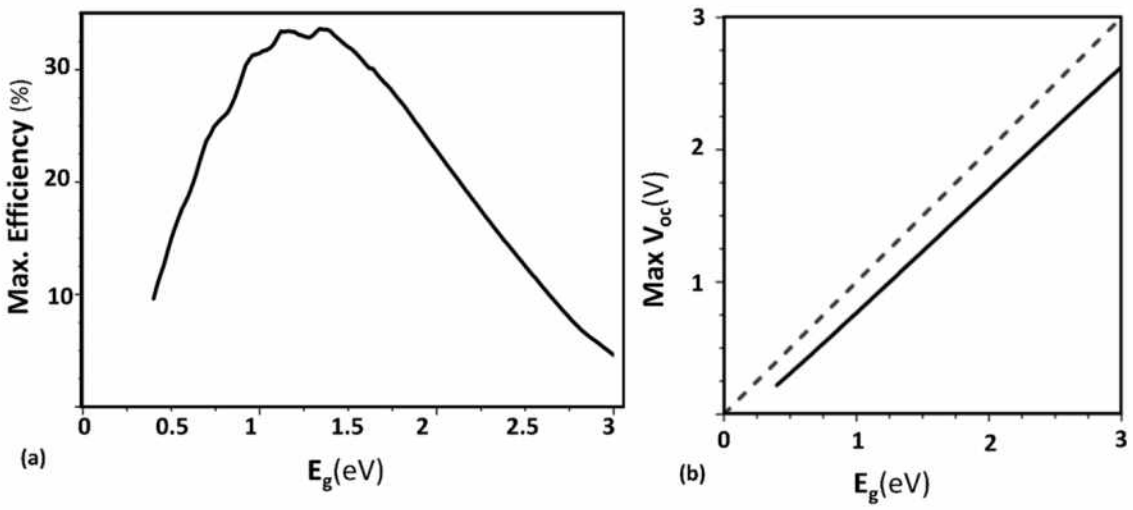

Figure 1-15: (a) SQ Limit for a single junction solar cell at AM1.5. (b) The limit for open-circuit voltage in the SQ model (red dotted line: the voltage is limited by recombination).

Highest values of the efficiency are produced with a range (1: 1.6 eV) of bandgaps, and the maximum efficiency of 33.7% is achieved by materials having E_g of ~1.4 eV. Since the limit for open-circuit voltage in the SQ model which refer to direct proportion relation of E_g with open circuit voltage V_{oc} (**Figure 1-15b**); small E_g produce devices having small working voltages. On the contrary large E_g produce small photocurrents, and loss mechanism in solar devices is thermalization (absorption for $h\nu \geq E_g$).

1.4.3.4 Incident photon-to-current efficiency

The measure of incident photon-to-current efficiency (IPCE), also known as external quantum efficiency (EQE), which defined as the ratio of the photogenerated charge carriers that are collected by the solar cell, to the number of incident photons; and used to reveal how efficiently the incident photons convert to the charge carriers collected at the electrodes. $IPCE$ can be calculated by dividing the photocurrent generated under monochromatic illumination by the incident light:

$$IPCE\ (\lambda) = \frac{N_{electrons}(\lambda)}{N_{Photons}\ (\lambda)} = \frac{h\ .\ c\ .\ J_{sc}(\lambda)}{e\ .\ \lambda\ .\ P_{in}\ (\lambda)} = \frac{1240\ .J_{sc}(\lambda)}{\lambda\ .\ P_{in}\ (\lambda)} \qquad Eq.1.10$$

where $J_{sc}\,(\lambda)$ and $P_{in}\,(\lambda)$ are the measured photocurrent and intensity of the incident light at the wavelength of λ.

If all photons are absorbed and generate charge carriers that are collected in the circuit, the *EQE* is 100%. Unfortunately, this ideal case is rare, as carrier recombination and optical losses play an important role in reducing the solar cell quantum efficiency. The measurement is usually made as a function of wavelength using a monochromatic beam. Devices are illuminated by a light beam at different wavelengths, and the current produced by the solar cell at each wavelength is measured.

IPCE measurements were performed on a computer-controlled set-up, which is composed of a Xenon lamp, a monochromator and a potentiostat.

1.4.3.5 Losses in solar cell devices

Energy losses can have a negative effect on the performance of solar cell systems. The following are the key reasons for these declines.

i) Optical losses

A solar cell includes various layers, such as FTO/ETL/Absorbing layer/ETL some of which can contribute to photon absorption that does not contribute in the formation of the charge carrier (electron/hole pair). Hence during the fabrication of solar cells, the absorption of the front layers like ETL (e.g. TiO_2) should be very low. Furthermore, reflection may contribute in optical losses. Recently, this effect is avoided with anti-reflective lacquers in conventional silicon solar cells.

ii) Resistive losses (shunt and series resistance)

As we discussed, in real solar cells is influenced by series (R_S), and shunt resistances (R_{SH}), which significant power losses caused by them; circuit diagram of a solar cell including both R_S *and* R_{SH} was shown in **Figure 1-13**b.

Moreover, **Figure 1-16** shows their influence on the shapes of the J-V curves. The R_S is commonly associated with thick absorbing layers, interface defect, low doping levels, contact resistance, and low conductivity of the ETL or the front transparent contact. Whereas the shunt resistance R_{SH} leads to power losses by providing an alternate current path for the light-generated current, and it's typically occurred due to manufacturing defects such as layers with

pinholes. The main impact of R_S is to decline the FF, while R_{SH} leads to is to reduce both FF and photogenerated current.

The resistances values can be estimated by calculating the inverse of the slope close to the V_{OC} and J_{SC} for R_S and R_{SH} respectively. In order to have the smallest influence on the solar cell, R_S should approach 0, whereas R_{SH} should tend toward infinity.

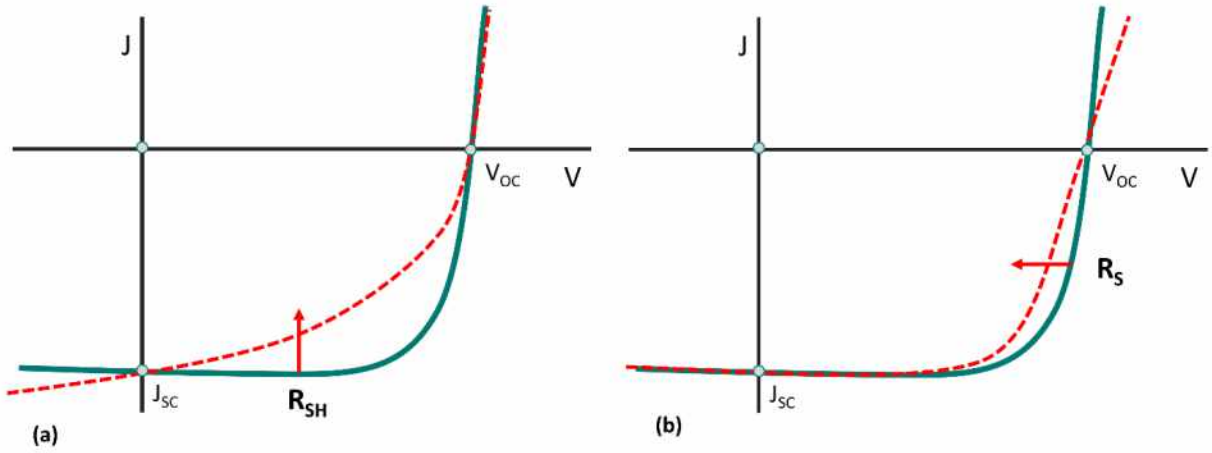

Figure 1-16: J-V curves showing the effect of shunt (a) and series (b) resistances on the curve.

iii) Recombination losses

The exited electron (in conduction band) may be lose energy and stabilize back to the valence band, recombining with a hole in the bulk; on the interface or in the depletion region. Recombination losses affect the performance parameter (J_{sc}, V_{oc} and FF) and are caused by impurities, defects, or break bonds.

Recombination of carriers can happen across several channels of relaxation. The most important are Auger recombination, Shockley–Read–Hall (SRH) trap-assisted recombination, band-to-band recombination, and surface recombination. These relaxation channels can be divided into radiative and non-radiative recombination as shown in **Figure 1-17**. However, non-radiative recombination takes place when the excess energy is converted into heat.

- ***Radiative Recombination***

This process occurs when excited electrons relax from the conduction band to the valence band and release the energy in the form of photons, this process is also known as *Band-to-band / bimolecular recombination.*[65]

Generally, the generated photons (a form of emission) have the same or less energy than those initially absorbed. A device where the recombination is optimized to give off light is also called a light emitting diode (LED). Due to a relatively little momentum in the photon, only direct-bandgap materials involve radiative recombination.

But when the incident photon interacts with an excited electron causing it to recombine and releases a photon with the same properties of the incident one, in terms of polarization, frequency, and direction; this process is known as *Stimulated emission*. However, the action of lasers and masers focuses on stimulated emissions along with the theory of population inversion.

- ***Non-radiative recombination***

This process occurs when charge carriers recombine and releasing phonons instead of photons. Phonons play a significant role in various physical properties, such as electric conductivity and thermal conductivity of condensed matter.

- ***Shockley–Read–Hall (SRH)***

the electron moves through a localized state (such a new energy states are called *traps*) created within the band gap by a defect or a dopant in the crystal lattice. Non-radiative recombination takes place at these sites mainly. The energy is exchanged as a lattice vibration, a phonon exchanging thermal energy with the material.

In silicon and other indirect bandgap materials SRH is the dominant recombination mechanism. However, SRH called as trap-assisted recombination which dominate in direct bandgap materials under conditions of very low carrier densities or in materials with high density of traps such as perovskites.[66,67] Furthermore, the traps may be electron

traps (if trap energy levels lies close to the conduction band) or hole traps (if trap energy levels are close to the valence band). However, depending about how close the electron/hole traps to the conduction/valance bands, the traps may be shallow traps (if the difference between trap and band is smaller than the thermal energy k_BT) or deep traps (if the posit).[68,69]

- ***Surface recombination***

This takes place when traps on the surface, or at the interface of the semiconductor, that's Because of weak bonds caused by the sudden discontinuation of the semiconductor crystal. In perovskite solar cells, surface recombination may be the dominant mechanism of recombination due to the collection and extraction of free carriers at the surface, while it is reduced by passivation techniques.[70]

- ***Auger recombination***

In Auger recombination (**Figure 1-17c**) the energy is passed to a third carrier that is excited to a higher energy level, then the third carrier relaxes and loses its energy to thermal vibrations. Auger recombination may occur when the carrier density is very high in non-equilibrium conditions. Since Auger recombination conserves both momentum and energy, this type or recombination can occur in indirect semiconductors.

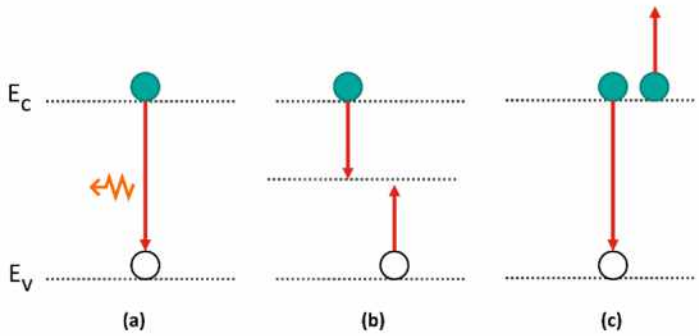

Figure 1-17: Electron/hole recombination mechanisms of radiative (a); trap-assistant (b); Au-ger recombination (c).

iv) Metal-semiconductor interface losses

While for Ohmic contacts electrons and holes are free to move in and out of a semiconductor with minimal energy losses, in Schottky junctions (rectifying contacts) the potential barrier causes a reduction in the carrier flow. Since in a solar cell the Schottky junction behaves similarly to a second diode, a 'roll-over' at forward bias may be recorded in a *J-V* curve (**Figure 1-18 a**), which may affect the *Voc* of the solar cell.[71]

1.4.3.6 Hysteresis

Hysteresis is a widely recorded phenomenon during perovskite solar cell efficiency studies. When the different scan directions are tested during current voltage behavior tests, different J-V (Revers, Forward) curves can be obtained,[72] as shown in **Figure 1-18**.

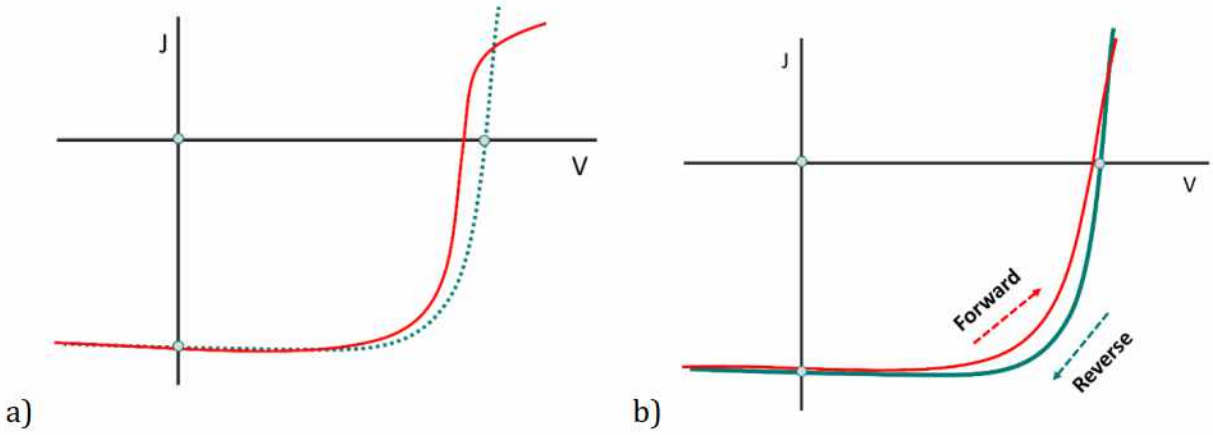

Figure 1-18: 'Roll-over' effect caused by a back-contact junction diode (a); J-V curves with forward and reverse scans showing hysteresis (b).

The J-V curve taken with a reverse scan (decreasing voltage) tends to exhibit higher currents at each voltage than the J-V curve taken with a forward scan (increasing voltage). This can overestimate the efficiency of perovskite devices. A variety of hypotheses, including trap states,[73] ferroelectricity, [74,75] and ion migration, have been suggested as the cause of this phenomenon. [76,77] Ever more scientists are supporting the concept that it is caused by ion migration, but more work is still required for better understanding and hysteresis avoidance.

However, Hysteresis has been found to be much more severe in planar devices than in mesoporous devices, and strongly dependent on the light-soaking, scan speed, and pre-biasing conditions,[78,79] perovskite crystal size,[80] temperature,[81] and contacts used.[82]

CHAPTER (2)

"Experimental Section"

Experimental Section

Here the generally applicable methods and fabrication procedures used in this thesis are outlined. More specialized procedures are described in the individual chapters of relevance.

2.1 Starting materials

The reagents lead iodide (PbI_2), lead bromide ($PbBr_2$), lead chloride ($PbCl_2$) (Sigma-Aldrich, > 99.999%), Sn (Merck, granules), $(CH_3)_3SBr$ (TCI, 98%), resublimed I_2, $SnBr_4$ (Sigma-Aldrich, > 99.9%), $SnCl_4$ (Sigma-Aldrich, > 99.9%), HBr (48%), HCl (36%), methyl chloroformate, methyl chloroformate (Sigma-Aldrich, > 99.9%), dimethyl sulfide $(CH_3)_2S$ (Sigma-Aldrich, > 99.9%). As well as the solvents ethanol, toluene, diethyl ether, isopropanol, acetone, dimethylformamide (DMF), dimethyl sulfoxide (DMSO), benzyl bromide and dichloromethane, chlorobenzene, acetonitrile, tert-butanol, chenodeoxycholic acid were purchased from Sigma Aldrich with purity >99.9% and were used without further purification.

For the construction of DSSCs and perovskite.

TiO_2 paste (30N-RD, 18-NRAO and WER4, Dyesol), titanium diisopropoxide, titanium diisopropoxide bis(acetylacetonate), $TiCl_4$ (Sigma-Aldrich), Z907 dye ((cis-bis(isothiocyanato) (2,2'-bipyridyl-4,4-dicarboxylato) (2'-bipyridyl-4,4'-dinonyl)-ruthenium(II), Dyesol), N719 dye (ditetrabutylammonium cis-bis(isothiocyanato)- bis(2,2′-bipyridyl-4,4′-dicarboxylato)-ruthenium(II), Sigma-Aldrich), MK-2 dye (2-cyano-3-[5‴-(9-ethyl-9H-carbazol-3-yl)-3′,3″,3‴,4-tetra-nhexyl-[2,2′,5′,2″,5″,2‴]-quater-thiophen-5-yl]acrylic acid, Sigma-Aldrich), D35 dye ((E)-3-(5-(4-(bis(2′,4′- dibutoxy-[1,1′-biphenyl]-4-yl)amino)phenyl)thiophen-2-yl)-2- cyanoacrylic acid, Dyenamo), Methylammonium bromide (MABr), Formamidinium iodide (FAI), Bis(trifluoromethane)sulfonimide lithium (Li-TFSI) (Acros) and tert-Butyl pyridine (TBP) (Sigma-Aldrich), $Co[t\text{-}BuPyPz]_3[TFSI]_3$ (FK209), Silver metal (Ag) and Gold (Au) (>99.9999, Sigma-Aldrich).

2.2 Synthesis

Different techniques (**Figure 2-1**) have been used to synthesize a novel perovskite based on trimethyl sulfonium cations, such as solvothermal technique used for preparation of trimethyl sulfonium iodide $(CH_3)_3SCl$, Solid synthesis using vacuum line to prepare $(CH_3)_3SSnI_3$, $(CH_3)_3SPbX_3$, $((CH_3)_3S)_2SnX_6$ where X is pure halide or mixed. Moreover, solution synthesis using reflux technique have been used also to prepare the same perovskite and some reagents, (e.g. SnI_4). However, the single-crystal synthesis technique has been used to prepare $(CH_3)_3SPbCl_3$.

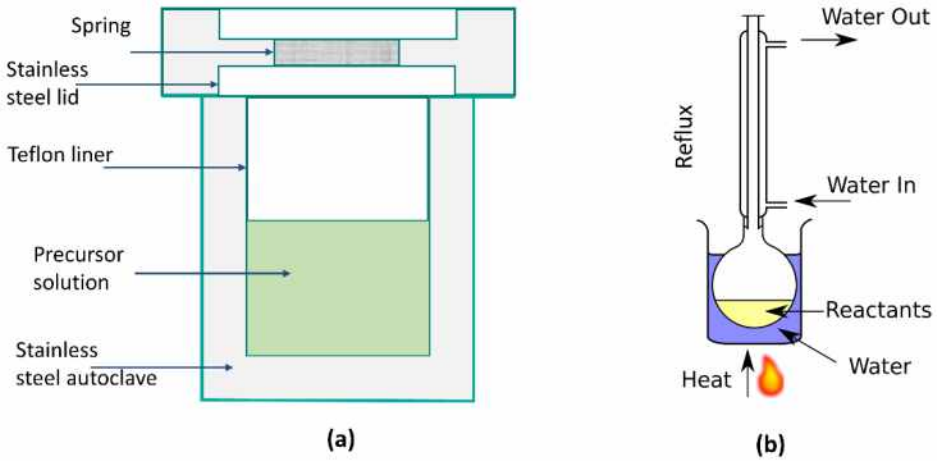

Figure 2-1: Teflon-lined stainless-steel autoclave used in solvothermal and hydrothermal synthesis (a); Solution synthesis using reflux technique (b).

2.2.1 Synthesis of $(CH_3)_3SX$ (X = Cl, Br, I)

For $(CH_3)_3SI$, equimolar amounts of CH_3I and $(CH_3)_2S$ were mixed in a round-bottomed flask and reacted at room temperature for 12 hours. White crystals of $(CH_3)_3SI$ were formed and washed twice with diethyl ether.[83]

For $(CH_3)_3SBr$, a solution of benzyl bromide (2.38 mL, 20 mmol) and DMSO (10 mL) contained in a round-bottomed flask equipped with a condenser was heated at 80 °C for 24 hours. When the reaction mixture was cooled to room temperature, trimethylsulfonium bromide $(CH_3)_3SBr$ precipitated, which was then thoroughly washed with acetone and dried with P_2O_5 under vacuum.[84]

$(CH_3)_3SCl$ was synthesized using solvothermal technique by mixing methyl chloroformate

(0.025 mol, 2.37 g) with dimethyl sulfide (0.05 mol, 3.1 g) in a pressure bottle at 80 °C overnight.[85] The produced white crystals were washed with diethyl ether and dried with P_2O_5 under vacuum. Due to its hygroscopic nature, $(CH_3)_3SCl$ was thereafter stored in an Argon-filled glove box with O_2 and H_2O levels typically below 1 ppm.

2.2.2 Synthesis of $(CH_3)_3SPbI_{3-x}Br_x$ and $(CH_3)_3SPbI_{3-x}Cl_x$ 1D-perovskites

Two different methods were incorporated for the synthesis of $(CH_3)_3SPbI_{3-x}Br_x$ and $(CH_3)_3SPbI_{3-x}Cl_x$ perovskites. In the solid-state synthesis, equimolar amounts of PbX_2 and $(CH_3)_3SX$ were ground together and loaded in a silica tube, which was flame-sealed under vacuum, and then heated in a furnace at 150 °C for 72 hours. In the solution synthesis, equimolar amounts of the above-mentioned reagents were dissolved in DMF and heated at 80 °C for three hours. The resulting yellowish products were washed with dichloromethane and dried in air.

2.2.3 Synthesis of $(CH_3)_3SSnI_3$ 1D-perovskite

Equimolar amounts of $(CH_3)_3SI$ and SnI_2 (Aldrich, 99.999%) reacted in sealed silica tubes under vacuum at 100 °C for 24 hours. The air-sensitive, yellow powder of $(CH_3)_3SSnI_3$ was handled in an Argon-filled glove box, with humidity and oxygen levels below 1 ppm. An alternative synthetic route of reacting equimolar amounts of $(CH_3)_3SI$ and SnI_2 in dimethylformamide solution at 60 °C was also pursued, in order to obtain crystals suitable for single-crystal X-ray diffraction. This method produced indeed yellow needle-shaped crystals of $(CH_3)_3SSnI_3$, but they suffered from diffuse scattering at high diffraction angles.

2.2.4 Synthesis of SnI_4

SnI_4 was synthesized by reacting Sn with I_2 in 1:2 molar ratio and approximately 100 mL CH_2Cl_2 at 50 °C for 3 h under vigorous stirring, followed by partial condensation to the half amount and cooling in ice water. The solution was decanted and orange crystals of SnI_4 were obtained and left to dry.

2.2.5 Synthesis of $((CH_3)_3S)_2SnX_6$ (X = Cl, Br, I) 0D-perovskite

$((CH_3)_3S)_2SnI_6$ was prepared in ambient air by reacting SnI_4 with $(CH_3)_3SI$ in 1:2 molar ratio by solid-state synthesis. The reactants were ground together and loaded in a silica tube, which was flame-sealed under vacuum, and then heated in a furnace at 140 °C for 48 hours,

and the black powder of $((CH_3)_3S)_2SnI_6$ was obtained.

$((CH_3)_3S)_2SnBr_6$ was prepared by reacting of $SnBr_4$ with $(CH_3)_3SBr$, in 1:2 molar ratio and approximately 20 mL HBr (48%) at 50 °C under stirring for 2 hours. The yellow crystals of $((CH_3)_3S)_2SnBr_6$ were recrystallized in absolute ethanol and dried in ambient air.

$((CH_3)_3S)_2SnCl_6$ was synthesized by reacting of $SnCl_4$ with $(CH_3)_3SCl$, in 1:1 molar ratio at 60 °C under stirring for 3 hours under N_2 due to the hygroscopic nature of both reactants. The small amount of unreacted $SnCl_4$ was removed with absolute ethanol and the reaction product was dried in ambient air to obtain white crystals of $((CH_3)_3S)_2SnCl_6$.

2.2.6 Synthesis of $((CH_3)_3S)_2SnI_{6-n}Cl_n$ and $((CH_3)_3S)_2SnI_{6-n}Br_n$ (n=1, 2) 0D-perovskites

Using solid-state chemistry protocols, $((CH_3)_3S)_2SnI_{6-n}Cl_n$ and $((CH_3)_3S)_2SnI_{6-n}Br_n$ (n=1, 2) perovskite were prepared. In particular, $((CH_3)_3S)_2SnI_5Cl$ was prepared by reacting 626.6 mg SnI_4 with 112.5 mg $(CH_3)_3SCl$ and 204 mg $(CH_3)_3SI$ in 1:1:1 molar ratio and $((CH_3)_3S)_2SnI_4Cl_2$ by reacting 626.6 mg SnI_4 with 225 mg $(CH_3)_3SCl$ in 1:2 molar ratio.

Regarding $((CH_3)_3S)_2SnI_5Br$ it was prepared by reacting 626.6 mg SnI_4 with 157 mg $(CH_3)_3SBr$ and 204 mg $(CH_3)_3SI$ in 1:1:1 molar ratio while $((CH_3)_3S)_2SnI_4Br_2$ was formed by reacting 626.6 mg SnI_4 with 314 mg $(CH_3)_3SCl$ in 1:2 molar ratio.

In all cases, equimolar precursor amounts were introduced in a silica tube sealed under vacuum (following grinding in a mortar and mixing) and heated in an oven at 110 °C for 2 days.

2.3 Characterization methods

2.3.1 X-ray powder diffraction (XRPD)

X-ray powder diffraction (XRPD) analysis was performed for all perovskites using a Siemens D-500 diffractometer, that operates in Bragg-Brentano geometry with Cu $K_{\alpha1}$ (λ = 1.5406 Å) and Cu $K_{\alpha2}$ (λ = 1.5444 Å) radiation. Data were collected over the angular range $5° \leq 2\theta \leq 80°$ counting for 3 seconds at each step of 0.02° in detector position.

2.3.2 Single crystal X-ray diffraction

A needle-shaped single crystal of $(CH_3)_3SPbCl_3$ (dimensions 0.02 x 0.03 x 0.3 mm) that was collected after slow evaporation of the solvent was cooled at -103 °C and diffraction meas-

urements were collected on a Rigaku R-AXIS SPIDER Image Plate diffractometer using graphite-monochromated Mo K_α radiation. Data collection (ω-scans) and processing (cell refinement, data reduction and absorption correction) were performed using the CrystalClear program package.[86] The structure was solved by direct methods using SHELXS-97 [87] and refined by full-matrix least-squares techniques on F^2 with SHELXL2014/6.[88,89]

Formula: $C_3H_9SPbCl_3$, Formula weight = 390.7, Z = 8, space group: *Pnma*, No. 62, a = 16.2359(5) Å, b = 13.2044(5) Å, c = 8.7900(5) Å, α = β = γ = 90°, V = 1884.45(11) Å^3, $\rho_{calcd.}$ = 2.754 g cm^{-3}, Absorption coeff., μ = 18.89 mm^{-1}, $F(000)$ = 1408, 3.054° ≤ θ ≤ 27.000°, No. of independent reflections = 17446, No. of data/restraints/parameters = 2143/6/121, Goodness-of-fit on F^2 = 1.05, Final R indices [I > 2σ(I)] = 2.82%, Final R indices [all data] = 4.22%.

The two $(CH_3)_3S$ units are symmetrically independent, but as they are close to symmetry elements, they are distributed with half occupancies on both pairs of disordered sites and thus they were refined using the Part -1 command. The hydrogen atoms for these groups were introduced at calculated positions. All hydrogen atoms were refined isotropically with the calculated ones, as riding on their respective bonded atoms. All non-hydrogen atoms were refined anisotropically.

2.3.3 Rietveld refinements

Rietveld refinements were performed using the FULLPROF software[90,91] for ABX_3 such as $(CH_3)_3SPbX_3$ and its derivatives, while JANA 2006 software[92] was used for A_2BX_6 such as $((CH_3)_3S)_2SnX_6$ and its derivatives.

2.3.4 Hirshfeld analysis

Molecular Hirshfeld surfaces calculations and fingerprint plots of $((CH_3)_3S)_2SnX_6$ (X = Cl, Br, I) were performed using the Crystal Explorer 17.5 package.[93] The results provide information on intermolecular contacts using a standard surface resolution with different surfaces mapped (3D d_{norm}, shape index, and curvedness). The 2D fingerprint plots were produced using the standard 0.6 – 2.6 Å view in the d_e and d_i distance scales.

2.3.5 Infrared spectroscopy

FTIR spectra were collected in transmission mode on a Thermo Scientific Nicolet 6700 FTIR equipped with N_2 purging system using KBr pellets. A total of 32 scans were averaged for

each sample at resolution 4 cm^{-1}. Data were collected in the range 4000–400 cm^{-1} and corrected against the single-beam spectrum of KBr.

2.3.6 Raman spectroscopy

Micro-Raman spectra were measured for all materials in the 30 – 3200 cm^{-1} range in backscattering configuration on a dispersive Renishaw in-Via Reflex spectrometer with 250 mm focal length equipped with a high sensitivity, deep depletion CCD detector. Excitation was performed by a near infrared (NIR) solid state laser emitting at a wavelength of 785 nm. The laser beam was focused on the sample's surface using a ×50 long focal distance objective lens of a Leica DMLM microscope providing a power density of approximately 1 mW μm^{-2}. Raman scattered signal was filtered by a 30 cm^{-1} cut-off dielectric filter and analyzed with a 1200 lines/mm diffraction grating. Measurements were carried out with circular polarization of the incident laser beam on perovskite crystals aligned at 45° relative to the direction of the spectrometer slit in order to record unpolarized Raman spectra. Spectral deconvolution was carried out by linear least squares fitting of the Raman peaks to a mixture of Lorentzian and Gaussian line shapes.

To investigate the dependence of the vibrational properties on the temperature, the samples was loaded into a THMS600PS Linkam temperature-controlled heating-cooling optical cell under an inert argon atmosphere for measurements over the temperature range of -195 °C to 220 °C.

However, the raw Raman spectra were reduced for the thermal population factor according to the expression given in eq. (2.1)[94]. This enhances the low frequency Raman features which is very informative for the SnI_6 vibrational characteristics.

$$I_{red}(\omega) = I(\omega)\frac{1}{n(\omega,T)+1}, \text{ with } n(\omega,T) = (e^{\frac{hc\omega}{k_B T}} - 1)^{-1} \qquad (Eq.\ 2.1)$$

where $I(\omega)$ and $I_{red}(\omega)$ are the measured and reduced Raman intensity, respectively. $n(\omega, T)$ is the Bose-Einstein statistic factor, h and k_B are the Planck and Boltzmann constants, respectively, c is the speed of light, ω is the Raman shift in cm^{-1}, and T is the temperature in K.

2.3.7 Ultraviolet-visible (UV-Vis) spectroscopy

UV-Vis spectra were recorded for the all samples as well as their precursors on a Hitachi U-3010 spectrophotometer. However, a spectrum of the material with lower bandgap E_g<1.5 eV (e.g. $(CH_3)_3S)_2SnI_6$), was recorded using Perkin Elmer Lambda 35 spectrophotometer. Both equipped with an integrating sphere. In the case diffuse reflectance measurements (bulk material): the materials were measured as 1 mm thick pellets in diffuse reflectance (R) mode and the band gap was determined using the Kubelka-Munk equation (eq. 2.2)[95]:

$$F(R) = (1-R)^2 / 2R \qquad (Eq.\ 2.2)$$

In contrast, the absorption and transmittance measurements (for films) were performed using the normal mode. Whereas, the perovskite film is coated on a microscopic glass or FTO using a rotating coating.

2.3.8 Photoluminescence spectroscopy

Photoluminescence (PL) spectra (for bulk perovskites) were obtained from solid pressed pellets, placed on quartz plates in a reflecting configuration, mounted on a Hitachi F-2500 FL spectrophotometer, employing a xenon 150 W lamp and a R928 photomultiplier. The excitation and detection slits were set at 5 nm and the accelerating voltage was set to 700 V, while spectra were acquired at 300nm/sec. Photoluminescence excitation was measured and corrected using the instrument's correction factor. Synchronous scans as well as 3D scans were employed to determine particular details of the samples' properties.

Moreover, Steady-state emission spectra of the perovskite films were recorded on a Horiba Fluorolog-3 JobinYvon-Spex spectrofluorometer (model GL3-21), equipped with a 450-W Xe lamp as excitation source and a TBX photomultiplier (250-850 nm) as detector. Data recorded and collected via the Horiba Fluorescence V3 software.

2.3.9 Time-resolved fluorescence spectroscopy

For the pico-second time-resolved fluorescence spectra a time-correlated-single-photon-counting (TCSPC) method via a Fluorohub single photon counting controller, a laser diode as an excitation source (NanoLED, 482 nm, pulse duration <200 ps) and a the TBX-PMT detector (250-850 nm), all by Horiba JobinYvon, was applied. Data recorded and collected with the Data Station software, whereas the lifetimes were determined by the Data Acquisition

Software (DAS), all provided by Horiba. Samples recorded in the form of thin films over FTO-coated glass substrates, with the aid of a FL-1057 sample holder.

2.3.10 Ultraviolet Photoelectron Spectroscopy

Ultraviolet photoelectron spectroscopy (UPS) measurements were performed in a UHV chamber ($P \sim 5x10^{-10}$ mbar) equipped with a SPECS LHS-10 hemispherical electron analyzer and a UV source (model UVS 10/35). The UPS spectra were recorded using HeI irradiation with $h\nu$=21.23 eV and the analyzer was working at the Constant Retarding Ratio (CRR) mode, with CRR = 10. With UPS the work function could be estimated by subtracting the secondary electron cutoff value, based on linear extrapolation toward background, from the He excitation source of 21.22 eV (Φ=21.22 eV - E_{SEC}). For these measurements a bias of −12.30 V was applied to the sample in order to avoid interference of the spectrometer threshold in the UPS spectra. Additionally, the ionization energy (energy difference between valence bands maximum (VBM) and vacuum level) can be measured directly from the sum of the measured energy values of the work function (WF) and the VBM cut off at the low binding energy (BE) side of the UP spectra. The VBM is determined by linear extrapolation toward background in the low binding energy region.

2.3.11 SEM and EDAX spectroscopy

The surface features of the perovskites (in the bulk) were analyzed on a Scanning Electron Microscopy Quanta 200 SEM instrument by accelerating the electron beam at 25 kV. The chemical composition of the samples was estimated using an Energy Dispersive X-ray (EDAX) spectroscopy detector.

Moreover, perovskite films morphologies were investigated using a higher resolution Field Emission Scan Electron microscope (FESEM) JEOL 7401f.

2.3.12 Atomic Force Microscopy (AFM)

Topographic imaging of the perovskite films was recorded with an AFM: Digital Instruments Nanoscope III, operating in tapping mode.

2.3.13 Contact angle measurements

The contact angle tests were performed with the Contact Angle Meter (CAM) 100, KSV Instruments, Ltd.

2.3.14 Solar cell characteristics

The solar cell performance was determined using a Xenon 300 W source solar simulator (Oriel) in combination with AM 1.5G optical filters (1 sun). The light intensity was calibrated with a Si reference cell.

2.3.14.1 Current density-voltage (J-V) characteristics

J-V curves were obtained with an Autolab potentiostat (PGSTAT-302N) at a scan rate of 150 $mV \cdot sec^{-1}$ and the illuminated (active) area were set to 0.10 cm^2. J-V curves were obtained by illuminating the solar cells under a Solar Light Co. 300W Air Mass Solar Simulator Model 16S-300 (1sun, 1000 W/m^2) calibrated using an Optopolymer Si reference cell. The measurements were carried out using Ossila's Push-Fit Test Board for Photovoltaic Substrates.

2.3.14.2 Impedance measurements (EIS)

EIS were performed on complete cells under dark and 1 sun illumination conditions, by applying forward bias at V_{MPP} conditions, using the PG-STAT-30 potentiostat and its built-in frequency response analyzer (FRA).

2.3.14.3 Maximum power point tracks

Data for stabilized maximum power point (MPP) conditions were recorded in voltage values corresponding to the MPP of the PSCs.

2.3.14.4 Incident photon-to-current efficiency (IPCE)

Incident photon-to-current efficiency plots were taken by a custom-made apparatus consisting of an Oriel monochromator and an Oriel Xe lamp working in combination with cut off optical filters (AM1.5G, AM0, and 400 nm) and the Autolab PG-STAT-30 potentiostat. Both lamps were calibrated using an Optopolymer Si reference cell. The 400 nm cut-off optical filter was added, in order to avoid problems arising from the photocatalytic activity of the titania (TiO_2) underlayer, which might cause possible degradation of the perovskite absorber.

2.3.14.5 Light stress measurements

Light stress tests were performed in an ATLAS SUNTEST CPS+ solar simulator, equipped with a xenon lamp covering the 300 - 800 nm spectral range. The J-V data were registered

using the Autolab potentiostat, following continuous illumination (765 $W.m^{-2}$) of the cells (at open circuit) under ambient conditions (humidity ~50%, ~ 50 °C) for 4 h in the ATLAS simulator.

2.4 Computational study

Density Functional Theory (DFT) of optimized geometry structure, electrostatic potential (ESP), highest occupied molecule orbital (HOMO)/ lowest un-occupied molecular orbital (LUMO) analysis for D35 organic dye was performed using Gaussian 09 computational package.[96] The calculation was carried out using CAM-B3LYP as calculation method, basis set = 6-31G(d,p).

Moreover, First-principles calculations have been performed using CASTEP (Cambridge Sequential Total Energy Package)[97,98] for crystalline perovskites systems with the GGA/PBE and GGA/PBESOL functions. A plane-wave energy cutoff 340 :420 eV and Monkhorst-pack[99]. Ab initio DFT calculations, have been carried out to predict the optimized parameters, band structure, the density of states (DOS) and partial density of states (PDOS) for all perovskites.

However, Extended Hückel (EHT) calculations[100] for lead-perovskites were made with an in-house code based on Slater type orbitals centered on all atoms, composed of single zeta *s* and *p* orbitals.

CHAPTER (3)

$(CH_3)_3SPbI_{3-x}Br_x$ and $(CH_3)_3SPbI_{3-x}Cl_x$ (x = 0, 1, 2, 3) perovskites

$(CH_3)_3SPbI_{3-x}Br_x$ and $(CH_3)_3SPbI_{3-x}Cl_x$ (x = 0, 1, 2, 3) perovskites

Organohalide metal perovskite solar devices have attracted much attention in the photovoltaic community, due to their efficiency in converting solar energy into electricity, which has reached values over 25% in the last five years.[101] Lead halide perovskites adopt an $APbX_3$ structure, where A is a monovalent organic cation (e.g. methylammonium ($CH_3NH_3^+$, MA^+), formamidinium ($CH(NH_2)_2^+$, FA^+)) or an inorganic cation (e.g. K^+, Rb^+, Cs^+), and X = Cl^-, Br^-, I^-. They also form solid solutions by changing the A-site or X-site ions so that their physical properties, such as band gap and charge carrier diffusion length, are precisely tuned.[26,27] Nevertheless, the chemical instability of $APbX_3$ (A = $CH_3NH_3^+$, $HC(NH_2)_2^+$, X = Br^-, I^-, Cl^-) perovskites due to moisture, light and heat has long been the main restriction for the industrialization of the corresponding devices.[102]

Our recent study on $(CH_3)_3SPbI_3$ has shown that this material is very stable in air.[42] In this context, we investigate here the role of different halogen atoms in $(CH_3)_3SPbX_3$ (X = Cl, Br, I). Also, the luminescence properties are being reported, as they convey information about the excitonic nature of these semiconductors, as well as for possible exciton engineering involving tuning the organic component in order to match the luminescence properties of the inorganic network. Finally, theoretical calculations are reported for relating observational data to models, while in particular the extended Hückel calculations demonstrate a simple and efficient method for more than qualitative prediction of the perovskites' properties. A comparison is also made between various ab initio models, some of which are the first successful application ab-initio models explaining the bandgap origin of perovskites based on face-sharing octahedra structures.

3.1.1 Structural analysis

$(CH_3)_3SPbI_{3-x}Br_x$ perovskites were obtained either from solid-state or solution synthesis in high crystallinity materials with hexagonal symmetry, same as in the previously reported room-temperature modification of $(CH_3)_3SPbI_3$ (space group $P6_3mc$, No. 186).[42] No extra peaks of unreacted precursors or other impurities were observed by XRPD analysis in all samples (**Figure 3-1**). A gradual shift of the diffraction peaks to higher angles occurs with

increasing Br content due to the decrease in lattice parameters. Structural analysis was performed for $(CH_3)_3SPbBr_3$ with the Rietveld method (**Figure 3-2**, **Table 3-1**) using initially the structural model of $(CH_3)_3SPbI_3$ without further refinement of the trimethyl sulfonium group. All thermal displacement values were set to 0.03 $Å^2$.

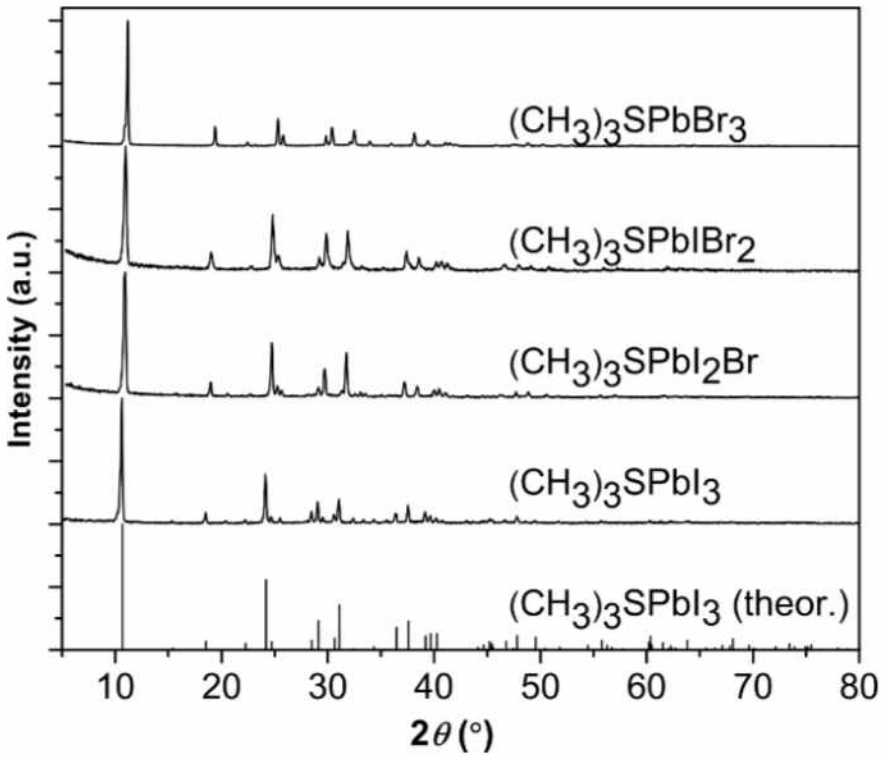

Figure 3-1: XRPD patterns for $(CH_3)_3SPbI_{3-x}Br_x$ (x = 0, 1, 2, 3) in comparison with the theoretical pattern of hexagonal $(CH_3)_3SPbI_3$.

Table 3-1: Atomic coordinates and site occupancy factors (SOFs) for $(CH_3)_3SPbBr_3$ with estimated standard deviations in parentheses. Space group: $P6_3mc$ (No. 186). Lattice parameters: $a = b =$ 9.1579(2) Å, c = 7.6869(3) Å.

Label	X	y	z	SOF
Pb	0	0	0.030(4)	1
Br	0.2983(8)	0.1491(8)	0.292(4)	1
S	0.3333	0.6667	0.1991	1
C	0.4278	0.8556	0.2973	1
H1	0.35	0.86	0.36	0.5
H2	0.51	0.86	0.36	0.5
H3	0.47	0.93	0.27371	0.5

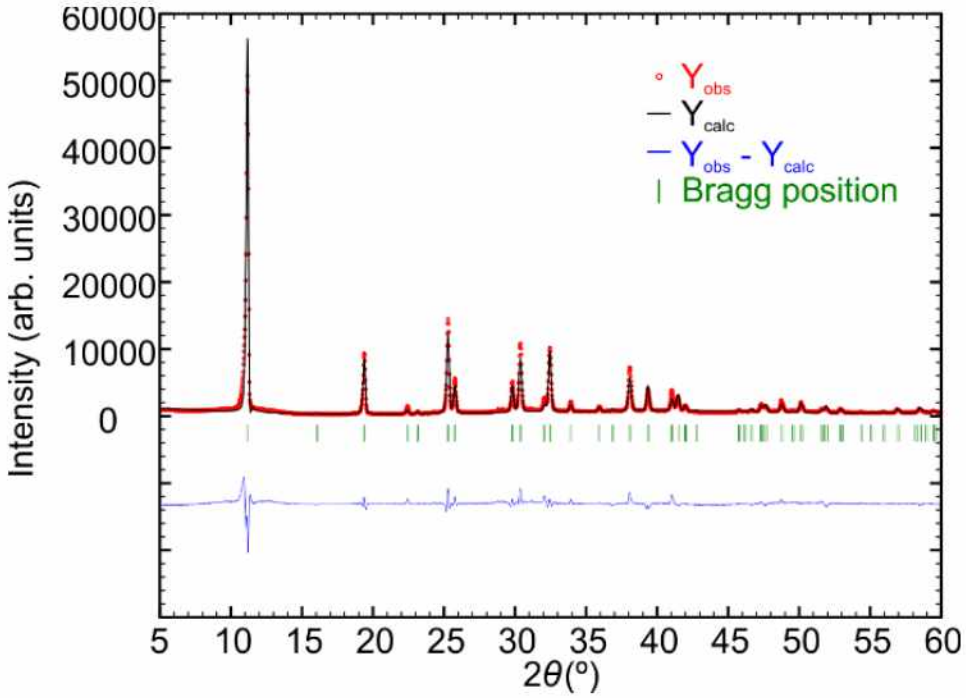

Figure 3-2: Rietveld plot for $(CH_3)_3SPbBr_3$. Residual values: $\chi^2 = 4.12$, $R_p = 14.4\%$, $wR_p = 18.5\%$.

The distorted, face-sharing [$PbBr_6$] octahedra form 1D chains along the *c* axis (**Figure 3-3**), and the trimethyl sulfonium cations occupy interstitial sites between the octahedra with their 3-fold rotation axis parallel to the crystallographic *c* axis.

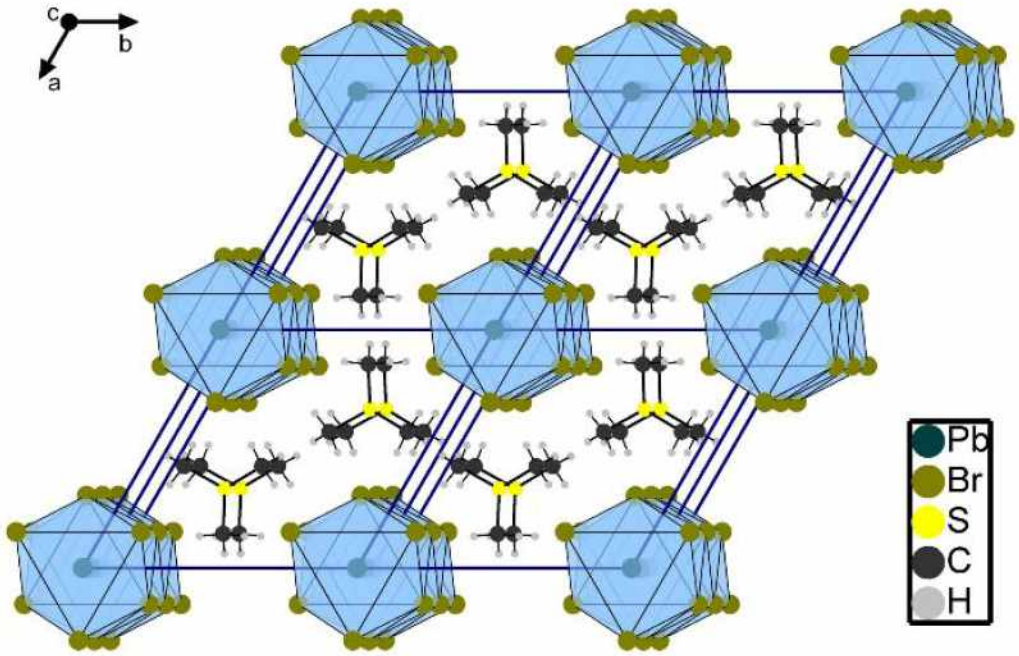

Figure 3-3: Crystal structure of the (2 x 2 x 2) unit cell $(CH_3)_3SPbBr_3$ across the c axis. Thick blue lines denote the unit cell edges.

The $(CH_3)_3SPbI_{3-x}Cl_x$ (x = 1, 2, 3) perovskites were also synthesized by solid-state and solution methods. No extra peaks of unreacted precursors or other impurities were observed by XRPD analysis for these samples, too. For x = 1, 2, Bragg peaks of hexagonal symmetry (space group *P6₃mc*, No. 186) are recorded with a gradual shift to higher angles with increasing Cl content (**Figure 3-4**).

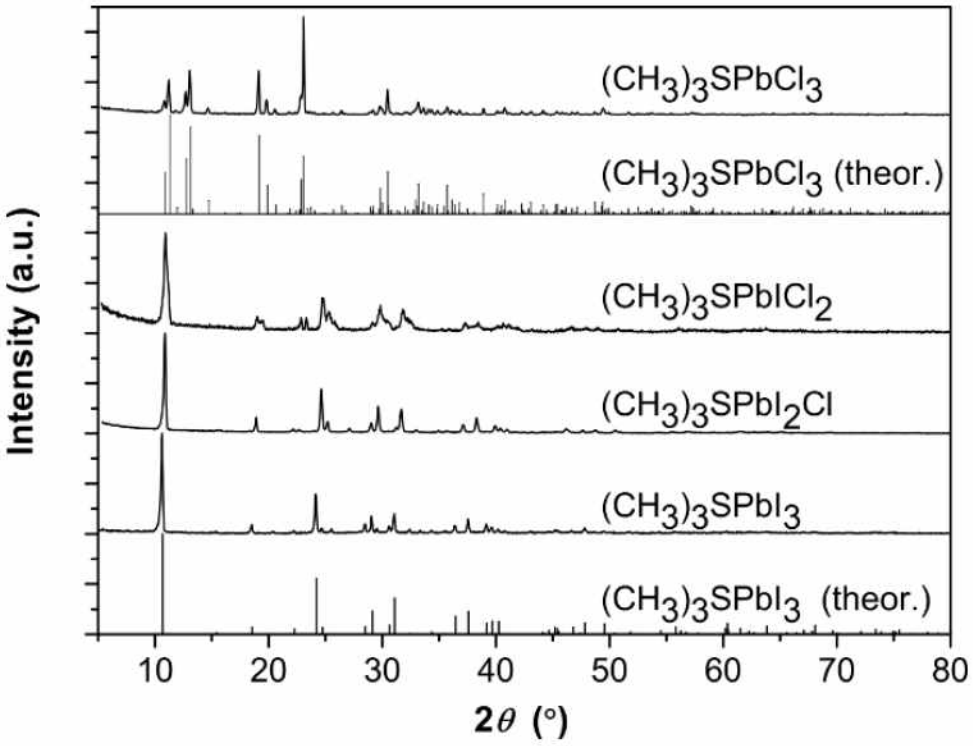

Figure 3-4: XRPD patterns for $(CH_3)_3SPbI_{3-x}Cl_x$ in comparison with the theoretical patterns of hexagonal $(CH_3)_3SPbI_3$ and orthorhombic $(CH_3)_3SPbCl_3$.

In contrast, according to single-crystal X-ray diffraction analysis $(CH_3)_3SPbCl_3$ crystallizes in orthorhombic symmetry (**Figure 3-5**, **Tables** 3-2:3-4). For a better description of the structure we have to consider as a formula unit the double of the above (which corresponds to the content of the asymmetric unit), i.e. $[(CH_3)_3S]_2Pb_2Cl_6$. The two $(CH_3)_3S$ units are symmetrically independent, but as they are close to symmetry elements, they are distributed with half occupancies on both pairs of disordered sites. That consisting of S1, C1, C2, C3 atoms are close to the mirror plane (x, -0.25, z) and those of S2, C3, C4 and C5 atoms are close to the center of symmetry (0.5,0,1). Units of two face-sharing $[Pb_2Cl_6]$ octahedra (through Cl1, Cl2, Cl3 atoms) connect to adjacent six units (three above and three below the plane of the central unit) through common vertices (through Cl5 and pairs of symmetry equivalent Cl4 atoms).

The three dimensional arrangement of pairs of face-sharing octahedra in the compound under study resembles that of $SrMnO_3$ structure (a 4H four layer hexagonal perovskite, with space group $P6_3/mmc$ (No. 194))[103–105] and the one to one correspondence of the different structure units of both structures renders them isostructural. In the present structure the trimethylsulfonium group, the Pb and Cl atoms have replaced the Sr atoms, Mn and oxygen atoms, respectively.

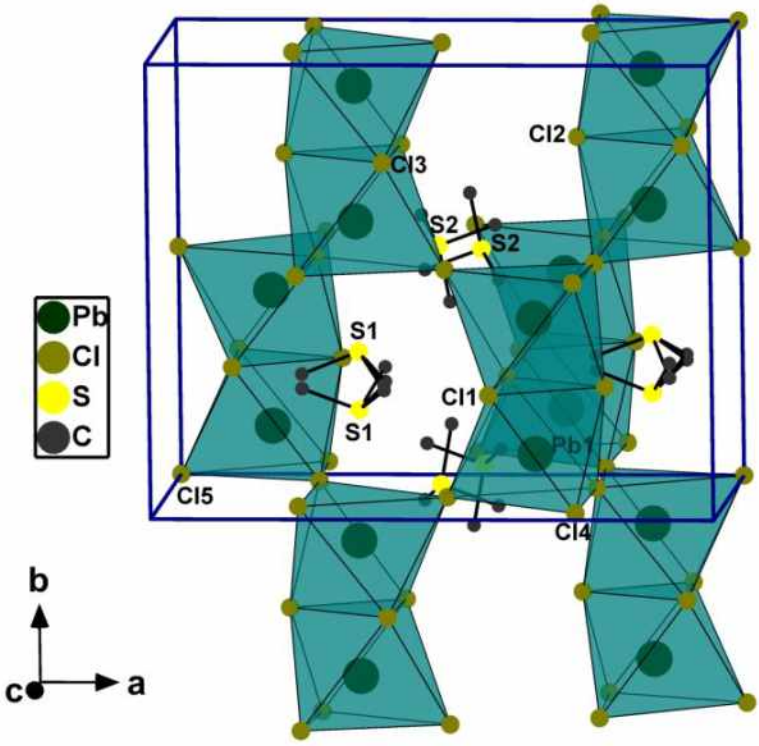

Figure 3-5: Crystal structure of $(CH_3)_3SPbCl_3$ with partially labeled atoms. H atoms are omitted for clarity. Thick blue lines denote the unit cell edges.

The difference in structure type among $(CH_3)_3SPbCl_3$ and the rest of the perovskites under investigation is attributed to the large decrease in crystal density with decreasing halogen size. The actual density of the orthorhombic $(CH_3)_3SPbCl_3$ is 2.754 g cm^{-3} (from single-crystal XRD data), whereas for the hexagonal $(CH_3)_3SPbI_3$, $(CH_3)_3SPbBr_3$ and $(CH_3)_3SPbICl_2$ perovskites, these values equal to 3.49, 3.12 and 2.71 g cm^{-3}, respectively (from XRPD data and Rietveld refinement). A hypothetic 1D-hexagonal $(CH_3)_3SPbCl_3$ would allow for very larger voids among the inorganic columns and the organic cations, leading to even lower crystal density which is thermodynamically unstable. Therefore, $(CH_3)_3SPbCl_3$ has higher structural

similarity with $((CH_3)_3S)_4Pb_3Br_{10}$ rather than with its heavier $(CH_3)_3SPbX_3$ analogues.[106] It is noteworthy also that $(CH_3)_3SPbCl_3$ is thermodynamically stable in a large temperature range (-103 °C to 25 °C) and retains its orthorhombic symmetry, in contrast to $(CH_3)_3SPbI_3$ that undergoes structural phase transitions below -5 °C.[102]

Table 3-2: Atomic coordinates and isotropic displacement parameters for $(CH_3)_3SPbCl_3$ with estimated standard deviations in parentheses.

Atom	SOF	x	y	z	U (Å²)
Pb1	1	0.66046(2)	0.10099(2)	0.55413(2)	-
Cl1	1	0.58915(12)	0.2500	0.7593(3)	-
Cl2	1	0.78547(12)	0.2500	0.5652(3)	-
Cl3	1	0.60066(13)	0.2500	0.3494(3)	-
Cl4	1	0.75537(9)	0.00319(15)	0.3176(2)	-
Cl5	1	0.5000	0.0000	0.5000	-
S1	0.5	0.65771(19)	-0.1861(3)	0.5574(5)	-
C1	0.5	0.6048(7)	-0.244(3)	0.4036(15)	-
H1A	0.5	0.5453	-0.2402	0.4208	0.127
H1B	0.5	0.6212	-0.3158	0.3966	0.127
H1C	0.5	0.6188	-0.2097	0.3085	0.127
C2	0.5	0.7582(6)	-0.234(4)	0.5396(15)	-
H2A	0.5	0.7740	-0.2685	0.6343	0.083
H2B	0.5	0.7966	-0.1788	0.5193	0.083
H2C	0.5	0.7601	-0.2830	0.4554	0.083
C3	0.5	0.6191(8)	-0.266(3)	0.7047(18)	-
H3A	0.5	0.5856	-0.2253	0.7748	0.171
H3B	0.5	0.6653	-0.2958	0.7602	0.171
H3C	0.5	0.5853	-0.3193	0.6600	0.171
S2	0.5	0.53318(17)	0.0127(2)	0.9080(3)	-
C4	0.5	0.5164(11)	-0.1158(9)	0.958(2)	-
H4A	0.5	0.4789	-0.1471	0.8847	0.106
H4B	0.5	0.4919	-0.1191	1.0602	0.106
H4C	0.5	0.5690	-0.1522	0.9583	0.106
C5	0.5	0.5722(8)	0.0633(11)	1.0769(15)	-
H5A	0.5	0.6216	0.0257	1.1072	0.070
H5B	0.5	0.5305	0.0581	1.1571	0.070
H5C	0.5	0.5864	0.1347	1.0611	0.070

C6	0.5	0.4319(7)	0.0590(11)	0.9051(17)	-
H6A	0.5	0.3994	0.0204	0.8313	0.069
H6B	0.5	0.4323	0.1306	0.8761	0.069
H6C	0.5	0.4074	0.0518	1.0065	0.069

Table 3-3: Anisotropic displacement parameters in $Å^2$ for $(CH_3)_3SPbCl_3$ with estimated standard deviations in parentheses.

Atom	U_{11}	U_{22}	U_{33}	U_{12}	U_{13}	U_{23}
Pb1	0.02305(13)	0.02554(14)	0.02657(14)	-0.00050(9)	-0.00043(9)	0.0002 (11)
Cl1	0.0341(11)	0.0536(15)	0.0313(13)	0.000	0.0008(10)	0.000
Cl2	0.0234(10)	0.0390(14)	0.0597(17)	0.000	-0.0051(11)	0.000
Cl3	0.0381(12)	0.0422(13)	0.0299(12)	0.000	-0.0069(10)	0.000
Cl4	0.0461(9)	0.0583(13)	0.0450(11)	0.0085(9)	-0.0065(8)	-0.0089(10)
Cl5	0.0393(13)	0.0551(17)	0.0574(16)	-0.0144(12)	0.0083(12)	-0.0049(14)
S1	0.0304(17)	0.057(2)	0.062(3)	0.0122(16)	-0.0120(18)	-0.017(2)
C1	0.056(8)	0.18(2)	0.054(10)	-0.03(2)	-0.011(7)	-0.07(2)
C2	0.023(5)	0.09(3)	0.054(8)	0.008(10)	0.003(5)	0.012(15)
C3	0.051(8)	0.35(4)	0.066(12)	-0.05(3)	-0.004(8)	0.10(3)
S2	0.0244(15)	0.0354(19)	0.0275(17)	0.0028(13)	0.0004(12)	-0.0063(14)
C4	0.088(13)	0.028(9)	0.110(17)	-0.011(8)	0.004(12)	-0.008(9)
C5	0.037(8)	0.063(10)	0.040(9)	-0.013(7)	-0.001(7)	-0.019(8)
C6	0.039(8)	0.050(9)	0.049(10)	0.013(7)	0.017(7)	0.005(7)

Table 3-4: Bond lengths in Å for $(CH_3)_3SPbCl_3$ with estimated standard deviations in parentheses.

Bond	Bond length	Bond	Bond length
Pb1 – Cl2	2.8285(14)	S1 – C1	1.739(14)
Pb1 – Cl3	2.8376(16)	S1 – C2	1.757(18)
Pb1 – Cl4	2.8925(17)	S1 – C3	1.845(14)
Pb1 – Cl1	2.9093(16)	S2 – C5	1.748(12)
Pb1 – Cl5	2.9651(2)	S2 – C4	1.761(13)
Pb1 – Cl4	3.0202(18)	S2 – C6	1.773(11)

3.1.2 Vibrational and optoelectronic properties

The micro-Raman spectra for the novel $(CH_3)_3SPbI_{3-x}Br_x$ and $(CH_3)_3SPbI_{3-x}Cl_x$ perovskite materials (**Figure 3-6**) show the vibrational modes of the organic moiety $(CH_3)_3S^+$ at ca. 3000, 2915, 1410, 1045, 730, 655, 280 cm^{-1} with a very small red shift (1 – 4 cm^{-1}) with increasing Br or Cl content. On the other hand, the vibrational modes of the inorganic framework appear at low frequencies (30 – 200 cm^{-1}). The strongest mode for $(CH_3)_3SPbI_3$ is the Pb-I stretching found at 100 cm^{-1} and it shifts to higher frequencies in the series of $(CH_3)_3SPbI_{3-x}Br_x$ and $(CH_3)_3SPbI_{3-x}Cl_x$ due to the decrease of the reduced mass of the Pb-Br and Pb-Cl bonds, respectively.[42,102]

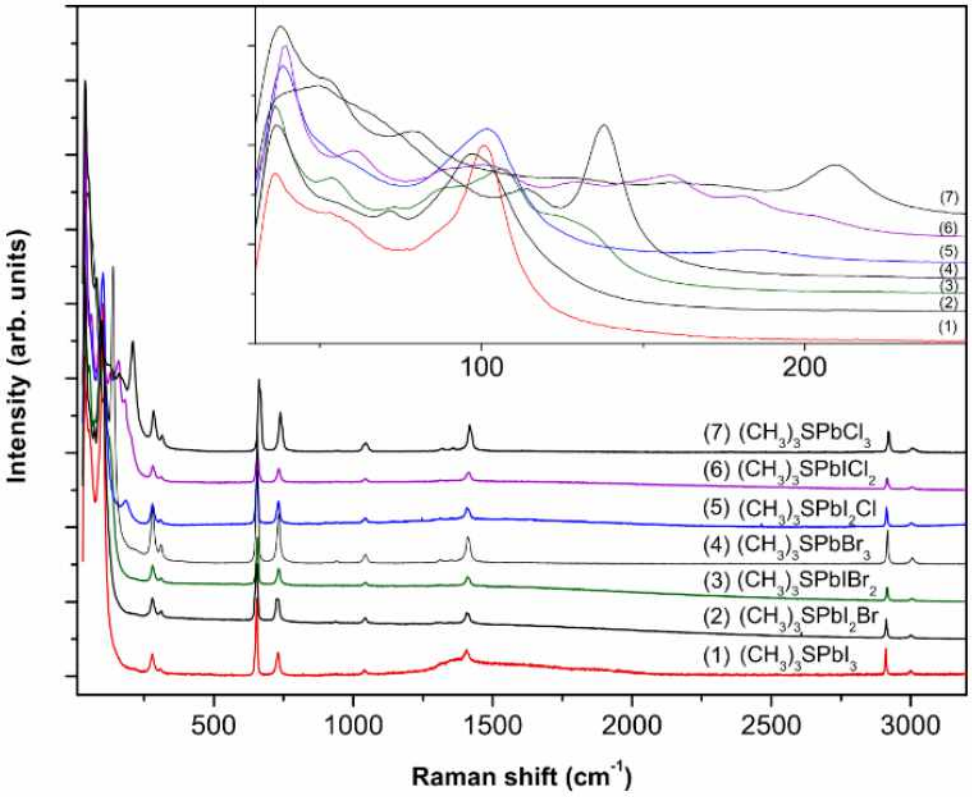

Figure 3-6: Raman spectra of $(CH_3)_3SPbI_{3-x}Br_x$ and $(CH_3)_3SPbI_{3-x}Cl_x$ (x = 0, 1, 2, 3). The inset zooms in the 30 – 250 cm^{-1} regions.

This behavior is in accordance with similar systems such as $CH_3NH_3PbX_3$ (X = Cl, Br, I)[107], where the spectra of the single halide samples present less and narrower low frequency Raman bands in comparison to the mixed halide samples which have mixed Pb-X bond character. Nevertheless, the spectra of the $CH_3NH_3PbI_2X$ samples are dominated by the Pb-I vibration at about 100 cm^{-1} suggesting possible segregation of the $CH_3NH_3PbI_3$ phase in

nanodomains. Electronic properties of $(CH_3)_3SPbI_{3-x}Br_x$ and $(CH_3)_3SPbI_{3-x}Cl_x$ were investigated using UV-Vis and photoluminescence spectroscopy at room temperature. The diffuse absorption spectra acquired from transforming the diffuse reflectance spectra Kubelka-Munk transforms of $(CH_3)_3SPbI_{3-x}Br_x$ and $(CH_3)_3SPbI_{3-x}Cl_x$ are presented in **Figure 3-7.** It is possible to find the energy band gap value (E_g) by considering the x-axis intercept of a linear extrapolation of the low energy part of the respective spectra, however, this is not an axiom. It is easy to see the intercepts for the I, Br and Cl analogues, yet those found by extrapolation of the mixed halide analogue spectra would have provided quite small E_g values. In many cases, it is more useful to keep as E_g the energy of the first absorption valley occurring at energy higher than the excitonic peak. The spectra reveal that the absorption onset energy increases for $(CH_3)_3SPbI_{3-x}Br_x$ from 2.5 to 3.2 eV with increasing Br content and for $(CH_3)_3SPbI_{3-x}Cl_x$ from 2.5 to 3.6 eV with increasing Cl content. However, the values of the absorption edge cannot be related to the E_g of the materials, for two reasons: i) due to the excitonic states present and ii) due to the fact they contradict the values provided for such face sharing $[PbX_6]$ quantum wires found in the literature.[108–112] For example, the $(CH_3)_3SPbBr_3$ semiconductor has similar structure of face-sharing $PbBr_6$ octahedra as in where in the latter refs.[108,113,114] an excitonic peak was observed at 328 nm, thus, the E_g of such quantum wires should be least 3.8 eV, and cannot be related to the lowest energy absorption appearing here at 3.2 eV. Therefore, the E_g values are estimated by drawing the tangential lines and taking the intercept to the x-axis not from the lowest energy bands but from the first high energy band in each case (see **Figure 3-7**a).

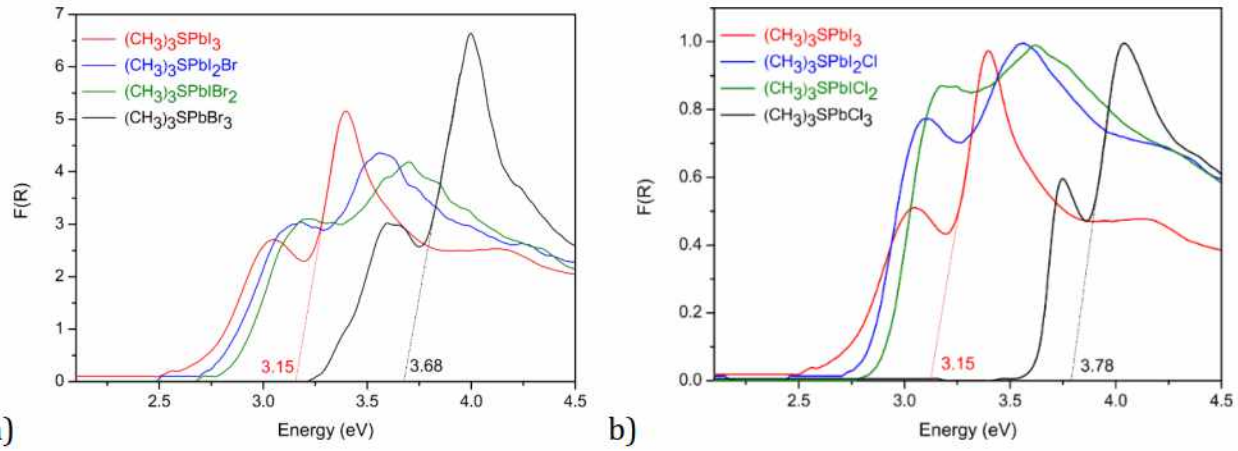

Figure 3-7: Diffuse reflectance UV-Vis spectra in Kubelka-Munk units for (a) $(CH_3)_3SPbI_{3-x}Br_x$ (b) $(CH_3)_3SPbI_{3-x}Cl_x$ (x = 0, 1, 2, 3).

For the mixed halides, these values are being found from the position of the first absorbance valley towards high energies; for the pure I-, Br-, Cl-compounds the two methods yield almost the same E_g. For $(CH_3)_3SPbI_3$ this estimation leads to E_g of 3.15 eV in accordance to reference[42], while for $(CH_3)_3SPbBr_3$ to 3.68 eV. It is anticipated that the mixed I/Br perovskites will have energy gap values varying in between as in the other corner-sharing perovskite materials.[107] The as above discussed E_g values are collected in **Table 3-5**. Similar conclusions could be drawn for the spectra of $(CH_3)_3SPbI_{3-x}Cl_x$, despite the fact that $(CH_3)_3SPbCl_3$ has different structural symmetry from the rest. Again, it can be safely deduced from the optical spectra of the Cl-I mixed variants that once iodine is incorporated as a mixed ion along with Cl, the optical absorption spectra are not distinctively different from each other, neither from those based on the I-Br materials since the onset of absorption starts at almost the same energy values.

Table 3-5: Band gap values for $(CH_3)_3SPbI_{3-x}Br_x$ and $(CH_3)_3SPbI_{3-x}Cl_x$ (x = 0, 1, 2, 3).

Compound	E_g (eV)	Compound	E_g (eV)
$(CH_3)_3SPbI_3$	3.15		
$(CH_3)_3SPbI_2Br$	3.29	**$(CH_3)_3SPbI_2Cl$**	ca. 3.2
$(CH_3)_3SPbIBr_2$	3.37	**$(CH_3)_3SPbICl_2$**	ca. 3.3
$(CH_3)_3SPbBr_3$	ca. 3.75	**$(CH_3)_3SPbCl_3$**	3.75

The PL spectra of the reported materials $(CH_3)_3SPbX_3$ (X = I, Br, Cl) are presented in **Figure 3-8,** yet the luminescence signal of the various one-dimensional face sharing octahedral wires is not strong compared to one dimensional corner sharing octahedra-based quantum wires. PL spectroscopy has been used here with excitation energies above 3.8 eV for all materials, while photoluminescence excitation spectra (PLE) have been acquired by monitoring the tails of the low and high energy luminescence peaks. The material for X = I, shows a broad PL centered around 470 nm and a weak signal centered at 382 nm. For the case X = Br, the same set of peaks appears, where the high energy peak at 379 nm peak is much stronger than in the case of the I, while for the X = Cl case, the high energy peak though appears strong and its center has blue shifted to at 364 nm. The broad band appearing around 470 nm for all three cases of X = I, Br, Cl is due to the organic component, however, the high energy peaks

of the semiconductors are not related in any of the spectra to the pristine organic component. On the other hand, $(CH_3)_3SCl$ exhibits PL signal centered at 380 nm, thus, the Cl analogue of the reported compounds is believed not to exhibit PL signal due to the inorganic network, or more possibly energy is being transferred from the inorganic onto the organic network appearing as organic molecule luminescence. The above described behavior is unique in the perovskite semiconductors. The small PL signal for the I at 382 nm (3.24 eV), for Br at 379 nm (3.27 eV) could be related to excitonic states, however, for the case of I this would imply some exciton higher than the observed band gap, which is discussed in terms of the band structure which shows two band gaps, the direct being slightly higher than the lowest indirect. In all cases, the signal of the organic moiety falls close to that of the inorganic lattice absorption and energy transfer effects are probably engaged in these systems.

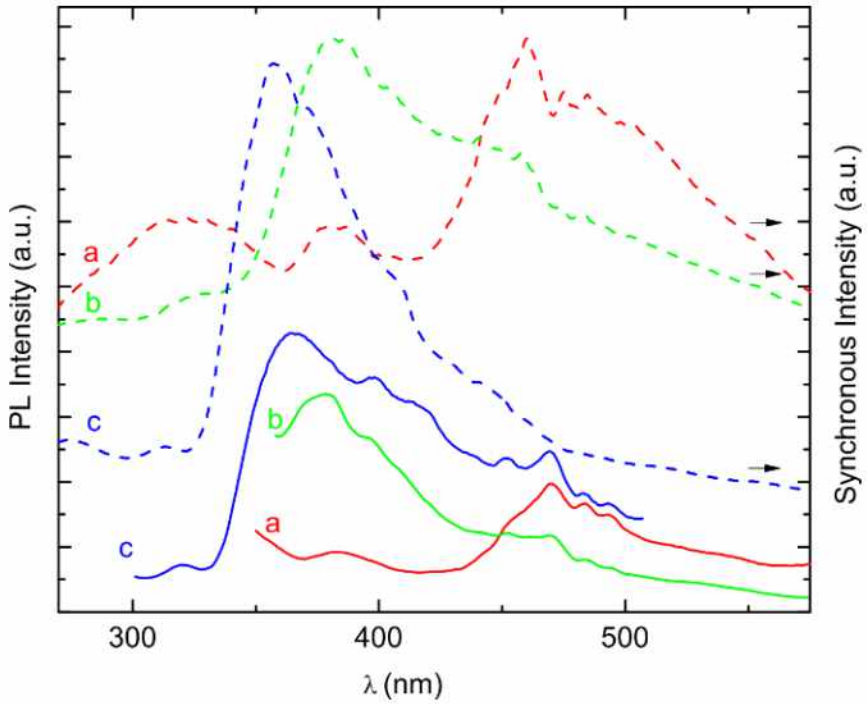

Figure 3-8: PL (solid lines) and synchronous (dashed lines) spectra for (a) $(CH_3)_3SPbI_3$, (b) $(CH_3)_3SPbBr_3$ and (c) $(CH_3)_3SPbCl_3$ (λ_{exc} = 300, 330, 250 nm, respectively).

In order to further resolve spectroscopic details, synchronous luminescence scans have been recorded and presented in **Figure 3-8** in relation to the PL data. In these spectra, $(CH_3)_3SPbI_3$ has shown absorbance related peaks at 380 nm and a broad band centered around 470 nm, while the Cl analogue shows a strong broad absorption peak around 370 nm. Thus, it appears that the broad band at 470 nm in the PL and synchronous scans of the precursor organic

molecule, is strong in the case of $(CH_3)_3SPbI_3$, while it is diminished for the Br and Cl analogues; in fact, it is almost vanished in the Cl case. Thus, we conclude that the organic component, although it shows a broad structure around 470 nm, its signal is being progressively weakened as the materials shift from I to Br and then to Cl. Moreover, in the same progression of materials the higher energy peaks at around 320 nm also change, indicating that the organic molecule is not on its own responsible for this complex PL signals observed, but it is the interaction of the organic to the inorganic component that creates these complex signals.

3.1.3 Stability and scanning electron microscopy

Poor stability of organic–inorganic perovskite materials in humid conditions has hindered the success of perovskite solar cells in real-life applications. The compounds are stable in air even after several months and do not dissolve or react with water.

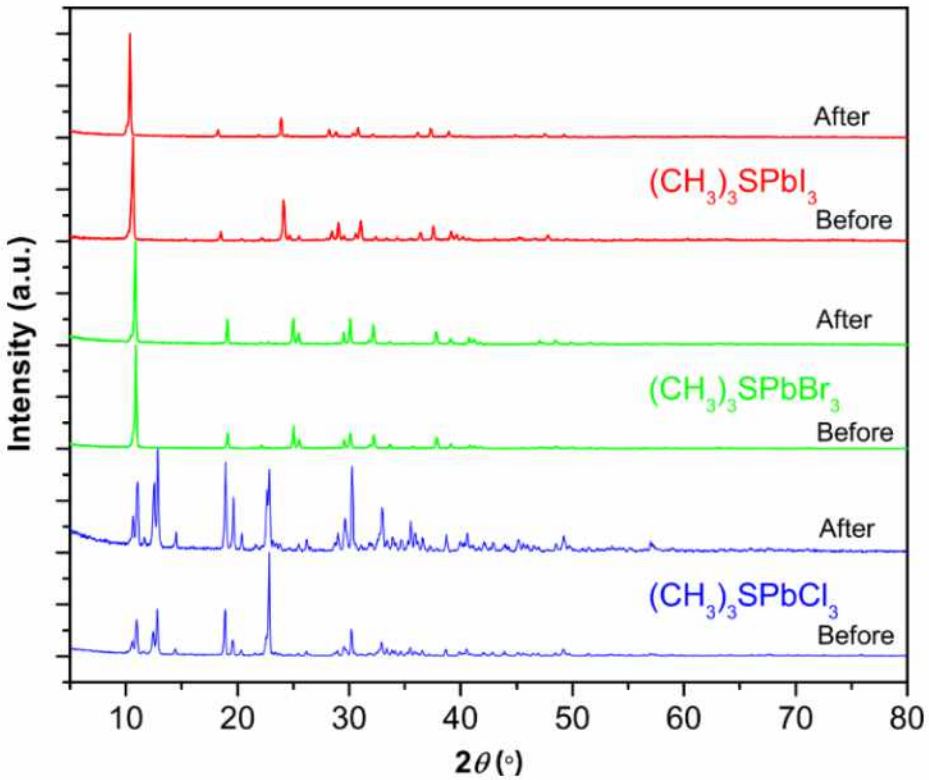

Figure 3-9: XRPD patterns of the samples before and after exposure to 80 °C for 24 hours in ambient air.

Moreover, XRPD analysis of the samples after exposure to 80 °C for 24 hours in ambient air shows no signs of degradation (**Figure 3-9**). Regarding photochemical stability, thin films of the compounds were deposited from DMF solution on glass/compact TiO_2 substrates

(glass/TiO_2/perovskite). XRPD analysis of the films after exposure to a solar simulator for 8 hours in ambient air shows no perovskite degradation (**Figure 3-10**).

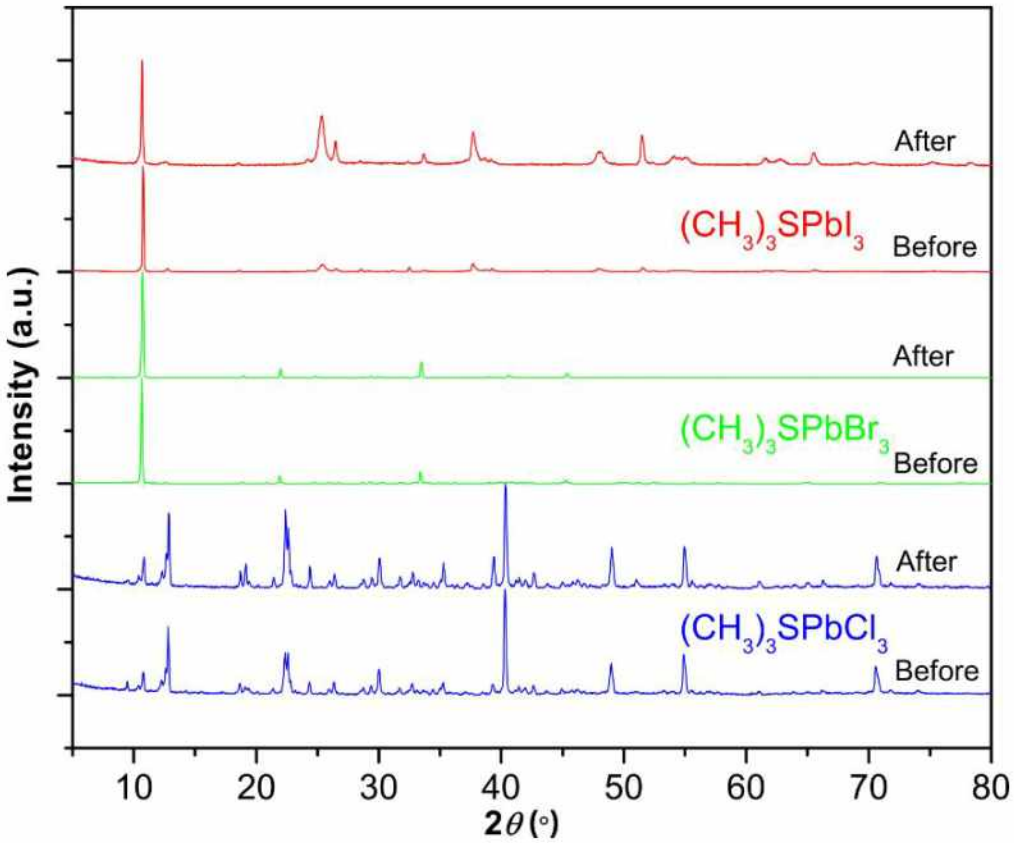

Figure 3-10: XRPD patterns of the glass/TiO_2/perovskite films before and after exposure to a solar simulator for 8 hours in ambient air.

The morphology of the $(CH_3)_3SPbI_{3-x}Br_x$ and $(CH_3)_3SPbI_{3-x}Cl_x$ bulk samples was analyzed using Scanning Electron Microscopy and their chemical composition was estimated by EDAX. $(CH_3)_3SPbBr_3$ appears as well-structured rods (**Figure 3-11**), whereas $(CH_3)_3SPbCl_3$ forms crystallites with almost spherical shape (**Figure 3-12**). **Figure 3-13** and **Figure 3-14** show the EDAX spectra of $(CH_3)_3SPbI_{3-x}Br_x$ and $(CH_3)_3SPbI_{3-x}Cl_x$ (x = 1, 2, 3) perovskites, confirming their Pb/X atomic ratio, e.g. for $(CH_3)_3SPbBr_3$ with atomic percentage Pb 9.45%, Br 28.28% (Pb/Br 1:2.99 atomic ratio). Noteworthy, I/Br and I/Cl ratios are almost constant on different spots of each mixed-halide sample, which proves that there are no inhomogeneous domains in the bulk materials.

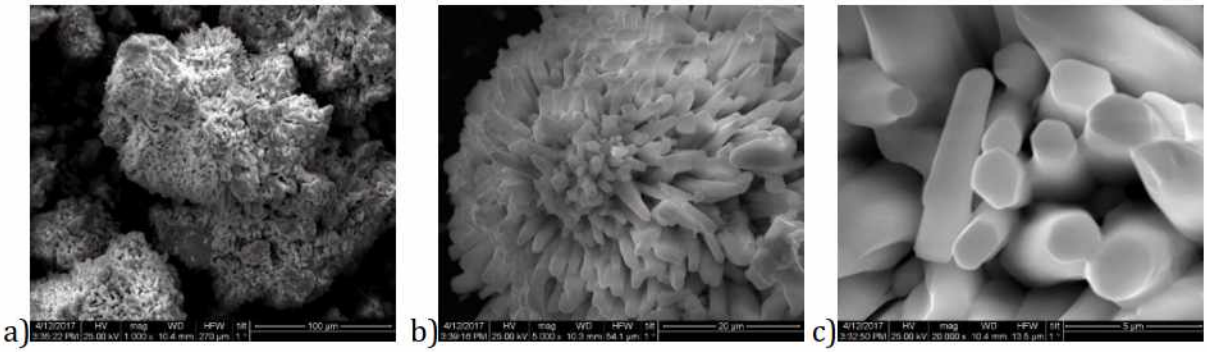

Figure 3-11: SEM images of $(CH_3)_3SPbBr_3$ perovskite with different magnification.

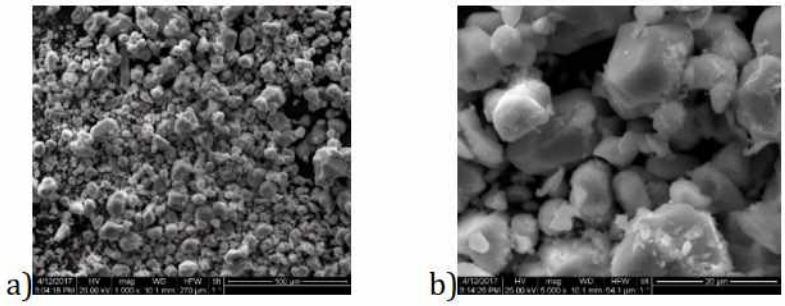

Figure 3-12: SEM images of $(CH_3)_3SPbCl_3$ perovskite with different magnification.

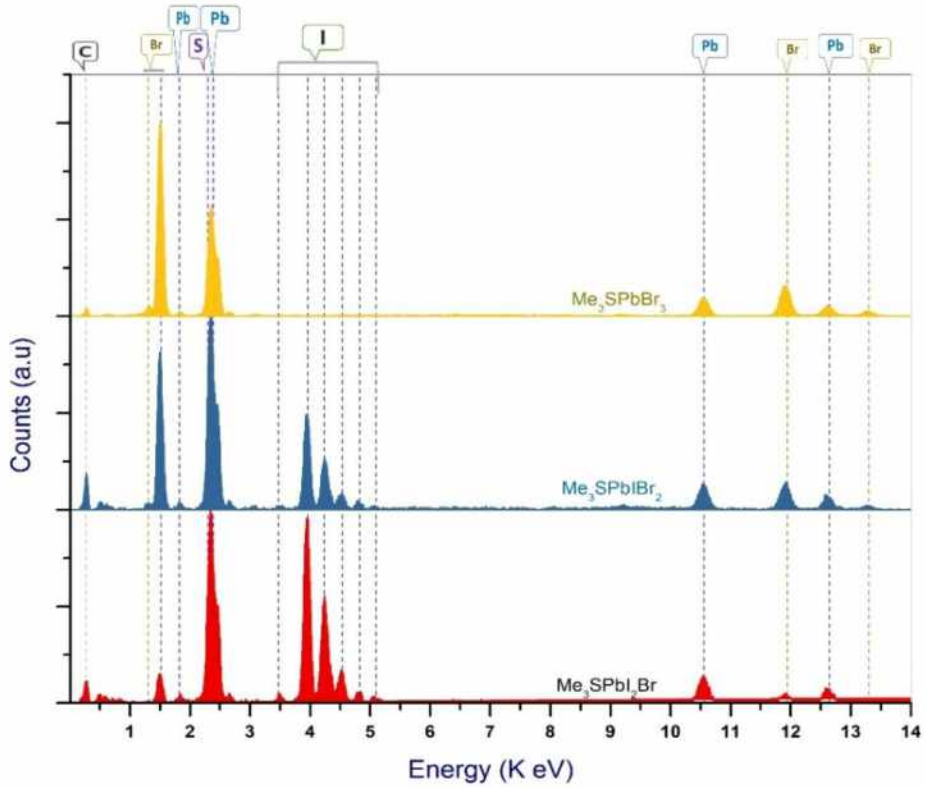

Figure 3-13: Energy Dispersive X-ray spectra of $(CH_3)_3SPbI_{3-x}Br_x$ perovskites.

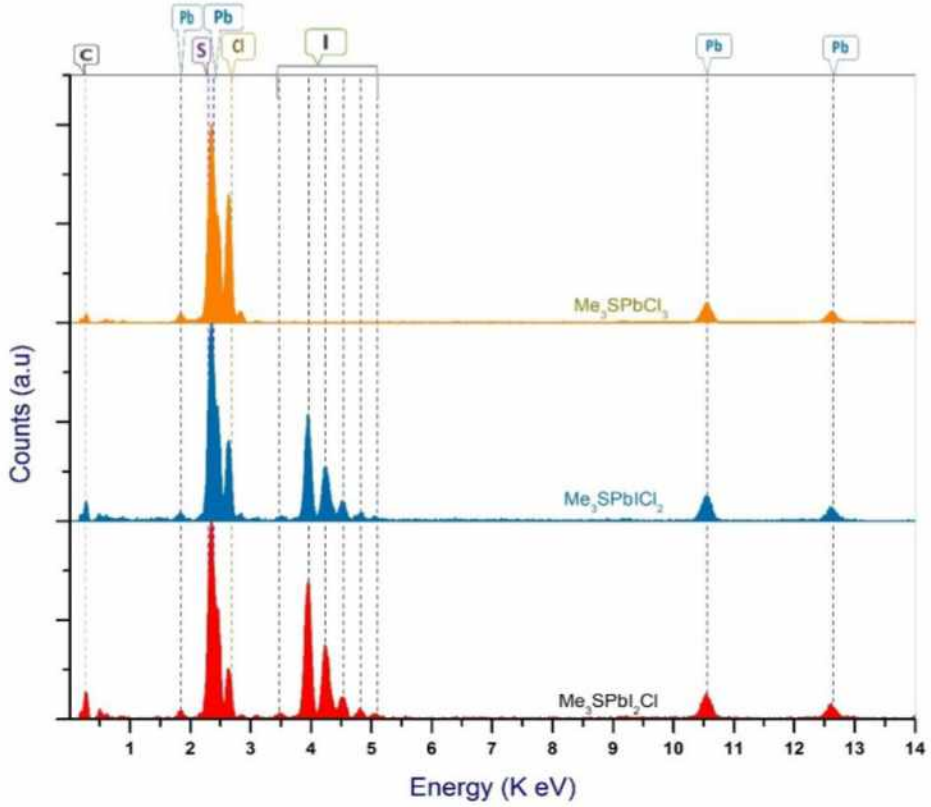

Figure 3-14: Energy Dispersive X-ray spectra of $(CH_3)_3SPbI_{3-x}Cl_x$ perovskites.

3.1.4 EHT calculations

In order to evaluate the band structure and energy band gap of the above reported materials as well as to understand the interplay of the quantum wires with the surrounding organic moiety, Extended Hückel calculations have been performed. In particular, given that this type of calculation is dependent on parameters, the methodology in reference[105] has been used, where the values of [115] have been utilized with the exception of the exponent of the halogen p Slater type orbitals which was varied in order to match the $CH_3NH_3PbX_3$ structure band gap to the experimental value. Some variation in these parameters from those reported in reference[112], is due to the different band gaps that were once used derived from optical experiments. Any other effort to vary other exponent is futile, added to the fact that such effort is not bearing any physical meaning since the halogen is the inorganic network's connecting component. Therefore, the E_g values for the 3D perovskite structures X = I, Br, Cl that have been fitted are 1.5, 2.3, 2.88 eV with found Slater exponents for the outer *p* orbitals to be 2.47, 2.321, 1.9275, respectively. It is stressed that the quantum wires in this work consist of face-sharing octahedra, whereas the 3D perovskites contain corner sharing octahedra.

Thus, the parameters are expected to be optimum, yet give a more than quantitative relation between structure and band gap as well as band dispersion curves. The EHT calculations have been performed either by keeping the organic and inorganic component, or by only using the inorganic component which had been charged negatively with the electrons donated by the organic moieties.

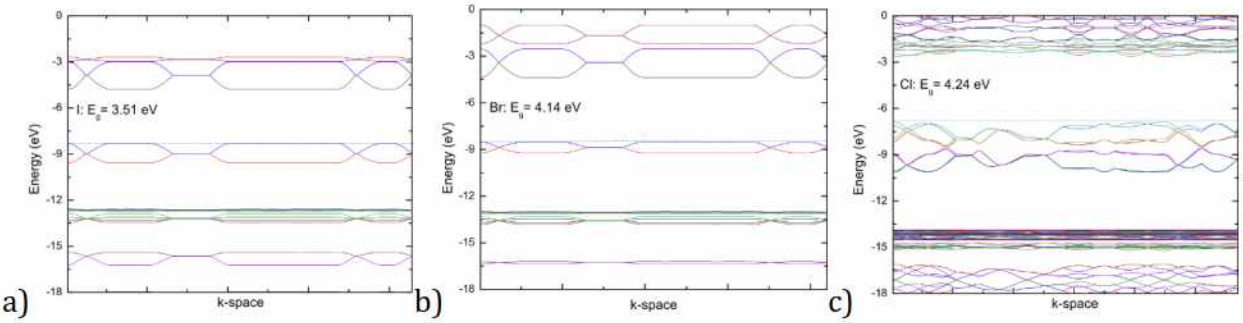

Figure 3-15: Calculated band structures along selected path in the Brillouin Zone for $(CH_3)_3SPbX_3$: a) X = I, b) X = Br and c) X = Cl.

In all cases, the organic component does not change the HOMO/LUMO energy offsets nor their dispersion except in the case of I and Br where the introduction of the organic component introduces a shift to the two indirect gap k point positions. $(CH_3)_3SPbCl_3$ is found to have a direct band gap, while all I and Br analogues appear to have an indirect band gap as well, however, with a slightly larger direct band gap. The calculated band dispersion diagrams can be found in **Figure 3-15**.

The calculated band gaps, without including the organic component, are found at 3.51, 4.14 and 4.24 eV for $(CH_3)_3SPbI_3$, $(CH_3)_3SPbBr_3$ and $(CH_3)_3SPbCl_3$, respectively. The iodide and bromide show indirect band gap, however the difference from the direct to indirect is much less than the thermal activation energy, while the chloride is direct band gap semiconductor. Also, in order to test the above calculations, we repeated the same type of method for $((CH_3)_3S)_4Pb_3Br_{10}$ appeared in[106], and $[C_6H_5CH_2SC(NH_2)_2]_4Pb_3I_{10}$ in[116], which consist of face-sharing octahedra broken or infinite wires, respectively. Moreover, EHT calculations were performed on the mixed halide analogues, assuming various configurations for the disordered I/Br or I/Cl atoms. For the first compound which is the second reported perovskite based on trimethyl sulfonium, our calculations with the specific exponents, as shown above

predict a gap of 3.58 eV, i.e. at 346 nm. This is in accordance with the optical spectra in the same reference as well as with previously reported results.[117] Calculations of the second compound, using the exponents described above, yielded a band gap of 4.43 eV (279 nm), while the organic part orbital energies appear within the band gap; these results are in agreement with the reference[110] (**Figure 3-7**), where the excitonic peak appears at 310 nm and the gap at about 4.3 eV. Also, calculations for the mixed halide analogue $(CH_3)_3SPbIBr_2$, for various positions of the Br and I within the unit cell predict band gap values from 2.9 to 3.5 eV, without assuming any supercell structure. These results are again in accordance with the optical spectra in this work, in the sense that all EHT band gap values computed coincide with the second peak of the experimental absorption spectra. It is predicted that the mixed halides are expected to have varying band gap values and it is natural that the experimental absorption spectra are so broad.

3.1.5 First-principles DFT calculations

Ab initio DFT calculations on $(CH_3)_3SPbI_2Br$ were carried out to predict the optimized lattice parameters, band structure, total density of states (TDOS) and partial density of states (PDOS), using different functions (LAD/CA-PZ, GGA/PBE, GGA/PBESOL) with 240 eV and 380 eV energy cutoffs. $(CH_3)_3SPbI_2Br$ is a characteristic example of mixed halide perovskite in which the site occupancy factors are equal to SOF(I) = 2/3 and SOF(Br) = 1/3. We discuss here the electronic properties of $(CH_3)_3SPbI_2Br$ from GGA/PBESOL with 380 eV energy cutoff (**Figure 3-16**).

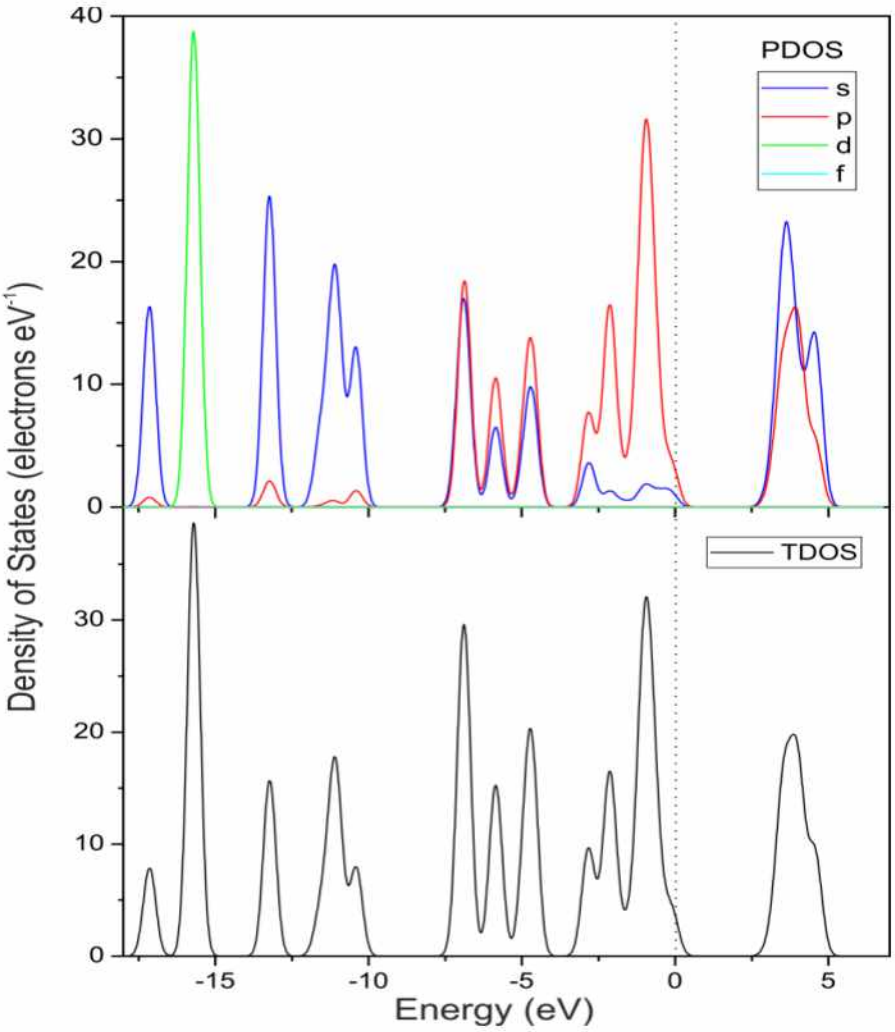

Figure 3-16: Total (bottom) and partial (top) density of states for $(CH_3)_3SPbI_2Br$.

It appears that *p* orbitals have higher contribution than *s* orbitals at the top of the valence band. The strong hybridization of orbitals can shift the location of the valence bands to the lower energy area with wider peaks. The PDOS for lead and halogen atoms indicate a weaker bonding between them. At the top of the valence band, the main contribution is from iodine and bromine (5p and 4p states, respectively) with overlapping of Pb 6s states. At the bottom of the conduction band, the main contribution is from X 5s, 6s, and Pb 6p. On the other hand, the organic cation has little contribution to the top of valence band and bottom of the conduction band (**Figure 3-17**).

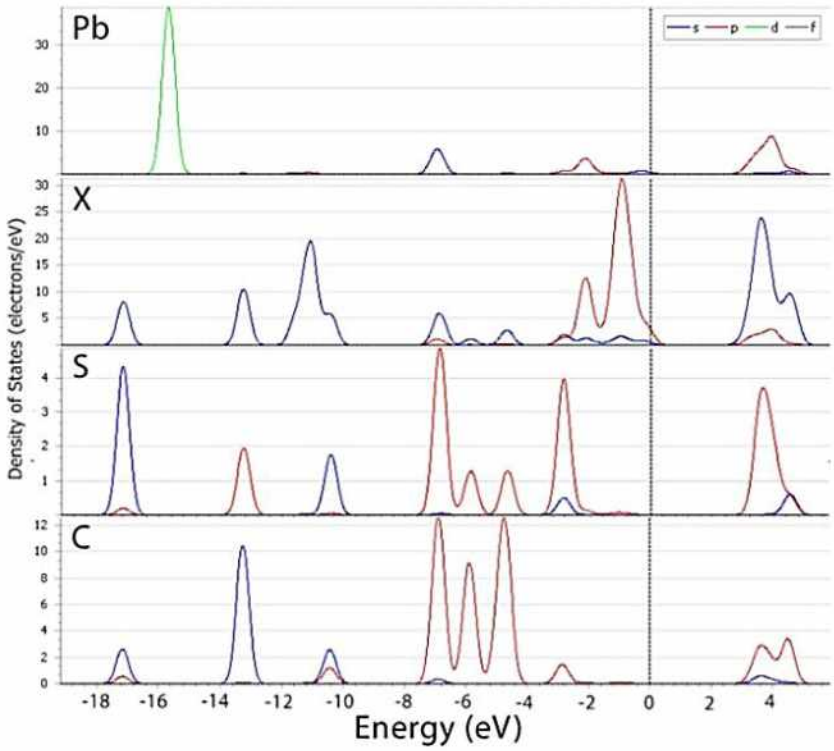

Figure 3-17: PDOS contribution to the top of valence band for each atom type of $(CH_3)_3SPbI_2Br$.

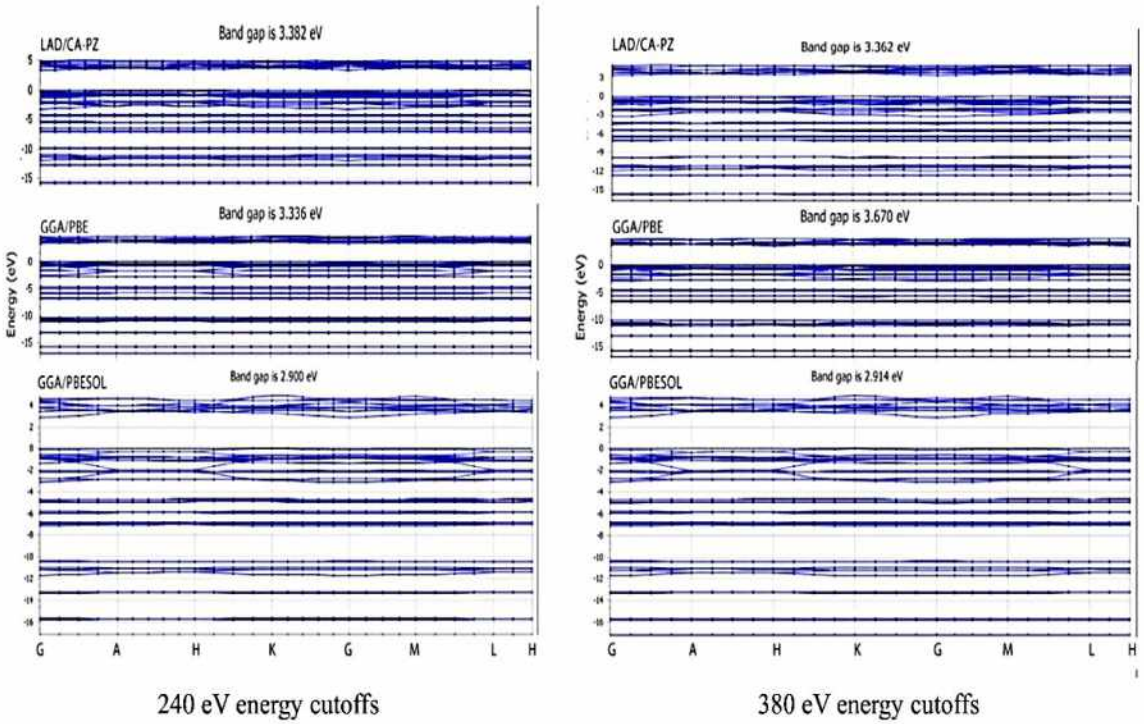

Figure 3-18: Electronic band structures of $(CH_3)_3SPbI_2Br$, using different functions with 240 eV and 380 eV energy cutoffs.

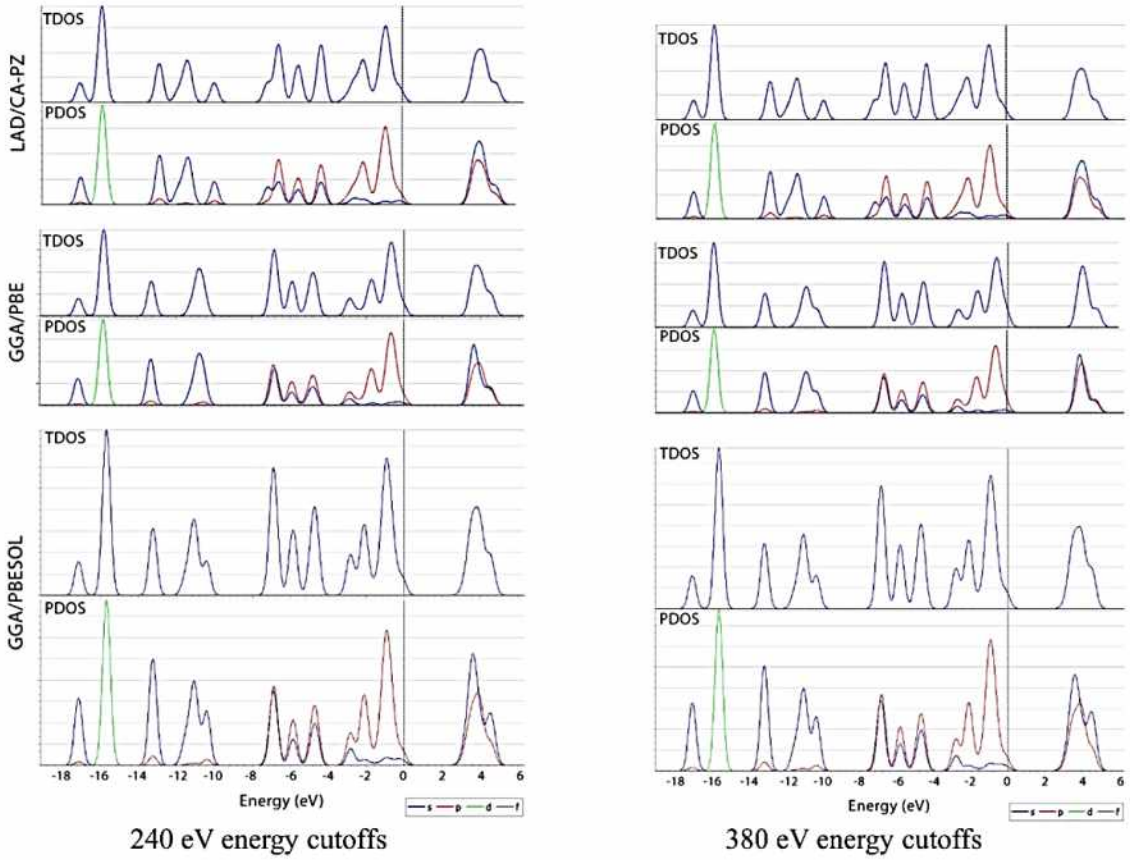

Figure 3-19: Total density of states (TDOS) and partial density of states (PDOS) of $(CH_3)_3SPbI_2Br$, using different functions with 240 eV and 380 eV energy cutoffs.

The electronic band structures (**Figure 3-18**) and DOS-PDOS (**Figure 3-19**) of hexagonal $(CH_3)_3SPbI_2Br$ using different functions (LAD/CA-PZ, GGA/PBE, GGA/PBESOL) with 240 eV and 380 eV energy cutoffs have been evaluated. The computed band gaps from the LAD/CA-PZ, GGA/PBE results are in good agreement with the experimental E_g, but GGA/PBESOL results are lower than experimental value. Our theoretical results support the strong relationship between structure properties and energy band gap of different compounds. **Figure 3-18** shows significant dispersion associated with the face-sharing networks of $[PbX_6]$ octahedra. For example, the obtained values from DFT/ LAD/CA-PZ calculation point to an indirect band gap of 3.38 eV with the minimum from the K to G symmetry point.

CHAPTER (4)

lead-free $(CH_3)_3SSnI_3$ 1-D perovskite

lead-free $(CH_3)_3SSnI_3$ 1-D perovskite

Metal halide perovskites have received great attention in the recent years due to their potential use as materials in solar cells[118], and in luminescent devices.[119] The main challenges to address are the toxicity of lead and the stability of the organic cation in humid conditions. In search of organic cations that can outperform the stability of well-studied amine-containing perovskites against ambient conditions [38,120], the research community also explores thiol compounds.[121] We have recently reported the use of the trimethyl sulfonium cation in hybrid perovskite compounds as a substitute for the hygroscopic methylammonium (MA) and formamidinium (FA) cations. This led to the new series of $(CH_3)_3SPbX_3$ (X = Cl, Br, I) compounds, which are very stable in ambient air but unfortunately have large band gaps of over 3 eV and cannot be used in solar cells.[42,122] Moreover, we extended our research into non-toxic, lead-free perovskites and focused on the air-stable $((CH_3)_3S)_2SnX_6$ (X = Cl, Br, I) series.[123] In this case of 0D compounds, also known as 'defect' perovskites, $((CH_3)_3S)_2SnI_6$ exhibits a band gap of 1.4 eV and acts as a hole-transporting material in dye-sensitized solar cells with power conversion efficiency (PCE) of 5%. The photovoltaic efficiency of the latter compound is significantly higher than of its purely inorganic analogues, such as $Cs_2SnI_3Br_3$ with PCE = 3.6% under 1-sun illumination.[124] As for the $ASnI_3$ compounds, many reports have been published with A being Cs, FA and MA. For example, $CsSnI_3$ acts as hole-transporter in dye-sensitized solar cells with power conversion efficiency of up to 10.2%[125] , whereas $(FA)_{0.75}(MA)_{0.25}SnI_3$ acts as absorber and has reached power conversion efficiency of up to 8% in perovskite solar cells. [126] Nevertheless, these compounds suffer from high oxidation rate of the divalent tin in ambient air. A way to overcome this problem is to alter the halogen content, either by direct substitution on halogen site with its lighter analogues, e.g. in $CH_3NH_3SnBr_xCl_{3-x}$ that can be processed in aqueous solution[127], or by doping the material with SnF_2, as in the case of $CsSnI_3$ which leads to significant retardation of the oxidation process of the material.[128] Another way to improve the stability of the $ASnI_3$ compounds is to dope the A site with Cs, as in $FA_{1-x}CsSnI_3$ [129] or with bulky organic cations.[130,131] In the current work, we investigate for the first time the crystal structure, chemical stability and spectroscopic properties of $(CH_3)_3SSnI_3$. This lead-free perovskite material has not been reported so far and is expected to combine low toxicity with enhanced stability.

4.1.1 Structural analysis

Powder X-ray diffraction showed that the perovskite compound crystallizes at room temperature with hexagonal symmetry (space group *P*6$_3$*mc*, No. 186), lattice parameters of *a* = *b* = 9.5209(9) Å and *c* = 7.9872(8) Å, molecular formula $C_3H_9SSnI_3$, *Z* = 2 (**Figure 4-1**).

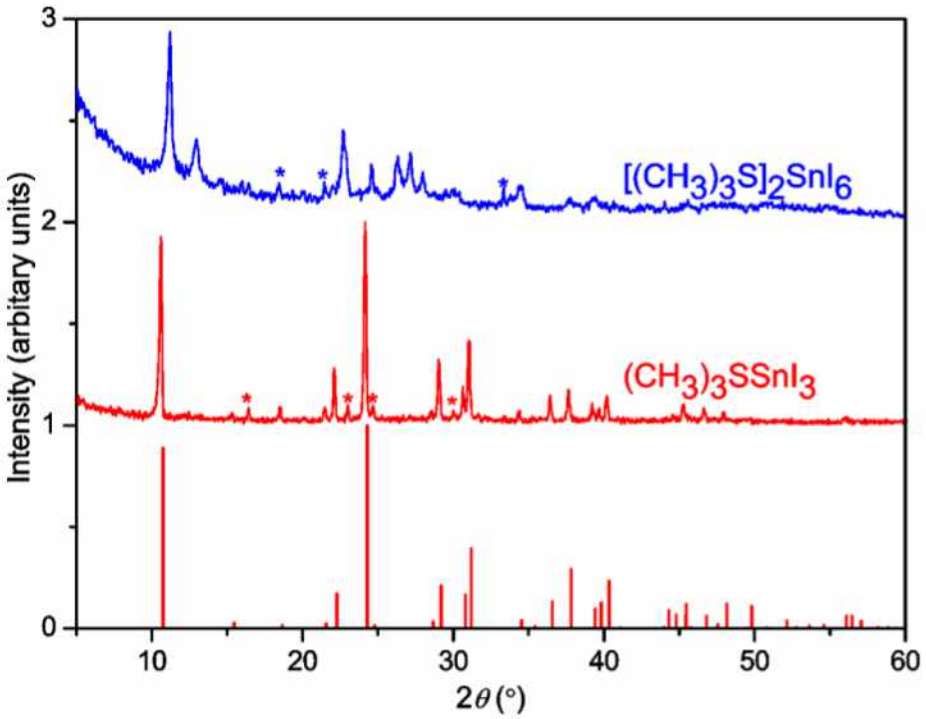

Figure 4-1: X-ray powder diffraction pattern of as-synthesized $(CH_3)_3SSnI_3$ as well as its decomposition product $((CH_3)_3S)_2SnI_6$ upon exposure of the sample to ambient air for several days. A theoretical histogram of $(CH_3)_3SSnI_3$ is given below. Reflections marked with an asterisk may be attributed to diffuse scattering of the samples.

Fractional atomic coordinates: Sn (0, 0, 0.514(11)), I (0.3074(9), 0.1537(9), 0.275(8)), S (1/3, 2/3, 0.19910), C (0.42780, 0.85560, 0.29730). The distorted, face-sharing $[SnI_6]$ polyhedra form 1D chains along the *c* axis (**Figure 4-2**). This resembles the crystal structures of $(CH_3)_3SPbI_3$ and δ-$FAPbI_3$ [132,133], which are also yellow and thermodynamically stable at room temperature. In fact, the lattice parameters are almost identical with those of $(CH_3)_3SPbI_3$ (*a* = *b* = 9.5635(9) Å and *c* = 7.9795(8) Å). The trimethylsulfonium cations occupy interstitial sites between the distorted, face-sharing $[SnI_6]$ octahedra.

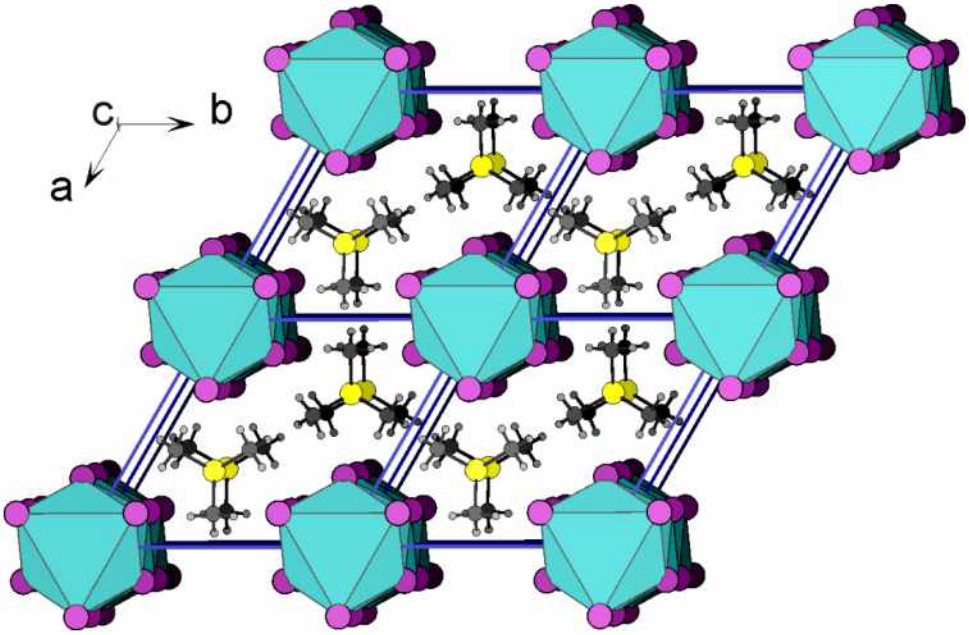

Figure 4-2 : View of the 2 × 2 × 2 unit cell of $(CH_3)_3SSnI_3$ along the c axis. Sn atoms (not shown) reside in the center of the octahedra.

Unfortunately, the intense diffuse scattering of the polycrystalline material did not allow for an accurate determination of the atomic positions in the trimethylsulfonium group, which were kept constant based on the structural model of hexagonal $(CH_3)_3SPbI_3$.[42] The thermal displacement values of all atoms were set to 0.03 $Å^2$ without refinement. In comparison with the structural characteristics of the amine cations, the $(CH_3)_3S^+$ cation behaves similarly to the bulky $N(CH_3)_4^+$ cation which also forms a 1D-hexagonal structure in $[N(CH_3)_4]SnI_3$ [134], rather than to the CH_3NH_3 cation which forms a 3D structure in $CH_3NH_3SnI_3$.[127]

4.1.2 Optoelectronic properties

Polycrystalline powder of $(CH_3)_3SSnI_3$ was measured in two ways: a) in a sealed quartz tube under vacuum and b) after pressing under argon atmosphere (glove box) into a 10 mm diameter × *ca.* 1 mm thick pellet using a set of stainless steel mould and dies, and then exposed to ambient air. Both samples were measured in diffuse reflectance (R) mode and the energy band gap was determined via the Kubelka-Munk equation: $F(R) = (1-R)^2 / 2R$. [95] The optical absorption spectrum of $(CH_3)_3SSnI_3$ (**Figure 4-3**a) shows a direct band gap at 2.85 eV. The compound is gradually oxidized to $((CH_3)_3S)_2SnI_6$ with a band gap of 1.4 eV [123] upon exposure to ambient air, accompanied by color change from bright yellow to orange-brown and eventually black. To investigate the oxidation rate of $(CH_3)_3SSnI_3$, UV–Vis spectra were collected on a pellet as a function of the exposure time

in ambient air (ca. 5 minutes passed before the 'as-prepared' spectrum in **Figure 4-3**b). A significant decrease of the absorbance over the whole spectrum at the wavelength position of the energy gap after the first three hours was observed for the $(CH_3)_3SSnI_3$ pellet. Similarly, the energy band gap and the curve profile constantly shift downwards over a duration of one day, as it eventually converts to the $((CH_3)_3S)_2SnI_6$ spectrum (verified by the corresponding XRPD pattern in **Figure 4-1**). Therefore, the trimethyl sulfonium cation plays an important role in the slow degradation of the sample, compared with previous reports on 3D hybrid Sn perovskite films[135] and $CsSnI_3$ [128] that are oxidized within minutes after exposure to ambient air. This strong stereochemical hindrance in 1D ABX_3 compounds has been recently proposed as a way to improve the efficiency and stability of the perovskite solar cells[136].

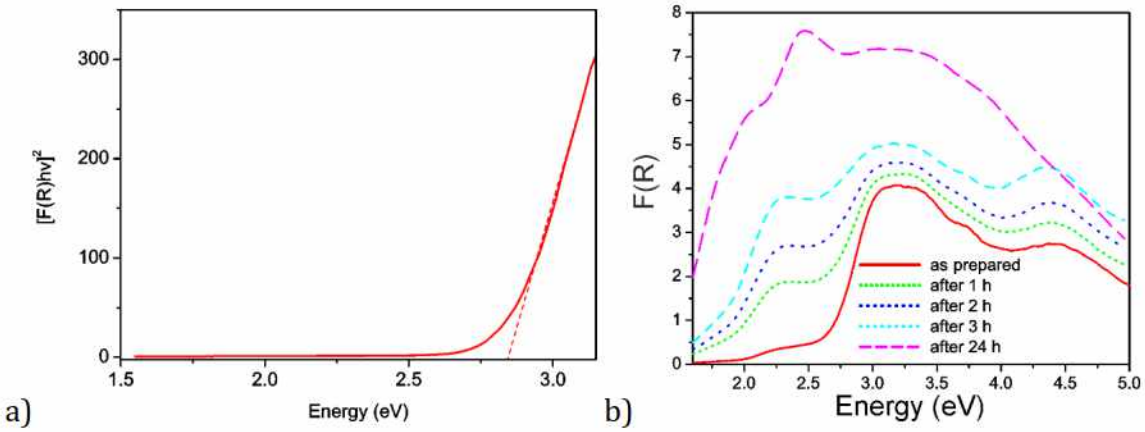

Figure 4-3: Diffuse UV-Vis reflectance spectra in Kubelka-Munk units for $(CH_3)_3SSnI_3$ in the form of: (a) powder sealed in a silica tube under vacuum and (b) a pellet exposed to ambient atmosphere and measured at various times up to 24 hours.

Photoluminescence (PL) spectra were recorded for a sample in the sealed quartz tube, and the title compound also exhibits weak luminescence with an emission maximum at 414 nm (**Figure 4-4**), which is related to the 1D exciton recombination that resides in the infinite chains; it is possible that due to partial degradation, evident in the absorption peak at ca. 2.25 eV in the as-prepared absorbance spectrum (**Figure 4-3**b) some Sn-I chains may have a finite length, resulting in a blue shift of the PL peak. In general, perovskites compounds with 1D face-sharing octahedra do not have appreciable luminescence signal[137], whereas higher dimensionality compounds such as monoclinic 2D-$((CH_3)_3S)_4Pb_3Br_{10}$ exhibit broad photoluminescence signal.[106] The $(CH_3)_3SSnI_3$ perovskite exhibits significantly weaker luminescence after exposure to air for ca. 24 hours (not shown), due to its gradual decomposition into $[(CH_3)_3S]_2SnI_6$.

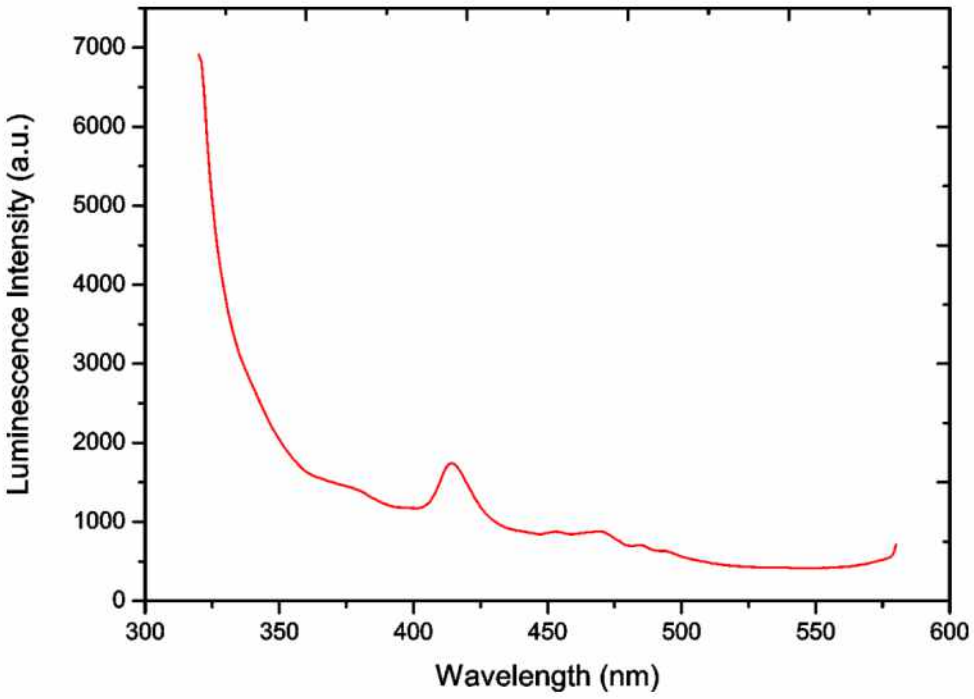

Figure 4-4: PL Emission spectrum of $(CH_3)_3SSnI_3$ with excitation wavelength at λ_{ex} = 300 nm.

4.1.3 Vibrational properties

Multi-temperature micro-Raman spectra of the $(CH_3)_3SSnI_3$ perovskite show characteristic vibrational modes both of the organic moiety and the inorganic framework. As it also happens in the case of the lead analogue, $(CH_3)_3SPbI_3$ [42], the low frequency region, below 200 cm^{-1}, comprises mainly the vibrations in the octahedral SnI_6 inorganic framework. As shown in **Figure 4-5**, the frequencies and linewidths of the peaks in the low frequency region depend strongly on the temperature. In more detail, the peak at 113 cm^{-1} is attributed to the Sn-I symmetric stretching vibration.[42] There is a blue shift with regard to the corresponding Pb-I vibration in the Pb counterpart compound primarily due to the significantly lower reduced mass of the I-Sn system. The very broad mixed band that appears in our Raman spectra at 44 cm^{-1}, is attributed to the overlap of the I-Sn-I antisymmetric bend deformation mode with the lattice mode, which involves vibrations of the organic moiety $(CH_3)_3S^+$ into the rigid $[SnI_6]$ lattice[42]. As the temperature drops between 0 °C to -10 °C, the position of the 112 cm^{-1} peak shifts abruptly to approximately 117 cm^{-1}. It is noticeable that thereafter, the frequency of this band remains practically constant in a wide temperature range, indicating that the SnI_6 octahedra are hardly affected by thermal contraction. Another remarkable observation is that as the temperature drops below -20 °C, the two broad bands observed at RT split towards many more narrow bands which become progressively more distinguished, suggesting a first structural

phase transition which lowers the symmetry of the SnI_6 octahedra. Furthermore, a second phase transition occurs at -160 °C as evidenced by the emergence of a new Raman band at ~50 cm^{-1} and the fine structuring of several other bands up to 300 cm^{-1}.

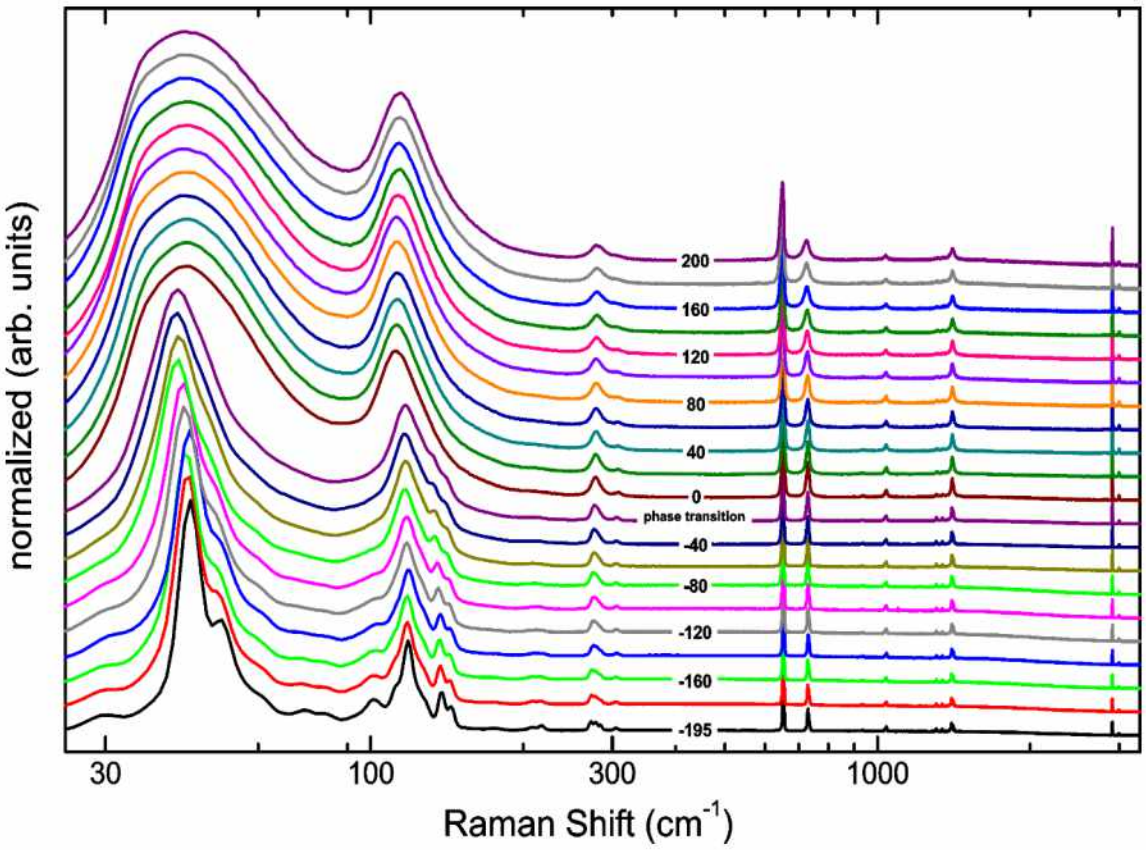

Figure 4-5: Multi-temperature Raman spectra for $(CH_3)_3SSnI_3$. Temperature values are given in °C.

The Raman spectra above 200 cm^{-1} consist exclusively of the $(CH_3)_3S^+$ vibrations. The assignment of the modes has been done according to ref [138] (**Table 4-1**). In a general consideration, their frequencies show a small shift, either blue or red, with regard to those observed in $(CH_3)_3SI$ at the same temperature (see Fig. S3 in Ref.[42]), which is a consequence of the different local environment of the organic cations i.e. inside the $[SnI_6]$ inorganic framework. The splitting of several bands at low temperatures (e.g. the SC_3 deformation at 278 cm^{-1} below -160 °C) suggests that organic moieties undergo a progressive increment of their ordering in the perovskite cage and confirm the above-mentioned second phase transition. The successive phase transitions show perfect reversibility as the sample converted back to the hexagonal modification when returned to room temperature. Using the Linkam temperature cell, high resolution images (not shown) were recorded by the Raman microscope camera on bulk powder. We thus confirmed that the

color remains yellow over the temperature range -170 to ca. 200 °C. The material decomposes at ca. 230 °C, due to the thermal instability of the trimethylsulfonium group.

Table 4-1: Raman frequencies (in cm^{-1}) at RT for $(CH_3)_3SSnI_3$.

Raman shift	Vibration type	Mode
44	I-Sn-I antisymmetric bend deformation	F_{2g}
113	Sn-I symmetric stretching	A_{1g}
278	SC_3 deformation	A_1
309	SC_3 deformation	A_1
651	SC_3 symmetric stretching	A_1
729	SC_3 antisymmetric stretching	E
937	CH_3 rocking	E
1041	CH_3 rocking	E
1308	CH_3 symmetric deformation	A_1
1346	CH_3 symmetric deformation	A_1
1405	CH_3 antisymmetric deformation	E
1412	CH_3 antisymmetric deformation	E
1425	CH_3 antisymmetric deformation	E
2910	CH_3 symmetric stretching	A_1
2999	CH_3 antisymmetric stretching	A_1

CHAPTER (5)

$((CH_3)_3S)_2SnX_6$ (X = Cl, Br, I) Perovskites

Lead-free Tin (IV) halide $((CH_3)_3S)_2SnX_6$ perovskites

Perovskite compounds of the general stoichiometry ABX_3 exhibit a wide range of chemical composition from inorganic oxides (e.g. $CaTiO_3$)[22] to metal-organic frameworks (e.g. $[(CH_3)_2NH_2]M(HCOO)_3$ where M = Mn, Zn)[139–141], and are multi-purpose functional materials[43,133]. Halide perovskites have attracted considerable attention over the past five years due to their application in third generation solar cells and light emitting diodes [124,142–145]. In particular, three-dimensional (3D) hybrid perovskites, such as $CH_3NH_3PbI_3$, have already reached more than 20% of power conversion efficiencies in solar cells[146–148]. However, this class of compounds suffers from long-term instability in ambient air due to the hygroscopic amine cations and from the toxicity of lead[55]. In this regard, non-toxic Sn-based perovskites are being studied. On one hand, tin(II) halide perovskites are very sensitive to oxygen or moisture, due to the oxidation of Sn^{2+} to Sn^{4+}, which inevitably reduces the photovoltaic performance[56,57,128,149,150]. On the other hand, defect perovskites of the type A_2SnX_6 form the so-called '0D structures' (also known as K_2PtCl_6 structure type), provided that the $[SnX_6]$ octahedra are isolated from each other. Their band gaps are tunable by altering the halogen content and they may readily be solution-processed for the fabrication of solar cells. In particular, Cs_2SnI_6 has been used either as absorber in perovskite solar cells[151], or as hole-transporting material (HTM) in dye-sensitized solar cells (DSSCs) with promising power conversion efficiency (PCE) up to 7.8% [152,153]. First principle density functional theory (DFT) calculations have widely been employed to understand electronic structures and chemical bonding in this class of compounds[154–156].

In our previous work, we investigated the role of the trimethylsulfonium cation in lead perovskites halides and mixed halides $(CH_3)_3SPbX_3$ (X = Cl, Br, I) as a stable organic cation compared to the humidity sensitive methylammonium (MA) and formamidinium (FA) cations. Unfortunately, the electronic band gaps of these compounds are over 3 eV, and therefore the materials are not applicable as solar cell absorbers[42,122]. On the other hand, the tin-based defect $((CH_3)_3S)_2SnCl_6$ perovskite was reported in the literature, but without full crystallographic determination[157]. With regard to the dimensionality of the perovskite and perovskite-related structures[158,159], the trimethyl sulfonium cation allows for a large variety of polyhedra interconnection. In **Figure 5-1**, some characteristic examples are shown: a) orthorhombic 3D-$(CH_3)_3SPbCl_3$[122] with vertex- and face-sharing octahedra,

b) monoclinic 2D-$((CH_3)_3S)_4Pb_3Br_{10}$ [106] with vertex- and face-sharing octahedra, c) hexagonal 1D-$(CH_3)_3SPbX_3$ (X = Br/I) with face-sharing octahedra, and d) cubic 0D-$((CH_3)_3S)_2SnX_6$ (X = Cl, Br, I) with no sharing of the octahedra (from the current study).

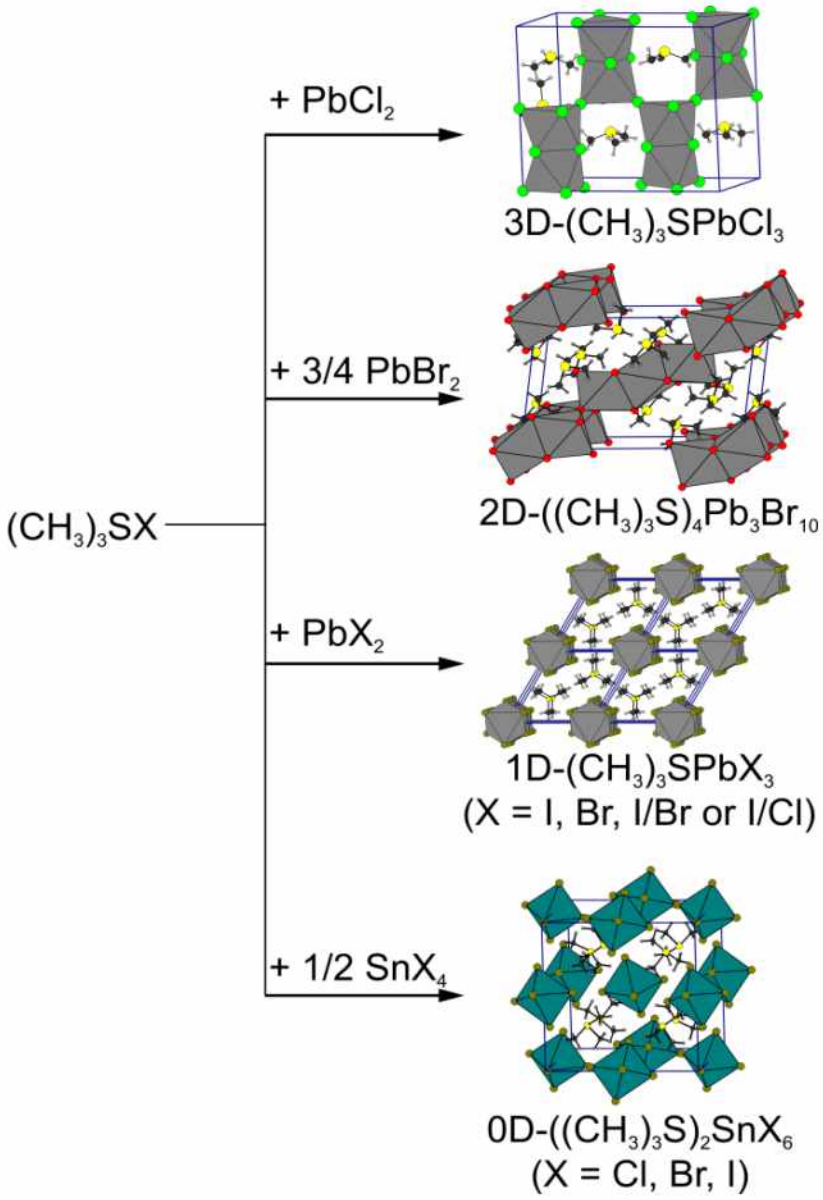

Figure 5-1: Various crystal structures at room temperature of Pb and Sn halides that contain the trimethyl sulfonium cation and exhibit different connectivity of the inorganic octahedra. For simplicity, the disorder of the trimethyl sulfonium cation in $(CH_3)_3SPbCl_3$ and $((CH_3)_3S)_4Pb_3Br_{10}$ is not shown.

In this work, highly stable trimethyl sulfonium tin(IV) halide defect perovskites were synthesized and characterized. Their structural and optoelectronic properties strongly depend on the nature of the halogen atom. The $((CH_3)_3S)_2SnI_6$ hybrid was used for the first time in electrolyte-free, solid-state, dye-sensitized solar cells, reaching high efficiency and stability of the corresponding devices.

5.1 Structural analysis

The reaction products of $((CH_3)_3S)_2SnX_6$ (X = Cl, Br, I) were obtained in high purity and crystallinity. No extra peaks of unreacted precursors or other impurities were observed by XRPD analysis for all samples (**Figure 5-2**). The compounds were indexed in the cubic space group $Pa\bar{3}$, (No. 205), as previously reported for $((CH_3)_3S)_2SnCl_6$. The lattice parameters increase from 12.4493(2) to 12.8525(4) and 13.4586(15) Å for X = Cl, Br, I, respectively.

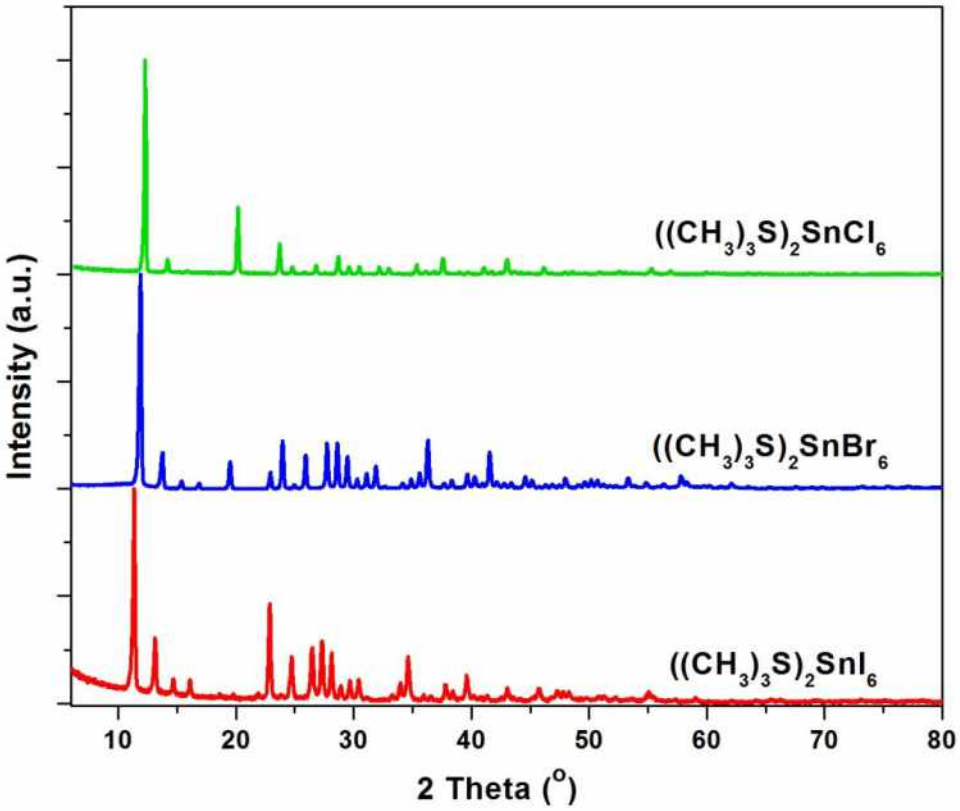

Figure 5-2: XRPD patterns for $((CH_3)_3S)_2SnX_6$ (X = Cl, Br, I).

The crystal structure refinement of $((CH_3)_3S)_2SnX_6$ (X = Cl, Br, I) (**Figure 5-3**) was performed with the Rietveld method using the following Wyckoff sites: Sn atoms on 4*b* (0.5,0.5,0.5), X atoms on 24*d* (x,y,z), S atoms on 8*c* (x,x,x), C atoms on 24*d* (x,y,z) and 3 crystallographically non-equivalent H atoms 24d (x,y,z). The thermal displacement values of all non-hydrogen atoms were refined isotropically. Hydrogen atoms were added using the "Keep" command with default values for C-H bond lengths without further refinement. All structural parameters (expect for hydrogen atomic positions) and residual values are listed in **Table 5-1**. Bond lengths and bond angles are listed in **Table 5-2** and **Table 5-3**, respectively.

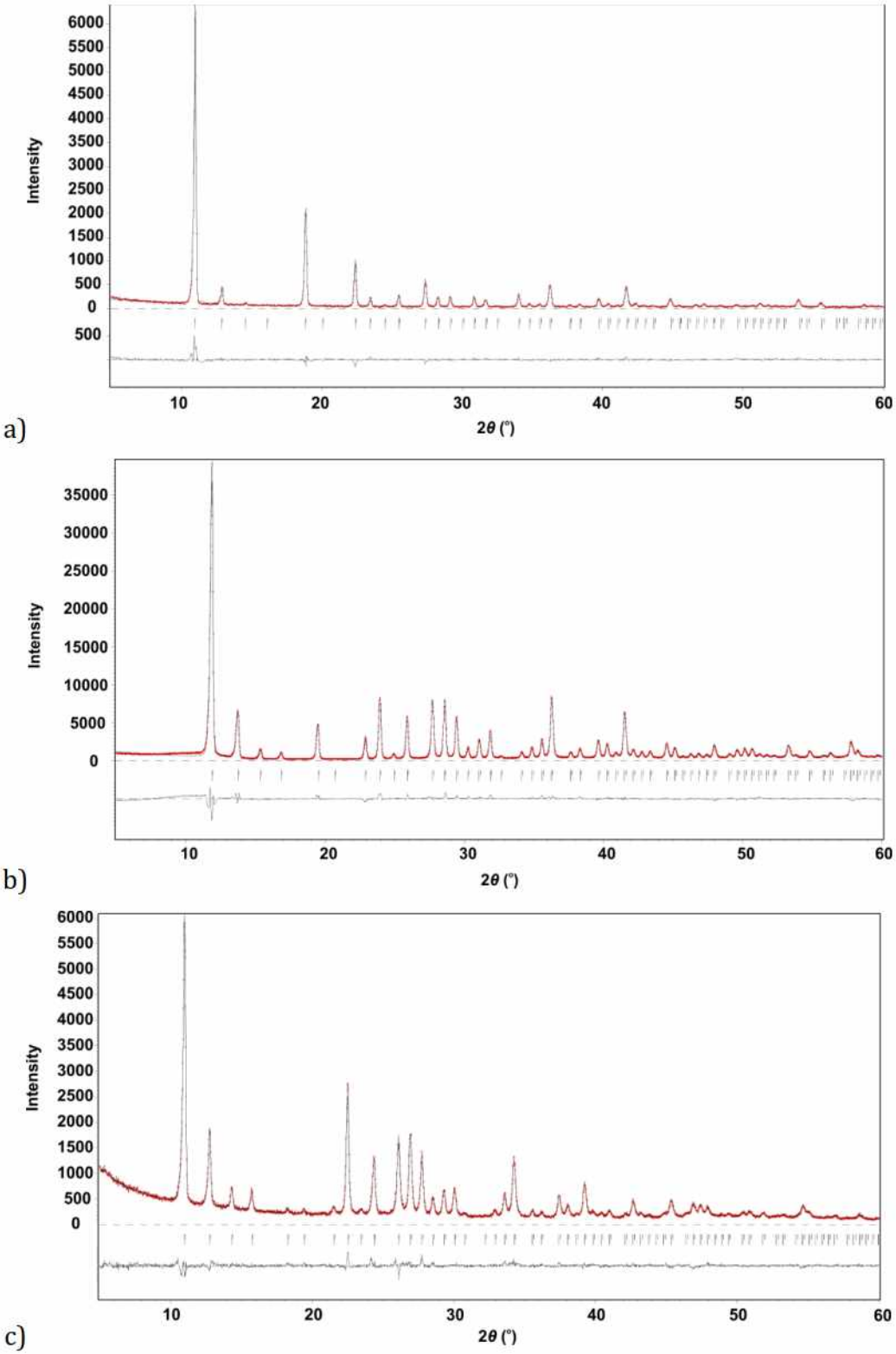

Figure 5-3: Rietveld plots using X-ray powder diffraction data for $((CH_3)_3S)_2SnX_6$: a) X = Cl, b) X = Br and c) X = I.

The $[SnX_6]$ octahedra form a 0D network (**Figure 5-1**) and the $(CH_3)_3S$ units occupy interstitial sites between the octahedra with their 3-fold rotation axis in the [111] direction. The two opposite $(CH_3)_3S$ units are rotated by 60° to each other and they exhibit no disorder. In the case of $((CH_3)_3S)_2SnCl_6$, the thermal displacement values of C

atoms had to be constrained due to the strong correlation with the atomic coordinates. Noteworthy, the analogue cubic compounds of FA_2SnI_6 and MA_2SnI_6 (FA = formamidinium, MA = methylammonium) show very large structural disorder of the organic cations[160].

Table 5-1: Refined crystal structure parameters and atomic positions for $((CH_3)_3S)_2SnX_6$ (X = Cl, Br, I) determined by powder X-ray diffraction. Estimated standard deviations are given in parentheses.

Composition	$((CH_3)_3S)_2SnCl_6$	$((CH_3)_3S)_2SnBr_6$	$((CH_3)_3S)_2SnI_6$
Formula weight (g mol^{-1})	485.8	752.5	1034.5
Space group	$Pa\bar{3}$	$Pa\bar{3}$	$Pa\bar{3}$
Lattice parameter, a (Å)	12.4493(2)	12.8525(4)	13.4586(15)
Calculated density (g cm^{-3})	1.6723	2.3541	2.8185
Volume ($Å^3$)	1929.46(6)	2123.06(11)	2437.81(50)
Z	4	4	4
GOF (F^2)	2.30	3.85	1.58
R_p (%)	9.30	8.21	6.13
R_{wp} (%)	11.90	11.28	8.23
x(Sn) = y(Sn) = z(Sn)	0.5	0.5	0.5
U(Sn) ($Å^2$)	0.0331(9)	0.0366(18)	0.052(9)
x(X)	0.3119(2)	0.30347(17)	0.2919(4)
y(X)	0.0449(3)	0.0420(2)	0.0414(6)
z(X)	0.0345(4)	0.0361(3)	0.0360(6)
U(X) ($Å^2$)	0.0420(15)	0.0421(13)	0.061(4)
x(S) = y(S) = z(S)	0.2309(3)	0.2326(4)	0.2362(18)
U(S) ($Å^2$)	0.051(3)	0.039(4)	0.07(2)
x(C)	0.3068(8)	0.3067(14)	0.305(4)
y(C)	0.1557(8)	0.1639(13)	0.171(6)
z(C)	0.3302(8)	0.3292(13)	0.336(5)
U(C) ($Å^2$)	0.0036	0.021(7)	0.03(3)

Table 5-2: Bond lengths for $((CH_3)_3S)_2SnX_6$ (X = Cl, Br, I) with estimated standard deviations in parentheses.

Compound	**Bond**	**Bond length (Å)**	**Bond**	**Bond length (Å)**

$((CH_3)_3S)_2SnCl_6$	Sn-Cl1	2.4455(48)	Sn-Cl6	2.4455(38)
	Sn-Cl2	2.4455(27)	S-C1	1.8160(106)
	Sn-Cl3	2.4455(38)	S-C2	1.8160(106)
	Sn-Cl4	2.4455(48)	S-C3	1.8160(106)
	Sn-Cl5	2.4455(28)		
$((CH_3)_3S)_2SnBr_6$	Sn-Br1	2.6242(38)	Sn-Br6	2.66243(26)
	Sn-Br2	2.6242(23)	S-C1	1.7969(181)
	Sn-Br3	2.6242(26)	S-C2	1.7969(178)
	Sn-Br4	2.6243(38)	S-C3	1.7969(178)
	Sn-Br5	2.66243(23)		
$((CH_3)_3S)_2SnI_6$	Sn-I1	2.8964(56)	Sn-I6	2.8972(80)
	Sn-I2	2.8964(80)	S-C1	1.8525(690)
	Sn-I3	2.8964(80)	S-C2	1.8525(761)
	Sn-I4	2.8972(56)	S-C3	1.8525(718)
	Sn-I5	2.8972(80)		

Table 5-3: X-Sn-X Bond angles for $((CH_3)_3S)_2SnX_6$ (X = Cl, Br, I), with estimated standard deviations in parentheses.

Compound	Atom 1	Atom 2	Atom 3	Angle 2-1-3 (°)
$((CH_3)_3S)_2SnCl_6$	Sn	Cl	Cl	89.4(1)
		Cl	Cl	90.6(1)
		Cl	Cl	180
$((CH_3)_3S)_2SnBr_6$	Sn	Br	Br	89.51(7)
		Br	Br	90.49(7)
		Br	Br	180.0(1)
$((CH_3)_3S)_2SnI_6$	Sn	I	I	89.5(2)
		I	I	90.4(2)
		I	I	180.0(1)

5.2 Hirshfeld surface analysis

The Hirshfeld surface maps and their associated 2D fingerprint plots are important tools for characterizing the surface and intermolecular interactions of molecules[161]. Hirshfeld surfaces and 2D fingerprint plots of $((CH_3)_3S)_2SnX_6$ (X = Cl, Br, I) were generated based on results of X-ray powder diffraction analysis and refinements. All calculations used a standard high surface resolution with three different kind of surfaces the 3D d_{norm}, shape index and curvedness surfaces over color range red to blue (-0.24 to 1.84, -1 to 1 and -4.0 to 0.4), respectively. The 3D d_{norm} surface has been used for to identify close interactions between $(CH_3)_3S$ and $[SnX_6]$ as well as between adjacent SnX_6 units. The negative values (red regions) of d_{norm} indicate intermolecular contacts shorter than van der Waals (vdW) radii and the positive values (blue regions) refer to intermolecular contacts longer than vdW radii. White regions with a d_{norm} value of zero indicate contact distances equal to the vdW radii. Shape index depicts the type of surface curvature (from -1, concave to +1 convex) and curvedness estimates the magnitude of curvature, from -4.0 (flat), through 0 (spherical) to +0.4 (singular).

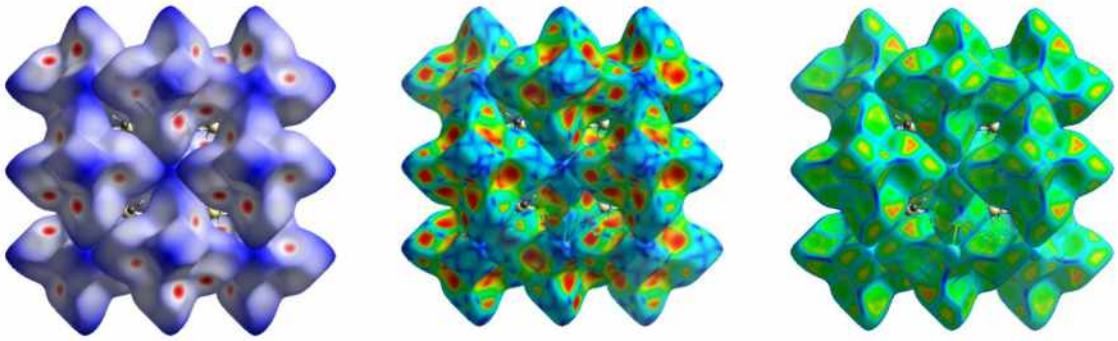

(a) (b) (c)

Figure 5-4: The Hirshfeld surface of the inorganic octahedra in $((CH_3)_3S)_2SnI_6$: a) d_{norm}, b) shape index and c) curvedness surface.

The Hirshfeld surfaces mapped with d_{norm}, shape index, and curvedness of $((CH_3)_3S)_2SnI_6$ (**Figure 5-4**) illustrate a close interaction between $(CH_3)_3S$ and $[SnI_6]$ in between corner iodine atoms (**Figure 5-5**), and non-interacting neighboring $[SnI_6]$ units. The flat green areas of the curvedness surface are attributed to low values of curvedness, whereas sharp blue curvature correspond to high values of curvedness and usually refer to divide the surface into patches, indicating the interactions between neighboring species.

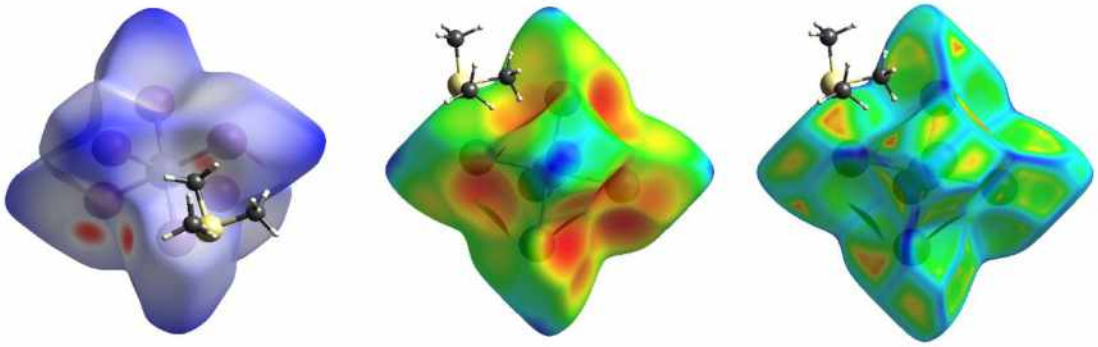

(a) (b) (c)

Figure 5-5: Hirshfeld surface for the $[SnI_6]$ unit in $((CH_3)_3S)_2SnI_6$: a) d_{norm}, b) shape index and c) curvedness.

The 2D fingerprint plots can be deconstructed to highlight particular atom-pair contacts. This deconstruction enables the separation of contributions from different interaction types that overlap in the full fingerprint. The Hirshfeld surface analysis of $((CH_3)_3S)_2SnI_6$ shows I-H, I-S, I-I interactions of 83.8%, 8.4% and 7.9%, respectively. This reveals that the main interactions are between I and H atoms which represent the largest region in the 2D fingerprint plot with d_i and d_e ranging from 1.8 to 3 Å, where d_i and d_e are the distances from a point of the surface to the nearest nucleus inside and outside the surface, correspondingly. Hence, the total distance ($d_i + d_e$) is about 2.72 Å for I-H interactions (**Error! Reference source not found.**a). The I-S and I-I interactions represent a small a rea on the top and middle left side, respectively (b,c).

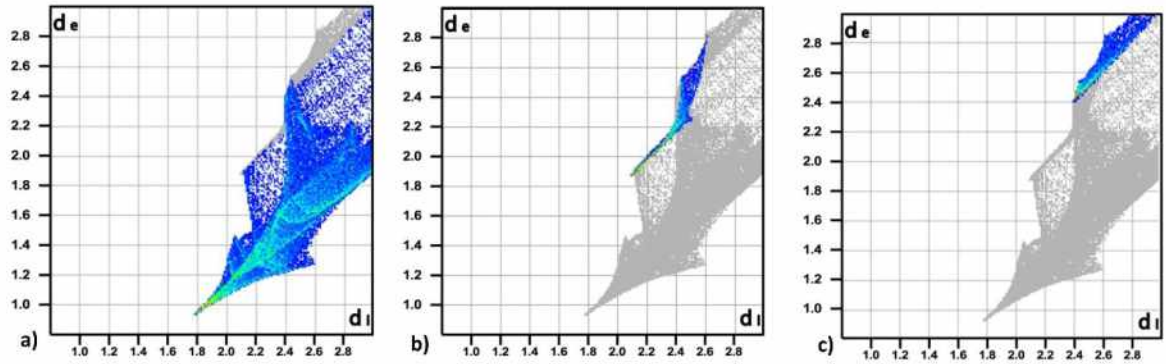

Error! Reference source not found. The Hirshfeld surface analysis (d_{norm}, shape index, and c urvedness) and 2D fingerprint plots for $((CH_3)_3S)_2SnX_6$ (X = Cl, Br) which are shown in **Figure 5-6** and **Figure 5-7**, are quite similar to $((CH_3)_3S)_2SnI_6$, as summarized in **Table 5-4**.

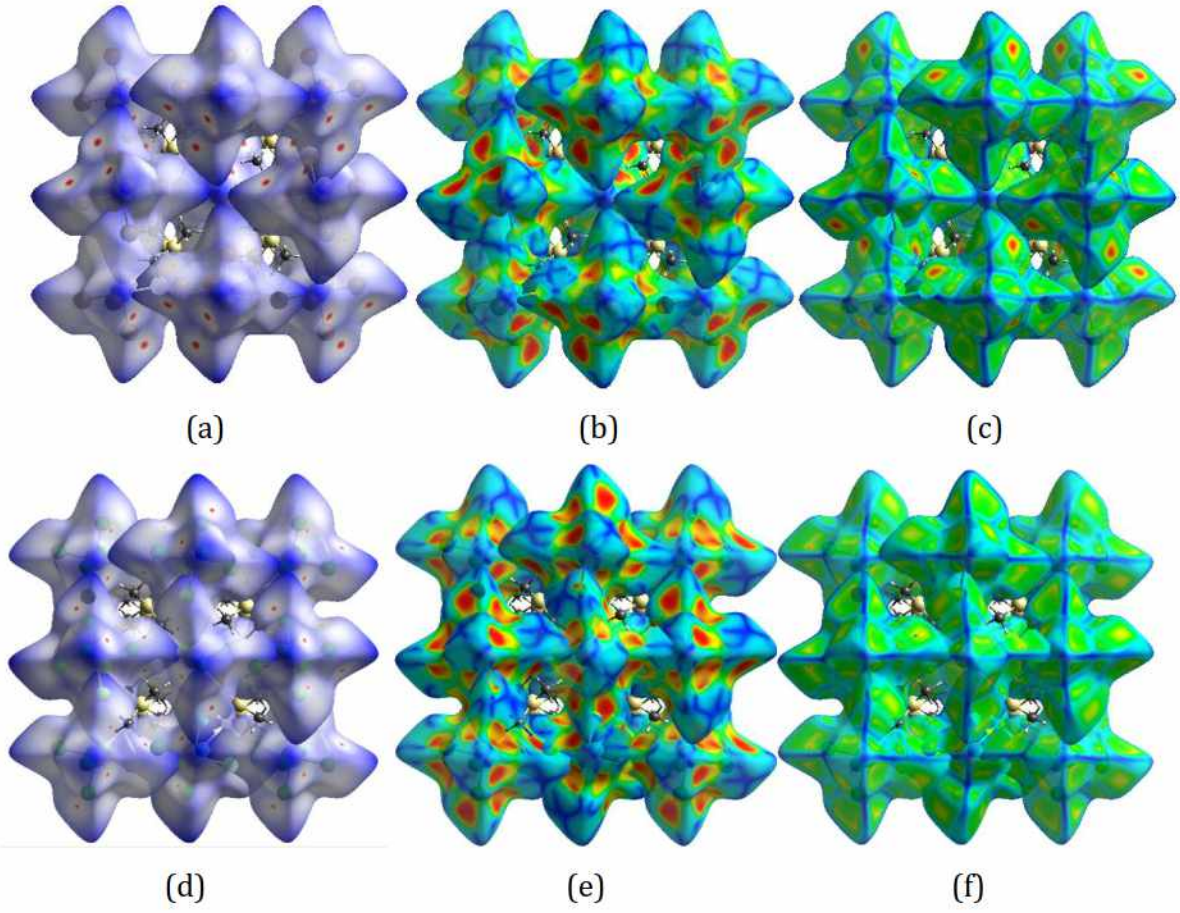

Figure 5-6: Hirshfeld surface analysis: a) dnorm, b) shape index and c) curvedness for $((CH_3)_3S)_2SnBr_6$, d) dnorm, e) shape index and f) curvedness for $((CH_3)_3S)_2SnCl_6$.

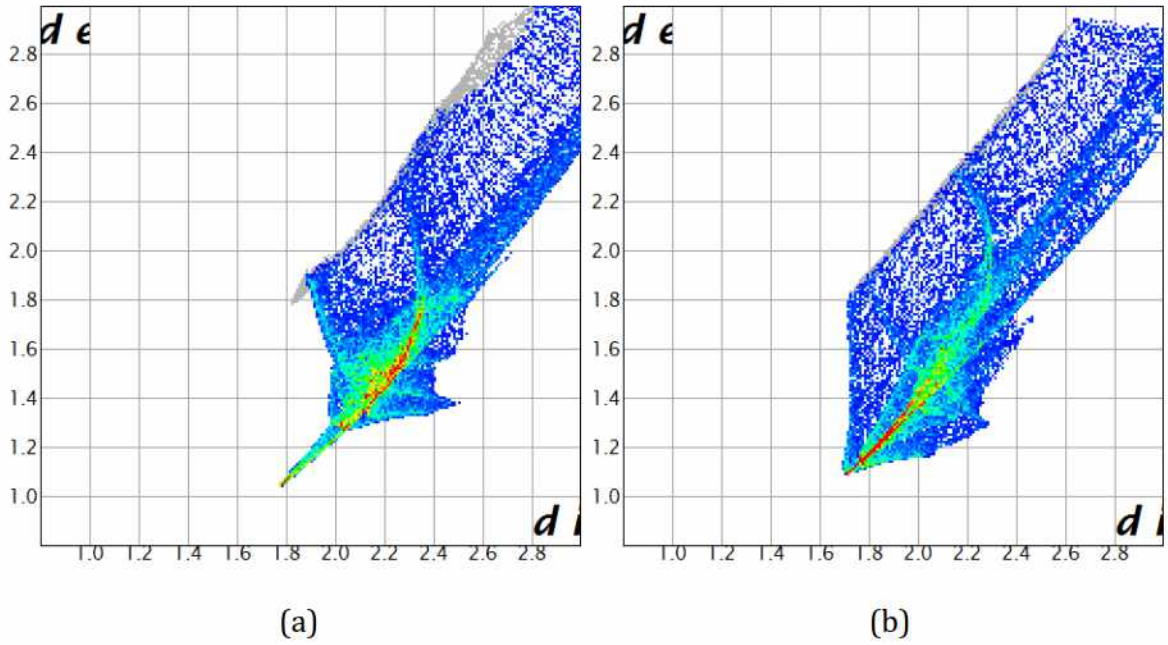

Figure 5-7: 2D fingerprint plots of a) H-Br interactions in $((CH_3)_3S)_2SnBr_6$, b) H-Cl interactions in $((CH_3)_3S)_2SnCl_6$

Table 5-4: Hirshfeld surface analysis for $((CH_3)_3S)_2SnX_6$ (X = Cl, Br, I).

		$((CH_3)_3S)_2SnCl_6$	**$((CH_3)_3S)_2SnBr_6$**	**$((CH_3)_3S)_2SnI_6$**
Surface area included (%)	X-H	91.4	90.4	83.8
	X-S	8.6	8.4	8.4
	X-X	—	1.1	7.9
Color scale	d_{norm}	-0.017 to 1.89	-0.070 to 1.945	-0.245 to 1.84
	shape index	-0.999 to 0.999	-0.997 to 0.997	-0.998 to 0.999
	curvedness	-3.123 to 0.270	-2.911 to 0.062	-3.339 to 0.411
Volume of the anion (Å³)		214.06	268.64	355.24
Area of the anion (Å²)		221.33	255.78	328.93
H-X distance (Å)		2.81	2.83	2.72

Regarding H-X interactions (**Figure 5-8**a), the wireframe of $((CH_3)_3S)_2SnI_6$ shows that every $[SnI_6]$ octahedron has 12 H-I bonds with 8 $(CH_3)_3S$ units, considering that every iodine atom is bonded to two hydrogen atoms of $(CH_3)_3S$ on opposite sides at H-I distances of 2.85 Å and H-I-H angle of 165.14°.

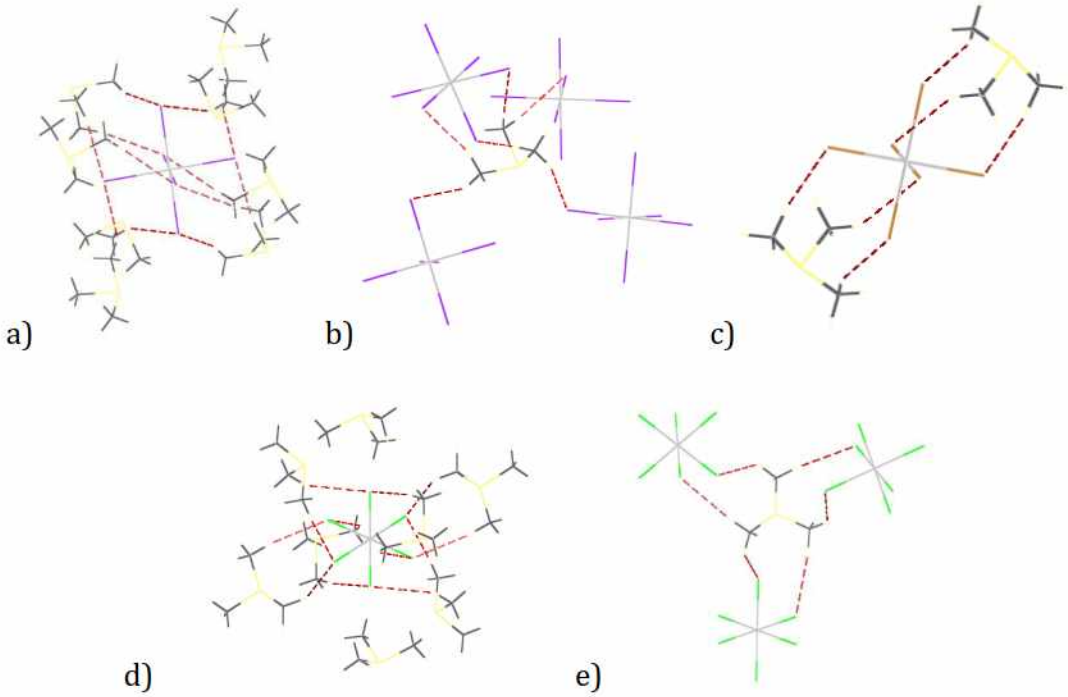

Figure 5-8: Wireframes of $((CH_3)_3S)_2SnX_6$: a) $[SnI_6]$ unit surrounded by $(CH_3)_3S$ units, b) $(CH_3)_3S$ unit surrounded by $[SnI_6]$ units, c) $[SnBr_6]$ unit surrounded by $(CH_3)_3S$ units, d) $[SnCl_6]$ unit surrounded by $(CH_3)_3S$, b) $(CH_3)_3S$ unit surrounded by $[SnCl_6]$ units. Dotted, red lines denote hydrogen bonds.

Figure 5-8b shows that each organic moiety $(CH_3)_3S$ is connected to four adjacent $[SnI_6]$ units. In the case of $((CH_3)_3S)_2SnBr_6$, each $[SnBr_6]$ unit is connected to only two $(CH_3)_3S$ units through three H-Br bonds (one from each methyl group) at a distance of 2.83 Å. Regarding the $(CH_3)_3S$ units, each one is bonded to only one $[SnBr_6]$ unit without any other interaction (**Figure 5-8**c). **Figure 5-8**d,e shows the wireframe design of $((CH_3)_3S)_2SnCl_6$ where every $[SnCl_6]$ unit is connected to six $(CH_3)_3S$ units. Each $[SnCl_6]$ octahedron has twelve H-Cl bonds, where every Cl atom is bonded to two hydrogen atoms in $(CH_3)_3S$ units facing opposite to each other. The corresponding H-Cl bond lengths are at 2.81 Å and the H-Cl-H angle is at 133.05°. Each organic moiety is connected to three adjacent $[SnCl_6]$ units through H-Cl bonds. It is important to notice that similar extensive hydrogen bonding has been reported for platinum $((CH_3)_3S)_2PtI_6.CH_3CN$ and $((CH_3CH_2)_3S)_2PtI_6$ analogues[162], where the latter material crystallizes in the same group as the title compounds.

5.3 Vibrational and electronic properties

The micro-Raman spectra of $((CH_3)_3S)_2SnX_6$ (X = Cl, Br, I) perovskite materials show two different kinds of Raman active modes, **Figure 5-9**.

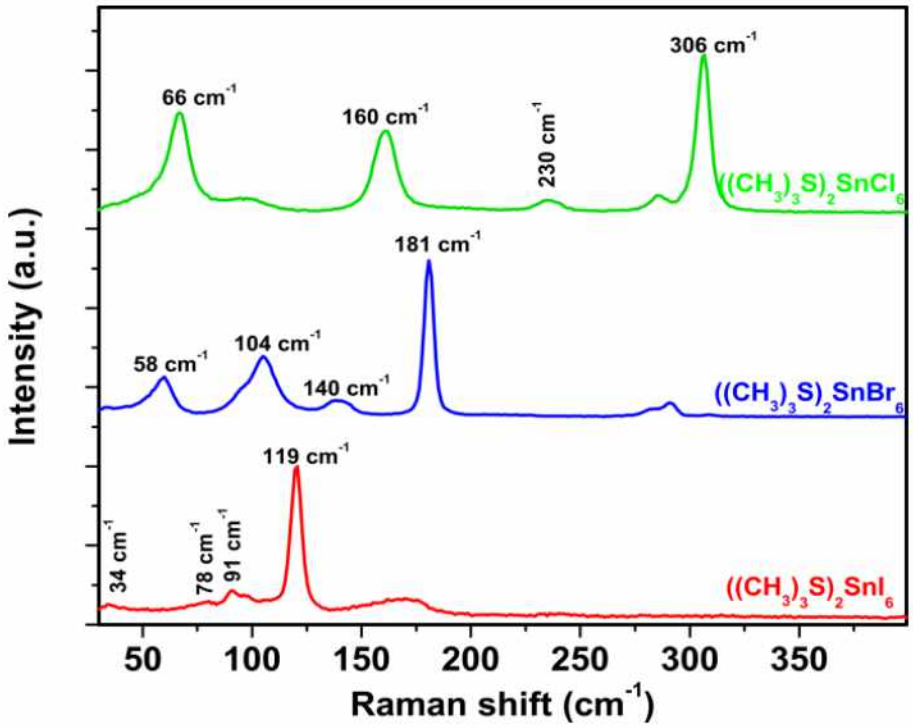

Figure 5-9: Raman spectra of $((CH_3)_3S)_2SnX_6$ (X = Cl, Br, I).

Firstly, vibrational modes of the inorganic SnX_6 octahedra appear at low frequencies (30 – 400 cm^{-1}), namely the no degenerate $\nu(A_{1g})$ due to the Sn-X symmetric stretching,

doubly degenerate $\nu(E_g)$ due to the Sn-X asymmetric stretching vibration, and triply degenerate $\delta(F_{2g})$ as the X-Sn-X asymmetric bending deformation. The lowest frequency detected Raman band is due to the triply degenerate $\nu^L(F_{2g})$ lattice mode, which involves vibrations of the organic moiety $(CH_3)_3S^+$ in the rigid $[SnX_6]$ lattice[153,163,164]. Frequencies of these vibrational modes are recorded in **Table 5-5** and are very similar to those observed in Cs_2SnX_6 (X = Cl, Br, I)[153]. In particular, the frequency shift of the Sn-X symmetric stretching mode upon halide substitution follows the change of the reduced atomic mass of the Sn-X harmonic oscillator. Secondly, the rest of Raman active modes which appear at frequencies above 400 cm^{-1} are related to internal vibrations of the organic moiety $(CH_3)_3S^+$. A list of them with their attribution according to[138] is included in **Table 5-5**.

Table 5-5: Frequencies (in cm^{-1}) of Raman active modes for $((CH_3)_3S)_2SnX_6$ (X = Cl, Br, I).

Mode	Type	$((CH_3)_3S)_2SnCl_6$	$((CH_3)_3S)_2SnBr_6$	$((CH_3)_3S)_2SnI_6$
$\nu^L(F_{2g})$	Lattice	66	58	34
$\delta(F_{2g})$	X-Sn-X asymmetric bending	160	104	78
$\nu(E_g)$	Sn-X asymmetric stretch	230	140	91
$\nu(A_{1g})$	Sn-X symmetric stretch	306	181	119
	SC_3 symmetric	657.4	655.1	650.7
	SC_3 asymmetric	733.8	732.1	727.1
	CH_3 rocking	1051.6	1048.2	1043.6
	CH_3 asymmetric deformation	1430.8	1424.9	1419.9
	CH_3 symmetric	2926.2	2920.0	2913.7
	CH_3 asymmetric	3011.7	3006.8	3003.1

The nature of the halide strongly affects these modes by shifting them to higher frequencies towards the light halide derivatives. This indicates strengthening of the interaction between hydrogens in the organic cation and the halides in the inorganic cage. A similar trend is found for all of methylammonium Raman modes in the $MAPbX_3$ series[107], which is attributed to the smaller cavity formed inside the inorganic cage of the lighter halides that reduces the hydrogen-halide distance.

The electronic properties of $((CH_3)_3S)_2SnX_6$ (X = Cl, Br, I) were investigated using UV-Vis spectroscopy at room temperature. The diffuse absorption spectra calculated by transforming the diffuse reflectance spectra to Kubelka-Munk units are presented in **Figure 5-10**. By extrapolating the absorption curves to the energy axis, E_g values are estimated at 4.1, 2.9 and 1.4 eV for X = Cl, Br and I, respectively.

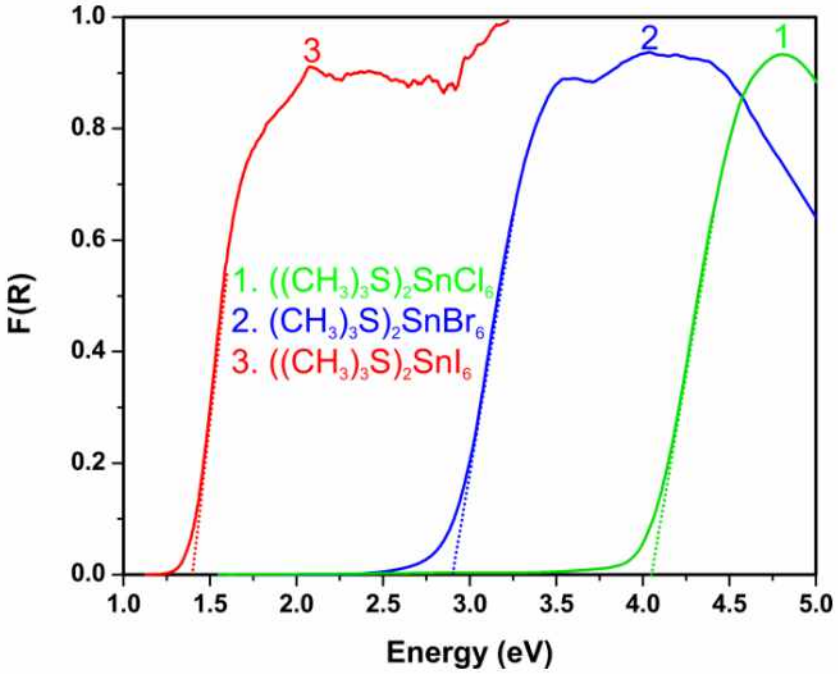

Figure 5-10: Diffuse reflectance UV-Vis spectra in Kubelka-Munk units for $((CH_3)_3S)_2SnX_6$ (X = Cl, Br, I).

Moreover, the band gap values of $((CH_3)_3S)_2SnX_6$ (X = Cl, Br, I) are slightly larger than the analogous Cs_2SnX_6 compounds with 3.9, 2.7 and 1.26 eV for X = Cl, Br and I, respectively.[153] Similarly, to conventional A_2BX_6 perovskite materials, substitution of halogen atoms at the X-site will subsequently affect optical absorption properties, which are attributed to the smaller and more electronegative nature of the chloride and bromide anions; in both cases this would increase the magnitude of the band gap[164,165]. Further, the analogue compounds of MA_2SnI_6 and FA_2SnI_6 show a monotonic increase in optical band gap 1.35 eV and 1.37 eV, respectively[164]. Despite the absence of connectivity between the octahedra, all A_2SnI_6 (A = Cs, CH_3NH_2, H_2NCHNH_2, $(CH_3)_3S$) compounds exhibit a direct optical band gap around 1.3 eV. This behavior is attributed to the close-packed iodine sub-lattice, which gives a rather non flat dispersive conduction band. Similarly to conventional perovskite materials, the valence and conduction band edges are derived from the inorganic framework. Photoluminescence spectroscopy did not reveal any luminescence from these compounds regardless the excitation energy.

5.4 Scanning electron microscopy

The morphology of the $((CH_3)_3S)_2SnX_6$ (X = Cl, Br, I) bulk samples was analyzed using Scanning Electron Microscopy (SEM) and their chemical composition was estimated by Energy-dispersive X-ray spectroscopy (EDXS). SEM micrographs of (X = Cl, Br) derivatives exhibit angular grain shapes, whereas the (X = I) crystallites form sub-angular shapes as shown in **Figure 5-11**.

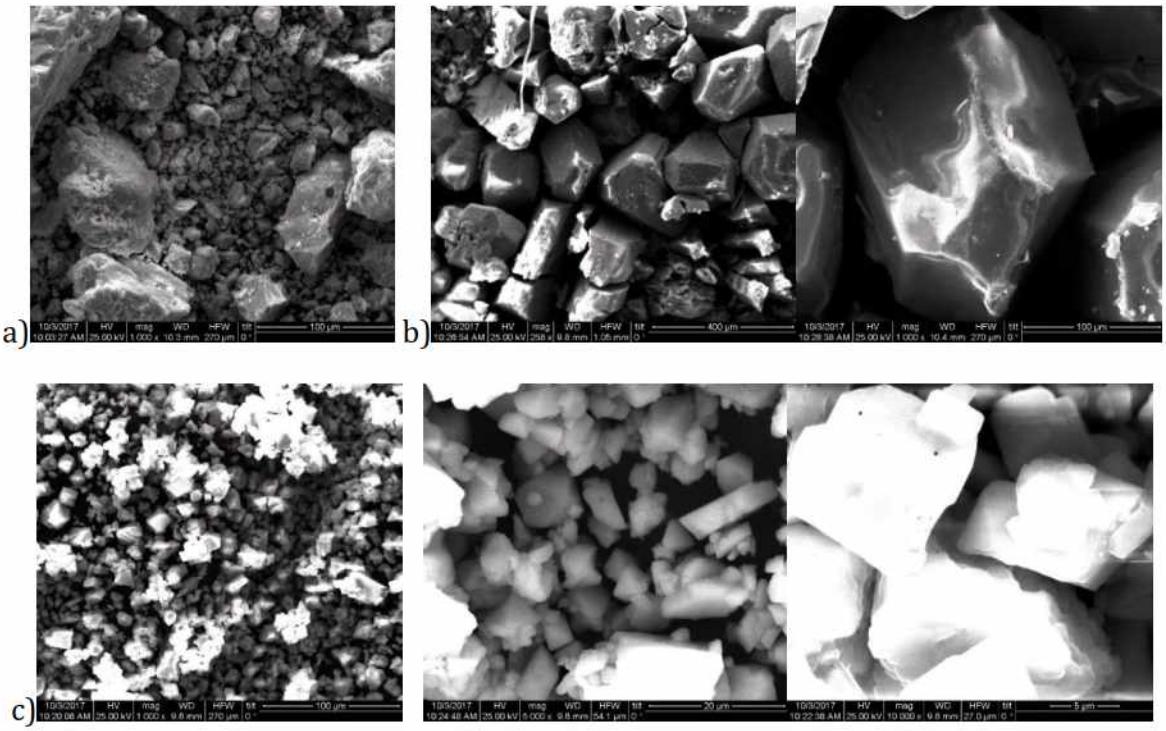

Figure 5-11: SEM images for $((CH_3)_3S)_2SnX_6$: a) X = I, b) X = Cl and c) X = Br

Noteworthy, the iodide-based material is very sensitive to the electron beam thus SEM images can only be gained with up to x1000 magnification.

Table 5-6: Atomic weight percentages from EDX analysis for $((CH_3)_3S)_2SnX_6$ (X = Cl, Br, I) in comparison with the theoretical values.

	$((CH_3)_3S)_2SnCl_6$		**$((CH_3)_3S)_2SnBr_6$**		**$((CH_3)_3S)_2SnCl_6$**	
	Experimental (Avg.)	Theoretical	Experimental (Avg.)	Theoretical	Experimental (Avg.)	Theoretical
S	13.01	13.2	6.7	8.52	5.31	6.2
Sn	21.91	24.44	10.995	15.78	12.64	11.48
X	39.9	43.79	63.46	63.71	72.06	73.61

EDXS spectra were obtained from three morphologically different spots for each of the $((CH_3)_3S)_2SnX_6$ (X = Cl, Br, I) perovskites (**Figure 5-12**) According to EDXS results (**Table 5-6**), there is lateral uniformity across the samples, whereas the measured elemental content matches well the nominal chemical composition of the samples.

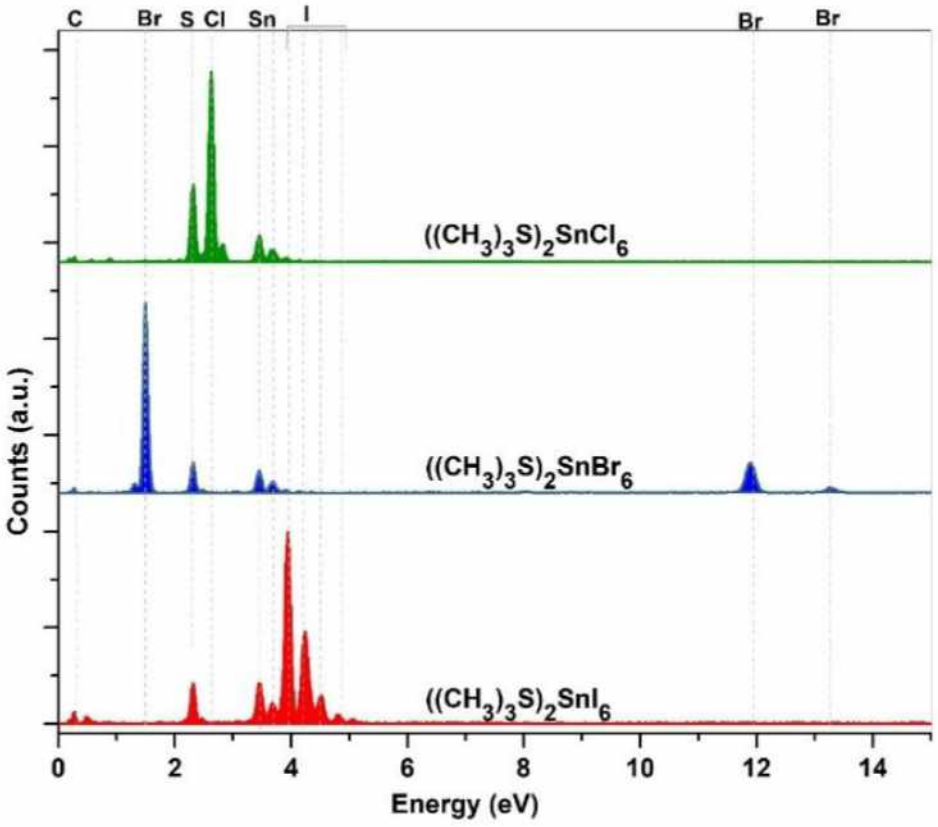

Figure 5-12: Energy Dispersive X-ray spectra for $((CH_3)_3S)_2SnX_6$ (X = Cl, Br, I).

5.5 Thermal stability

The bulk materials of $((CH_3)_3S)_2SnX_6$ (X= Cl, Br, I) are stable in air even after stay for several months. XRPD analysis of the chloride and bromide samples after exposure to 80 °C for 24 hours in ambient air showed no signs of degradation. Nevertheless, the XRPD analysis of $((CH_3)_3S)_2SnI_6$ after exposure to 80 °C for one day in ambient air showed a very small extra peak at 2θ = 13.2°, but the sample fully decomposed into SnI_4 after 5 days at the same temperature as shown in **Figure 5-13**. No sign of $(CH_3)_3SI$ or other crystalline impurities is observed in the powder diffraction pattern. The relative thermal instability of iodide compared to the chloride and the bromide are attributed to some extent to weakening of H-X bonds, with increasing halogen size[166]. It is noteworthy that other trimethylsulfonium-containing compounds can withstand much higher temperatures without decomposition, for example $[(CH_3)_3S]$TFSI (TFS = bis(trifluorosulfonimide)) is stable up to 280 °C[167].

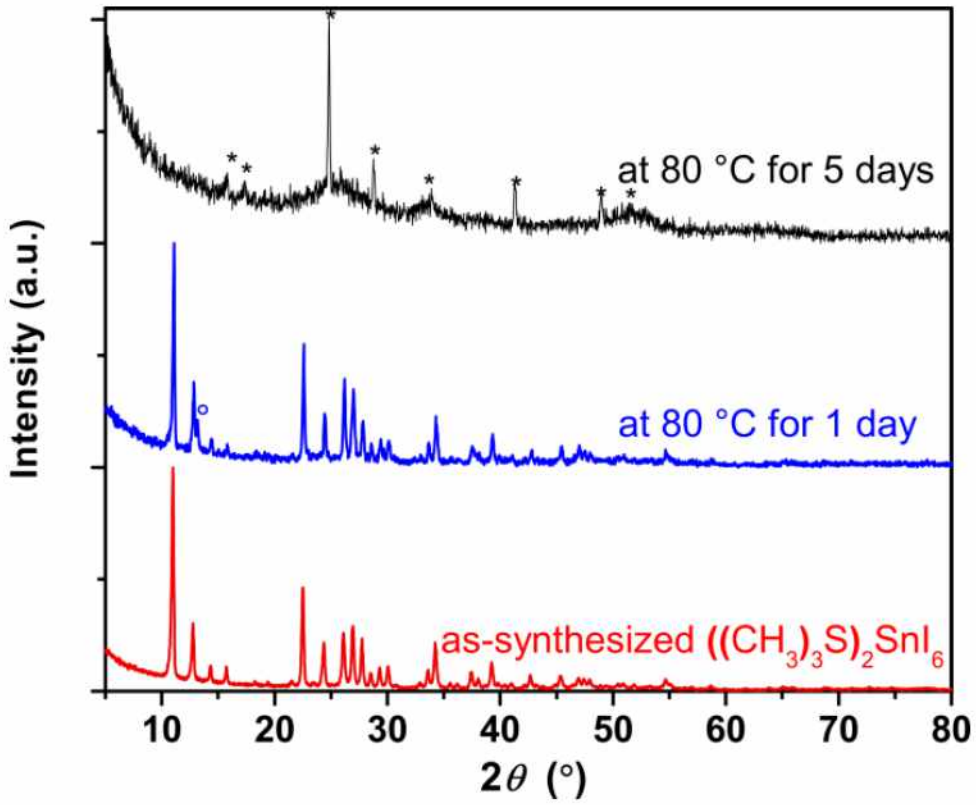

Figure 5-13: XRPD patterns of $((CH_3)_3S)_2SnI_6$ before and after exposure to 80 °C in ambient air for 1 and 5 days. The blue circle and the black stars denote an unindexed peak and SnI_4 peaks, respectively.

5.6 First principles DFT calculations

Ab initio DFT calculations of $((CH_3)_3S)_2SnX_6$ (X = Cl, Br, I) were carried out on the optimized structures using the initial crystallographic data to predict the band structure, total density of states (TDOS) and partial density of states (PDOS). Two functional revised for solids were employed in this study: the Perdew, Burke and Ernzerhof (PBE)[168] and PBEsol[169], with a plane wave cut-off of 340 eV. The electronic band structures (**Figure 5-14**) of cubic $((CH_3)_3S)_2SnX_6$ (X = Cl, Br, I) using different functions have been evaluated. In all cases, the computed band gaps (**Table 5-7**) were lower than the experimental values, because the band edges are not located at the special k-points[170]. Also, the obtained values point to direct band gaps with the minimum from the G symmetry point (at the center of the unit cell in real space). The PDOS peaks of *p* orbital are closer and sharper than those of the *s* orbital to Fermi energy level and appear to have high contribution at the top of the valence band (**Figure 5-15**). The strong hybridization of the orbitals can shift the location of the valence bands to the lower energy area with wider peaks[171].

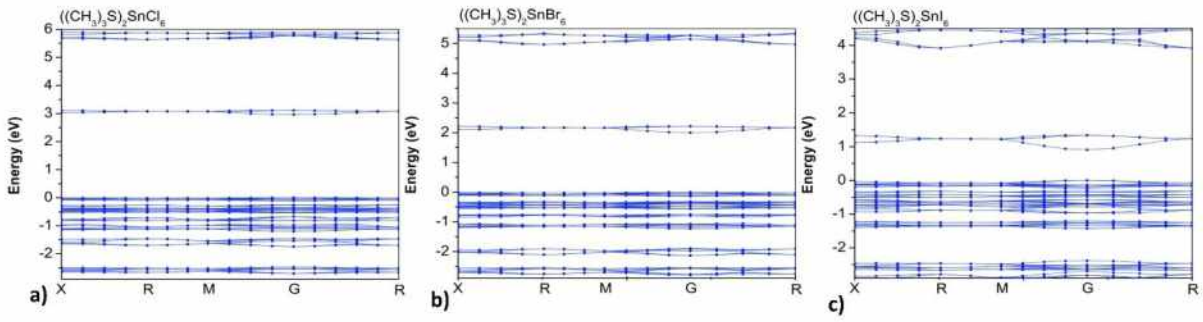

Figure 5-14: Band structures for $((CH_3)_3S)_2SnX_6$ (X = Cl, Br, I).

Table 5-7: Experimental and theoretical values of band gaps for $((CH_3)_3S)_2SnX_6$ (X = Cl, Br, I).

Compound	Experimental E_g (eV)	Computational E_g (eV)	
		GGE/BPE	GGE/BPESOL
$((CH_3)_3S)_2SnCl_6$	4.1	2.96	2.98
$((CH_3)_3S)_2SnBr_6$	2.9	2.00	2.03
$((CH_3)_3S)_2SnI_6$	1.4	0.91	0.89

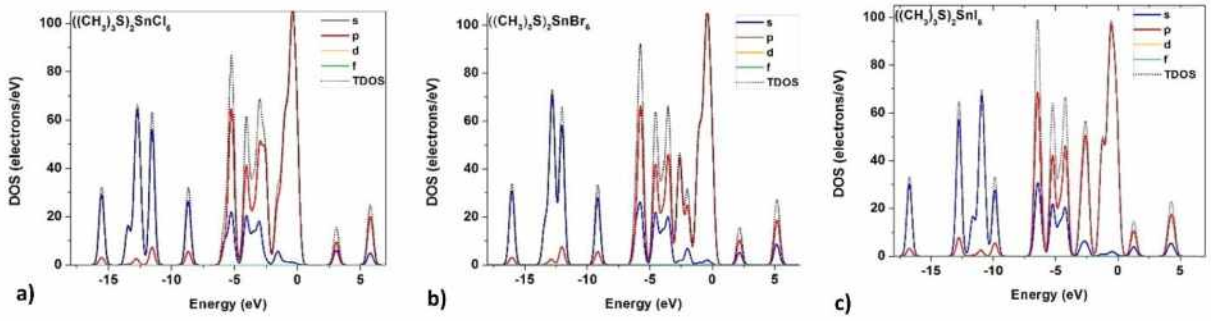

Figure 5-15: Total DOS for $((CH_3)_3S)_2SnX_6$ (X = Cl, Br, I).

PDOS show the contribution of each atom in hybridization of orbitals. As an example, the PDOS of $((CH_3)_3S)_2SnI_6$ (**Figure 5-16**) indicates that the main contribution of the top the valence band is from 5p states (97.7%) and 5s states (1.1%) of iodine and about 0.15% from 5s states of Sn and a small percentage of organic moiety atoms. At the bottom of the conduction band, the main contribution is from anti-bonding (72.96% 5p states and 5.87% 5s states) of the I atom and 21.17%, 5S states of Sn. The present results explain a strong covalent nature of the Sn–I bond in the $[SnI_6]$ framework, leading to the formation of I 5p – Sn 5s conduction band and transferring electrons to the Sn ion, which improves the stability of the $((CH_3)_3S)_2SnI_6$ phase.

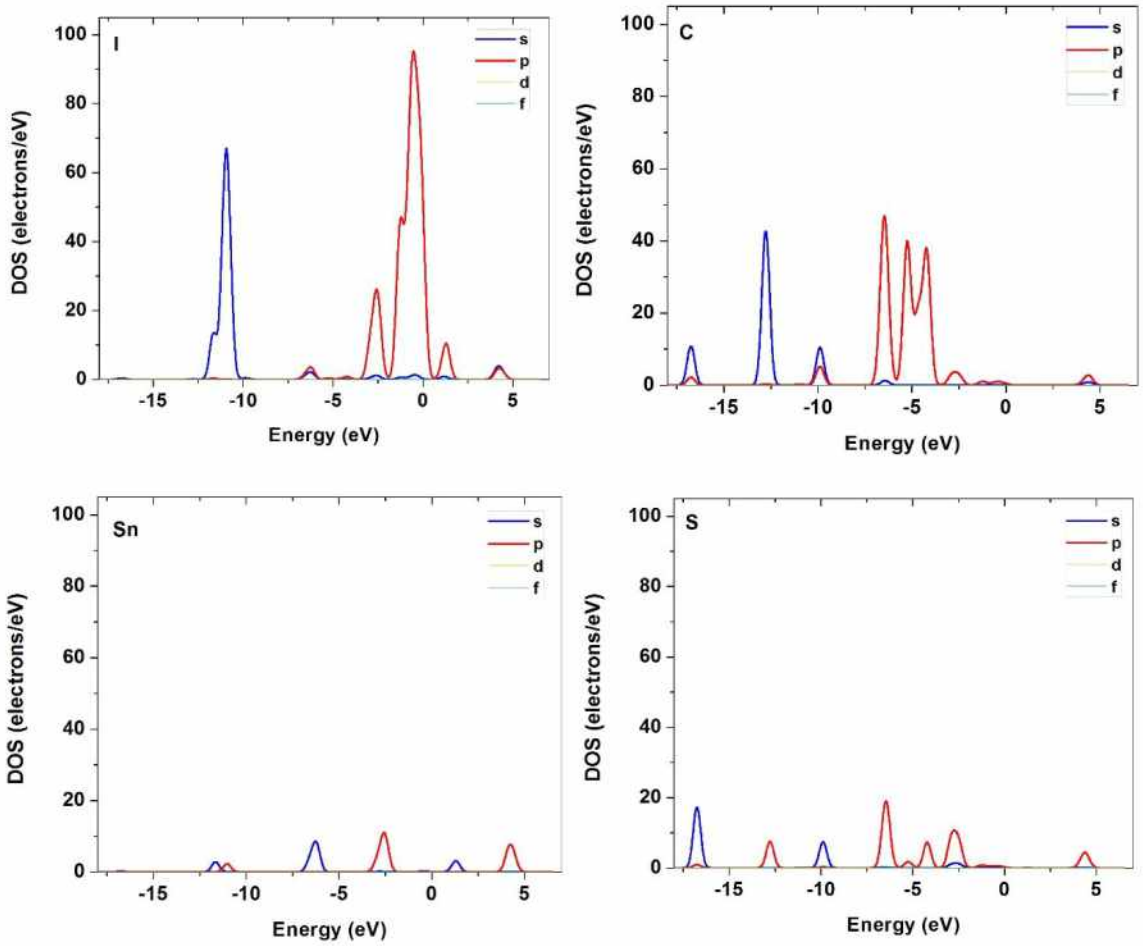

Figure 5-16: Partial DOS for $((CH_3)_3S)_2SnI_6$.

5.7 Solar cells fabrication

Fluorine-doped tin oxide (FTO) transparent conductive glass plates (7 ohms/Ω, Sigma-Aldrich) were ultrasonically cleaned with Detergent (Hellmanex 2% in water), deionized water and ethanol successively. After cleaning, the glasses were dried out at room temperature. For the preparation of approximately 6-7 µm thickness of TiO_2 layer, 18-NRAO (Dyesol) paste was deposited by doctor blade technique on the FTO glasses which were then annealed at 500 °C. Subsequently, a 6 µm thickness TiO_2 layer of average nanoparticle size 400 nm (WER4, Dyesol) was also deposited by doctor-blading. The films were gradually annealed at 125 °C for 5 min, 325 °C for 15 min and 525 °C for 30 min.

The modified electrodes were post-treated with $TiCl_4$ aqueous solution 20 mmol/L at 70 °C for 10 min and after cleaning with deionized water and ethanol were annealed at 500 °C for 30 min. The as-prepared TiO_2 films were immersed into a solution of 3.0 10^{-4} mol/L in Z907 dye (Dyesol) (cis-bis(isothiocyanato) (2,2'-bipyridyl-4,4-dicarboxylato)(2'-bipyridyl-4,4'-dinonyl)-ruthenium(II)) and 3.0×10^{-4} mol/L chenodeoxycholic acid

solution in a 1:1 v/v mixture of acetonitrile/tert-butanol for approximately 8 hours.

For the use of the perovskites in solar cells, 103.4 mg of $((CH_3)_3S)_2SnI_6$, 24.2 mg of $((CH_3)_3S)_2SnCl_6$ and 37.6 mg of $((CH_3)_3S)_2SnBr_6$ were dissolved in 0.4 mL DMF under stirring at 40 °C for 10 minutes (for $((CH_3)_3S)_2SnI_6$) or at 60 °C for 20 minutes ((for $((CH_3)_3S)_2SnCl_6$ and $((CH_3)_3S)_2SnBr_6$). Efforts were made to increase the efficiency of the $((CH_3)_3S)_2SnI_6$-based cells by adding dopants in the perovskite solution. tert-Butyl pyridine (TBP) was added to this solution as dopant with a volume-to-mass ratio of 1:26 μL/mg TBP: $((CH_3)_3S)_2SnI_6$. Another stock solution was prepared by dissolving 520 mg bis(trifluoromethane)sulfonimide lithium (Li-TFSI) in 1 mL acetonitrile, and then 15 μL of this solution were also introduced as additive. A drop of the perovskite solution was placed on top of a platinized (100 nm thick prepared by sputtering) FTO glass (cathode electrode) and left to dry at 40 °C. The same procedure was followed for the Z907/TiO_2 films (photoelectrode). The cathode electrode was placed on top of the photoelectrode after an extra drop of the perovskite solution was casted on it. Illumination of the samples was made with Xenon 300 W source solar simulator in combination with AM 1.5G optical filters (Oriel). Current density-voltage (*J-V*) characteristics were drawn with an Autolab PGSTAT-302N potentiostat using linear sweep voltammetry in a 2-electrode system at a scan rate of 50 mV sec^{-1}. The active area of the device was set to 0.152 cm^2 by using a mask in front of the cell.

The newly synthesized tin(IV) defect perovskites were incorporated in electrolyte-free solar cells of the type **FTO/TiO_2-Z907//$((CH_3)_3S)_2SnX_6$//Pt/FTO**, using the nanoparticulate titania films sensitized with the Z907 dye and their photovoltaic properties were evaluated. **Figure 5-17** presents the J-V plots recorded under 1 sun illumination, for the $((CH_3)_3S)_2SnI_6$ –based solar cells, with and without additives (tert-Butyl pyridine and bis(trifluoromethane)sulfonimide lithium), as dopants. The calculation of the solar cells' efficiency was achieved by integrating the obtained J-V curves using equation (Eq. 5.1):

$$\eta\% = \frac{(\mathrm{JV})\mathrm{max}}{\mathrm{P}} \times 100 \qquad (Eq.\,5.1)$$

where (J V)max is the maximum value of the J V product, as extracted from the J-V plot, and P is the power density of the incident light. For the FF calculation we used the equation (Eq. 5.2):

$$FF = \frac{(\mathrm{JV})\mathrm{max}}{\mathrm{J_{sc}V_{oc}}} \qquad (Eq.\,5.2)$$

By recording J-V plots for the solar cells containing the $((CH_3)_3S)_2SnI_6$ perovskite with

and without additives in the solution we have seen significant increasing of the cells' efficiency by 92%. More specifically, the V_{oc} as well as the J_{sc} increases significantly with the use of dopants in the $((CH_3)_3S)_2SnI_6$ perovskite solution (**Table 5-8**).

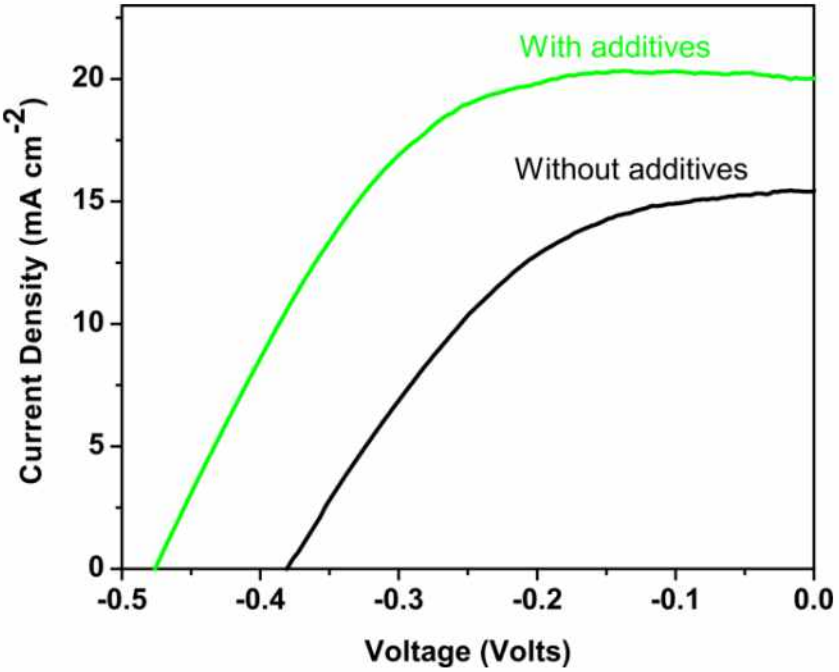

Figure 5-17: Current Density – Voltage plots for the DSSCs containing $((CH_3)_3S)_2SnI_6$ with and without additives under 1 sun illumination.

The J_{sc} for the cell without the use of additives was recorded at 15.48 mA cm^{-2} and the V_{oc} at 0.38 V. The efficiency was calculated at 2.64% and the FF at 0.45. The short-circuit photocurrent value for the cell containing the $((CH_3)_3S)_2SnI_6$ perovskite with additives in the solution was 20.05 mA cm^{-2}, while the V_{oc} was 0.48 V and the cell efficiency was calculated at 5.07%. J-V plots were also obtained for cells using $((CH_3)_3S)_2SnCl_6$, and $((CH_3)_3S)_2SnBr_6$ with additives.

Table 5-8: J-V Characteristics (1 sun-illumination) for $((CH_3)_3S)_2SnI_6$ containing DSSCs with or without additives in the electrolyte and for $((CH_3)_3S)_2SnCl_6$, $((CH_3)_3S)_2SnBr_6$ with additives.

HTM in solar cell	J_{sc} (mA cm^{-2})	V_{oc} (V)	FF	η (%)
$((CH_3)_3S)_2SnI_6$ without additives	15.48	0.38	0.45	2.64
$((CH_3)_3S)_2SnI_6$ with additives	20.05	0.48	0.53	5.07
$((CH_3)_3S)_2SnBr_6$ with additives	0.75	0.77	0.52	0.30
$((CH_3)_3S)_2SnCl_6$ with additives	0.39	0.48	0.21	0.04

The results shown in **Table 5-8** are not as encouraging as the cells using $((CH_3)_3S)_2SnI_6$. The very low efficiencies of 0.04% for $((CH_3)_3S)_2SnCl_6$ and 0.30% for $((CH_3)_3S)_2SnBr_6$ are attributed to the non-uniform deposition on the photoanode electrode and their lower concentration in DMF because of their low solubility.

For the better understanding of the electrical parameters of the solar cells containing the $((CH_3)_3S)_2SnI_6$ perovskite (with additives), electrochemical impedance spectroscopy was applied. The analysis was performed under 1 sun illumination and **Figure 5-18** shows the characteristic Nyquist plot.

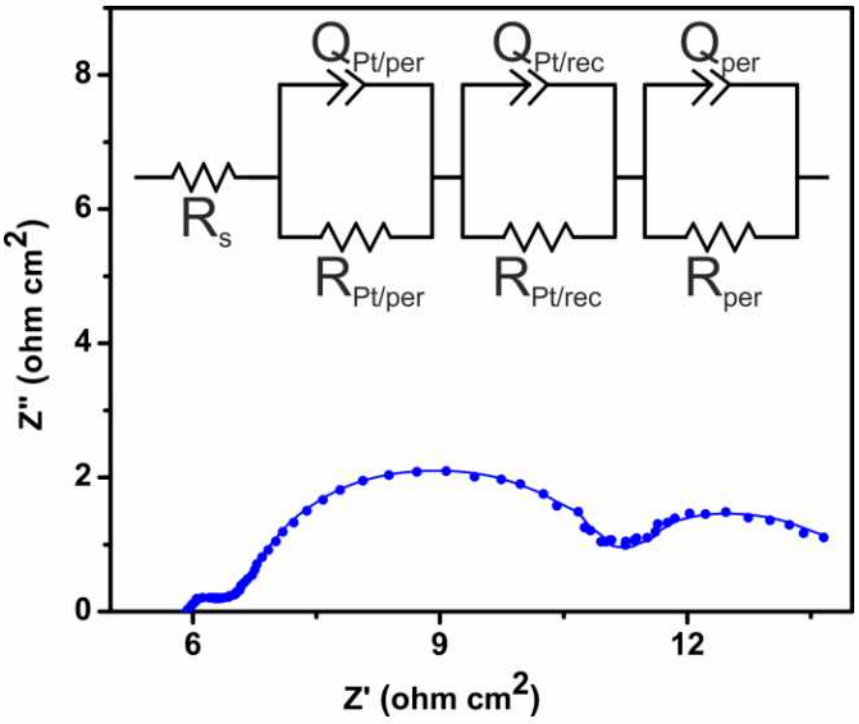

Figure 5-18: Nyquist plot for $((CH_3)_3S)_2SnI_6$-containing solar cell under 1 sun illumination. The inset shows the equivalent electrical circuit model used for the simulation of the EIS data.

In the Nyquist plot, 3 separate semicircles appear and only one single semicircle is shown at the high frequency range depicting the compact character of the Pt sputtered counter electrode. It consists of (i) R_S, the ohmic series resistance that is determined from the resistance of the contacts and the perovskite and the substrate, (ii) The $R_{Pt/perovskite}$ charge transfer resistance and the constant phase element $Q_{Pt/perovskite}$ at the interface of the Pt and perovskite, (iii) the R_{rec}, recombination resistance and Q_{rec} which corresponds at the interface of photoanode with the perovskite and (iv) the R_{per} transport resistance and Q_{per} of the perovskite. The corresponding values are shown in **Table 5-9**.

Table 5-9: Calculated values for the equivalent circuit parameters R_S, $R_{Pt/per}$, R_{rec} and R_{per} of a $((CH_3)_3S)_2SnI_6$-containing solar cell.

	R_S (Ohm)	$R_{Pt/per}$ (Ohm cm^2)	R_{rec} (Ohm cm^2)	R_{per} (Ohm cm^2)
1 sun illumination	39	0.65	4.06	3.02

The quality of the curve fitting is verified by the obtained mean square deviation that is below 0.008. Noteworthy, the R_{per} (S = active area, 0.152 cm^2) value of 3.02 Ohm cm^2 is much lower than that obtained from the standard HTM spiro-OMeTAD[172], revealing easier charge transport and confirming the advantage of using $((CH_3)_3S)_2SnI_6$ perovskite in DSSCs.

CHAPTER (6)

$((CH_3)_3S)_2SnI_{6-n}Cl_n$ and $((CH_3)_3S)_2SnI_{6-n}Br_n$ (n=1, 2) perovskites and use in dye-sensitized solar cells

$((CH_3)_3S)_2SnI_{6-n}Cl_n$ and $((CH_3)_3S)_2SnI_{6-n}Br_n$ (n=1, 2) perovskites

Hybrid perovskites are currently among the most promising materials for optoelectronic applications including solar cells and light emitted diodes (LEDs), due to their high efficiency, solution processing ability and low-cost production [173–175]. Recently, engineering approaches and optimization of the preparation procedures led to perovskite solar cells (PSCs) with power conversion efficiency (PCE) exceeding 23%[173,176–182] However, the practical application of these devices still remains under question, as serious environmental (toxicity) and technological issues (stability) are reported, mainly due to the presence of toxic lead (central metal) and highly hydrophilic organic cations (methyl ammonium-MA or formamidinium-FA) [55].

As a good alternative to lead perovskites, less toxic tin-based analogues were developed but the long-term performance of the corresponding devices is seriously affected by the progressive oxidation of Sn^{2+} to Sn^{4+}[56,57]. On the contrary, the Sn^{+4}–based molecular semiconductors Cs_2SnX_6 show enhanced stability and have been successfully employed as hole transporting materials (HTMs) in efficient dye-sensitized solar cells (DSSCs)[124,152,153]. These defect perovskites render DSSCs more attractive photovoltaics combining robustness, air-stability and low manufacturing costs [145,183–187]. In addition, some attempts were undertaken to replace the humidity sensitive FA and MA cations in the perovskite structure. Thus recently, the hydrophobic trimethylsulfonium $[(CH_3)_3S^+]$ organic cation was incorporated in $(CH_3)_3SPbX_3$ (X = Cl, Br, I) perovskites presenting enhanced chemical stability and very interesting structural and electronic properties[123]. Herein, we report in depth analysis of the trimethyl sulfonium tin (iv) mixed halide defect perovskites [$((CH_3)_3S)_2SnI_{6-n}Cl_n$ and $((CH_3)_3S)_2SnI_{6-n}Br_n$ (n=1, 2)] and their use as HTMs in DSSCs, confirming efficient hole extraction across $((CH_3)_3S)_2SnX_6$ to the Pt counter electrode in these devices.

6.1 Structural analysis

For all samples, the XRPD patterns did not show peaks of unreacted precursors or other impurities (**Figure 6-1**a). The new perovskites $((CH_3)_3S)_2SnI_{6-n}Cl_n$ and $((CH_3)_3S)_2SnI_{6-}$

$_nBr_n$ (n=1, 2) obtained from solid-state synthesis present high crystallinity and have 0D cubic symmetry (space group $Pa\bar{3}$, (No. 205), in agreement with our previous work on $((CH_3)_3S)_2SnX_6$ (X= Cl, Br, I) [123]. A small gradual shift of the characteristic peaks around 11.3, 13.1, 26.4 and 27.2° is observed towards higher 2θ values with increasing Cl or Br content. The partially substitution of iodide (ionic radius, I^- = 220 pm) by smaller size chloride (ionic radius, Cl^- = 181 pm) or bromide (ionic radius, Br^- = 196 pm)[43], is accompanied with the octahedral deformation. Their distortion and shrinkage are confirmed by the observed shift of XRD peaks to higher angles, as shown in **Figure 6-2**. Structural analysis was performed for $((CH_3)_3S)_2SnI_{6-n}Cl_n$ and $((CH_3)_3S)_2SnI_{6-n}Br_n$ (n=1, 2) with the Rietveld method using initially the structural model of $((CH_3)_3S)_2SnI_6$, without further refinement of the trimethyl sulfonium group. For the 0D crystal structure refinement, the following Wyckoff sites were used: Sn atoms on 4*b* (0.5,0.5,0.5), S atoms on 8*c* (x, x, x), C atoms on 24*d* (x, y, z) and split position of mixed halide on 24*d* (x, y, z). In the last case the halide sites are mixed occupied by I and Cl/Br atoms in a 0.167:0.833 ratio for I_5Cl and I_5Br and a 0.333: 0.667 ratio for I_4Cl_2 and I_4Br_2. Moreover, the default values for C - H bond lengths have been added for the three non-equivalent crystallographic H atoms at 24d (x, y, z) without any more refinement and thermal displacement values were refined isotropically for all non - hydrogen atoms. Thus, the obtained refined crystal structure is shown in **Figure 6-1**b, and the atomic parameters are listed in **Table 6-1**.

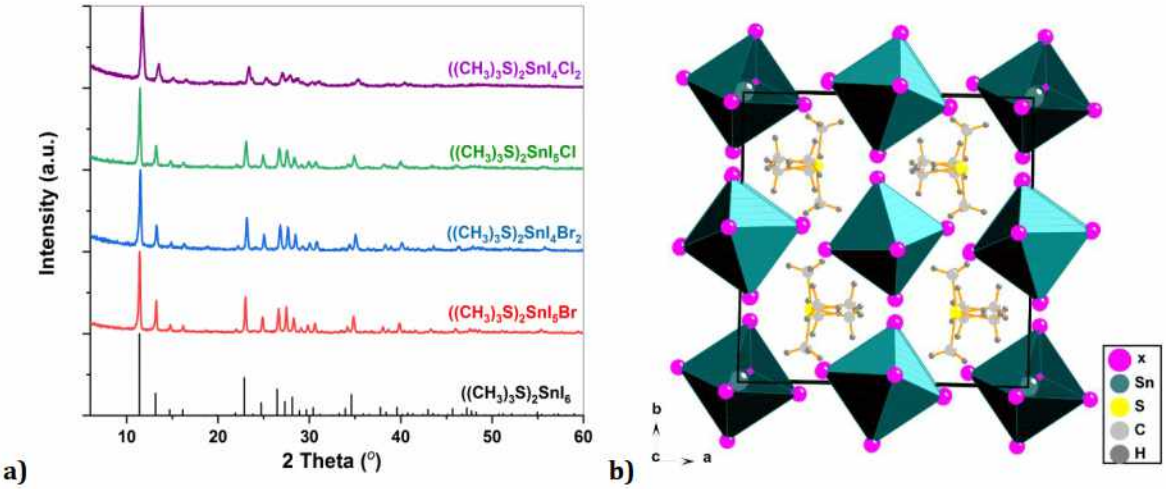

Figure 6-1: a) XRPD patterns of $((CH_3)_3S)_2SnI_{6-n}Cl_n$ and $((CH_3)_3S)_2SnI_{6-n}Br_n$. b) Crystal structures of the compounds based on Rietveld refinement.

The lattice parameters of $((CH_3)_3S)_2SnI_{6-n}Br_n$ decreased from 13.46 to 13.37 and 13.29 Å for n= 1 and 2, respectively. Accordingly, the lattice parameters of $((CH_3)_3S)_2SnI_{6-n}Cl_n$ decreased from 13.46 to 13.33 and 13.21 Å for n= 1 and 2 respectively.

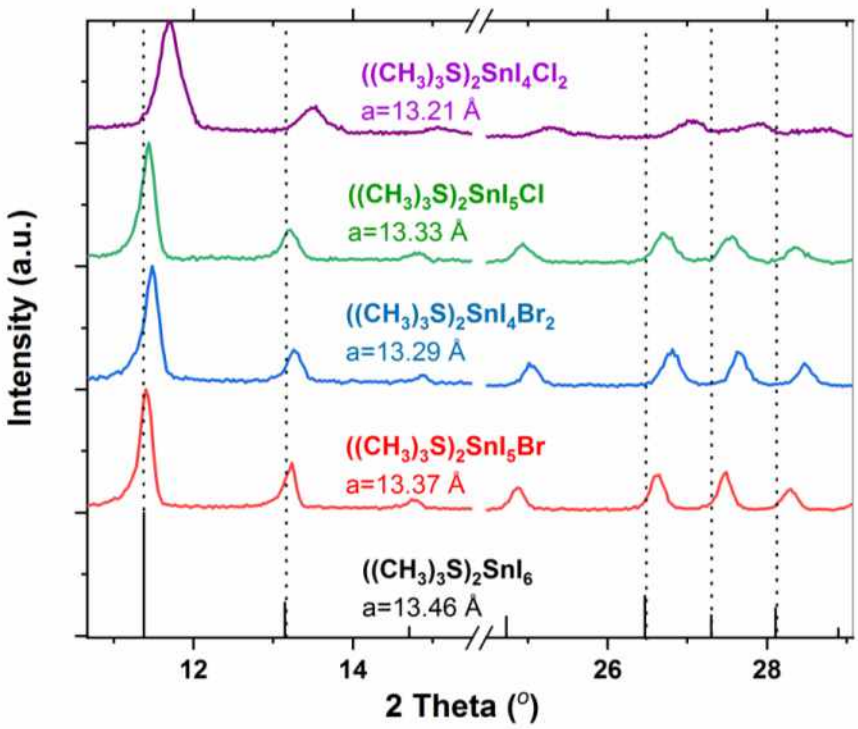

Figure 6-2: XRPD patterns of $((CH_3)_3S)_2SnI_{6-n}Cl_n$ and $((CH_3)_3S)_2SnI_{6-n}Br_n$ (n = 1,2) with gradual shift of the diffraction peaks to higher angles compared to $((CH_3)_3S)_2SnI_6$ as a result of halogen substitution.

Table 6-1: Atomic parameters of $((CH_3)_3S)_2SnI_{6-n}Cl_n$ and $((CH_3)_3S)_2SnI_{6-n}Br_n$ (n=1, 2) based on the XRPD analysis.

	Atom	Wyck. site	S.O.F.	x/a	y/b	z/c
$((CH_3)_3S)_2SnI_5Br$	I	24d	0.833	0.2915	0.0415	0.0359
	Br	24d	0.167	0.2915	0.0415	0.0359
	Sn	4b	1	½	½	½
	S	8c	1	0.237	0.237	0.237
	C	24d	1	0.307	0.168	0.337
	H1c	24d	1	0.27070	0.17220	0.39820
	H2c	24d	1	0.31440	0.10010	0.31780
	H3c	24d	1	0.37130	0.19790	0.34550
$((CH_3)_3S)_2SnI_4Br_2$	I	24d	0.667	0.29110	0.04170	0.03580
	Br	24d	0.333	0.29110	0.04170	0.03580
	Sn	4b	1	½	½	½
	S	8c	1	0.23770	0.23770	0.23770
	C	24d	1	0.30840	0.16620	0.33840
	H1c	24d	1	0.26970	0.16510	0.39840
	H2c	24d	1	0.31990	0.09930	0.31640

	H3c	24d	1	0.37080	0.19830	0.35090
$((CH_3)_3S)_2SnI_5Cl$	I	24d	0.833	0.29110	0.04170	0.03580
	Cl	24d	0.167	0.29110	0.04170	0.03580
	Sn	4b	1	½	½	½
	S	8c	1	0.23770	0.23770	0.23770
	C	24d	1	0.30810	0.16640	0.33820
	H1c	24d	1	0.27000	0.16620	0.39840
	H2c	24d	1	0.31880	0.09920	0.3 1660
	H3c	24d	1	0.37110	0.19780	0.35000
$((CH_3)_3S)_2SnI_4Cl_2$	I	24d	0.667	0.29010	0.04230	0.03550
	Cl	24d	0.333	0.29010	0.04230	0.03550
	Sn	4b	1	½	½	½
	S	8c	1	0.23850	0.23850	0.23850
	C	24d	1	0.30990	0.16030	0.34260
	H1c	24d	1	0.27130	0.15970	0.40260
	H2c	24d	1	0.31940	0.09340	0.31980
	H3c	24d	1	0.37340	0.19030	0.35550

6.2 Electronic and Vibrational properties

Figure 6-3 shows the micro-Raman spectra of $((CH_3)_3S)_2SnI_{6-n}Cl_n$ and $((CH_3)_3S)_2SnI_{6-n}Br_n$ (n=1, 2) perovskite materials. Two different types of Raman active modes are observed, external vibrations in the $[SnI_{6-n}Cl_n$ or $I_{6-n}Br_n]$ octahedra, appearing at frequencies between 30 and 200 cm^{-1} as well as internal vibrations of the organic trimethyl sulfonium $(CH_3)_3S$ molecule, at wavenumbers above 200 cm^{-1}. In addition, for the pure iodide perovskite, three Raman vibrational modes of the SnI_6 octahedra are observed: the no degenerate $\nu(A_{1g})$ due to the Sn-I symmetric stretching, doubly degenerate $\nu(E_g)$ due to the Sn-I asymmetric stretching vibration, and triply degenerate $\delta(F_{2g})$ as the halogen-Sn-I asymmetric bending deformation, which were approximately located at 119, 91 and 78 cm^{-1}, respectively. Amongst them, the $\nu(A_{1g})$ is by far the most intense. In mixed halide materials $((CH_3)_3S)_2SnI_{6-n}Cl_n$ and $((CH_3)_3S)_2SnI_{6-n}Br_n$ halide ions (I, Br/Cl) occupy the octahedron corners randomly like in $MAPbI_{3-x}Br_x$ [188]. For this reason, several new high energy $\nu(A_{1g})$ bands are observed in the Raman spectra, at 134, 146, 164 cm^{-1} for $((CH_3)_3S)_2SnI_{6-n}Cl_n$ and 126, 133 and 149 cm^{-1} for $((CH_3)_3S)_2SnI_{6-n}Br_n$. The new bands are attributed to randomly occupied octahedral corners by I and Cl/Br ions, according to

their halide compositions. Moreover, we fitted the most intense $\nu(A_{1g})$ phonon band with a Gaussian curve (**Figure 6-3**), for all investigated perovskite, which indicates a red frequency shift of this band was observed from 119 to 126 and 134 cm^{-1} upon iodide substitution with Br or Cl, correspondingly. This is in agreement with the model of harmonic oscillator [122], taking into account the differences in the atomic mass of the Sn–Cl and Sn-Br halides. Furthermore, the relative intensities of the newly formed high energy $\nu(A_{1g})$ bands considerably change for the di-substituted $((CH_3)_3S)_2SnI_4Br_2$ and $((CH_3)_3S)_2SnI_4Cl_2$ compounds, reflecting the uniform distribution of substituting anions in the atomic level. Recorded frequencies of all these vibrational bands are in good agreement with the Cs_2SnX_6 (X = Cl, Br, I) analogues [153].

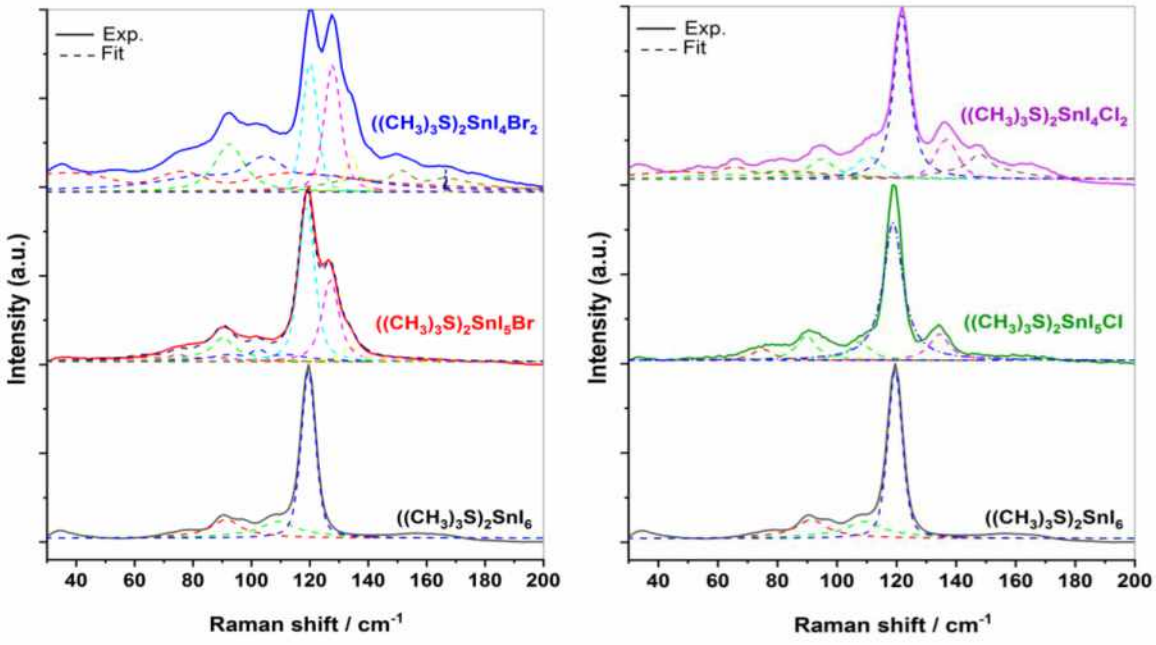

(a) (b)

Figure 6-3: Raman spectra of $((CH_3)_3S)_2SnI_{6-n}Br_n$ (a); and $((CH_3)_3S)_2SnI_{6-n}Cl_n$ (b) perovskite, where (n=1, 2)

Moreover, Temperature dependent Raman experiments were performed in order to study the lattice vibrational modes and phase transitions over wide range (-190 to 100° C of temperature. The results for the $((CH_3)_3S)_2SnI_6$ compound, presented in **Figure 6-4**, show that a phase transition at lower symmetry occurs below -50°C. This phase transition most likely incorporates tilting of the inorganic octahedra, as already reported for $MAPbI_3$ perovskite and other defect perovskite compounds (Cs_2SnI_6) [153].

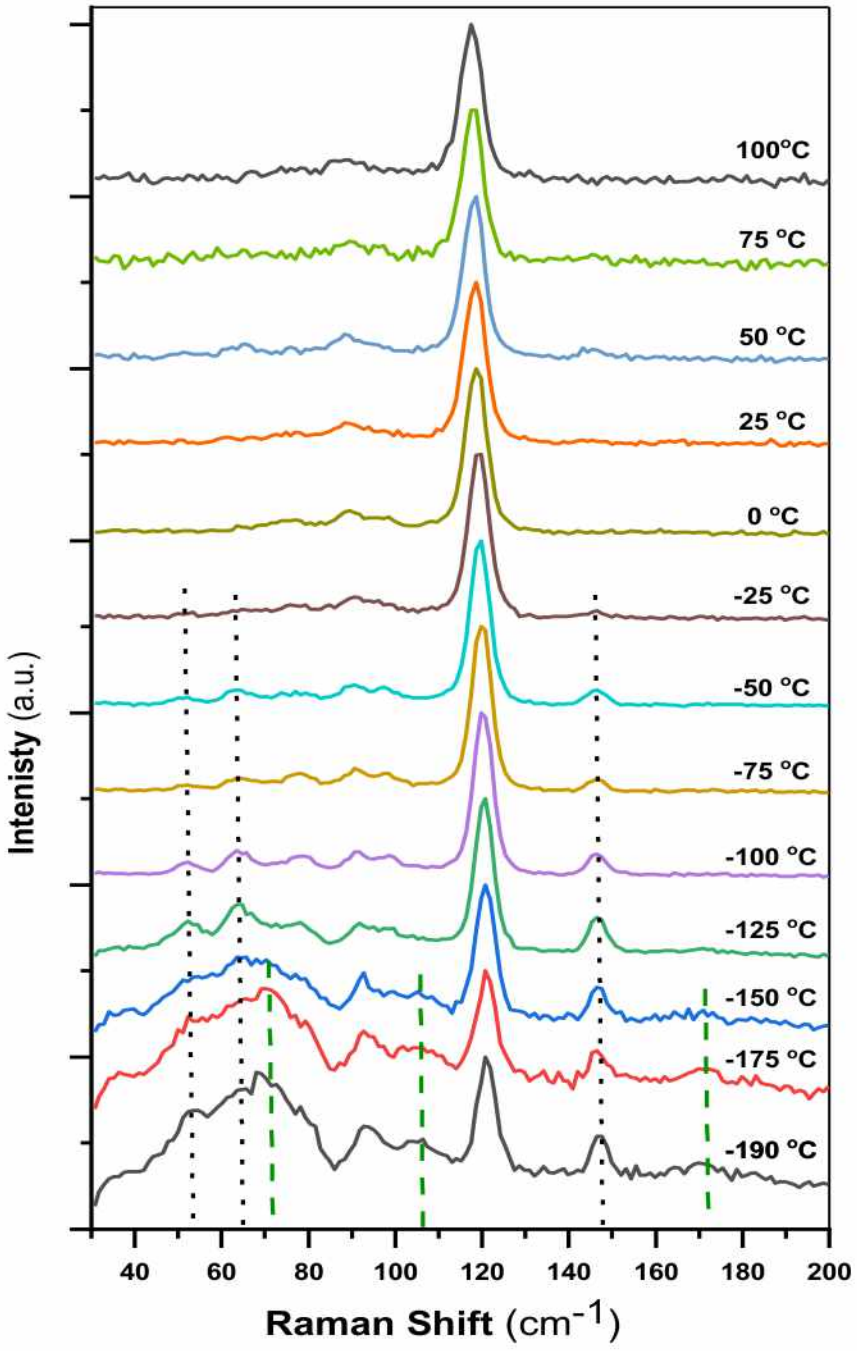

Figure 6-4: Temperature dependent Raman spectra of the $((CH_3)_3S)_2SnI_6$ perovskite.

To determine the optoelectronic properties of the $((CH_3)_3S)_2SnI_{6-n}Cl_n$ and $((CH_3)_3S)_2SnI_{6-n}Br_n$ (n=1, 2) perovskites, **Figure 6-5**a shows the corresponding diffuse reflectance spectrum. The bandgap energies gradually increased from 1.43 to 1.50 eV upon partial Iodide substitution. Accordingly, E_g values equal to 1.43, 1.46, 1.47 and 1.49 eV are estimated for $[I_5Br]$, $[I_5Cl]$, $[I_4Br_2]$ and $[I_4Cl_2]$ inorganic frameworks, respectively, thus confirming their close dependence on the chemical composition of the perovskite and especially on the nature of the anionic (halogen) species .

The experimental results are in good agreement with the performed DFT calculations. As example, the corresponding band diagram along the crystal symmetry directions in the first Brillouin zone are presented in **Figure 6-5**b for $((CH_3)_3S)_2SnI_5Br$. The coordinates of the special points of the Brillouin zone are G (0, 0, 0), X (0.5, 0, 0), R (0.5, 0.5, 0.5), M (0.5, 0.5, 0), in terms of the reciprocal lattice unit vectors, give a direct band gap value of about 1.55 eV.

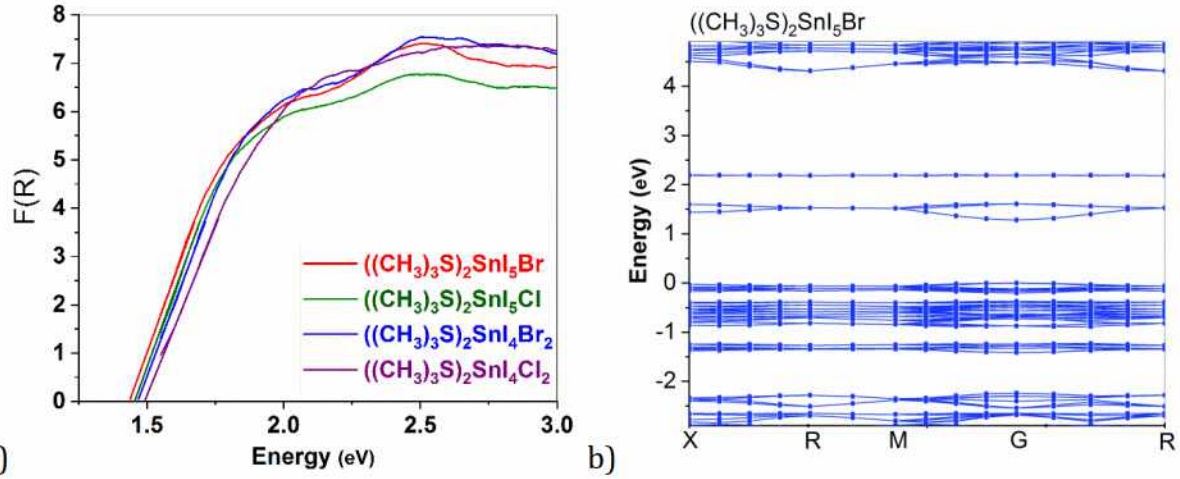

a) b)

Figure 6-5: a) Diffuse reflectance spectra (in Kubelka-Munk units) for $((CH_3)_3S)_2SnI_{6-n}Cl_n$ and $((CH_3)_3S)_2SnI_{6-n}Br_n$. b) Band structures of the $((CH_3)_3S)_2SnI_5Br$ compound.

Relatively higher E_g values were obtained for the $((CH_3)_3S)_2SnI_{6-n}Cl_n$ and $((CH_3)_3S)_2SnI_{6-n}Br_n$ compounds (**Figure 6-6**). The calculated bandgap values gradually increase with increasing bromide or chloride substitution (**Table 6-2**) and refer to direct band gaps between the valence and conduction bands at the G symmetry point for all samples.

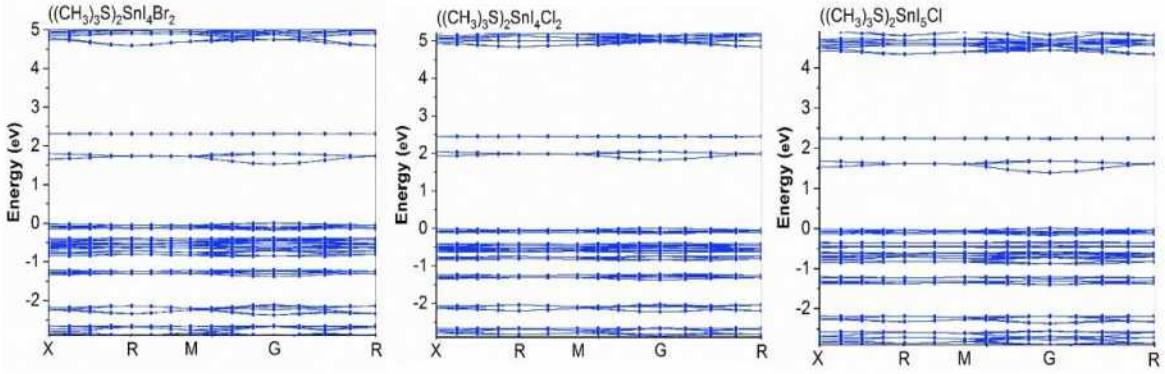

Figure 6-6: Band structure of mixed-halide perovskites.

Table 6-2: Experimental and theoretical band-gap values (using GGE/BPESOL function) for $((CH_3)_3S)_2SnI_{6-n}Cl_n$ and $((CH_3)_3S)_2SnI_{6-n}Br_n$ (n= 0,1,2)

Compound	Experimental E_g (eV)	Computational E_g (eV)
$((CH_3)_3S)_2SnI_6$	1.38	0.89

$((CH_3)_3S)_2SnI_5Br$	1.43	1.2
$((CH_3)_3S)_2SnI_4Br_2$	1.47	1.5
$((CH_3)_3S)_2SnI_5Cl$	1.46	1.4
$((CH_3)_3S)_2SnI_4Cl_2$	1.49	1.8

6.3 Morphology and chemical composition

The morphology of the bulk materials of $((CH_3)_3S)_2SnI_{6-n}Cl_n$ and $((CH_3)_3S)_2SnI_{6-n}Br_n$ was investigated using Scanning Electron Microscopy (SEM) and their chemical composition was determined by Energy-dispersive X-ray spectroscopy (EDXS). SEM micrographs of mixed halide compounds are very similar to those recorded for $((CH_3)_3S)_2SnI_6$ [123] exhibiting angular grain shapes. EDXS data were obtained from three different spots for each compound and the mean values of elemental content match well the nominal (theoretical) chemical composition of the samples (**Table 6-3**).

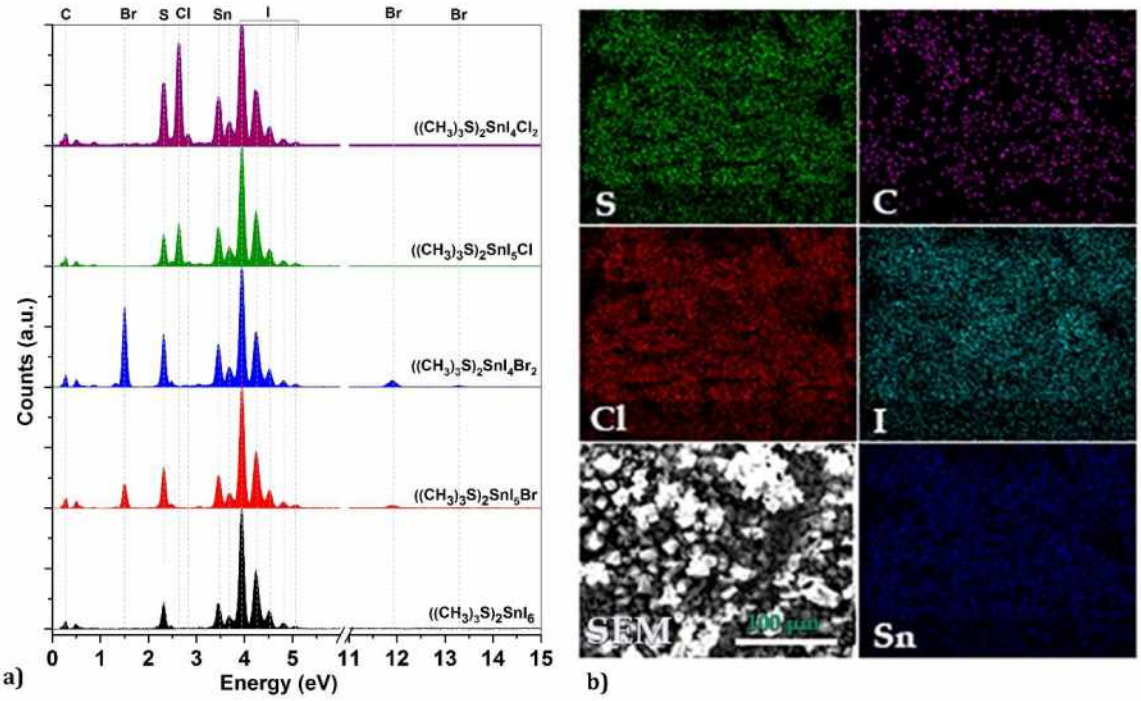

Figure 6-7: a) EDX spectra of $((CH_3)_3S)_2SnI_{6-n}Cl_n$ and $((CH_3)_3S)_2SnI_{6-n}Br_n$. b) EDXS mapping of $((CH_3)_3S)_2SnI_4Cl_2$ and corresponding SEM picture.

Table 6-3: Chemical composition of $((CH_3)_3S)_2SnI_{6-n}Cl_n$ and $((CH_3)_3S)_2SnI_{6-n}Br_n$ (n=1, 2) based on EDX analysis along with the theoretical values.

	$((CH_3)_3S)_2SnI_5Br$	**$((CH_3)_3S)_2SnI_4Br_2$**	**$((CH_3)_3S)_2SnI_5Cl$**	**$((CH_3)_3S)_2SnI_4Cl_2$**

	exp.	calc.	exp.	calc	exp.	calc.	exp.	calc.
C	8.07	7.3	9.27	7.66	6.2	7.45	10.16	8.46
S	5.6	6.49	5.8	6.82	3.69	4.34	6.83	7.53
Sn	13.47	12.02	14.19	12.62	19.52	17.51	17.66	13.94
I	62.26	64.26	47.79	53.97	63.7	64.79	53.77	59.61
Br	10.59	8.09	22.29	16.99	-	-	-	-
Cl	-	-	-	-	6.88	5.91	11.58	8.33

The characteristic EDXS spectra are shown in **Figure 6-7**a and the EDXS maps for $((CH_3)_3S)_2SnI_4Cl_2$ (**Figure 6-7**b) show large areas with good lateral uniformity which verifies the uniform distribution of different atoms on the bulk materials.

6.4 First principles DFT calculations

All first principles calculations were performed to obtain electronic partial density of states (PDOS) and energy band structure, using the plane wave pseudopotential method of quantum density functional theory (DFT) in the gas phase (CASTEP package) [98]. The electron-ion interaction was simulated with the GGA/PBE exchange-correlation [97,189,190]. The cut-off energy was set at 450 eV for all compounds and equilibrium geometry optimization was carried out using BFGS algorithm to get well relaxed structures. The DFT calculations (**Figure 6-6**, **Figure 6-8**) of the cubic structures of $((CH_3)_3S)_2SnI_{6-n}Cl_n$ and $((CH_3)_3S)_2SnI_{6-n}Br_n$ (n=1, 2) were carried out on the optimized geometry of cell structures refined from XRD data. The XRD results were used in order to make an in-depth analysis of their structural, electronic, and energetic properties. Partial density of state (PDOS) diagrams reported in **Figure 6-8**c,d, shows that the main contribution to the top valance band comes from the 5p state of mixed halogen I_5Br with little participation of the 5s state. In contrast, the main contribution to the top valance band of $((CH_3)_3S)_2SnI_5Cl$ is the 5p state of mixed halogen I_5Cl, which predicts stronger covalent bond with Sn atoms than subtitled bromide.

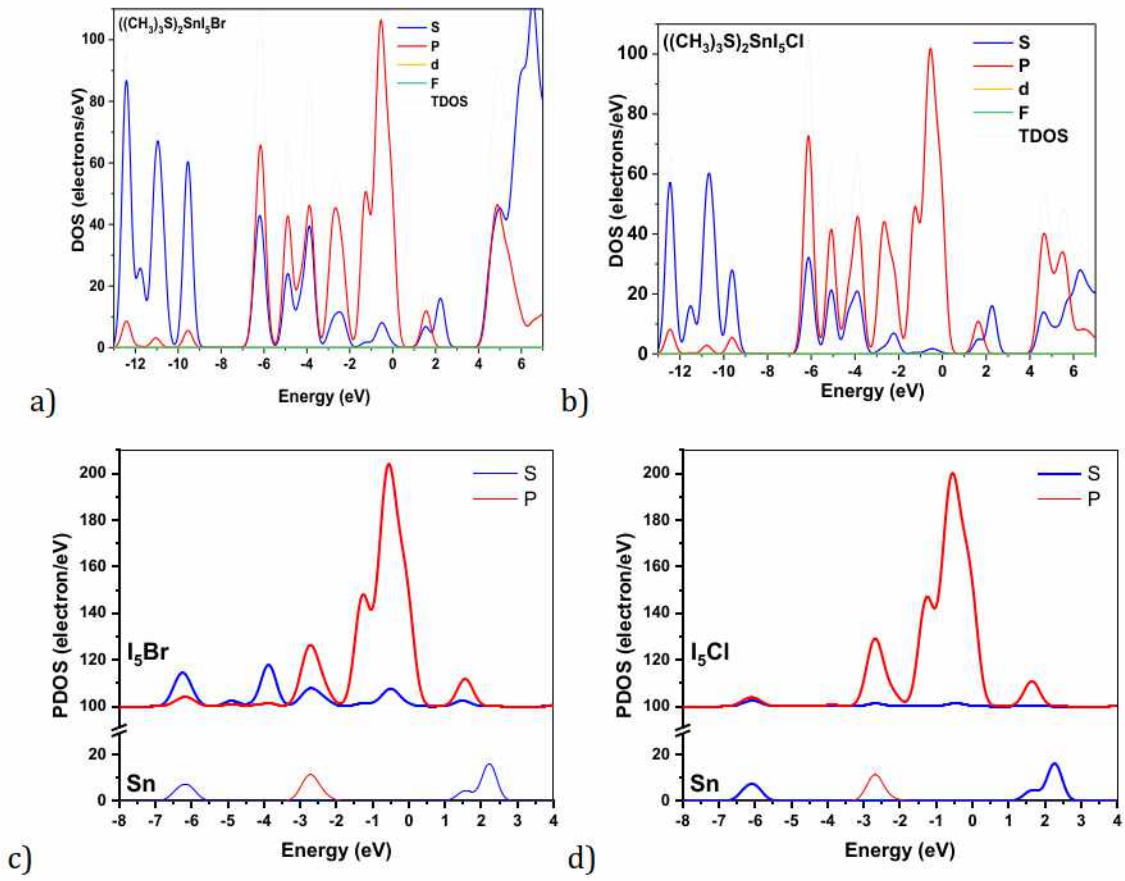

Figure 6-8: a, b) Density of state $((CH_3)_3S)_2SnI_5Br$ and $((CH_3)_3S)_2SnI_5Cl$ compounds, respectively. c, d) Partial density of state of Sn and mixed halogen in $((CH_3)_3S)_2SnI_5Br$ and $((CH_3)_3S)_2SnI_5Cl$ compounds.

On the other hand, the main contribution to the conduction band arises from anti-bonding 5p states of the halogen atoms and 5s states of Sn atoms. The strong hybridization of halogen (5p)-Tin(5s) bonds leads to mostly covelent interaction and permits the transfer of electrons from halogens to tin atoms, thus improving the stability of compounds.

6.5 Electrodes and solar cells fabrication

The solar cells were prepared following a well-established procedure in our lab [123]. FTO conductive glass electrodes (7 ohms/cm²) were cleaned in ultrasounds (successively with Triton X100, deionized water and ethanol, for 15 min each step) and dried using N_2 flow. On the FTO electrodes, a 6 µm thick TiO_2 layer was deposited by doctor blade using the 18-NRAO paste, dried in air and then annealed for 60 min at 500 °C. This was followed by the deposition of a second TiO_2 scattering layer (also 6 µm thick), prepared using the WER4 paste with average particle size of 400 nm. The composite films were sequentially annealed [at 125 °C (5 min), 325 °C (15 min) and 525 °C (30 min)] and post-treated with a $TiCl_4$ aqueous solution (20 mmol/L) at 70 °C for 10 min. Then, the obtained composite

titania electrodes were washed with deionized water and ethanol, dried and finally annealed at 500 °C for 30 min. The TiO_2 electrodes were sensitized by immersion into dye solutions for approximately 72 hours. For Z907, 0.3 mmol/L of dye and 0.3 mmol/L chenodeoxycholic acid in a 1:1 v/v mixture of acetonitrile: tert-butanol were used. In the case of N719 and D35 dyes, the electrodes were immersed into a 0.3 mmol/L and 0.2 mmol/L dye solution in ethanol, respectively. As for the MK-2 dye, the electrodes were immersed into a 0.3 mmol/L dye solution in a 1:1:1 v/v/v mixture of toluene: acetonitrile: tert-butanol.

For the perovskite solutions, 103.4, 98.7, 94.1, 94.3 and 85.2 mg of $((CH_3)_3S)_2SnI_6$, $((CH_3)_3S)_2SnI_5Br$, $((CH_3)_3S)_2SnI_4Br_2$, $((CH_3)_3S)_2SnI_4Cl$ and $((CH_3)_3S)_2SnI_4Cl_2$ respectively, were dissolved in DMF (0.4 mL) under stirring at 50 °C (10 min.). The perovskite solutions were filtered by PTFE 0.45 μm filter and then, 10.4 μL of TBP and 15 μL of Li-TFSI (from a stock solution of 520 mg Li-TFSI in 1 mL acetonitrile) were added as dopants to increase the conductivity of the $((CH_3)_3S)_2SnI_{6-n}Cl_n$ and $((CH_3)_3S)_2SnI_{6-n}Br_n$ HTMs. A drop of the perovskite solution was placed on top of the dye/TiO_2 photoelectrode and left to dry at 50 °C. An extra drop of the perovskite solution was casted on the platinized (100 nm thick prepared by Pt sputtering on FTO glass) cathode electrode which was placed on top of the photoelectrode and the sandwich structure was dried again at 50 °C.

$((CH_3)_3S)_2SnI_{6-n}Cl_n$ and $((CH_3)_3S)_2SnI_{6-n}Br_n$ perovskites were employed in electrolyte-free DSSCs of the type: **FTO/TiO_2-dye//Mixed halide perovskite//Pt/FTO**. The mesoporous nanocrystalline TiO_2 electrodes were sensitized by different molecular antennas including both metal organic (Z907, N719) and organic (MK2, D35) dyes. *The J–V* curves of the DSSCs incorporating $((CH_3)_3S)_2SnI_{6-n}Cl_n$ or $((CH_3)_3S)_2SnI_{6-n}Br_n$ as HTMs are shown in **Figure 6-9**a. It should be noted that in all cases the perovskites were doped with Li-TFSI and TBP additives in order to increase their hole carrier concentration and improve the corresponding DSSCs photovoltaic characteristics as previously reported [191,192].
From the *J-V* plots (**Figure 6-9**) the values of short-circuit photocurrent density (J_{sc}), open-circuit voltage (V_{oc}), fill factor (*FF*) and power conversion efficiency (PCE) were deduced. PCE is defined as the ratio of the maximum electrical power produced by the cell $(JV)_{max}$ over the incident light power (P), following equation (Eq. 6.2):

$$PCE\ \% = \frac{(\mathrm{JV})\mathrm{max}}{\mathrm{P}} \times 100 \qquad (Eq.\ 6.1).$$

For the calculation of the fill factor values we used the equation (Eq. 6.2):

$$FF = \frac{(JV)max}{J_{sc}V_{oc}} \qquad (Eq.\,6.2)$$

Table 6-4 summarizes the photovoltaic parameters. Among the different types of cells, those combining the Z907 sensitizer (transition metal complex) with the perovskite (HTMs) based on pure iodide and monosubstituted Bromide/chloride, achieved the highest performance, 5.07% and ~ 4%, correspondingly, **Figure 6-9**a. The highest value of the photocurrent density (20.05 mA/cm²) was recorded for the pure iodide-based perovskite. This value was reduced to 14.03 and 12.06 mA/cm² for monosubstituted bromide and chloride respectively. In contrast, the fill factor (FF) increased with increasing the electronegativity of the substituted halogen taking values of (0.53, I), (0.56, Br) and (0.60, Cl), respectively. It is well known that doping the perovskite with a small amount of Cl or Br results in a decrease of recombination rate and increase of charge carriers lifetime [193,194]. Also, quite high efficiency of 2.7% was observed for the N719 sensitizer (**Figure 6-9**b) than those obtained with organic of MK2 and D35 dyes (1.77% and 1.12%, respectively).

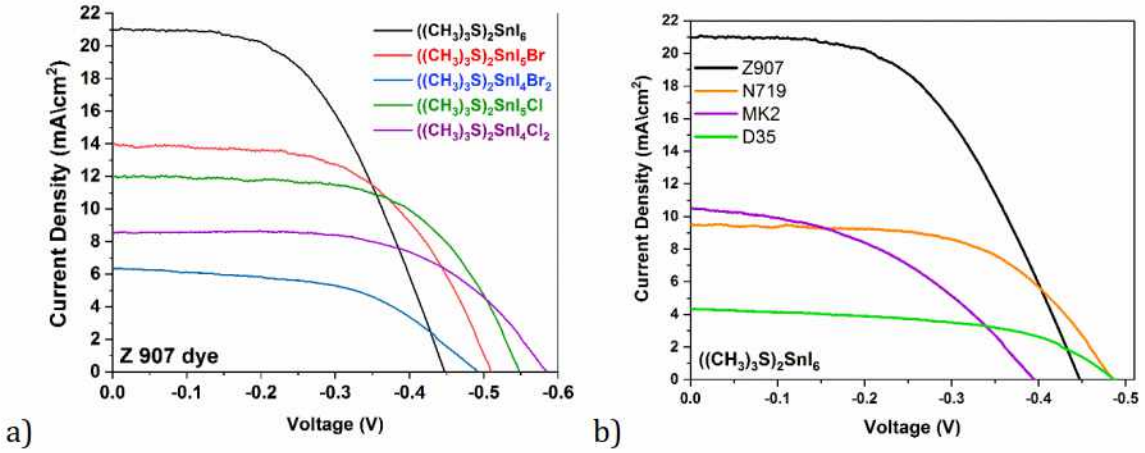

Figure 6-9: a) Photovoltaic performance of $((CH_3)_3S)_2SnI_{6-n}Cl_n$ and $((CH_3)_3S)_2SnI_{6-n}Br_n$ compounds on Z 907 dye. B) I-V curve of $((CH_3)_3S)_2SnI_6$ based on different type of transition metal complex (Z907, N719) and organic (MK2, D35) dyes.

Table 6-4: Photovoltaic parameters of cells employing the entitled perovskite compounds and different dye sensitizers.

Dye	Compound	J_{sc} (mA/cm²)	V_{oc} (V)	FF	PCE %
D35	$((CH_3)_3S)_2SnI_6$	4.34	0.49	0.53	1.12
MK2	$((CH_3)_3S)_2SnI_6$	10.50	0.4	0.42	1.77
N719	$((CH_3)_3S)_2SnI_6$	9.54	0.49	0.57	2.68

Z 907	$((CH_3)_3S)_2SnI_6$	20.05	0.48	0.53	5.07
	$((CH_3)_3S)_2SnI_5Br$	14.03	0.51	0.56	4.02
	$((CH_3)_3S)_2SnI_4Br_2$	6.36	0.49	0.53	1.64
	$((CH_3)_3S)_2SnI_5Cl$	12.06	0.55	0.60	4.00
	$((CH_3)_3S)_2SnI_4Cl_2$	8.66	0.59	0.58	2.95

In fact, electrochemical impedance spectroscopic analysis performed (**Figure 6-10**) confirms that the mono substituted halogen (chloride or bromide) perovskites in cells based on Z907 sensitizer present higher recombination resistance (R_{rec}) than the pure iodide-based reference (**Table 6-5**). This implies suppressed recombination rates and can justify the slight increase in the observed V_{oc} values. In contrast, the recombination resistance of cells employing perovskites with di-substituted halogens regained low values, similar to those of the pure iodide-based perovskite. This complies with the decrease of V_{oc} for $((CH_3)_3S)_2SnI_4Br_2$, however it cannot justify the V_{oc} increase for $((CH_3)_3S)_2SnI_4Cl_2$, which is rather due to down-shift in the valence band energy level of this particular perovskite.

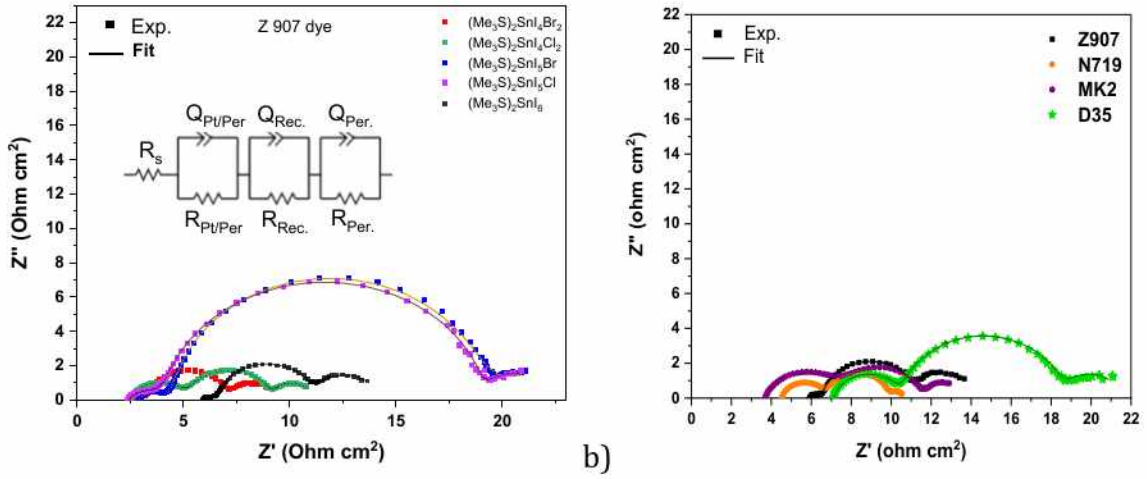

Figure 6-10: a) Nyquist plot for $((CH_3)_3S)_2SnI_{6-n}Cl_n$ and $((CH_3)_3S)_2SnI_{6-n}Br_n$ compounds on Z 907 sensitizer dye (The equivalent electrical circuit employed to simulate the EIS data is shown in the inset). B) Nyquist plot for $((CH_3)_3S)_2SnI_6$ based on Z907, N719, MK2, and D35.

Despite the suppressed recombination kinetics for the monosubstituted halogen perovskite in Z907-based solar cells, the charge transfer resistance at the perovskite/platinum interface ($R_{Pt/per}$) increased in all cases. Thus, a $R_{Pt/per}$ value of 0.65 Ohm cm² was attained for the pure iodide perovskite and increased to 2.13, 3.44 and 4.14 Ohm cm² for mono-substituted bromide and chloride and disubstituted chloride perovskites, respectively. This tendency comprises well with decrease of the short-curcuit photocurrent for all cells

with mixed halides. Moreover, **Figure 6-10**b presents comparative impedance spectra for cells with $((CH_3)_3S)_2SnI_6$ based on different, Z907, N719, MK2, and D35 dyes. **Table 6-5** summarizes the corresponding EIS fitting parameters. The cells based on the organic dye present higher charger transfer and lower recombination resistance which shows off the reasons behind their relatively low photovoltaic efficiency. The poor photovoltaic behavior of the cells with organic dyes could be attributed to the fact that the TiO_2 layer (thickness, structure) was optimized for the organometallic dyes but not for the organic dyes [124].

Table 6-5: Calculated values for the equivalent circuit parameters (R_s, $R_{Pt/per}$, R_{rec}, R_{pre}) of various solar cells.

Dye	Perovskite (HTM)	R_S (Ohm)	$R_{Pt/per}$ (Ohm cm²)	R_{rec} (Ohm cm²)	R_{per} (Ohm cm²)
MK2	$((CH_3)_3S)_2SnI_6$	24	2.85	4.11	3.81
D35	$((CH_3)_3S)_2SnI_6$	46	3.52	8.28	2.88
N719	$((CH_3)_3S)_2SnI_6$	30	0.64	2.31	3.18
Z 907	$((CH_3)_3S)_2SnI_6$	39	0.65	4.06	3.02
	$((CH_3)_3S)_2SnI_5Br$	20	2.13	14.61	2.88
	$((CH_3)_3S)_2SnI_4Br_2$	17	0.77	3.96	2.06
	$((CH_3)_3S)_2SnI_5Cl$	16	3.44	15.05	2.10
	$((CH_3)_3S)_2SnI_4Cl_2$	16	4.14	1.93	2.71

CHAPTER (7)

3D/1D - Dimensionality Engineering of (FA/MA/Cs) $PbI_{3-x}Br_x/(CH_3)_3SPbI_3$ Perovskite solar cells

3D/1D - Dimensionality Engineering of (FA/MA/Cs) $PbI_{3-x}Br_x$ /$(CH_3)_3SPbI_3$ perovskite solar cells

Photovoltaics (PVs) constitute a widespread power source with 402GW of globally grid-connected panels.[195] Lately, the dominant Si-based devices are challenged by emerging 3rd generation PV technologies, focusing on cheap and potentially eco-friendly nano-materials synthesized with wet-chemistry techniques, where their optical, electrical and physicochemical properties can be readily tuned. Perovskite solar cells (PSCs) evolved from the solid-state, dye-sensitized solar cells (DSSCs)[28,29] by replacing the dye absorber with an ABX_3 type perovskite material where A is an inorganic or/and organic cation (Cs^+, $CH_3NH_3^+$, $(HC(NH_2)_2^+)$, B is a metal cation (e.g Pb^{2+}, Sn^{2+}), and X is a halogen anion (Cl^-, Br^-, I^-). The efficiency of PSCs has increased within only a few years of development and researchers elaborate intensively on their optimization. In fact, novel synthetic procedures,[173,174] solar cell architectures[176,196] and interface engineering approaches [145,182,197] raised the power conversion efficiency (PCE) of PSCs to values as high as 25.2%,[9,177–181] whilst their incorporation in tandem devices has already outperformed the single junction Si solar cells.[198]

However, substantial issues, namely poor stability against environmental factors (oxygen, humidity, UV radiation and heat), hysteresis [199–201] (inconsistency between J-V curves depending on the scan direction) and the presence of toxic elements remain under thorough investigation.[202] The instability issues are associated among others, with ion segregation[25,203,204] under light exposure along with the highly hygroscopic and disordered methyl ammonium (MA) and formamidinium (FA) organic cations. [55,205] In addition, the stability of the operating perovskite devices suffers also from the hygroscopic additives (Li salts) usually added to the hole transporting materials (e.g. Spiro-MeOTAD).[206] With regard to the hygroscopic and volatile nature of the organic cations hybrid perovskites rapidly degrade to hydrated perovskites phases in humid conditions, [207,208] e.g. the $MAPbI_3$ and $FAPbI_3$ progressively decompose to the initial PbI_2 precursor.[209,210] Moreover, the cubic black α-phase of $FAPbI_3$ readily transforms to the hexagonal yellow δ-phase under ambient conditions.

Thus, a significant contribution towards solving the stability challenge embraces the use of mixed ions perovskites (e.g. $MAFAPbI_{3-x}Br_x$). This leads to enhanced photovoltaic performance and stability of the crystal structure in dark and dry conditions; however, the

materials remain vulnerable under humidity, temperature and illumination stresses. Thus, the addition of Cs and/or Rb inorganic cations to the mixed perovskite improved its thermal and phase stability but many studies are still necessary in order to definitively overcome these problems. [211–213] In this context, the formation of a $FA_{0.88}Cs_{0.12}PbI_{3-x}(PF_6)_x$ interlayer between the perovskite absorber and the HTM has been recently proposed towards improving the photovoltaic performance and stability of the devices through an ion exchange reaction with the $FAPF_6$ solution.[214] In addition, sulphur-based perovskites also showed a great application potential.[42,215] This is the case of novel perovskites based on the organic trimethylsulfonium [$(CH_3)_3S^+$] cation, presenting improved chemical stability in ambient conditions.[42,122,123,216,217] Moreover, the air stable $((CH_3)_3S)_2\,SnI_6$ 'defect' perovskite material has been also employed as HTMs in dye sensitized solar cells. [123,218] Herein, we report for the first time, a perovskite tridimensional/monodimensional (3D/1D) bilayer consisting of (FA/MA/Cs) $PbI_{3-x}Br_x$ (3D) and $(CH_3)_3SPbI_3$ (1D) perovskites fabricated by facile wet chemistry processes. In general, 1D perovskites are primarily considered to be effective active materials for light emission devices due to their low exciton dissociation efficiency, following their large exciton binding energies and strong quantum confinement phenomenon. [219] Thus, only a few reports have been published alluding their incorporation in PV applications.[220,221] The 1D perovskite phases since isolated by large organic cations in two dimensions can have theoretically better stability than their 2D and 3D counterparts.[221] Moreover, it was recently demonstrated that individual metal halide octahedra could be more thermodynamically stable than connected ones.[222] There are literature reports exploring the concept of hydrophobic species to improve the stability of PSCs. Most of them concern nitrogen derivatives including alkylammonium cations;[223] phenylalkylamine;[224] or pyrazol-yl pyridine 1D-3D hetero-structure.[220] Very recently, a 1D perovskite epilayer proposed by Gao et al. for PSC leads to devices with improved stability,[225] due the thiazole ammonium iodide used having an aromatic moiety (thiazo ring) and preserving the quaternary ammonium group. However, sulfonium-based ionic materials have generated substantial interest in solar cells as potential alternatives for their ammonium counterparts, due to practical benefits including higher chemical and electrochemical stabilities.[226–228] Thus, taking also into account that sulfur based organo-compounds are more hydrophobic than the nitrogen ones, in the present work we focus on a tertiary sulfonium compound. Indeed, the results obtained in our case, confirmed the beneficial effect of an air stable $(CH_3)_3SPbI_3$

extra layer toward enhanced stability against humidity and light. As a result, we obtained PSCs based on a 1D/3D perovskite bilayer which although unencapsulated, retained 58% of their initial efficiency after one month of storage in ambient, dark conditions. A similar behavior, superior to the reference devices, was also observed for the modified PSCs after prolonged light exposure. Finally, the PSCs containing the 1D perovskite were more reproducible during fabrication, a fact that confirms the beneficial influence of the 1D perovskite in the stability of the perovskite photoactive underlayer.

7.1 Device fabrication

The solar cells were prepared following a well-established procedure in our lab. FTO conductive glass electrodes (7 ohms/sq) were cleaned in ultrasounds (successively with Triton X100, deionized water, ethanol, isopropanol and acetone for 15 min each step) and dried using N_2 flow. Then the cleaned glasses were treated with UV-ozone for 20 min. On the FTO electrodes, a blocking TiO_2 layer was spin-coated (2000 rpm, 60 s) and calcinated at 450°C for 45 min. A compact TiO_2 layer was deposited by spin-coating (2000 rpm, 20 s) of a precursor solution of 0.1 g TiO_2 18NRT dissolved in 0.8 ml EtOH. The substrates were immediately dried at 125°C for 5 minutes, and then sintered at 325°C, 375°C, 450°C, for 5min, 5min and 30min respectively. Then, 0.1 mol/L of Li-TFSl in acetonitrile was spin-coated (3000 rpm, 10 s) and the samples were immediately sintered at 450°C for 30 minutes. The perovskite film was deposited in an Ar-filled glovebox by spin coating upon the TiO_2 substrates. The perovskite precursor solution was prepared using 1.1 mol/L PbI_2, 0.2 mol/L $PbBr_2$, 1 mol/L FAI and 0.2 mol/L MABr in 850 µl of mixed DMSO: DMF (1:4, volume ratio) solvent. 50µl of CsI (1.5 mol/L stock solution) was added to the perovskite solution which was spin-coated at 1.000 rpm for 10 s and, continuously at 6.000 rpm for 20 s. In addition, 150 µL of anhydrous chlorobenzene was poured on the film after 15 s during the second step. The films were post-annealed at 100 °C for 50 min. In the case of the modified films, 1 mg of $((CH_3)_3SCl$/ 1ml isopropanol was spin-coated at 4.000 rpm for 10 s, followed by post-annealed at 100°C for 10 min. In both cases of reference (3D) and modified (3D/1D) films, a passivation FABr layer (5mg/1ml isopropanol) was spin-coated at 5.000 rpm for 10 s, followed by post-annealing at 100°C for 10 min again. After cooling down to room temperature, Spiro-MeOTAD was spin-coated at 4.000 rpm for 10 s. The 70 mM Spiro-MeOTAD solution was prepared using anhydrous chlorobenzene. In addition to that, Li-TFSI in acetonitrile, 4-tert-butylpyridine, and FK209 in

acetonitrile were added at the molar ratio of Spiro-MeOTAD: TBP: Li-TFSI: FK209 of 1: 3.3: 0.5: 0.03. Finally, the devices were completed with thermal evaporating of 100 nm thick silver (Ag) counter electrodes.

Figure 7-1a depicts the solar cells fabrication procedure of the PSCs. The perovskite PV devices (**Figure 7-1b**) consist of multiple layers in the following order: fluorine-doped transparent oxide conductive glass (FTO)/ compact TiO_2 (c-TiO_2)/ mesoporous TiO_2 (m-TiO_2)/ (FA/MA/Cs)$PbI_{3-x}Br_x$ / $(CH_3)_3SPbI_3$ /Spiro-MeOTAD /Ag, where TiO_2 and Spiro-MeOTAD act as the electron and hole selective contacts, respectively.

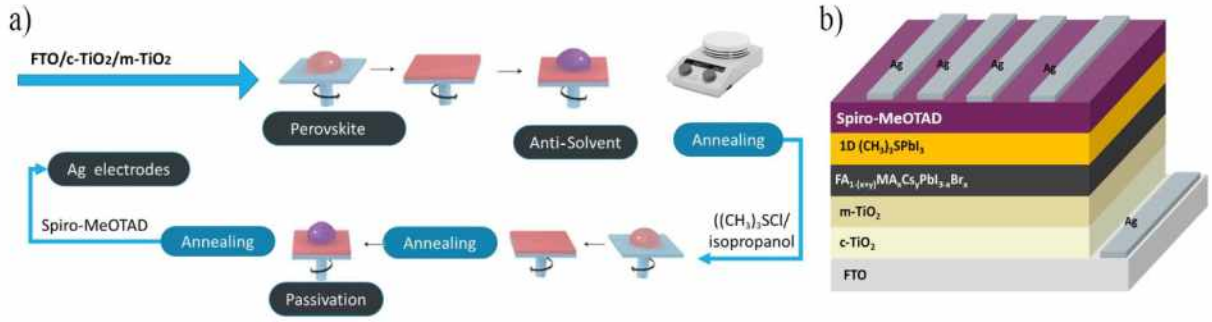

Figure 7-1: PSCs fabrication procedure (a) and solar cells architecture (b).

The mixed (FA/MA/Cs) $PbI_{3-x}Br_x$ perovskite was used as the absorber and the corresponding interface with HTM was further engineered by applying a stable 1D $(CH_3)_3SPbI_3$ high band gap perovskite layer on top of the absorber. For comparison, reference solar cells (3D) without the 1D component were also fabricated. Preliminary experiments showed that the optimum concentration of the solution used for the synthesis of $(CH_3)_3SPbI_3$ is 1 mg·ml^{-1} of $(CH_3)_3SCl$ in isopropanol. Thus, we used this concentration in order to fabricate and evaluate the PV devices and the employed materials.

7.2 Device analysis

As previously reported by our group,[42] single-crystal X-ray powder diffraction (XRPD) analysis showed that $(CH_3)_3SPbI_3$ has hexagonal symmetry in the space group *P*6$_3$*mc* (No. 186) with distorted, face-sharing PbI_6 polyhedra that form 1D chains along the c axis. In this structural modification, the trimethylsulfonium cations occupy interstitial sites between the octahedra (**Figure 7-2a**). Consequently, we performed a structural analysis of the 3D perovskites coated upon titania substrates with and without the 1D perovskite layer. **Figure 7-2b** presents the corresponding XRPD patterns of the reference (3D) and

engineered (FA/MA/Cs)$PbI_{3-x}Br_x$/$(CH_3)_3SPbI_3$(3D/1D) perovskite bilayer deposited on m-TiO_2. The XRPD analysis confirmed the presence of the main reflections from the 3D-(FA/MA/Cs)$PbI_{3-x}Br_x$ perovskite (at 2θ =13.5, 19.4°), titania (at 2θ =26 °) and the FTO (at 2θ =24, 27.8 °) layers. [229] By using the optimum amount of $(CH_3)_3SCl$, it becomes clear that the 3D/1D structure offers exceptional stability to the triple cation perovskite film based on formamidinium (FA), methylammonium (MA), and cesium (Cs) without any degradation, even when the films were left for a month in ambient and dark conditions (without encapsulation). In contrast, the 3D films progressively degraded to PbI_2 under the same conditions. In order to identify the exact nature of the bilayer, we tried higher concentrations of the modifier (3mg ml^{-1} of $(CH_3)_3SCl$ in isopropanol). Thus, the top layer has been indexed as the 1D $(CH_3)_3SPbI_3$ hexagonal perovskite (XRPD pattern in **Figure 7-3**), while its crystal structure is presented in **Figure 7-2a**. In addition, in **Figure 7-3**, the presence of the main diffraction peaks from the 3D-(FA/MA/Cs)$PbI_{3-x}Br_x$ underlayer was also confirmed, the shift of reflections for the 1D-$(CH_3)_3SPbI_3$ phase compared to the theoretical histogram [42] is attributed to the slight dislocation of the film from the surface of the XRPD sample holder. Moreover, the optoelectronic properties of the perovskite bilayer were studied using UV-Vis spectroscopy. **Figure 7-2c** shows the absorption and the corresponding steady photoluminescence (PL) spectra of samples with the following structure: TiO_2/(FA/MA/Cs)$PbI_{3-x}Br_x$/$(CH_3)_3SPbI_3$, denoted as 3D/1D and TiO_2/(FA/MA/Cs)$PbI_{3-x}Br_x$ denoted as 3D. The slight lower absorption of theTiO_2/(FA/MA/Cs)$PbI_{3-x}Br_x$/ $(CH_3)_3SPbI_3$ composite (compared to that of TiO_2/(FA/MA/Cs)$PbI_{3-x}Br_x$) could be attributed to the thickness of the 1D perovskite formed on the top surface of the absorber.

From the plots presented it is also derived that the absorbance onset of the 3D perovskite is not affected by the presence of the $(CH_3)_3SPbI_3$. Moreover, a clear photoluminescence increase was observed in the case of the modified perovskite (**Figure 7-2**c, right, spectra taken at room temperature upon excitation at 482nm). The signal PL enhancement is associated with less radiative recombinations due to the presence of the 1D perovskite, which probably increases the charge carrier's separation and facilitates hole injection efficiency to the cathode.

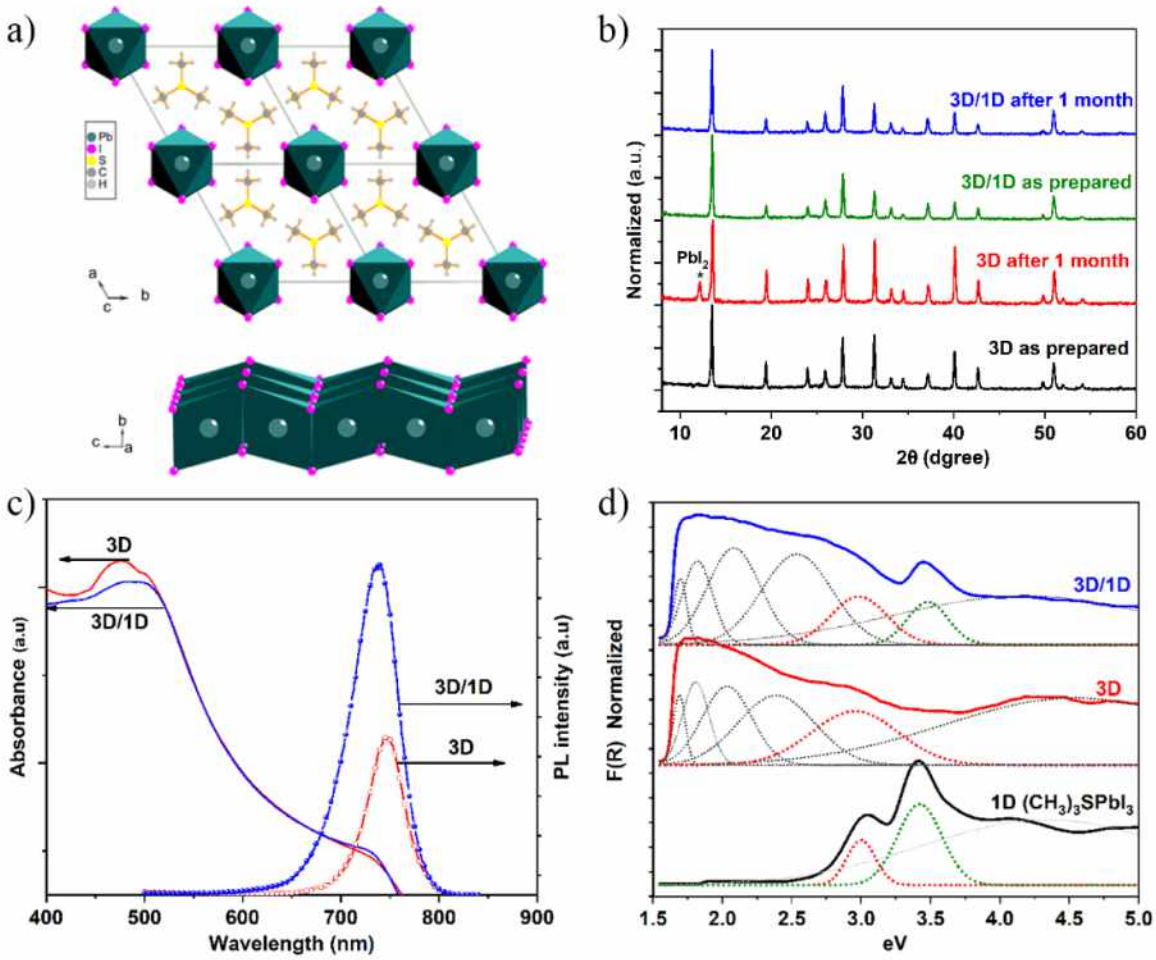

Figure 7-2: Crystal structure of the $(CH_3)_3SPbI_3$ compound with 1D framework of $[PbI_6]$ octahedral (a); XRD patterns of TiO_2/(FA/MA/Cs)$PbI_{3-x}Br_x$/$(CH_3)_3SPbI_3$(3D/1D) and TiO_2/(FA/MA/Cs)$PbI_{3-x}Br_x$ (3D) films, as prepared and after a month in ambient conditions (b); Absorbance and steady-state PL spectra of TiO_2/(FA/MA/Cs)$PbI_{3-x}Br_x$ samples with $(CH_3)_3SPbI_3$ on top (3D/1D) and without modification (3D) (c); Diffuse reflectance spectra of TiO_2/(FA/MA/Cs)$PbI_{3-x}Br_x$/$(CH_3)_3SPbI_3$ (blue line) and TiO_2/(FA/MA/Cs)$PbI_{3-x}Br_x$ (red line) films, compared to individual $(CH_3)_3SPbI_3$ (black line) compound, including the Gaussian deconvolution of the corresponding peaks (dot lines) (d).

Apart from that, the PL spectrum of the 3D/1D sample presents a 9 nm blue shift of the peak and a narrowing of the full width at half-maximum (FWHM) from 52 to 47 nm. The blue shift is associated with decrease in the trap density of the (MA/FA/Cs)$PbI_{3-x}Br_x$ film, especially in the surface grain boundaries where traps are located, a fact accompanying the presence of the 1D perovskite.[230,231] On the other side, the narrowing of the FWHM confirms the ability of the $(CH_3)_3SPbI_3$ top layer to reduce non-radiative recombination in the system,[232] while it also indicates a declining interaction between charge carriers

and lattice vibrations (phonons) due to improved film homogeneity and lattice order.[233,234] These results were also confirmed by performing the steady-state PL experiments under two additional laser excitations lines (440 and 650 nm)-**Figure 7-4**.

The steady-state PL data are supported by transient PL experiments. In fact, time-correlated single photon counting (TCSPC) fluorescence spectra were acquired in order to further elucidate the hole-pair recombination processes within the photoexcited perovskite layers. The samples were excited with a 482nm NanoLED and the fluorescence intensity was probed at 750nm, which corresponds to the band-to-band radiative recombination.

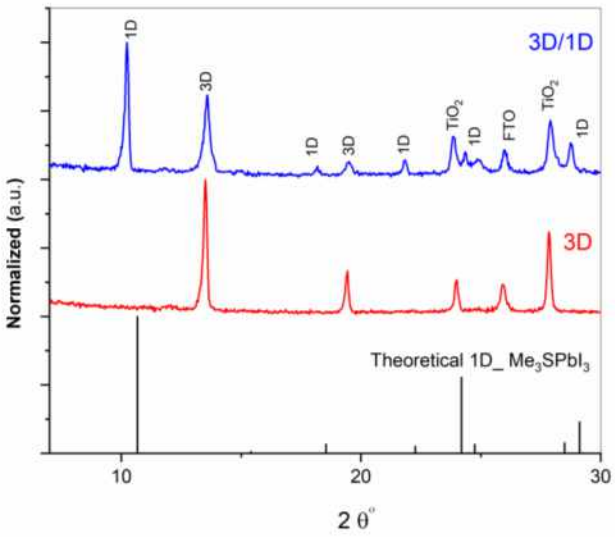

Figure 7-3: XRPD of TiO_2/(FA/MA/Cs) $PbI_{3-x}Br_x$/$(CH_3)_3SPbI_3$ (3D/1D) and TiO_2/(FA/MA/Cs) $PbI_{3-x}Br_x$ films (3D). The 1D layer consists of 3mg $(CH_3)_3SCl$/ml isopropanol)

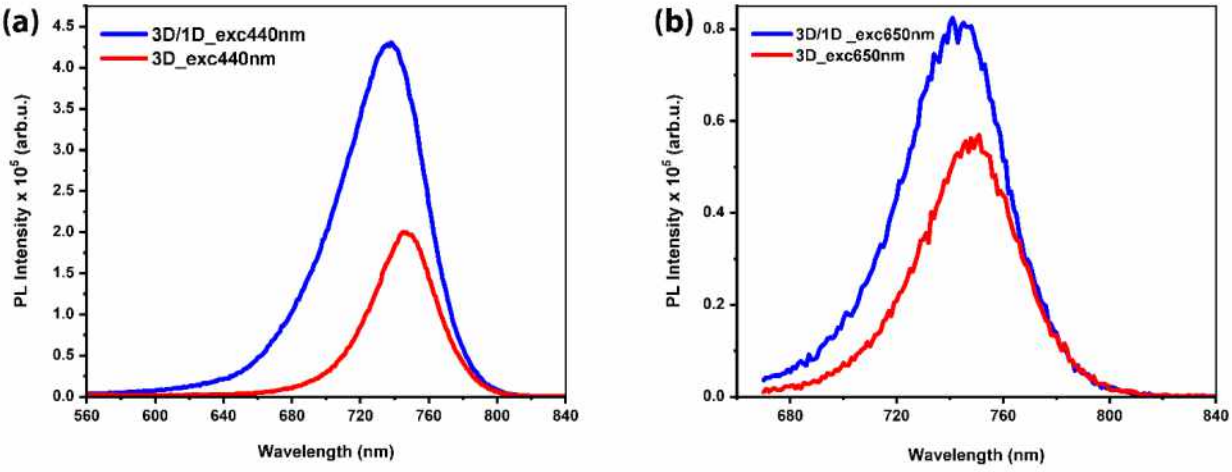

Figure 7-4: Steady-state PL spectra taken using additional laser excitation beams at 440 (a) and 650 nm (b), respectively.

As show in **Figure 7-5**, the 3D/1D samples display a slower decay than the control 3D indicating that slower recombination dynamics taking place.

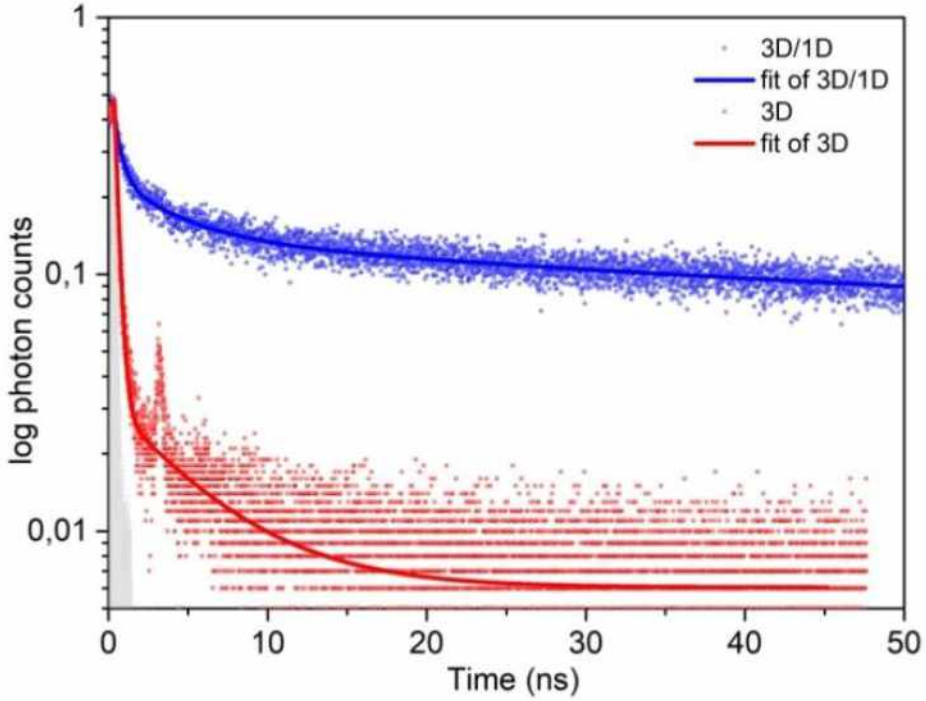

Figure 7-5: Time-correlated single photon counting (TCSPC) fluorescence spectra at room temperature upon excitation at 482nm. Dots indicate the fluorescence lifetime decay curves and solid lines the corresponding fittings: 3D sample (blue dots, blue solid line) and 3D/1D sample (red dots, red solid line). The fluorescence intensity was probed at 750nm.

Actually, the decay curve of the (MA/FA/Cs)$PbI_{3-x}Br_x$ perovskite was best fitted by three decay components, namely a short-time decay component of 544ps with a relative population of 10.45%, a medium-time decay component of 5.32 ns (46.02%) and a long-time component of 24ns (43.52%). We assume that the long-lived component arises from the band-to-band recombination while the two other from trap states (i.e. structural and chemical defects) enabling the faster deactivation of the excited states. Concering the decay curve of 3D/1D it was best fitted with three decay components. In this case a dominant long-lived population was observed. More specific the long-lived component has a lifetime of 54ns (78%) accompanied by two faster populations of 1.2ns (6.88%) and 700ps (15.09%). The increased fluorescence lifetime recorded for 3D/1D represents the suppression of trape state-induced recombination towards a more pronounced trap state-free behavior.[235]In addition, diffuse reflectance spectra were recorded and transformed in Kubelka-Munk units (**Figure 7-2d**). By extrapolating the reflectance curves,

the band gap energies have been estimated at 1.63 eV for both bilayer and reference films, indicating that the optical bandgap of the 3D perovskite is not altered by the presence of $(CH_3)_3SPbI_3$. Furthermore, the normalized Gaussian fitting (dot lines) has been calculated for the reflectance spectra of bilayer, reference and $(CH_3)_3SPbI_3$ compound. It is clear that the extra peaks of the bilayer at around 3.0 and 3.5 eV are due to the formation of the $(CH_3)_3SPbI_3$ layer on top of the triple cation perovskite absorber.

In order to focus on the effect of the $(CH_3)_3SPbI_3$ on the active layer morphology, scanning electron microscopy (SEM) was used to characterize the perovskite films with and without treatment. **Figure 7-6** clearly indicates that in the case of modified films, the 3D $MAFAPbI_{3-x}Br_x$

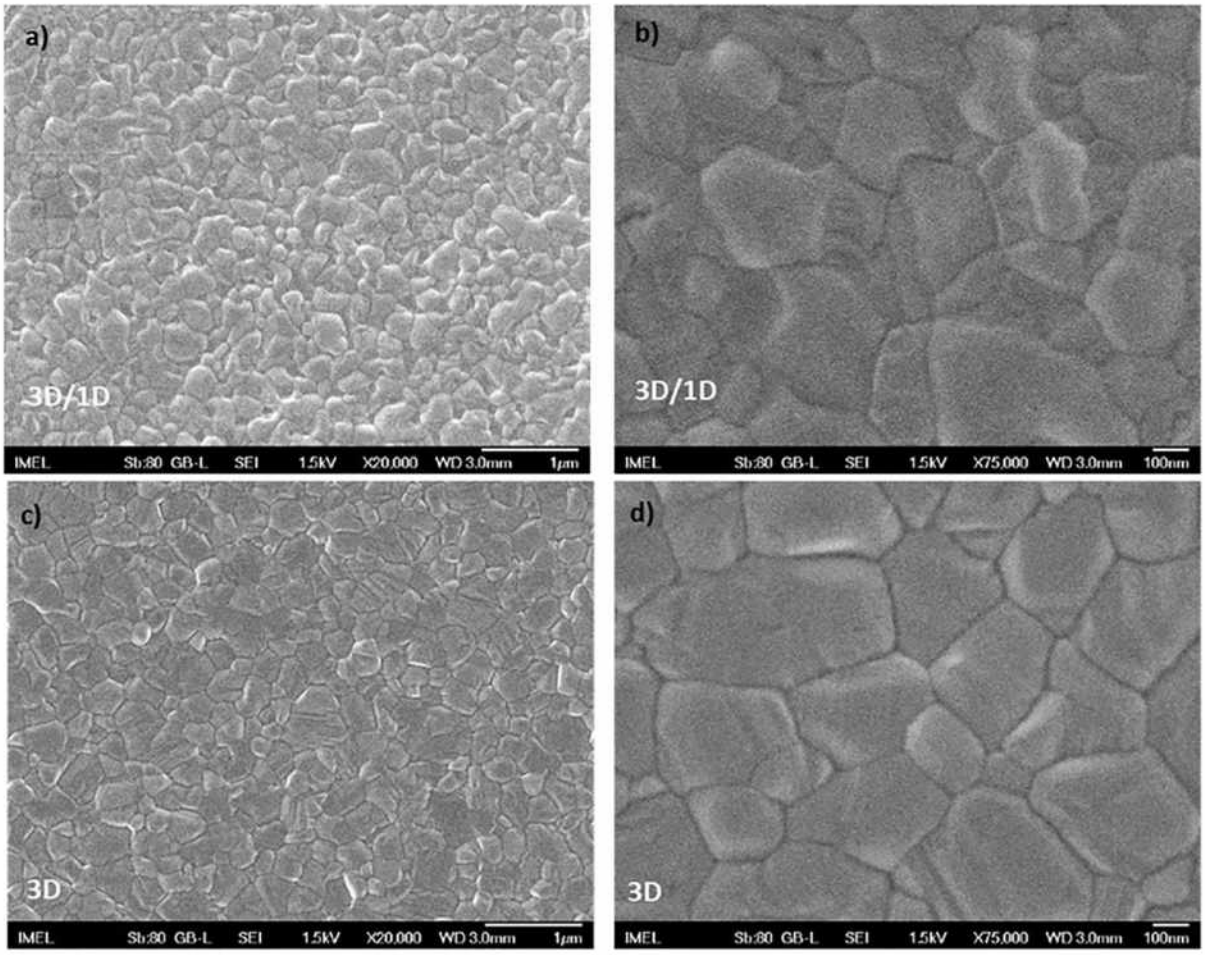

Figure 7-6: SEM images of the 3D/1D bilayer (a,b) and the 3D perovskite (c,d) films on FTO/TiO_2 substrates (different magnification scales).

layer has been covered by the 1D $(CH_3)_3SPbI_3$ perovskite and that the latter is mainly deposited at the valleys of grain boundaries, thus producing an additional local protective

layer which further improves homogeneity (**Figure 7-7**), makes the surface smoother by decreasing height differences and subsequently creates a more stable perovskite morphology. The addition of the 1D capping layer is not expected to affect the grain size of the 3D absorber. However, it is clear that additional features of lower size appear, especially near the grain boundaries. The surface topology of the samples was examined via atomic force microscopy (AFM) analysis (**Figure 7-8**), which confirmed a significant decrease in the surface roughness of the 3D perovskite layer (RMS = 21.24 nm) compared to the 3D/1D bilayer (RMS = 14.70nm).

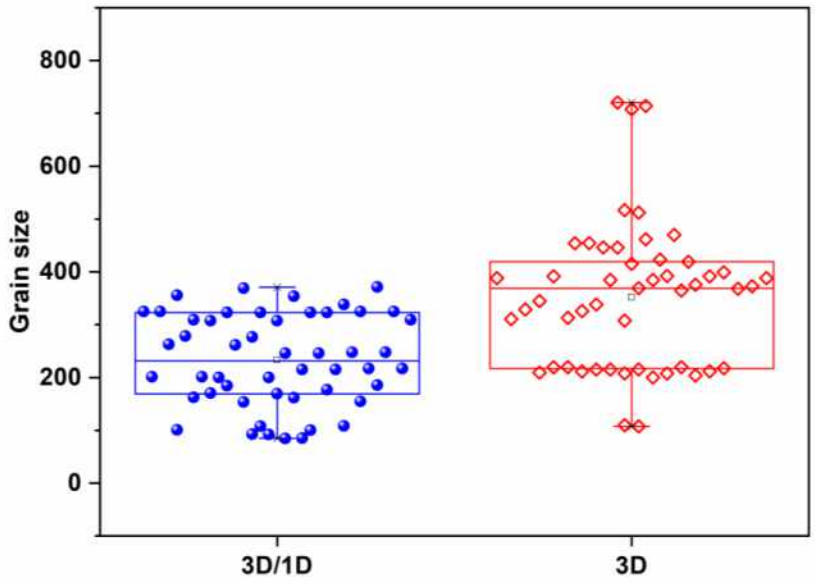

Figure 7-7: Grain size distribution of TiO_2/(FA/MA/Cs)$PbI_{3-x}Br_x$/$(CH_3)_3SPbI_3$ (3D/1D) and TiO_2/(FA/MA/Cs)$PbI_{3-x}Br_x$ films (3D).

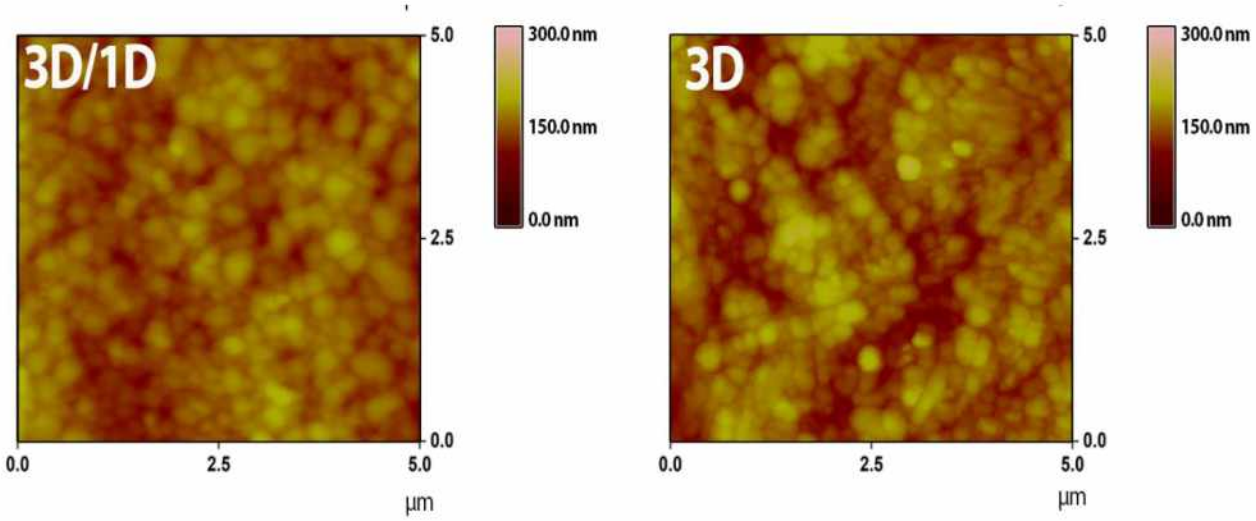

Figure 7-8: AFM top surface topography of the 3D/1D bilayer (left) and the 3D perovskite layer (right).

Moreover, **Figure 7-9** shows top surface topography with depth histograms and colored scales for both 3D/1D bilayer and 3D perovskite films, which indicate a narrower distribution with a significant decrease of the maximum height of surface features for the modified bilayer (30-150nm with max:73.5 nm for 3D control film to 30-120nm with max: 63.3nm for 3D/1D bilayer).

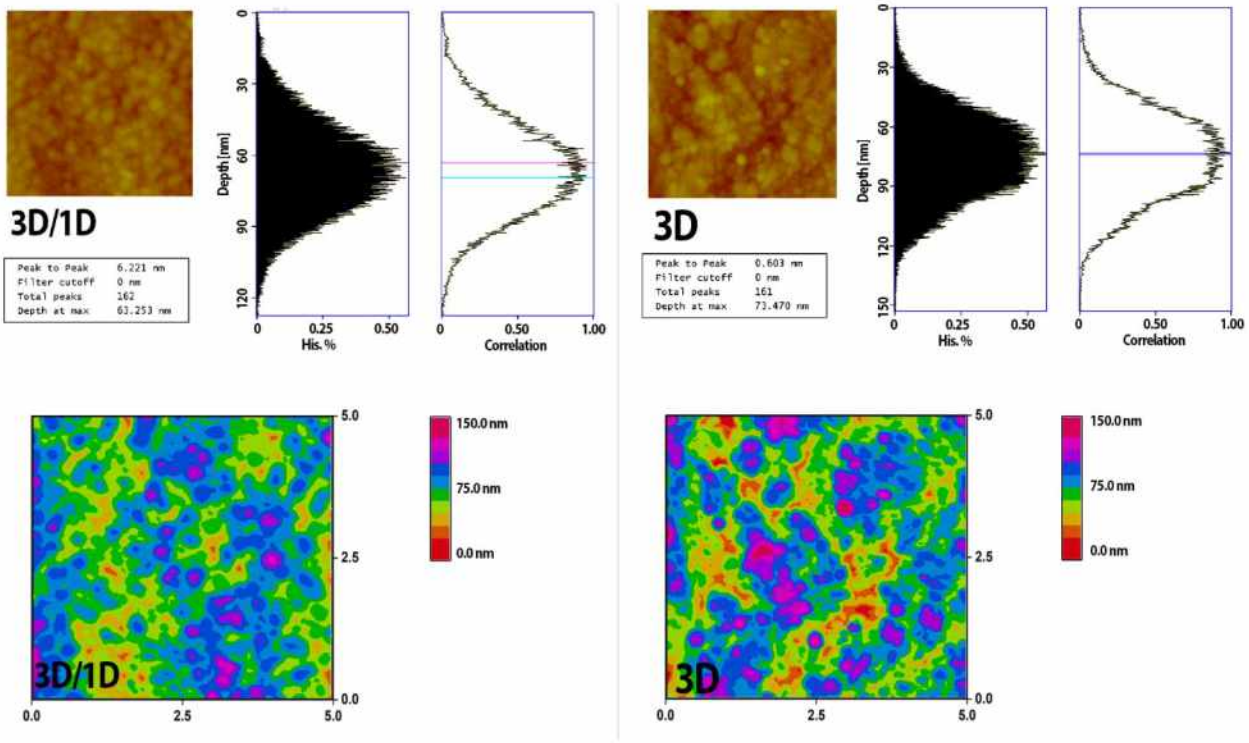

Figure 7-9: AFM top surface topography with depth histogram of the 3D/1D bilayer (top-left) and the 3D perovskite layer (top-right); AFM Surface topography colored scale for both 3D/1D bilayer (down-left) and the 3D perovskite layer (down-right).

The hydrophobic $(CH_3)_3SPbI_3$ interlayer is expected to offer additional protection against humidity for the 3D perovskite absorber during the device operation, where very hygroscopic Li-salts are added as Spiro-MeOTAD dopants to enhance its electric conductivity. It is worth mentioning that a similar phenomenon has been observed on perovskite surfaces passivated using phenethyl ammonium iodide.[236] In order to further examine the effect of the 1D $(CH_3)_3SPbI_3$ perovskite in the wettability of the 3D perovskite film, we performed contact angle measurements with water droplets (**Figure 7-10**).

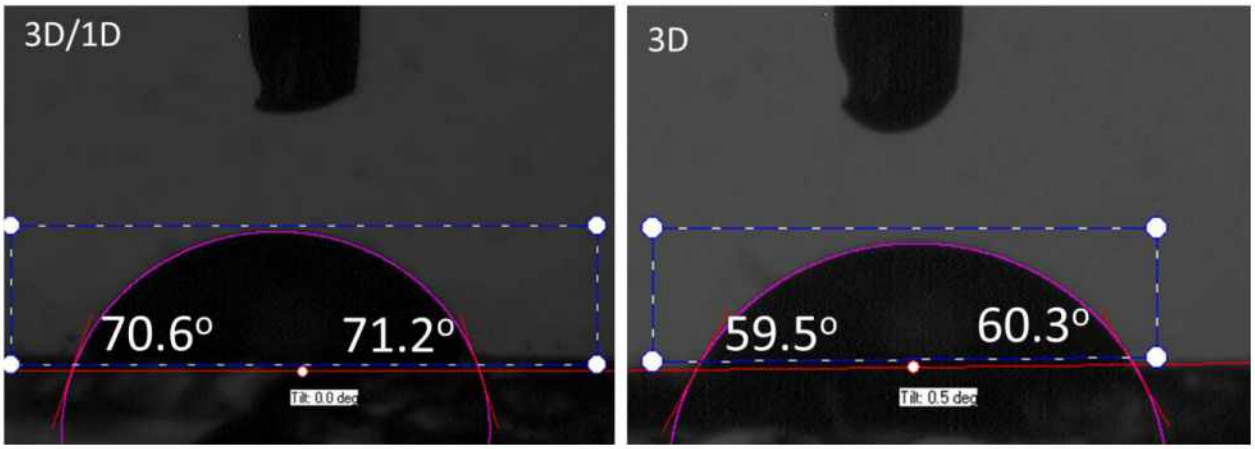

Figure 7-10: Contact angle measurements of 3D/1D modified film upon meso-TiO_2 surfaces and the 3D film without modification.

The contact angle θ of the 3D/1D bilayer (mean value θ=70.9°) indicated enhanced hydrophobicity for the absorber layer compared to the 3D reference film (mean value θ=59.9°). The lower surface wetting of the 3D/1D layer is associated with possible improved self-shield stability for the corresponding PV device. Moreover, based on the contact angle measurements the surface free energy values were calculated using Neumann's equation (Eq. 7.1):

$$\cos(\theta) = -1 + 2(\gamma_S/\gamma_L)^{0.5} \cdot \exp(-\beta(\gamma_L-\gamma_S)^2 \qquad (Eq.\ 7.1)$$

(Surface tension of water γ_{LV} = 72.0 mJ/m² and the Neumann's constant β = 0.000115 m²/mJ).[237] The obtained results refer to surface free energy of 40.09 mJ/m² for the 3D/1D perovskite film, a value lower than the one got for the 3D perovskite film (46.91 mJ/m²).

Figure 7-11 shows the ultraviolet photoelectron spectroscopy (UPS) measurements performed over samples with the following structures: FTO/TiO_2/(FA/MA/Cs)PbI_xBr_{3-x} (3D) and FTO/TiO_2/(FA/MA/Cs)PbI_xBr_{3-x}/Me_3SPbI_3 (3D/1D). **Figure 7-11a** shows the High Binding Energy cutoff region where the work function can be calculated from the equation $W_F = h\nu - E_{cutoff}$. E_{cutoff} is the secondary electron cutoff value and hν is the photon energy of the HeI irradiation (21.22eV).

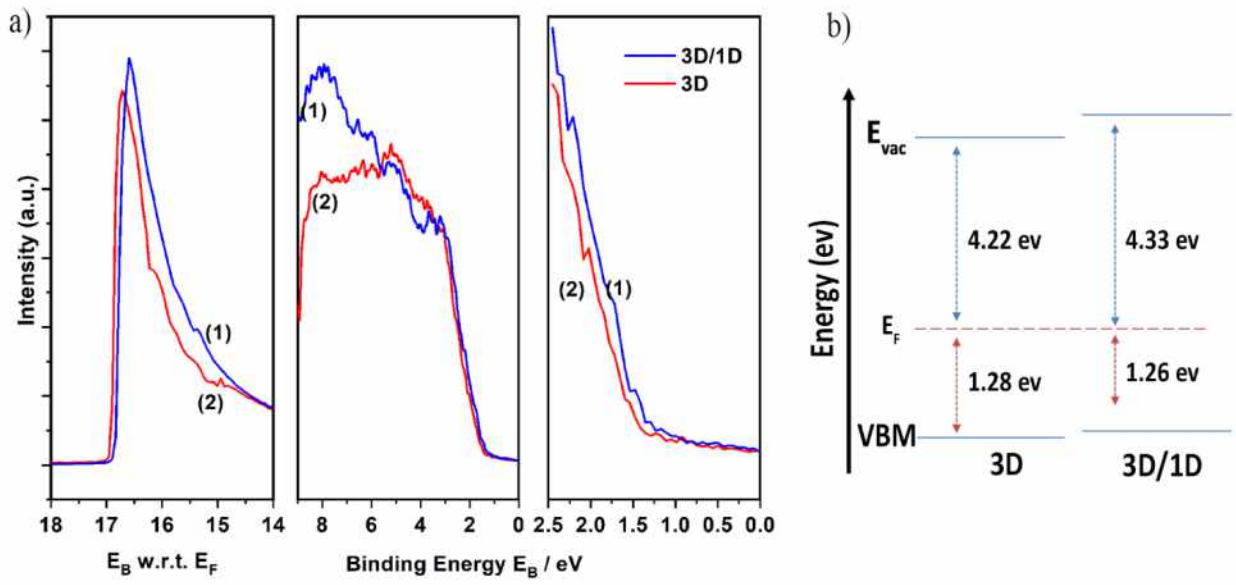

Figure 7-11: Ultraviolet photoemission spectra (UPS): (a) Secondary electron cutoff (left), valence band region (center) and close-up of valence band region (right) of ITO / TiO_2 / (FA/MA/Cs) $PbIxBr_{3-x}$ / Me_3SPbI_3 (1) and ITO /TiO_2 / (FA/MA/Cs) $PbIxBr_{3-x}$ (2). The work function and VBM were determined with a linear extrapolation of the secondary electron cutoff and the leading edge of the valence band, respectively; (b) Energy levels diagram of the corresponding 3D/1D and 3D samples.

The valence band maximum (VBM) cut off values (the distance between E_v and E_F; **Figure 7-11b**) can be determined by linear extrapolation of the leading edge to the baseline. The Ionization potential (IP) (energy difference between VBM cut off and Vacuum level) derives by the sum of W_F and VBM cut off. As seen from the UPS data (**Figure 7-11, Figure 7-12 and Table 7-1**), the VBM of the 1D/3D perovskite heterostructure upshifts by 0.02eV as compared to the 3D one. This shift, along with the increase of the work function by 0.11 eV recommends an upward band bending of the energy levels. Moreover, the blue shift as derives from the PL measurement indicates a bandgap widening of the 3D perovskite due to the 1D perovskite modification, which in comparison with the upward band bending are expected to affect energy band alignment of the PSCs and consequently the value of V_{oc}. The photovoltaic performance of the modified perovskites incorporated in PSCs was evaluated under 1 sun illumination conditions (A.M. 1.5G).

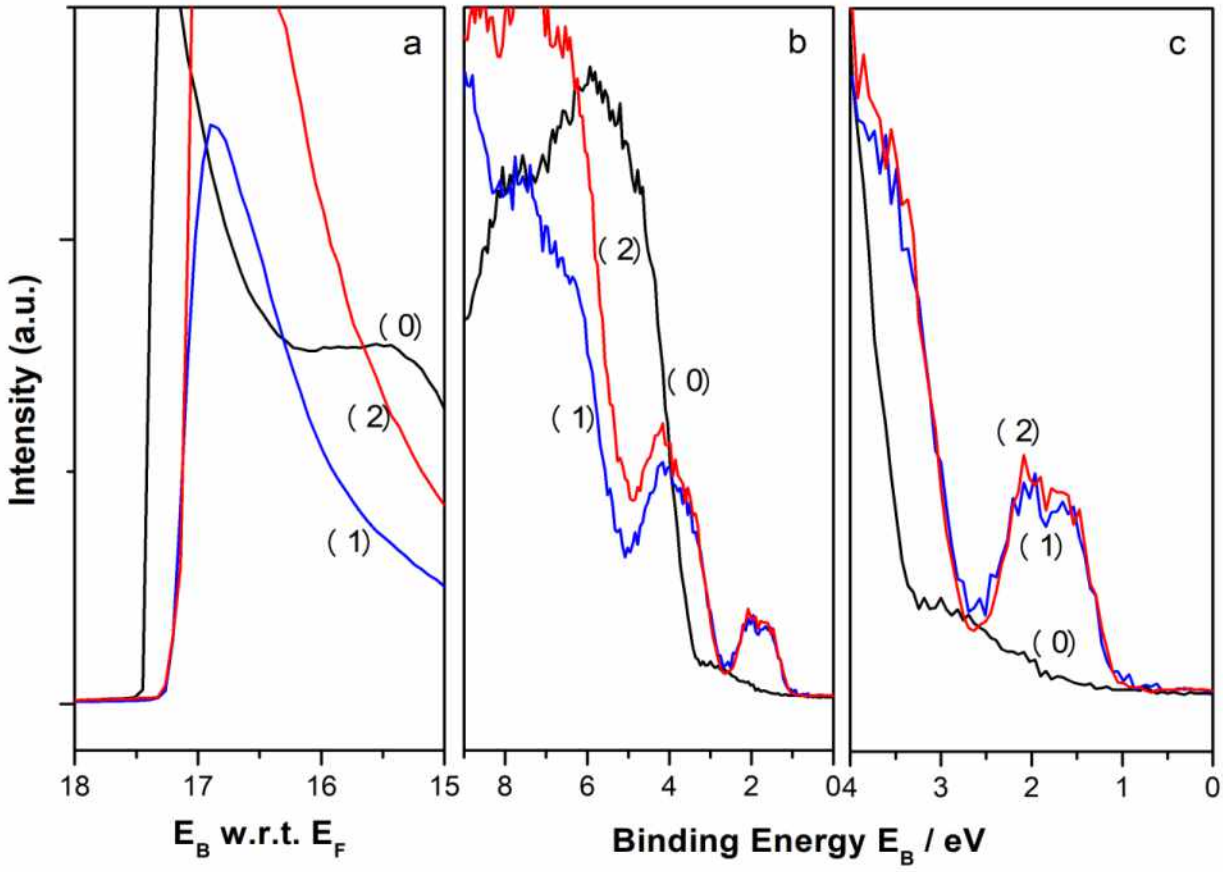

Figure 7-12: Ultraviolet photoemission spectra (UPS): Secondary electron cutoff (left), valence band region (centre) and close-up of valence band region (right) of ITO/TiO_2 (0), ITO/TiO_2/(MA/FA/Cs)PbI_xBr_{3x}/Me_3SPbI_3/Spiro-MeOTAD (1) and ITO/TiO_2/(MA/FA/Cs)PbI_xBr_{3x}/Spiro-MeOTAD (2). The work function and VBM were determined with a linear extrapolation of the secondary electron cutoff and the leading edge of the valence band, respectively.

Table 7-1: Work function, valence band maximum and ionization potential values resulting from UPS data.

Sample	WF (±0.1) eV	VBM cut off (±0.1)	Ionization Potential or HOMO (±0.1) eV
ITO/TiO_2	3.76	3.2	6.96
ITO/TiO_2/(MA/FA/Cs)PbI_xBr_{3-x}	4.22	1.28	5.5
ITO/TiO_2/ (MA/FA/Cs)PbI_xBr_{3-x} /Spiro-MeOTAD	4	1	5
ITO/TiO_2/ (MA/FA/Cs)PbI_xBr_{3-x} /Me_3SPbI_3	4.33	1.26	5.59
ITO/TiO_2/ (MA/FA/Cs)PbI_xBr_{3-x} /Me_3SPbI_3/Spiro-MeOTAD	4	1	5

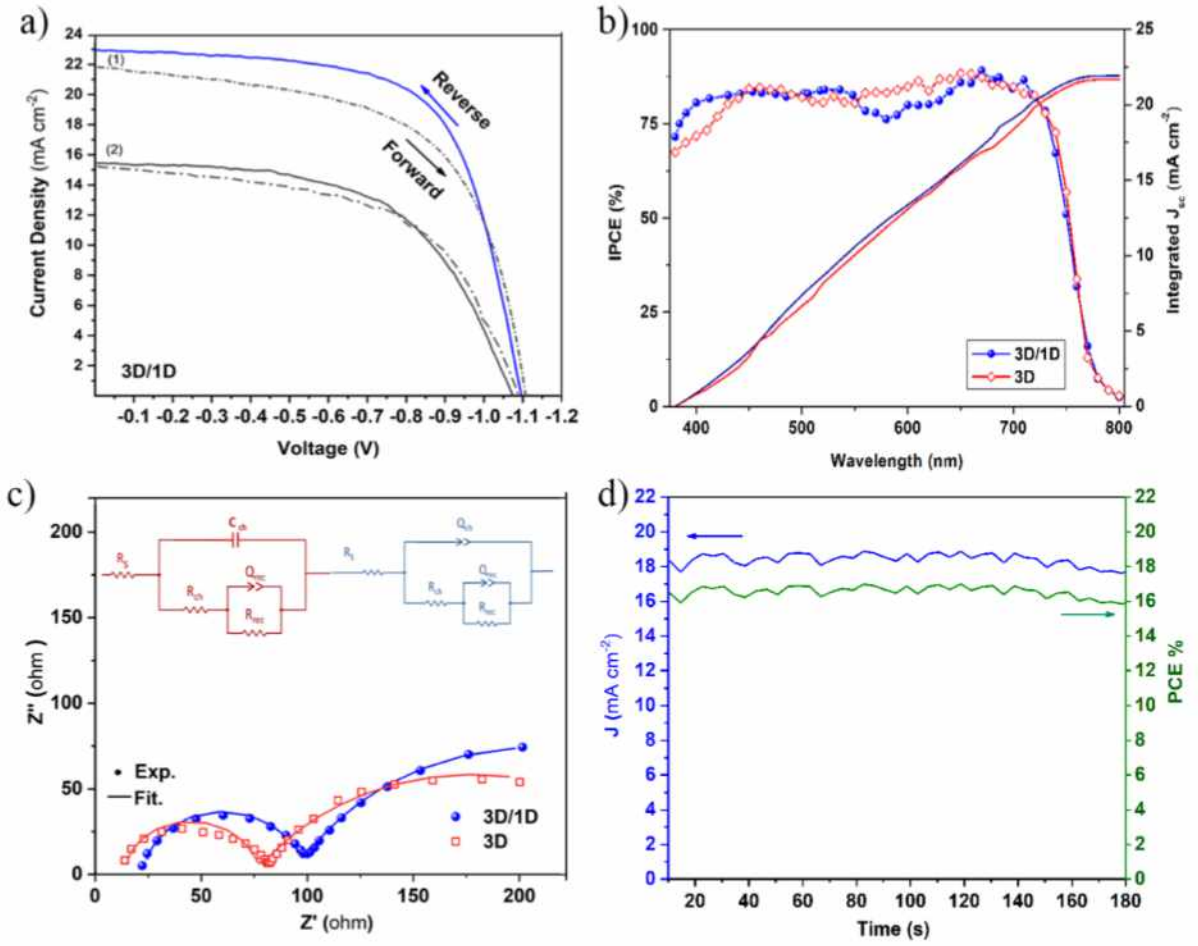

Figure 7-13: J-V curves (forward and reverse scans) of the best performing cells based on the 3D/1D bilayer as prepared (1) and after (2) one month under storage in dark and ambient conditions (a); The IPCE spectra and integration currents of the PSCs (b); The corresponding Nyquist plots with the equivalent electrical circuits (inset) after simulation of the EIS data (c); and the steady-state current density and power conversion efficiency outputs under 1 sun illumination for the 3D/1D solar cell (d).

Figure 7-13a show the J-V characteristics of the best performing modified cells, while the determined parameters (J_{sc}, V_{oc}, FF and PCE) are summarized in **Table 7-2**. The corresponding data for solar cells based on the (FA/MA/Cs)$PbI_{3-x}Br_x$ perovskite are also presented in **Figure 7-14,** and the parameters are given in **Table 7-2**. The short circuit photocurrent density (J_{sc}) of the solar cells based on the (FA/MA/Cs)$PbI_{3-x}Br_x$/$(CH_3)_3SPbI_3$ bilayer got an average (between reverse and forward scans) value of 22.52 mA·cm^{-2}, very close to that of the reference ones, based on the (FA/MA/Cs)$PbI_{3-x}Br_x$ perovskite (23.09 mA·cm^{-2}). Moreover, similar open-circuit voltage (V_{oc}) values were observed for both bilayer and reference solar cells (about 1.10 V), a fact that can be attributed to the key role of the 3D (FA/MA/Cs)$PbI_{3-x}Br_x$ absorber. Finally, this is also the case of the fill factor (FF),

where the difference is due to a slight decrease during the forward scan. Thus, power conversion efficiencies (PCE) of 15.65% and 16.97% (average values) were determined for the bilayer and reference solar cells, respectively. The small difference is in good agreement with the observed absorbance decrease in the case of the composite bilayer. However, it is important to notice that for modified cells we also obtained much better performances, with cells reaching PCE values as high as 19% (data not shown) however, these cells were not characterized by relatively poor stability.

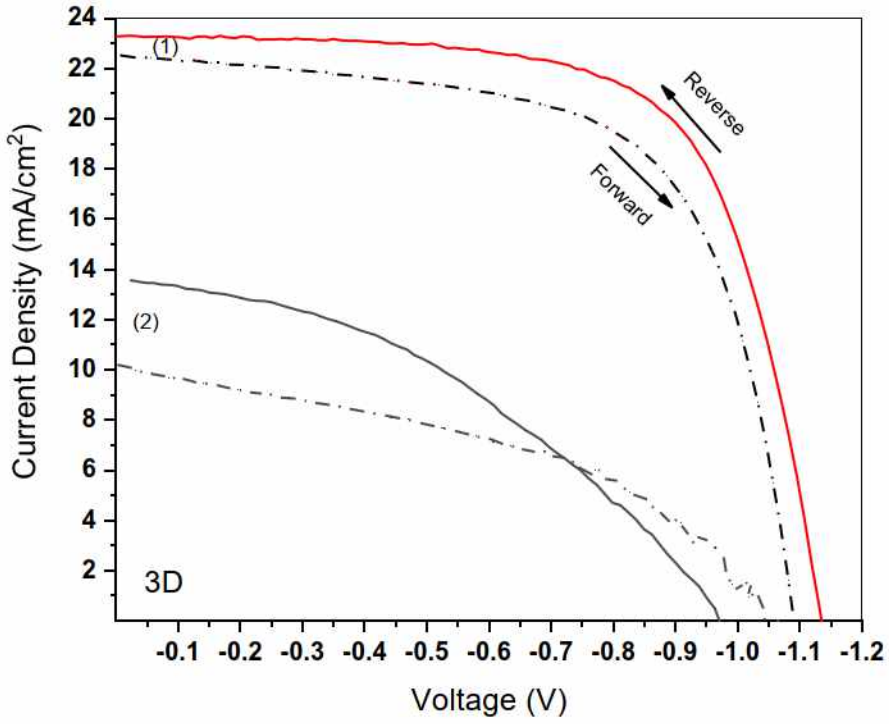

Figure 7-14: J-V curves (forward and reverse scans) of the best performing solar cells based on the 3D perovskite, as prepared (1) and after one month (2) under storage in dark and ambient conditions.

Figure 7-13a confirms that the best performing PSCs retain good performance upon 1D modification of the perovskite absorber. It is well established that perovskite solar cells (especially using a spin coated TiO_2 compact layer in planar architectures) usually suffer from hysteresis effect, due to various reasons such as charge carrier traps resulting from a large defect density within or near the surface of the material; dipole ordering resulting from ferroelectric properties and polarization of the material; ion migration due to excess ions that serve as interstitial defects; imbalanced charge injection capacitive.[238–240]

Table 7-2: Photovoltaic parameters for stable solar cells (fresh and after storage in ambient and dark conditions for 1 month) based on the (FA/MA/Cs) $PbI_{3-x}Br_x/(CH_3)_3SPbI_3$ 3D/1D bilayer and (FA/MA/Cs) PbI3-xBrx 3D perovskite. Voc: open-circuit voltage; Jsc: short-circuit current density; FF: fill factor; PCE: power conversion efficiency; SPCE: Stabilized PCE; HI: Hysteric Index; HF: Hysteresis factor.

Cells	Time	Scan Direction	J_{sc} (mA cm^{-2})	V_{oc} (V)	FF	PCE (%)	SPCE (%)	HI	HF
3D/1D	(Fresh cells)	Reverse	23.09	1.10	0.66	16.67			
		Forward	21.94	1.11	0.60	14.63	15.95	0.09	0.122
		Average	22.52	1.10	0.63	15.65			
	(After 1 month)	Reverse	15.55	1.07	0.57	9.58			
		Forward	15.30	1.09	0.57	9.41	9.45	0.05	0.018
		Average	15.43	1.08	0.57	9.50			
3D	(Fresh cells)	Reverse	23.52	1.13	0.67	17.97			
		Forward	22.65	1.09	0.65	15.97	17.85	0.07	0.111
		Average	23.09	1.12	0.66	16.97			
	(After 1 month)	Reverse	13.70	0.99	0.39	5.32			
		Forward	10.20	1.07	0.43	4.71	5.12	0.27	0.115
		Average	11.95	1.03	0.41	5.02			

Our devices also present hysteresis, however, the phenomenon is less pronounced for the mesoporous PSCs based on the 3D/1D bilayer (**Figure 7-13a** and **Figure 7-14**). Indeed, hysteric indexes (HI) were calculated for the J-V curves using the following equation (Eq. 7.2):

$$HI = \frac{J_{R(V_{OC}/2)} - J_{F(V_{OC}/2)}}{J_{R(V_{OC}/2)}} \quad (Eq.\ 7.2)$$

where $J_{R(V_{oc}/2)}$ is the photocurrent at $V_{oc}/2$ $bias$ for the reverse scan, while $J_{F(V_{oc}/2)}$ is the corresponding photocurrent for forward scan.[241,242] The obtained data, also reported in **Table 7-2** did not reveal any change in hysteresis (hysteric index of 0.09 in the case of the cells based on the bilayer against 0.07 for reference cells). After a month however, while the modified cells remain unaffected (HI = 0.05), the reference cells show a significant deterioration (increase of HI at 0.27), thus confirming the beneficial role of the 1D additive on top of the 3D perovskite for impeding charge migration and stabilizing the interface between the absorber and the hole transporting material. Moreover, the I-V hysteresis factor (HF) [243,244] defined as (Eq. 7.3):

$$HF = (PCE_{Reverse} - PCE_{Forward}) / PCE_{Reverse} \quad (Eq.\ 7.3)$$

was also calculated and the obtained values (incorporated in **Table 7-2**) confirmed that the modified cells outperform the reference ones, in excellent agreement with the results based on the hysteric index (HI).

The performance of the devices was further examined with incident photon-to-current efficiency (IPCE) measurements performed in PSCs with and without the 1D perovskite layer. As shown in **Figure 7-13b** the difference in the J_{sc} values obtained with the J-V measurements is reflected also in the IPCE measurements and the corresponding integrated photocurrents of (21.86, and 21.68 mA cm^{-2}) for 3D and 3D/1D bilayer, respectively. The beneficial effect of the $(CH_3)_3SPbI_3$ interface layer on the charge carrier transfer and recombination procedures was further investigated by electrochemical impedance spectroscopy (EIS) measurements, carried out at V_{oc} reverse bias, under 1 sun illumination. **Figure 7-13c** illustrates the Nyquist plots and the equivalent circuits (as an inset) of the perovskite solar cells. As reported elsewhere,[245,246] the appearance of two arcs is attributed to charge transfer (the low frequency semicircle) and charge recombination (the high frequency semicircle) phenomena. The collected data [ohmic series resistance (R_s), charge transfer resistance (R_{ch}) and recombination resistance (R_{rec})] are summarized in **Table 7-3.**

Since the devices except for the presence of the 1D component are identical, any differentiation in the resistance parameters may be attributed to the presence of $(CH_3)_3SPbI_3$ in the perovskite/HTL interface. The recombination resistance (R_{rec}) for the PSCs with the 3D/1D structure is significantly higher than that of the 3D reference solar cells, which

confirms that the additional $(CH_3)_3SPbI_3$ interface layer prevents the excited electrons of $MAFAPbI_{3-x}Br_x$ from recombination with the HTM.

Table 7-3: Ohmic resistance values obtained from EIS analysis for PSCs based on the 3D/1D bilayer, in comparison to devices employing only the 3D perovskite absorber

Solar Cell	R_s (ohm)	R_{ct} (ohm)	R_{rec} (ohm)
3D/1D	23.1	72.8	223.6
3D	14.1	61.7	204.7

In parallel, the R_{ct} and Rs (equal to the value of high-frequency intercept on the real axis) resistances in the modified device are slightly higher, a fact well attributed to the presence of the $(CH_3)_3SPbI_3$ extra layer. In addition, the stabilized output photocurrent density corresponding to the maximum power point (MPP) of the J–V plots and the resulting power conversion efficiency were also determined. The results reported in **Figure 7-13d** confirm exceptional working strength under maximum electrical output for PSCs based on the 3D/1D perovskite bilayer, as both parameters remain practically unchanged under 1sun continuous illumination for a period of 180 s.

In order to check the experimental accuracy, the statistical data for batches of 15 individual devices with and without the 1D superlayer are presented in **Figure 7-15**, The 3D/1D bilayer approach also results to PSCs with enhanced stability. Thus, non-encapsulated solar cells were stored under ambient conditions for one month in the dark and their photovoltaic performance was again evaluated. The analysis of the PV parameters in **Figure 7-13a** and **Figure 7-14** confirms that the 3D/1D devices retained more than 60% of their initial PCE after 720 h, considerably outperforming the reference cells (based only on the 3D perovskite) which kept only 30% of their initial PCE. This superiority is mainly expressed in terms of higher values for both Jsc and FF.

Table 7-4. The obtained results demonstrate that PSCs based on the modified 3D/1D bilayer clearly outperform the reference ones, showing a rather ordinary behavior without high variation in cell parameters and significantly higher performance, expressed in terms of higher mean values and lower dispersion of the cell parameters.

In fact, the average Jsc of the 1D modified solar cells (0.96) is higher than that of the reference devices, while the average Voc and FF values are similar for both types of cells (mean values). And more important, the normalized average power conversion efficiency

(PCE) value (0.97) for PSCs using 3D/1D bilayer outperforms that for devices using only the 3D perovskite (0.87). The above superiority is also reflected in the corresponding standard deviation values (0.03 against 0.07).

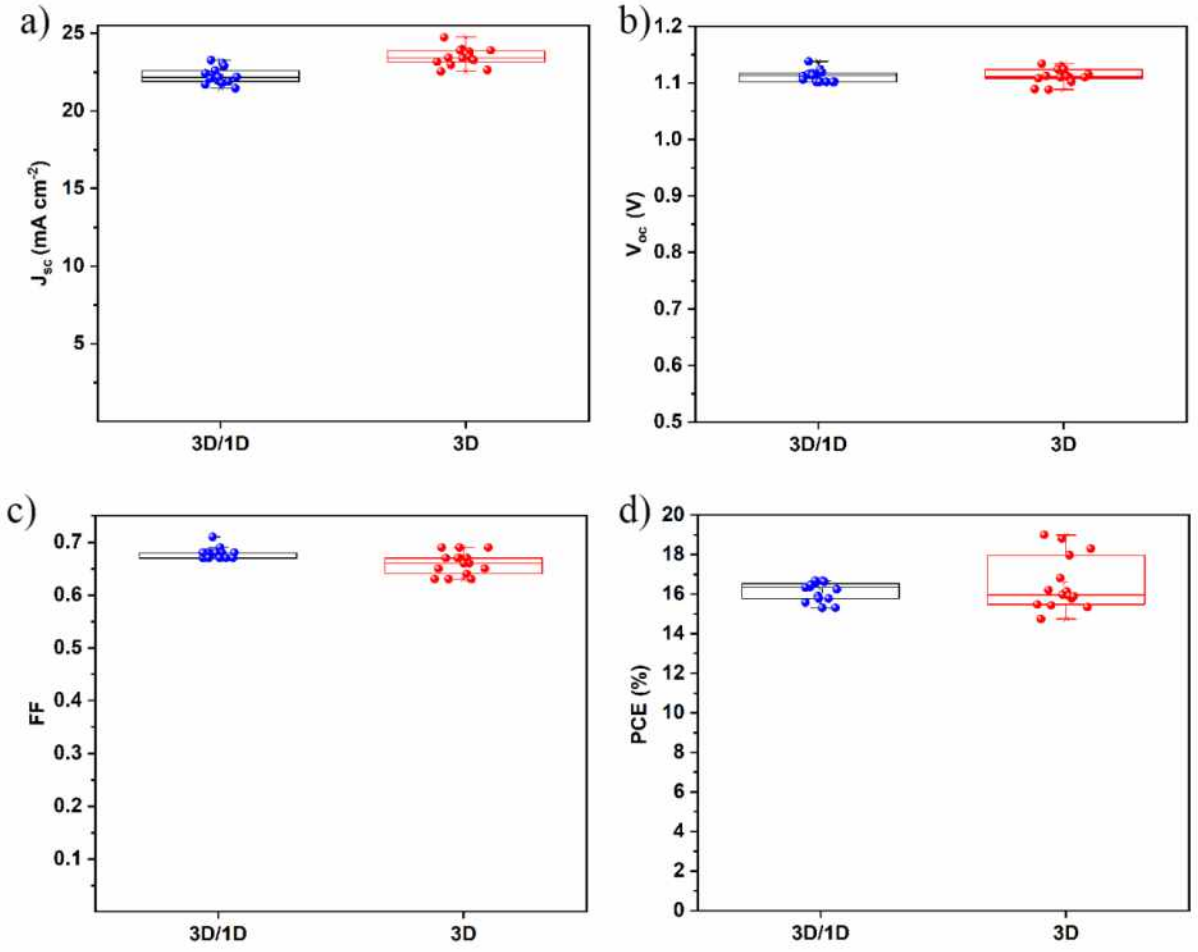

Figure 7-15: Statistical analysis of the photovoltaic parameters concerning two batches of 15 cells based on 3D/1D bilayer and 3D perovskite of PCE (a); J_{sc} (b); V_{oc} (c); FF (d).

The 3D/1D bilayer approach also results to PSCs with enhanced stability. Thus, non-encapsulated solar cells were stored under ambient conditions for one month in the dark and their photovoltaic performance was again evaluated. The analysis of the PV parameters in **Figure 7-13a** and **Figure 7-14** confirms that the 3D/1D devices retained more than 60% of their initial PCE after 720 h, considerably outperforming the reference cells (based only on the 3D perovskite) which kept only 30% of their initial PCE. This superiority is mainly expressed in terms of higher values for both J_{sc} and FF.

Table 7-4: Photovoltaic parameters with respect to the best performing cells for modified (3D/1D bilayers) and 3D PSCs. SD: Standard deviation, SE: Standard error, V_{oc}: open-circuit voltage, J_{sc}: short-circuit current density, FF: fill factor, PCE: power conversion efficiency. Normalized values are also given in parentheses.

		J_{sc} (mA cm^{-2})	V_{oc} (V)	FF	PCE (%)
3D/1D	Average	22.27 (0.96)	1.11 (0.98)	0.68 (0.96)	16.14 (0.97)
	SD	0.52 (0.02)	0.01 (0.01)	0.02 (0.01)	0.49 (0.03)
	SE	0.13 (0.01)	0.003 (0.01)	0.003 (0.01)	0.13 (0.01)
3D	Average	23.48 (0.95)	1.11 (0.98)	0.66 (0.96)	16.85 (0.87)
	SD	0.56 (0.02)	0.01 (0.01)	0.02 (0.03)	1.35 (0.07)
	SE	0.14 (0.01)	0.003 (0.01)	0.006 (0.01)	0.35 (0.02)

The advantage in stability reflects higher solar cell quality that is also corroborated by an unexpected exceptional improvement in hysteresis effect. In fact, hysteresis index (HI) values as low as 0.004 (**Table 7-2**) were determined for devices based on the 3D/1D bilayer after one month, whereas on the contrary for the same period, the corresponding values for reference cells increased by a factor of three.

Moreover, in order to get a more precise estimation on the long-term stability, the five best operating devices were selected from each batch and the mean value of photovoltaic parameters (J_{sc}, V_{oc}, FF and PCE) for both reference and modified cells was determined. The results (normalized data with respect to initial mean values) reported on **Figure 7-16** as a function of the storage time indicates a relatively good long-term stability for PSCs using the $(CH_3)_3SPbI_3$ interface layer. In fact, even after 450 h, the mean V_{oc} value remains constantly unchanged while there is a small decrease in J_{sc}(16%) and FF(9%) values. These correspond to a total decline of 24% in the PCE mean value.

On the contrary for reference devices, more significant losses were observed in average values of J_{sc}(32%), V_{oc}(7%) and FF(27%) parameters, which lead to a marked decrease of 53% in PCE in the same aging period. Such a significant stability improvement for the 3D/1D bilayer-based devices can be attributed to the presence of the chemically stable high band-gap $(CH_3)_3SPbI_3$ layer which can improve the quality of the absorber and pro-

tect both the absorber and the entire solar cell from humidity, without excluding beneficial effects from possible function as ionic migration barrier between $MAFAPbI_{3-x}Br_x$ and Spiro-MeOTAD.[214,247]

Since perovskite materials are highly sensitive to light stress and temperature, we examined the impact of the absorber modification on the device performance under continuous illumination. **Figure 7-17** illustrates the J-V curves obtained on representative PSCs selected from the previous two batches stock of 15 cells, which were stressed for a period of 4 hours, under continuous illumination of 765 $W \cdot m^{-2}$ incident irradiance.

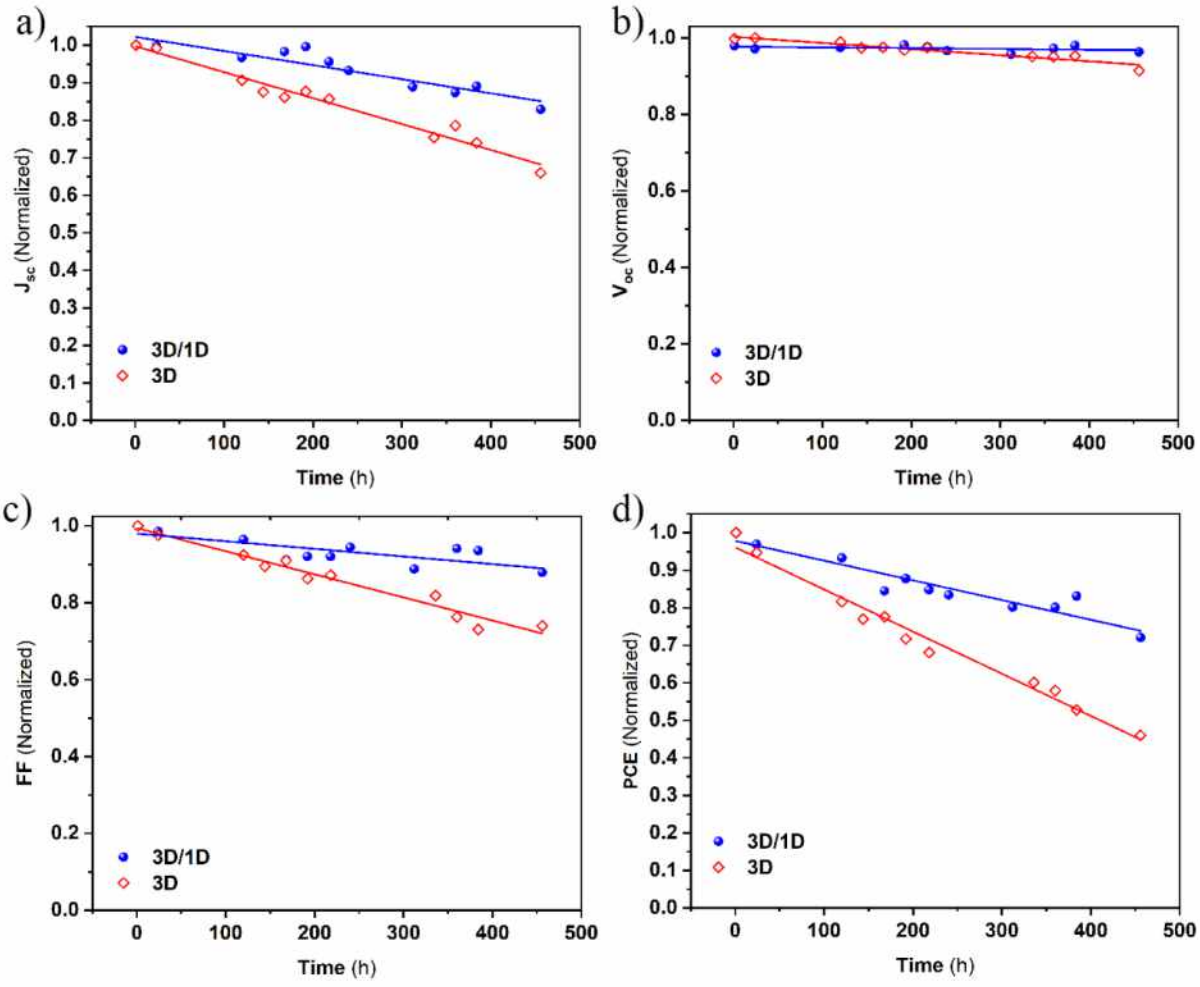

Figure 7-16: Evolution of the normalized photovoltaic parameters: PCE (a); J_{sc} (b); V_{oc} (c); FF (d), over time for PSCs with the 3D/1D bilayer and 3D absorber.

The recorded values of the PV parameters extracted from the analysis of the J-V curves are reported on **Table 7-5** while their relative decline (expressed as the percentage of their initial value) are presented in **Table 7-6**. Thus, high stability was observed for PSCs based on the 3D/1D bilayer. In fact, although they present a decline in power conversion

efficiency, they achieve to preserve at least 72% of their initial performance, following a light stress of 4 hrs.

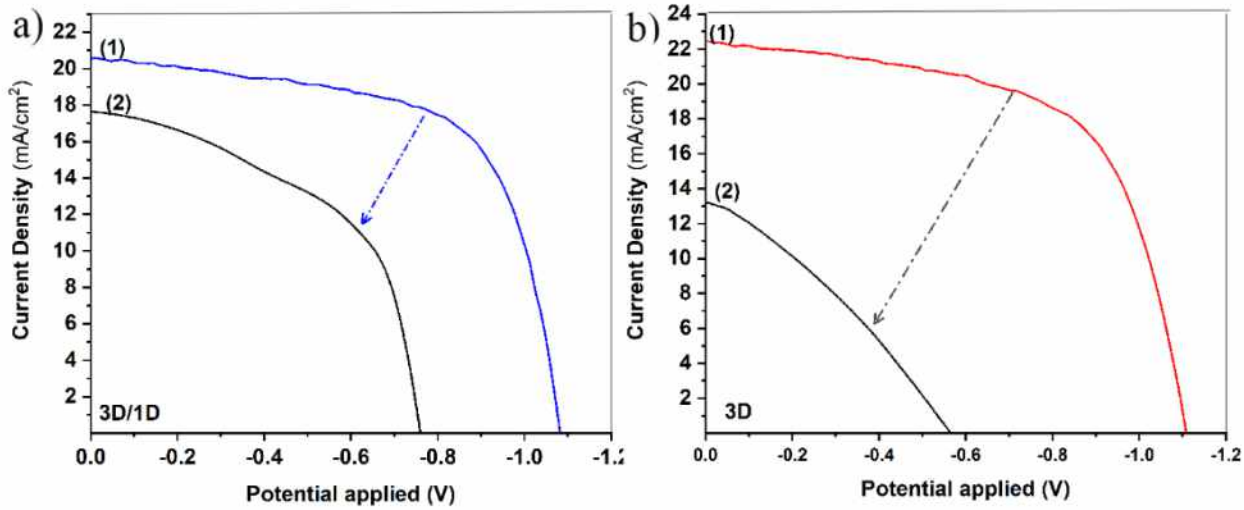

Figure 7-17: J-V curves (reverse scans) before (1) and after (2) light-stress, for PSCs based on 3D/1D bilayer (a) and 3D perovskite (b), respectively.

In contrast, under exactly the same conditions, the reference cells (based on 3D perovskite) show a significant degradation, losing more than 83% of their initial PCE.

Table 7-5: Photovoltaic parameters of reference (3D) and modified solar cells (3D/1D) after 4 h of light stress. V_{oc}: open-circuit voltage, J_{sc}: short-circuit current density, FF: fill factor, PCE: power conversion efficiency

Cells		J_{sc} (mA cm^{-2})	V_{oc} (V)	FF	PCE (%)
3D/1D	Fresh cells	20.74	1.08	0.64	14.33
	After 4h	17.84	0.78	0.53	7.38
3D	Fresh cells	22.54	1.108	0.61	15.34
	After 4h	13.22	0.6	0.27	2.5

Table 7-6: Decline of photovoltaic parameters (expressed as percentage of the initial value) for PSCs after 4 h of light stress

PSCs	J_{sc} (%)	V_{oc} (%)	FF (%)	PCE (%)
3D/1D	13.90	13.98	48.50	27.54
3D	41.35	45.85	55.74	83.70

Recent literature reports have shown that light soaking of hybrid perovskite cells induced much more significant degradation (>80%) in the photovoltaic performances than their exposure to heat in the dark. The observed degradation was attributed to damages of chemical composition and/or structural modification (phase transition).[248] Moreover, it is well established that ion migration and ionic defects lead to device degradation that can be avoided by adding an extra layer between perovskite and HTL. In this context, the formation of a higher bandgap chemically stable 1D $(CH_3)_3SPbI_3$ interlayer between the absorber and the HTL can work as a barrier against ionic migration/charge carrier recombination, leading to improved photovoltaic stability.[225,249–252] It must be mentioned that improved thermal stability (although in dry conditions) has also been observed in the literature by adding small quantities of inorganic cations (like Cs or Rb) to mixed cation $MAFAPbI_{3-x}Br_x$ perovskite, attributed to their non-hygroscopic nature.

CHAPTER (8)

Interface Engineering via a Functional D-π-A Organic dye

Interface Engineering via a Functional D-π-A Organic Layer at the Absorber/Hole Transporter

Perovskites are in the forefront of the research towards the introduction of novel, solution-processed materials in photovoltaic (PV) applications. Within only a few years[28,45,253] solar cells based on perovskite absorbers presented a rapid development, reaching a 25.2% power conversion efficiency (PCE)[9] and creating great expectations for a cheap and versatile energy source, a good alternative to the silicon-based PV technology. Despite high efficiencies, stability challenge remains unsettled[254] thus various strategies have been proposed to enhance the performance of perovskite solar cells (PSCs), including dimensionality optimization,[232,255] interface engineering [145,256–260] and utilization of fully inorganic perovskite absorbers.[261] Moreover, a comprehensive understanding of the physicochemical procedures occurring during perovskite formation and PSCs operation is still lagging. Poor stability of the absorber is an additional issue, often related to the existence of ionic defects,[262,263] such as undercoordinated lead cations,[264]which are present at the grain boundaries,[265] of the perovskite film surface and can act as charge recombination and moisture/oxygen penetration sites. This happens because most of the solution-processed devices are fabricated using polycrystalline perovskite thin films treated at low-temperature conditions. This creates dense defect traps (≈1016 cm^{-3}) at the grain boundaries and the film surface of polycrystalline perovskites, several orders of magnitude higher than single crystals.[266] Therefore, fine-tuning and full control of the crystal growth procedure are necessary, especially for large-scale implementation of highly efficient and robust devices.

In this context, organic molecules with carbonyl or other active groups have drawn the attention for the effective modification of the perovskite absorbers due to their facile processability and appropriate electronic properties. Feng et al.[267]proposed the utilization of an Eu-porphyrin complex creating 2D perovskite platelets within the grain boundaries, while Zhao et al.[268] incorporated a near IR organic molecule to modulate the photo response of the device. Additional approaches include the insertion of organic molecules

with rich carboxyl groups towards efficient passivation,[269,270] or the use of different functional compounds offering multi-passivation effect,[271] while other efforts focused on the synergistic effect of metallated porphyrins[272]and pthalocyanins, [273,274] in the operation of PSCs.

Herein, I introduce a Donor-π-Acceptor (D-π-A)[145] organic compound as an efficient interlayer that successfully passivates the surface trap states of a triple-cation perovskite layer while simultaneously acts as an effective charge carrier transporting interlayer between the perovskite absorber and 2,2',7,7'-Tetrakis[N,N-di(4-methoxyphenyl)amino]-9,9'-spirobifluorene (Spiro-MeOTAD), HTM. In general, donor-π-acceptor compounds dispose intramolecular charge transfer (ICT) properties. Moreover, the passivation effect is supposed to increase with the polarity of the D-π-A molecule. So, a strong electron-donating unit on the donor part would increase the electron density on the acceptor group and make it much more electron-rich.[275] Such dipolar electron density distribution delivers improved conditions for coordination with the under-coordinated Pb^{2+} defects. This is the case of D35 D-π-A compound, bearing a strong electron donating amino center and a cyano group with extremely high electron attracting ability. Thus, a small amount of (E)-3-(5-(4-(bis(2',4'-dibutoxy-[1,1'-biphenyl]-4-yl)amino)phenyl)thiophen-2-yl)-2 cyanoacrylic acid (D35), a triphenylamine (TPA)-based D-π-A molecule, was dissolved in chlorobenzene in different concentrations and was spin coated upon (FA/MA/Cs) $PbI_{3-x}Br_x$ films. The donor, π-spacer, and acceptor parts are triphenylamine, thiophene, and cyanoacrylic acid, respectively. The multi-cation perovskite polycrystal ((FA/MA/Cs) $PbI_{3-x}Br_x$) layers below the D35 interlayer showed high crystallinity and upgraded light absorbance while the corresponding perovskite/hole transporter interface was smoothened. In addition, the energy bands of the employed materials were aligned appropriately towards the facilitation of charge carrier's extraction and transfer. Moreover, the films containing the organic chromophore showed reduced trap density due to the coordination of Pb^{2+} with the carboxylic group of D35. As a result, we obtained devices with improved power conversion efficiency by 22%, in comparison to the reference ones. In addition, the modified devices presented superior stability, preserving 83% of their initial PCE after 37 days of storage in dark and ambient (RH=25%) conditions, owing to the hydrophobic nature of D35.

8.1 Device fabrication

FTO conductive glass electrodes (7 ohms·sq^{-1}) were cleaned in ultrasounds (successively with Hellmanex 2% (v/v) in deionized water, ethanol, isopropanol and acetone for 15 min each step). Finally, the conductive substrates were rinsed with isopropanol and dried using N_2 flow. Then the cleaned glasses were treated with UV-ozone for 15 min. Immediately after cleaning, the TiO_2 compact layer (c-TiO_2) was deposited by using spray pyrolysis of titanium diisopropoxide bis(acetylacetonate) diluted in ethanol on substrates, followed by 1h annealing at 450°C. Afterward, a mesoporous layer of TiO_2 (m-TiO_2) 30 NR-D (150 mg/mL) was spin-coated at 4000 rpm for 20 s, followed by immediate dry at 125°C for 5 minutes, and sintering at 325°C, 375°C, 450°C, for 5min, 5min and 30min respectively. The perovskite film was deposited in an Ar-filled glovebox by spin coating upon the TiO_2 substrates. The perovskite precursor solution was prepared using 1.1 mol/L PbI_2, 0.2 mol/L $PbBr_2$, 1 mol/L FAI and 0.2 mol/L MABr in an 850 µl aliquot of mixed DMSO: DMF (1:4, volume ratio) solvent. 50µl of CsI (1.5 mol/L stock solution) was added to the perovskite solution which was spin-coated at 1000 rpm for 10 s and, continuously at 6000 rpm for 20 s. In addition, 150 µL of anhydrous chlorobenzene (for reference PSC) was poured on the perovskite film 7 s prior to the end of process (anti-solvent treatment). When D35 was used during anti-solvent treatment, it was poured dissolved in anhydrous chlorobenzene (10^{-5} mol/L). When D35 was used as an extra interlayer upon perovskite, 150 µL of D35 diluted in anhydrous chlorobenzene (10^{-3},10^{-4},10^{-5},10^{-6} mol/L) was poured on the film with the same strategy as for the reference films, followed by post-annealing at 100°C for 45 min. After cooling down to room temperature, Spiro-MeOTAD was spin-coated at 4000 rpm for 20 s. The 70 mmol/L Spiro-MeOTAD solution was prepared using anhydrous chlorobenzene. In addition, Li-TFSI in acetonitrile, 4-tert-butylpyridine, and FK209 in acetonitrile were added at a molar ratio of Spiro-MeOTAD:TBP:Li-TFSI:FK209=1:3.3: 0.5:0.03. Finally, the devices were completed with thermal evaporation of 60 nm of Au as counter electrodes.

8.2 Device analysis

At first, various preliminary experiments were performed in perovskite PV devices, using the dye molecule both as an additive during perovskite film's anti-solvent treatment,[276] and as an individual interlayer on top of the perovskite absorber. The results in the form of power conversion efficiencies are presented in **Table 8-1**. The D-π–A compound (D35)

was dissolved in chlorobenzene, while different concentrations were tested before choosing the optimum one, which is 10^{-5}M. Experiments were also performed using formamidiniumm bromide as an extra passivation layer.[277] As deriving, the presence of D35 is beneficial in every case, though the most promising results were obtained when using it as a functional layer on top of the perovskite absorber, without any further modification and with pure chlorobenzene as the anti-solvent material. Details on the exact device fabrication procedure are given in the experimental section. To optimize the deposition conditions of the D35 layer, additional experiments were performed by varying the concentration (six different values between 10^{-6}M and 10^{-3}M) of D35 in chlorobenzene. The results presented in the revised **Figure 8-1,** confirm the successful optimization and directly indicate the impact of the functional D-π-A organic layer on the device performance. Therefore, we obtained the highest efficiency using a D35 solution of 10^{-5} M.

Table 8-1: Power conversion efficiencies from preliminary tests conducted with D35 introduced into PSCs as an interlayer and during anti-solvent treatment.

Cell structure	**Anti-solvent**	**C (mol/L)**	**PCE (%)**
FTO/TiO_2/Perovskite /Spiro-MeOTAD/Ag	Chlorobenzene		15.23
FTO/TiO_2/Perovskite /Spiro-MeOTAD/Ag	D35 in Chlorobenzene	10^{-4}	16.08
		10^{-5}	16.56
		10^{-6}	15.02
FTO/TiO_2/Perovskite/D35 /Spiro-MeOTAD/Ag	Chlorobenzene	10^{-5}	18.57
FTO/TiO_2/Perovskite /FABr/Spiro-MeOTAD/Ag	Chlorobenzene		14.29
FTO/TiO_2/Perovskite/FABr/Spiro-MeOTADAg	D35 in Chlorobenzene	10^{-5}	16.22
FTO/TiO_2/Perovskite/D35 /FABr/Spiro-MeOTAD/Ag	Chlorobenzene	10^{-5}	17.17

* C (concentration)

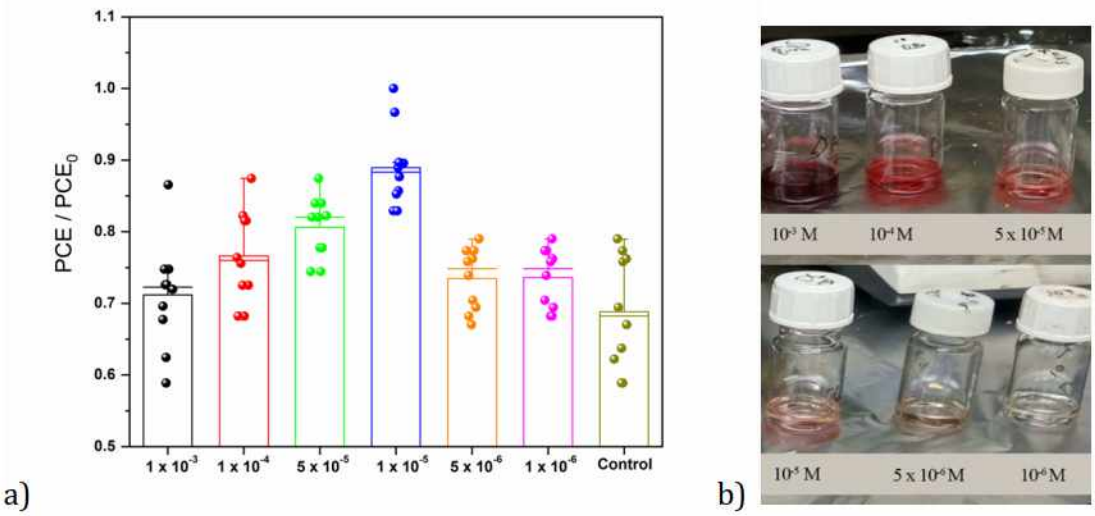

Figure 8-1: Normalized PCEs of cells, as a function of the D35 concentration (a); Picture of vials with D35 solutions (*10^{-6}M to10^{-3}M)* in chlorobenzene (b).

In that case, the roughness analysis gives an estimation of the corresponding thickness of about 5 nm. **Figure 8-2a** presents the absorption spectrum of D35 dissolved in chlorobenzene. D35 shows a broad absorption peak at 445nm,[278] attributed to the HOMO to LUMO transition, while the 323 nm peak corresponds to a HOMO-1 to LUMO transition.[279]

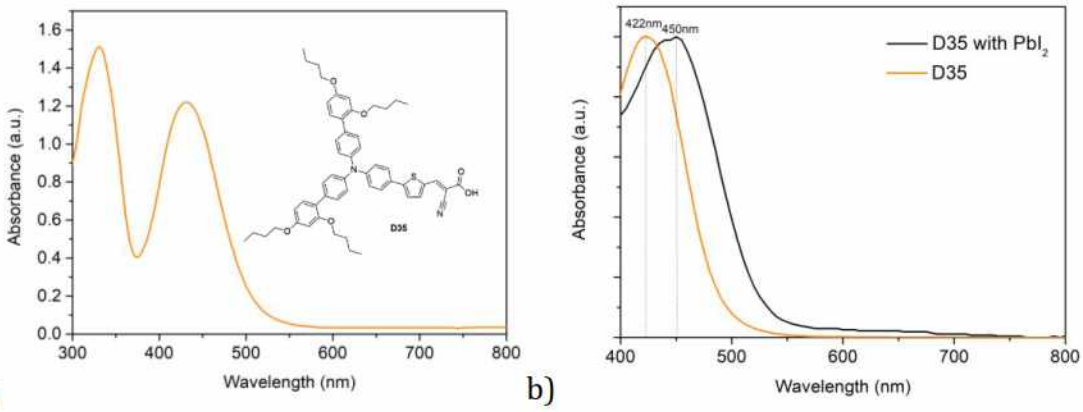

Figure 8-2: a) Absorption spectrum of D35 dissolved in chlorobenzene (10^{-5}M); its molecular structure depicting hydrophobic butoxy chains and cyanocrylic acid functional group (inset). b) HOMO to LUMO transition shift of D35 solutions with and without PbI_2 (molar ratio 1:1, in chlorobenzene)

Moreover, the absorbance of a D35 solution was measured with and without PbI_2. The UV-vis spectrum of the D35-PbI_2 complex (**Figure 8-2b**) presents a clear red shift (from 420nm to 450nm) of the main absorption peak which clearly reveals an interaction between the dye and lead cations. In conclusion, such an effect refers,[264] to the strong coordinated reaction of D35 with Pb^{2+} that affects the C=O bond of cyanoacrylic acid, partially

breaks the π-conjugated system and disturbs the intramolecular charge transfer absorption band of the D-π-A molecule.[280]

It is reported,[264] that the carboxylate group in a D–π–A molecular structure (**Figure 8-3a**) demonstrates high electron density, which favors interaction with the under-coordinated Pb^{2+} cations. To visualize the electron density distribution, electrostatic potential (ESP) analysis was performed, calculated from the density functional theory (DFT) method. As shown in **Figure 8-3b**, the electron scarce area mainly distributes around the electron-donor part, associated with the butyl chains of the triphenylamines.

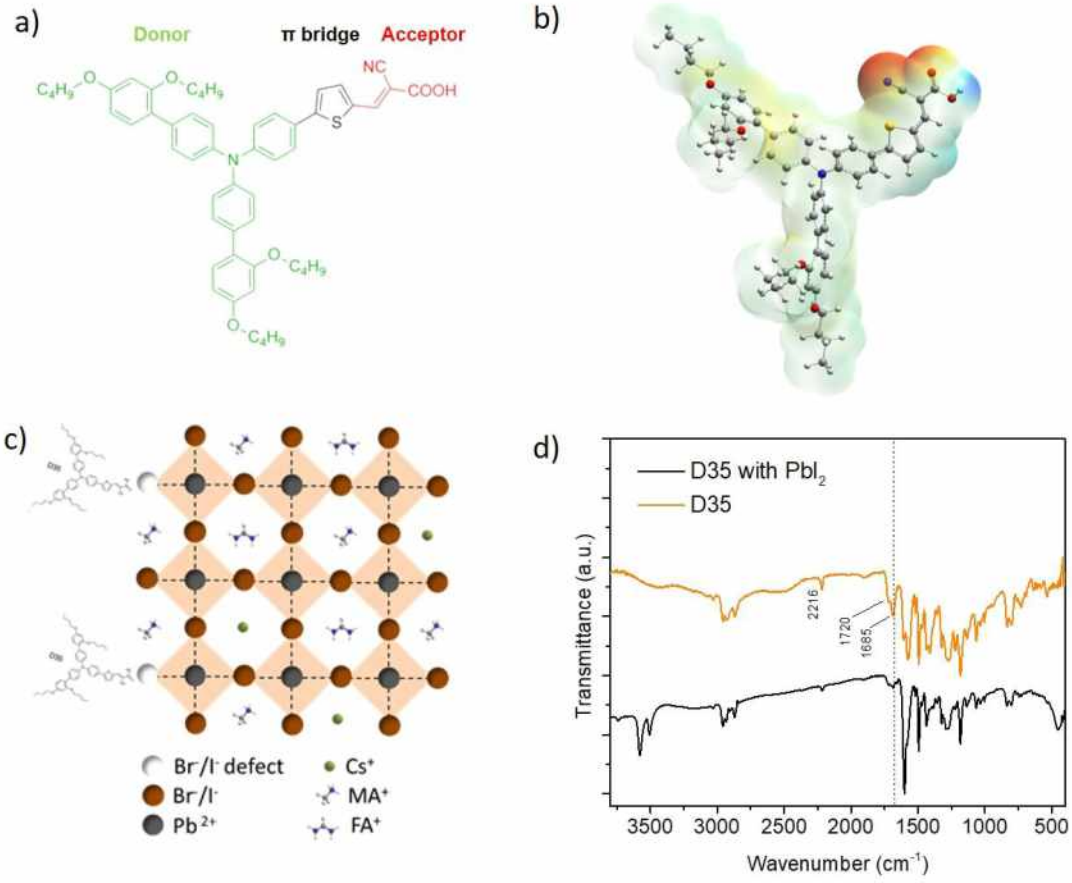

Figure 8-3: Chemical structure of D35 (a); Calculated ESP profiles of D35 (b); Schematic illustration of the passivation process of D35 molecules for the under-coordinated Pb^{2+} cations (c); Fourier-transform infrared spectroscopy (FTIR) measurements in D35 with and without PbI_2 (d).

On the other hand, the electron-rich cyanoacrylic acid group presents a high electron density which favors the coordination with the under-coordinated Pb^{2+} cations, as depicted in **Figure 8-3c**. In order to clarify the interaction of the organic molecule with the Pb^{2+} cations, Fourier-transform infrared spectroscopy (FTIR) measurements were performed

in D35 with and without PbI_2. **Figure 8-3d,** shows a strong quenching of the stretching vibrational mode at 1685 cm^{-1} of C=O in the carboxylic group of D35, which indicates the interaction of lead and dye through the carboxylic group.[267]

In **Figure 8-4a**, the absorbance of perovskite layers with and without D35 on top, grown upon FTO/TiO_2 substrates is presented. From the curves depicted, the presence of the organic compound increases the absorbance of the (FA/MA/Cs) $PbI_{3-x}Br_x$, specifically in the region below 650nm. Since D35 absorbs below 510nm as presented in **Figure 8-2**, we may attribute the increase in absorption partially in the presence of D35 and primarily to the improved perovskite film quality, namely compact and large perovskite grains.

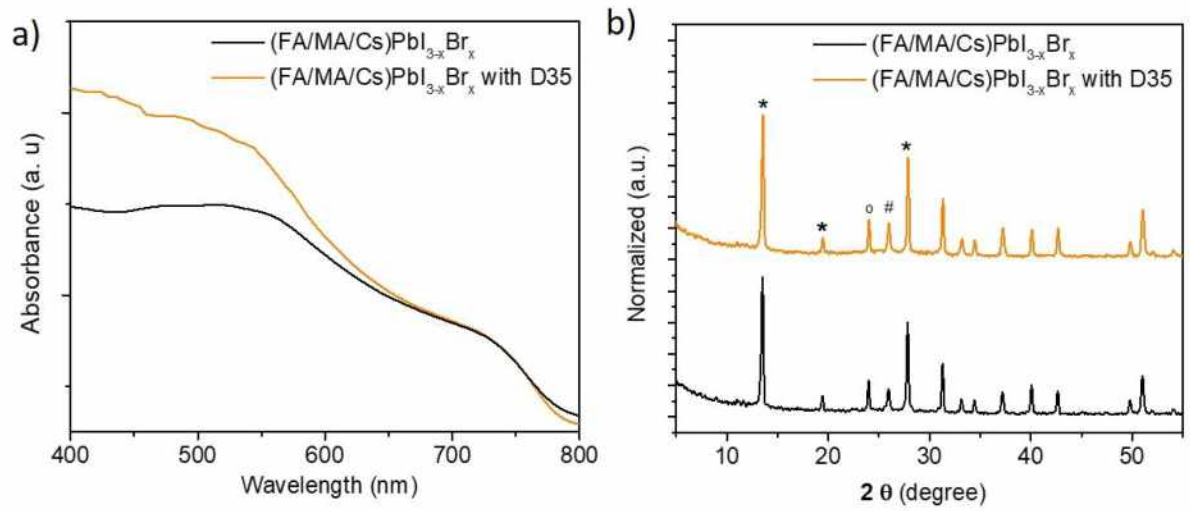

Figure 8-4: UV-vis absorption spectra (a); and XRPD patterns (b), of mixed perovskite films with and without D35 treatment. Symbols "*", "o" and "#" refer to the perovskite, FTO and TiO_2 peaks respectively.

The structural quality of the perovskites was examined and verified by the X-ray powder diffraction XRPD analysis (**Figure 8-4b**), which confirmed the presence of the main reflections from the (FA/MA/Cs) $PbI_{3-x}Br_x$ perovskite (at 2θ =13.5, 19.4, 27.8 °), titania (at 2θ =26 °) and the FTO (at 2θ =24 °) layers.[229,281,282] The trace of the two patterns is similar, however in the presence of D35, stronger perovskite diffraction peaks are grown, a fact associated with perovskite's improved crystallinity. On the other hand, full width half maximum (FWHM) analysis showed no difference (0.24° for the 001 peak for both samples). FWHM is associated with the size of crystallites via Scherrer's equation. However, this is a mean value estimation, thus the size will be precisely estimated by scanning electron microscopy (SEM) analysis. A more careful observation (**Figure 8-5a**) shows that

the peak position presents a slight shift (from 13.50° to 13.55°) upon D35 molecules interaction. This shift can be associated with the relative geometrical position of the sample however, the interaction of D35 with the perovskite lattice cannot be excluded.[283] However, even in the latter case, the permeation into the perovskite crystal induce neither a phase transition nor formed any 2D structures on the surface of the perovskite films.[262] Moreover, **Figure 8-5b** presents the diffuse reflectance spectra transformed in Kubelka-Munk according to the following equation 8.1:[256]

$$F(R) = \frac{(1-R)^2}{2r} \qquad (Eq\ 8.1)$$

where R is the reflectance and hv is the photon energy. $[F(R) \times hv]^2$ was plotted as a function of energy (eV). By extrapolating the curves, the band gap energies have been estimated at 1.62 eV for both D35-containing and reference samples, indicating that the optical bandgap of the mixed perovskite is not altered in the presence of the organic compound.

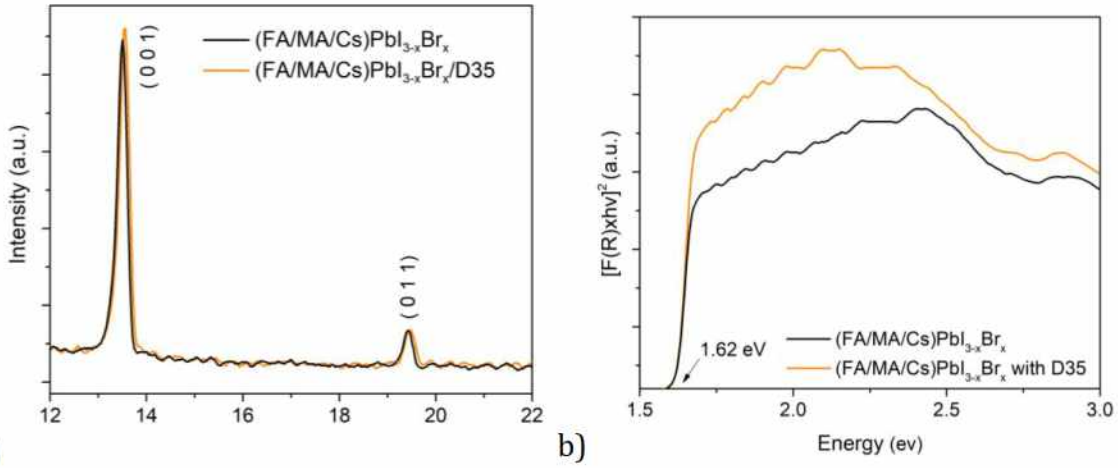

Figure 8-5: XRD patterns of mixed perovskite films with and without D35 treatment (a); Diffuse reflectance spectra of TiO_2/(FA/MA/Cs)$PbI_{3-x}Br_x$/D35 and TiO_2/(FA/MA/Cs)$PbI_{3-x}Br_x$ films (b).

Afterwards, the surface of the perovskite films was examined via contact-angle measurements and microscopy techniques. At first, the wettability of the chromophore interlayer was evaluated by the contact angle measurements presented in the supporting information (**Figure 8-6**). As shown, in the presence of D35, the contact angle increases from 62.63° for the reference to 89.98° for the modified film. This result verifies the beneficial role (effect) of the hydrophobic character of D35, stemming from the presence of the

butoxy groups that act as an insulating hydrophobic shield, protecting the perovskite absorber.[284]

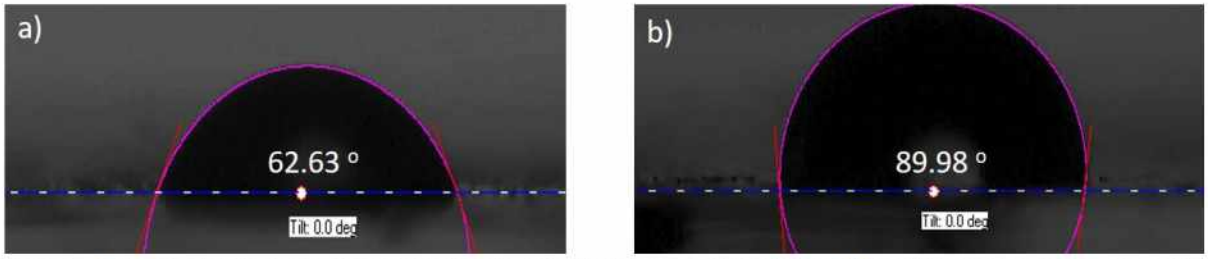

Figure 8-6: Contact angle measurements of reference and D35- modified films upon mesoscopic TiO_2 surfaces.

Subsequently, scanning electron microscopy (SEM) was used to thoroughly examine the effect of the D35- treatment on the perovskite morphology. **Figure 8-7** depicts the perovskite layers with (b,d) and without (a,c) D35 in two different magnifications.

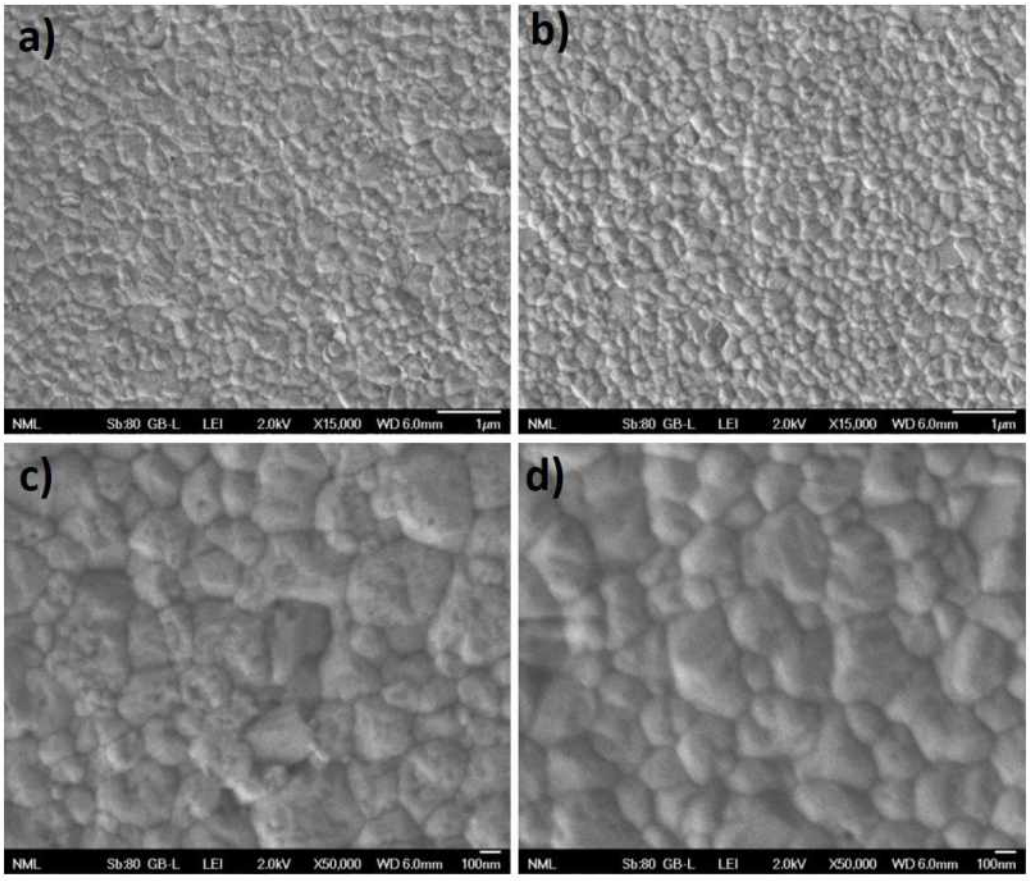

Figure 8-7: SEM images of perovskite films without (a,c); and with D35 treatment (b,c), under different magnifications.

The presence of D35 affects the morphology of the perovskite since the modified films exhibits a smoother surface morphology than the reference one, while the dye seems to polish the surface of the crystals and reduce the area of the grain boundaries. Since the

grain boundaries are considered to act as charge recombination sites, thus their repression entails improved charge transport and collection at the interface of perovskite film, leading possibly to higher FF values.[285]

The grains size distribution was estimated by the statistical analysis presented in **Figure 8-8** where the size distribution of a representative (N=100) number of perovskite grains from each sample is presented. From the results summarized in **Table 8-2**, it derives that in the case of the modified film the mean size of the crystals is slightly larger compared to the reference (254nm versus 240nm).

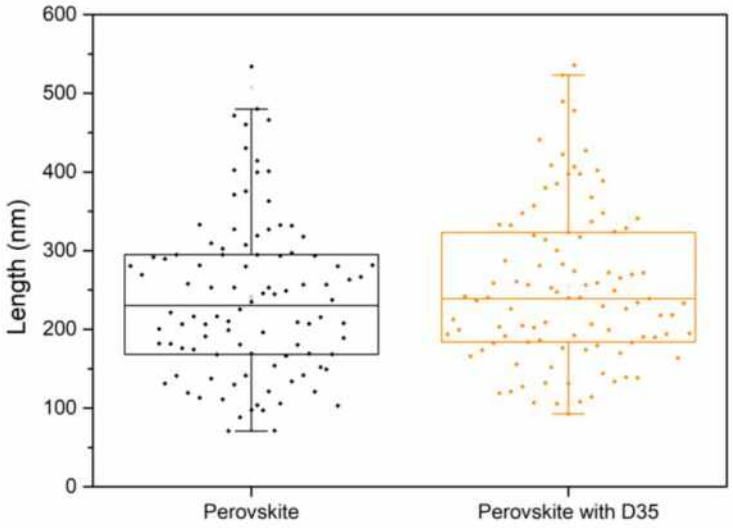

Figure 8-8: Grain size distribution of (FA/MA/Cs)$PbI_{3-x}Br_x$/D35and (FA/MA/Cs)$PbI_{3-x}Br_x$ films grown on TiO_2 substrates

Table 8-2: Statistical parameters of the grains size for (FA/MA/Cs)$PbI_{3-x}Br_x$/D35 and (FA/MA/Cs)$PbI_{3-x}Br_x$ films grown on TiO_2 substrates.

Sample	Mean (nm)	Standard deviation (nm)	Minimum(nm)	Median (nm)	Maximum (nm)
Reference	240,44	101,0	70,8	230,2	533,9
D35	254,34	100,0	92,8	239,1	535,7

The topology of the films was also examined via atomic force microscopy (AFM) analysis (**Figure 8-9**), which confirmed more homogeneous features with a significant decrease in the surface roughness of the modified perovskite layer (RMS=15.9nm) compared to the reference one (RMS=21.2nm).

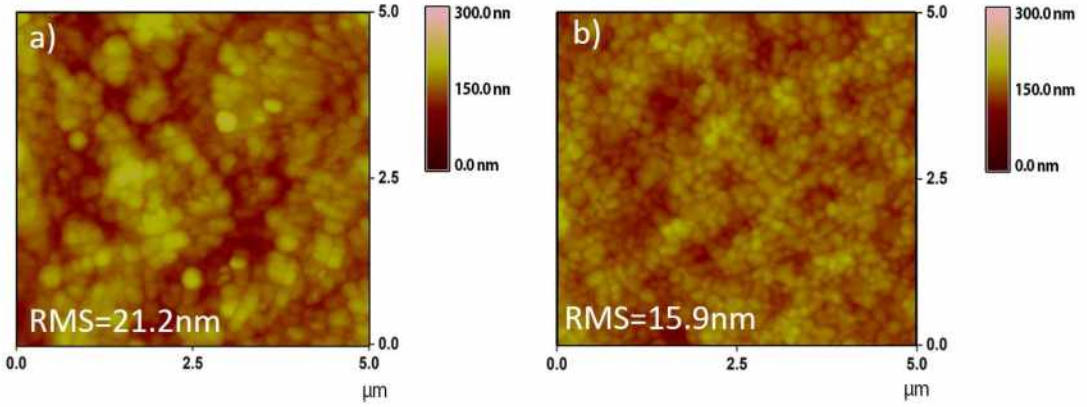

Figure 8-9: AFM images of perovskite films without (a); and with D35 treatment (b).

Moreover, **Figure 8-10** shows the depth histograms of the top surface topography with colored scales for the prepared perovskite films, which indicate a significant decrease of the height of surface features (30-120nm with max:73.5 nm for reference to 20-90nm with max: 50.04nm for the D35 PSC).

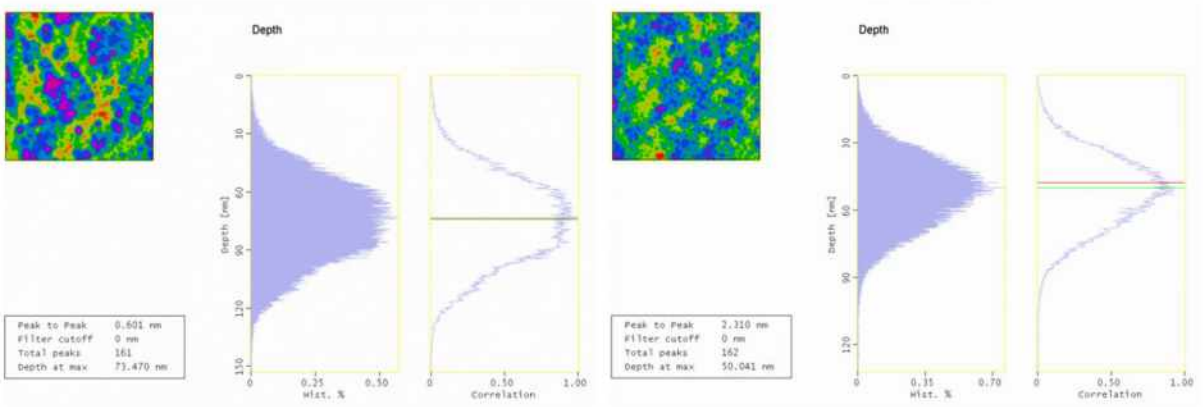

Figure 8-10: Depth histograms of top surface topography for (FA/MA/Cs)$PbI_{3-x}Br_x$/D35 (right), and (FA/MA/Cs)$PbI_{3-x}Br_x$ (left) films grown on TiO_2 substrates.

The roughness decrease in the case of perovskite films following D35-modification, can be attributed to hydrophobic molecules coordinating the perovskite via carboxylic acid binding groups and thus further controlling its crystallization.[286] Indeed, the obtained results clearly indicate that the presence of D35 atop of the perovskite layer affects the (FA/MA/Cs) $PbI_{3-x}Br_x$ /Spiro-MeOTAD interface, leading to a more homogenous and smoother absorber. Such perovskite films of higher quality and crystallinity are expected to affect the values of current density and fill factor parameters, thus improving the performance of the corresponding PSC devices.

In order to investigate the optoelectronic properties of the employed materials, ultraviolet photoemission spectra (UPS) measurements were performed in samples with and without the D35 chromophore modification. The results are presented in **Figure 8-11a** along with an illustration of the measured and calculated energy bands (**Figure 8-11b**) of the relevant materials. The energy band gaps were calculated using the data obtained by UV-Vis spectroscopy. The energy level diagram of D35 typically shows a highest occupied molecular orbital (HOMO) level of 5.50 eV and a bandgap of 2.43 eV.[287] The valence bands maxima of (FA/MA/Cs) $PbI_{3-x}Br_x$ and (FA/MA/Cs) $PbI_{3-x}Br_x$/D35 are located at 5.9eV and 5.3 eV, respectively.

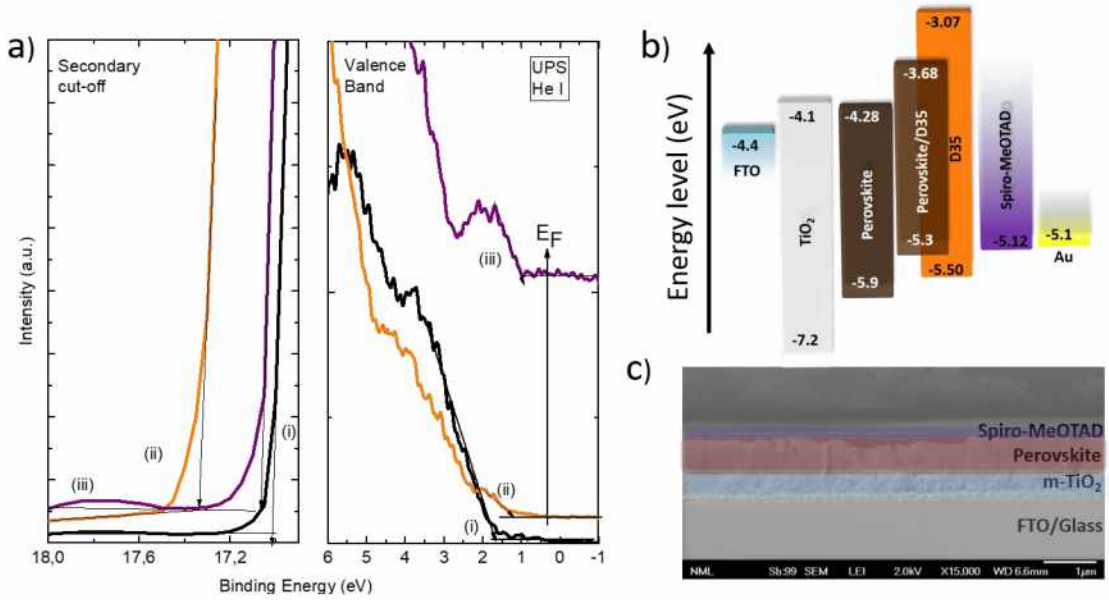

Figure 8-11: UPS spectra taken from the surface of (i) ITO/TiO_2/perovskite, (ii) ITO/TiO_2/perovskite/D35, (iii) ITO/TiO_2/perovskite/D35/Spiro-MeOTAD samples. Secondary electron cutoff region and valence band region are depicted (a); Energy levels diagram of the materials employed in the PSCs. (b); A SEM cross-section image of a TiO_2/perovskite/D35/Spiro-MeOTAD device (c).

This result claims that the presence of D35 affects the position of the energy bands in a way that favors the self-driven charge separation to the hole transporter by reducing the energy barrier, thus facilitates hole transport to the silver electrode via the hole transporting layer. In **Figure 8-11c**, a cross-section SEM image is presented, depicting the successive layers of a D35-containing device, built on FTO glass. D35 is not identified while the thickness of the layers is the same in the reference sample also (the corresponding SEM image is not presented). As estimated, the thickness of the (FA/MA/Cs)$PbI_{3-x}Br_x$ layer is 550nm while the Spiro-MeOTAD layer and titania layer are 165nm and 390nm respectively.

Furthermore, the influence of the donor-π-acceptor compound in the operation of perovskite solar cells was estimated, thus devices with the following structure were fabricated: FTO/TiO_2/Perovskite/Spiro-MeOTAD/Au denoted as 'Reference PSC', and FTO/TiO_2/Perovskite/D35/Spiro-MeOTAD/Au denoted as 'PSC with D35'. **Figure 8-12a** depicts the J-V curves of the champion devices for each batch and **Table 8-3** summarizes the corresponding photovoltaic characteristics.

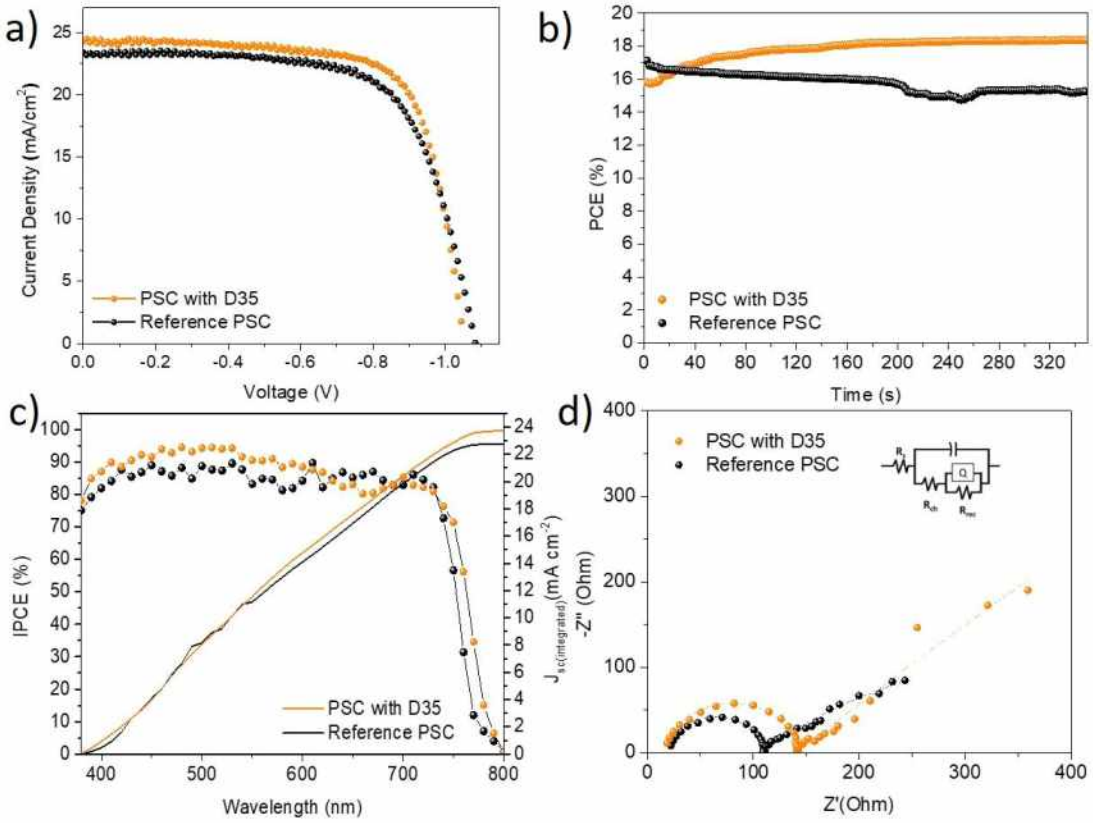

Figure 8-12: J-V curves of the best performing cells with and without D35 (a); the steady-state power conversion efficiency outputs under 1 sun illumination for reference and modified PSCs (b); The IPCE spectra and integration currents of the corresponding PSCs (c); The Nyquist plots obtained via EIS measurements, under 1 sun illumination and under V_{MPP} bias. Fitting of data has been done using the equivalent electrical circuit in the inset (d).

From these results, it is obvious that D35 improves the performance of the devices and specifically the values of current density and fill factor. Therefore, the maximum efficiency (18.57%) was improved by 8.45% in relation to the reference device. The presence of D35 apparently increased the mean photocurrent which reached a champion value of 24.60 mA·cm^{-2} while the fill factor was clearly improved from 0.67 for the reference to 0.72 for the best modified PSC. The improved J_{sc} may be attributed to the higher crystallinity of the D35-containing PSC that leads to increased light harvesting capability of the

absorber. Moreover, it implies the existence of improved charge separation and extraction.

Table 8-3: Photovoltaic parameters for the champion solar cells prepared. Values inside brackets refer to mean values and standard deviations. V_{oc}: open-circuit voltage, J_{sc}: short-circuit current density, FF: fill factor, PCE: power conversion efficiency, SPCE: Stabilized PCE. All data were taken under reverse scan at 50 $mV \cdot s^{-1}$

Sample	J_{sc} (mA cm^{-2})	V_{oc} (V)	FF	PCE (%)	SPCE (%)
Reference PSC	23.57 (22.73±1.55)	1.08 (1.00±0.07)	0.67 (0.62±0.07)	17.12 (14.24±1.40)	15.29
PSC with D35	24.60 (23.75±1.20)	1.05 (1.03±0.06)	0.72 (0.65±0.04)	18.57 (15.87±1.52)	18.45

The fill factor was also improved in the presence of D35, a fact attributed to the improvement of the corresponding interfaces and suppression of charge recombination process. In addition, the mean V_{oc} value was also increased; a fact associated with D35's passivation effect along with perovskite's energy bands upshifting and lowering of W_F from 4.3eV to 3.9eV (**Figure 8-11a**, left part)

In order to control the quality of the prepared PSCs, the steady-state PCE (**Figure 8-12b**) was calculated by measuring the cells under 1 sun illumination conditions and constant bias equal to the voltage of the maximum power point (V_{MPP}). The V_{MPP} values for the D35-containing and the reference device are 0.85 V and 0.83 V respectively. A PCE value of 18.45% was stabilized for the modified solar cell after 330 s of irradiation, which is well consistent with the value taken from the J–V measurements, indicating the robustness of the cells. On the other hand, the stabilized power output for the reference device showed a gradual decline and the corresponding stabilized PCE was lower (15.29%) than the one obtained from J–V measurements. In addition, internal photo-to-current (IPCE) spectra were recorded for the devices with and without D35 modification as shown in **Figure 8-12c**. The enhancement of the IPCE in the case of the D35-modified cell is consistent with the corresponding enhancement in the UV spectra. Indeed, the contribution of D35 in the collected photocurrent is important especially below 600nm, implying that D35 has a strong effect on the charge extraction efficiency of PSCs. The integrated current densities corresponding to J_{SC} were also calculated to be 23.67 $mA \cdot cm^{-2}$ and 22.89 $mA \cdot cm^{-2}$ for the devices with and without D35 respectively, values in relative agreement with

those obtained from the J–V curves. Furthermore, the effect of the D35 interface layer on the charge transfer and recombination procedures was estimated by electrochemical impedance spectroscopy (EIS) measurements, carried out in PSCs with and without D35. The experiments were carried out under dark and light (1 sun illumination conditions), while the devices were biased at the V_{MPP} values. The corresponding plots are presented in **Figure 8-12d** and **Figure 8-13**, whereas the extracted parameters are summarized in **Table 8-4**.

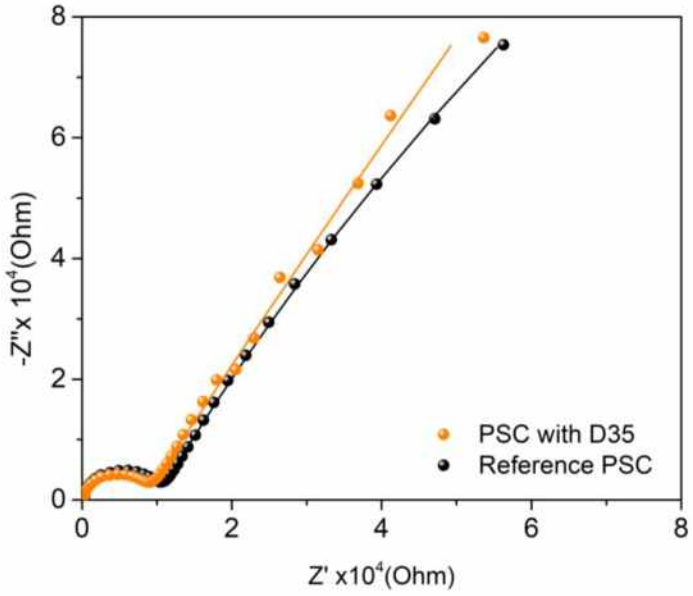

Figure 8-13: The Nyquist plots obtained via EIS measurements, under dark conditions and under V_{MP} bias. (Fitting of data has been done using the same equivalent electrical circuit as presented in the inset of Figure 12d).

Table 8-4: Ohmic resistance values obtained from EIS analysis for PSCs based on the D35 interlayer, in comparison to reference devices.

	Sample	R_s (ohm)	R_{ch} (ohm)	R_{rec} (ohm)
Dark	PSC with D35	154.2	8322	4.3E⁶
	Reference PSC	281.8	9663	7.5E⁵
Light	PSC with D35	17.9	85.1	5980
	Reference PSC	22.5	122.4	561

In the Nyquist plots (obtained under illumination- **Figure 8-12d**), we denote the appearance of two arcs which are associated with charge transfer (the low-frequency semicircle) and charge recombination (the high-frequency semicircle) processes. [245,246] The obtained parameters summarized in **Table 8-4** show that the series (R_s) and charge transfer (R_{ch}) resistances are reduced in the presence of D35, while recombination resistance (R_{rec}) for the D35-containing PSC is significantly higher than that of the reference solar cell. The higher R_{rec} manifests a lower recombination rate, while under dark the results (**Table 8-4** and **Figure 8-13**) also confirm that all resistive parameters (R_s, R_{rec}, R_{ch}) are improved in the presence of D35, affirming its beneficial effect to the device performance. Finally, a statistical analysis of their photovoltaic performance was done over 40 devices (**Figure 8-14**) of each batch, corroborating the superiority of the D35-modified devices.

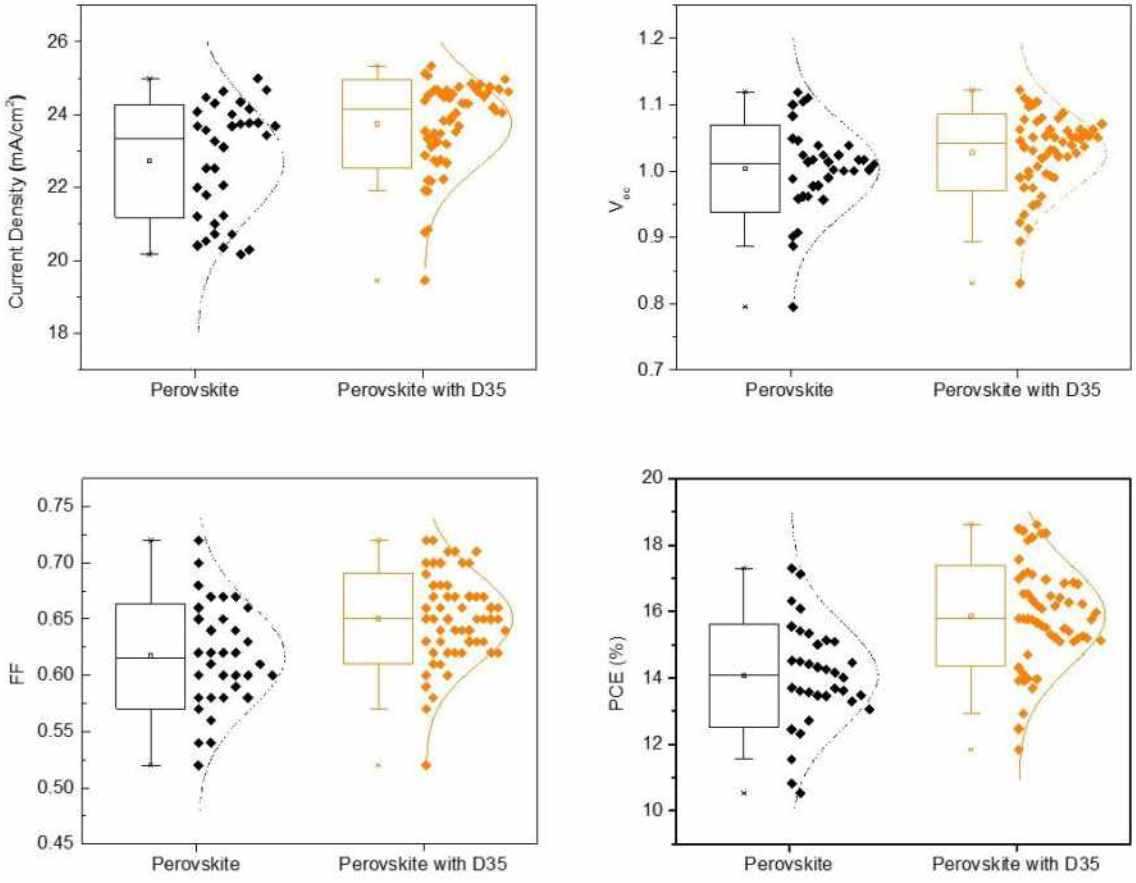

Figure 8-14: The statistical analysis of the photovoltaic parameters for PSCs with and without D35.

It has been demonstrated that the introduction of semiconducting molecules contributes to the efficient charge separation and extraction along perovskite grain boundaries.[288] In this context, the incorporation of the D-π-A D35 organic compound should enhance the

charge extraction across the photoexcited perovskite layer and thus eventually decrease the possibility of recombination. Steady-state and time-correlated single photon counting (TCSPC) fluorescence spectroscopy studies enabled the investigation of these electronic interactions taking place into the different device configurations under photoexcitation.

Initially, the FTO/TiO_2/perovskite/D35 device was examined with respect to the FTO/TiO_2/perovskite employed as reference (**Figure 8-15a, b**). Under photoexcitation at 482 and 650 nm, the emission intensity of the perovskite was found quenched by 75 and 45%, respectively, suggesting that the incorporation of the D35 dye decreases the recombination yield in the perovskite layer, hence highlighting an increased yield of electron-hole separation. More specifically, the transfer of photogenerated holes across the perovskite layer to the HOMO level of the Pb^{2+}-coordinated D35 molecules is expected, accompanied by injection of electrons from the D35 to the perovskite. It is known that the selected dye molecule has excellent electron injection properties, while the butoxy chains present on the triphenylamine core probably prevent the photogenerated electrons located on the perovskite from radiative recombination due to their insulating character.[289–292] The slight red-shift observed to the PL maxima of the FTO/TiO_2/perovskite/D35 device may represent the electron-hole recombination process at the perovskite/D35 interface. Interestingly, the 75% quenching recorded under 480 nm excitation is indicative of an improved charge separation in the spectral region where both the perovskite and the dye absorb light. This fact is also evident at the IPCE spectra shown in Figure 6c, where for FTO/TiO_2/perovskite/D35/Spiro-MeOTAD a broad shoulder around 500 nm is present, contrasting the reference ones obtained without the organic dye.

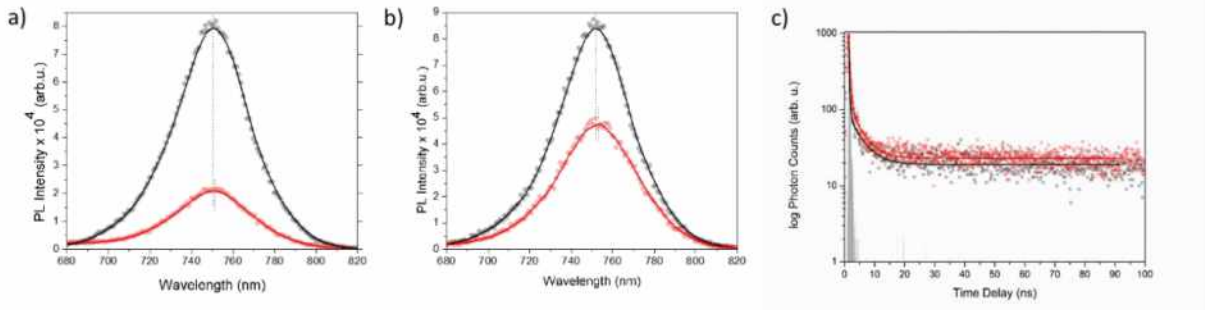

Figure 8-15: Steady-state photoluminescence spectra of FTO/TiO_2/perovskite (black) and FTO/TiO_2/perovskite/D35 (red) devices at room temperature upon excitation at a) 482 nm, and b) 650 nm. (c) Time-correlated single photon counting spectra obtained under 482 nm excitation and probed at 750 nm at room temperature.

As far as the time-resolved PL spectra recorded for the FTO/TiO_2/perovskite/D35 device concerns (**Figure 8-15c**), the average emission lifetime of the photoexcited perovskite was found 1.87 ns, increased by a factor of 0.4 as compared to the 1.32 ns emission lifetime recorded for the reference FTO/TiO_2/perovskite device (**Table 8-5**). We assume a synergistic effect, where the incorporation of the D35 at Pb^{2+} edges (a) furnishes a passivation effect to the exciton traps arise from peripheral crystal imperfections, and (b) retards the electron-hole recombination due to its bulk and insulating chemical structure.[291] Further, we investigated the steady-state and time-resolved fluorescence profiles for FTO/TiO_2/perovskite/Spiro-MeOTAD and FTO/TiO_2/Perovskite/D35/Spiro-MeOTAD devices, in comparison to FTO/TiO_2/perovskite employed as reference. Upon photoexcitation, the emission (at two wavelengths, i.e. 480 and 650 nm) of the perovskite layer was greatly quenched (especially by 98% under 480 nm excitation -**Figure 8-16, b**).

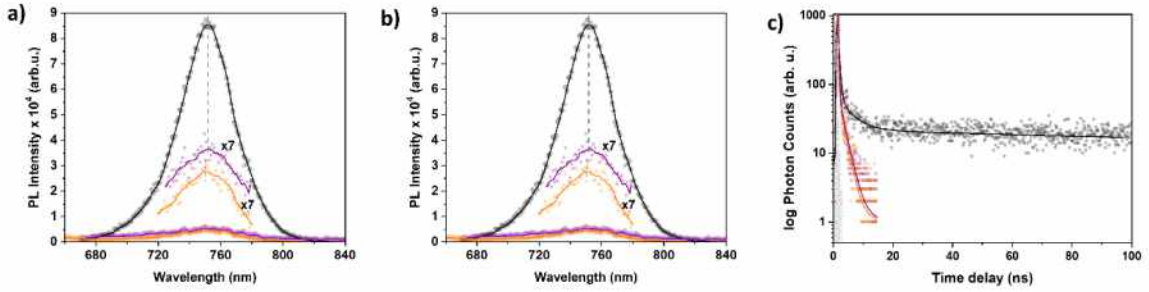

Figure 8-16: Steady-state photoluminescence spectra of FTO/TiO_2/perovskite (black), FTO/TiO_2/perovskite/Spiro-MeOTAD (purple) and FTO/TiO_2/Perovskite/D35/Spiro-MeOTAD (orange) devices at room temperature upon excitation at a) 482 nm, and b) 650 nm. (c) Time-correlated single photon counting spectra under 482 nm excitation probed at 750 nm obtained at room temperature.

Table 8-5: Biexponential fitting of the perovskite's fluorescence emission decay traces recorded via time-correlated single photon counting (TCSPC) spectroscopy under 482nm excitation at room temperature probed at 750nm. (t: decay lifetime; A: relative population)

Device	t_1(ns)	A_1	t_2(ns)	A_2	average (ns)
TiO_2/Perovskite	4.2	0.27	0.256	0.73	1.32
TiO_2/Perovskite/D35	3.9	0.42	0.395	0.58	1.87
TiO_2/Perovskite/Spiro-MeOTAD	2	0.58	0.194	0.42	1.20
TiO_2/Perovskite/D35/Spiro-MeOTAD	1.85	0.37	0.215	0.63	0.83

Although no spectral shifts were evident in the PL spectra of FTO/TiO_2/perovskite/Spiro-MeOTAD, as compared to FTO/TiO_2/perovskite, for FTO/TiO_2/Perovskite/D35/Spiro-MeOTAD a blue-shift of around 7 nm was clearly detected under the 480 nm excitation (and 2 nm for the 680 nm excitation). As long as the hole-transport layer of spiro-MeOTAD accelerates the extraction of the photogenerated holes from the perovskite layer through the perovskite/D35 interface, recombination of electron-hole pairs is mostly occurs in the bulk domains of the perovskite layer. The blue-shifted emission maxima for the FTO/TiO_2/Perovskite/D35/Spiro-MeOTAD device, located at 743 nm, illustrate enhanced charge recombination from the uniform crystal domains of the perovskite, manifesting the decrement of charge recombination events due to surface trap states.[231] Furthermore, it is also related to the conduction and valence band-edges filled by the photogenerated carriers, thus allowing transitions of higher energy.[293] Eventually, the reference FTO/TiO_2/perovskite/Spiro-MeOTAD shown no spectral shifts since the Spiro-MeOTAD layer is not beneficial for the surface trap states engineering of the perovskite layer.

Having in mind the earlier discussed red-shift in the PL spectra observed for the FTO/TiO_2/perovskite/D35 devices, we conclude that the exciton recombination maxima of the perovskite centered at 750 nm constitutes a gross emission fingerprint of the recombination events taking place at (a) the surface trap states (around 755 nm), and (b) the bulk uniform crystal domains (around 744 nm).[292]

Next, we assessed the emission time-resolved decay of the perovskite layer in the FTO/TiO_2/perovskite/Spiro-MeOTAD and FTO/TiO_2/Perovskite/D35/Spiro-MeOTAD devices under 480 nm excitation (**Figure 8-16c**). The average 1.87 ns fluorescence lifetime of the perovskite layer, composed by two populations of 4.2 ns (27%) and 256 ps (73%), was decreased by the addition of the Spiro-MeOTAD layer, affording an average lifetime of 1.2 ns, also composed by two populations of 2 ns (58%) and 194 ps (42%), in the FTO/TiO_2/Perovskite/Spiro-MeOTAD device. In line with the steady-state PL spectroscopy findings, the incorporation of Spiro-MeOTAD enhances the extraction of photogenerated charges, hence leading to an acceleration of the perovskite's PL lifetime decay due to a fast hole transfer process. Further decrement to the PL lifetime was recorded for the FTO/TiO_2/Perovskite/D35/Spiro-MeOTAD device, where the D35-passivated perovskite was interfaced the Spiro-MeOTAD, resulting to an average emission lifetime of 820 ps, based to the bi-exponential fitting of the decay trace with two components of 1.85 ns (37%) and 215 ps (63%).

In order to shed more light on the effect of the D35 compound, steady-state and time-resolved PL experiments were performed, albeit using plain glass substrates upon which, successively perovskite, D35, and Spiro-MeOTAD layers were coated. The FTO and TiO2 layers were excluded as to isolate the charge transport influence of the D35 interlayer. Initially, the deeply penetrating 650 nm laser was utilized to investigate the charge transport properties of the D35 dye in devices consisting of perovskite layers coated directly in plain glass substrates, by irradiating the samples from both the surface and the glass backside (**Figure 8-17**).

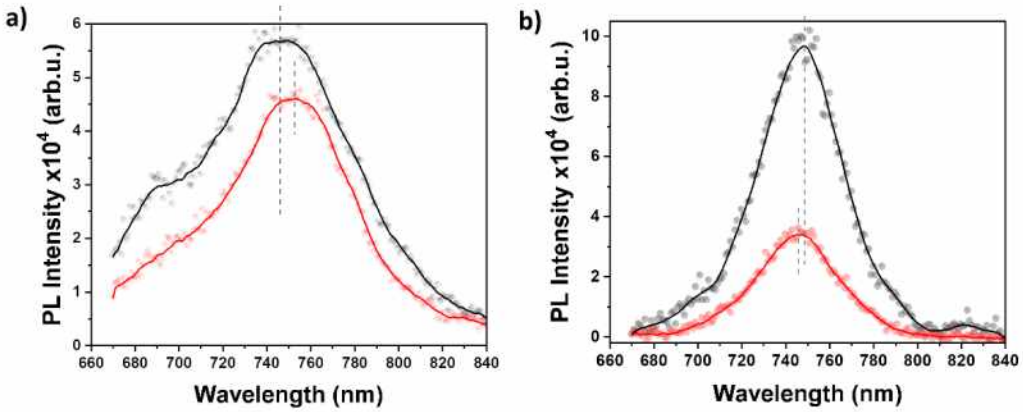

Figure 8-17: Steady-state photoluminescence spectra of glass/perovskite (black) and glass/perovskite/D35 (red) devices obtained at room temperature upon excitation at 650 nm, irradiated from a) the glass side, and b) the surface side.

In both cases, the PL emission of the perovskite was found quenched, underscoring the good charge transport properties of D35. Nevertheless, the broad emission trace recorded when irradiation was performed from the glass side, reveals that in the absence of the TiO_2 layer the perovskite is not uniformly distributed at the glass/perovskite interface. In contrast, irradiation at the perovskite surface side, suggests a better crystal growth and morphology as realized by the symmetric well-defined exciton recombination peak. Also, a slightly blue-shifted emission peak was evident in the presence of D35, suggesting the trap-states passivation role of the organic molecule. Irradiating the surface side of the glass/perovskite reference device with 482 and 650 nm, a maximum PL emission at 755 and 758 nm, respectively was detected (**Figure 8-18a, b**). These red-shifted bands, as compared to those obtained in the FTO/TiO_2/perovskite device, are probably related to the slightly different morphology of the perovskite layer on the glass, as compared to the FTO/TiO_2 substrate. Incorporation of the D35 compound resulted to a blue shift of 2 nm and significant quenching of the recorded emission spectra, both under 480

and 650 nm excitation. Moreover, the recorded PL lifetimes dictated a faster deactivation for the perovskite layer interfacing the D35 dye (**Table 8-6**). Eventually, the coordination of the D35 dye at the Pb^{2+} edges via the cyanoacrylic acid anchoring group passivates the crystal imperfections. Thus, in and in the absence of the electron transport layer the band-edges of the perovskite are populated with charges leading to a faster recombination of the photogenerated excitons from the bulk.

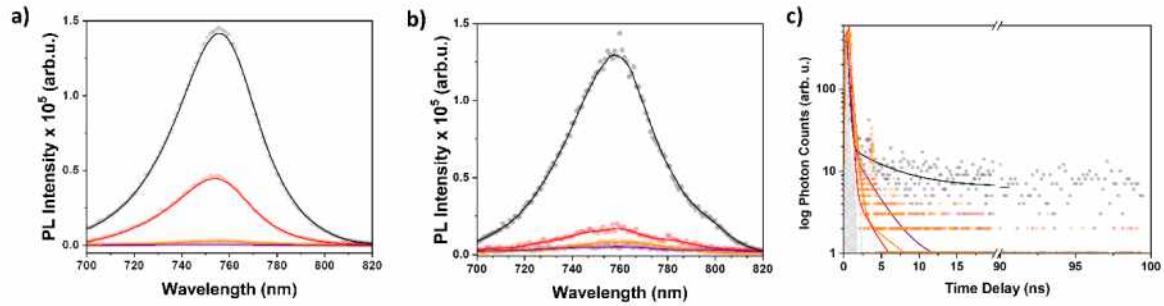

Figure 8-18: Steady-state photoluminescence spectra of glass/perovskite (black), glass/perovskite/D35 (red), glass/perovskite/Spiro-MeOTAD (purple) and glass/perovskite/D35/Spiro-MeOTAD devices obtained at room temperature upon excitation at a) 482 nm, and b) 650 nm. (c) Time-correlated single photon counting spectra under 482 nm excitation and probed at 750 nm at room temperature.

Table 8-6: Biexponential fitting of the perovskite's fluorescence emission decay traces recorded via time-correlated single photon counting under 482 nm excitation and probed at 750 nm at room temperature (t: decay lifetime; A: relative population).

Sample	t_1(ns)	A_1	t_2(ns)	A_2	average (ns)
Glass/perovskite	5.1	0.34	0.209	0.66	1.87
Glass/Perovskite/D35	2.2	0.09	0.201	0.91	0.38
Glass/ Perovskite /Spiro-MeOTAD	2.67	0.21	0.253	0.79	0.76
Glass/ Perovskite /D35/Spiro-MeOTAD	0.25	-	-	-	0.25

The passivating effect of the D35 was further examined by characterizing electron-only devices in the space-charge-limited-current (SCLC) regime.[294] **Figure 8-19** depicts the I-V response, measured for devices fabricated with the following structure: FTO/TiO_2/(MA/FA/Cs)$PbI_{3-x}Br_x$/$PCBM_{60}$/Ag corresponding to the reference device and FTO/TiO_2/(MA/FA/Cs)$PbI_{3-x}Br_x$/D35/$PCBM_{60}$/Ag corresponding to the D35-containing one. At low voltage values, the I-V plot is ohmic, while in mid-range values the current shows a rapid nonlinear rise, characterized by the transition to the trap filled limit (TFL) regime where all the available trap states are filled by the injected carriers. At high voltage values (not shown clearly due to the relative instability of the devices), the current

has a quadratic dependence against voltage (Child's regime).[295] As reported elsewhere,[296] the ohmic to TFL transition point (V_{TFL}) is related to the trap density (N_t) according to the following equation (8.3):

$$V_{TFL} = \frac{eN_t d^2}{2\varepsilon\varepsilon_0} \qquad (Eq\ 8.3)$$

where e is the elementary charge, d is the thickness of the active layer (550 nm), ε is dielectric constant (ε =28.8)[297] and ε_0 is the dielectric constant in vacuum. The calculated trap density (N_t) is 3.2 x 10^{15} cm^{-3} for the reference device and 1.9 x 10^{15} cm^{-3} for the modified one respectively. These results, confirming the PL measurements, indicate that the presence of D35 reduces the perovskite trap states.

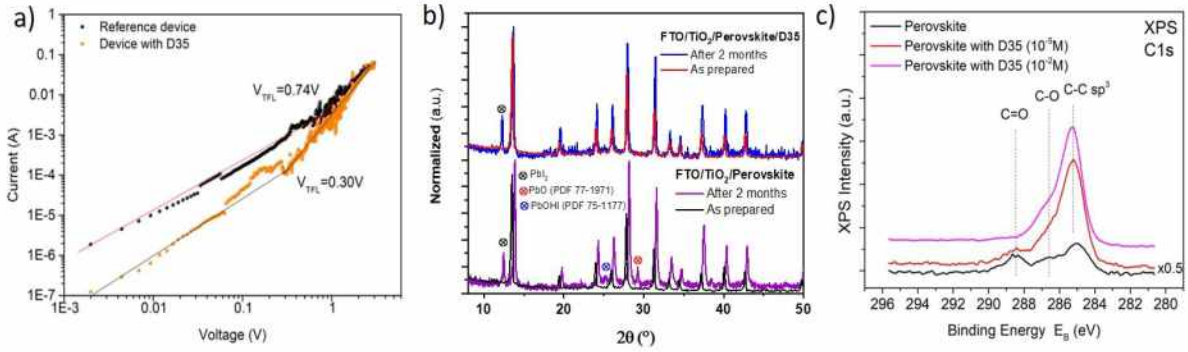

Figure 8-19: I-V curves for electron-only devices with and without D35. (a); XRPD patterns of fresh and aged perovskite films with and without D35 treatment (b); XPS measurements for perovskite films without and with D35 in two different concentrations (10^{-5} M and 10^{-2}M) (c).

Moreover, **Figure 8-19b** shows the corresponding XRPD patterns of perovskite films with and without D35 coated upon TiO_2, as prepared and after two months of storage in ambient and dark conditions (RH=25%, without encapsulation). The XRPD analysis of reference films shows extra peaks at 2θ = (12.45°, 25.02 °, and 29.22°) corresponding to PbI_2, PbO (PDF 77-1971), and PbO(HI) (PDF 75-1177), respectively, thus, confirming the progressive degradation of the reference film due to thermodynamic and humidity effect which lead to a change of chemical composition and phase transition of the perovskite. Despite some presence of PbI_2 at the modified film, the hydrophobic character of the D35 decreased the effect of humidity on the perovskite layer. The latter was also confirmed by X-ray photoelectron spectroscopy (XPS) measurements (**Figure 8-19c**), whereas the C=O peak (288.1 eV) seen for the control film associated with oxygen/moisture is significantly suppressed after D35 modification, indicating that D35 interlayer can slow the

degradation of the perovskite layer.[236] In the case of a dense D35 layer (10^{-2}M), the peak completely vanished.

Finally, the stability of the cells was evaluated by storing the cells (in the dark) and periodically measuring their J-V characteristics. The PSCs were stored unsealed in a desiccator under dark and relatively humid conditions (RH=25%). The results are presented in **Figure 8-20,** where the main photovoltaic parameters are plotted against time.

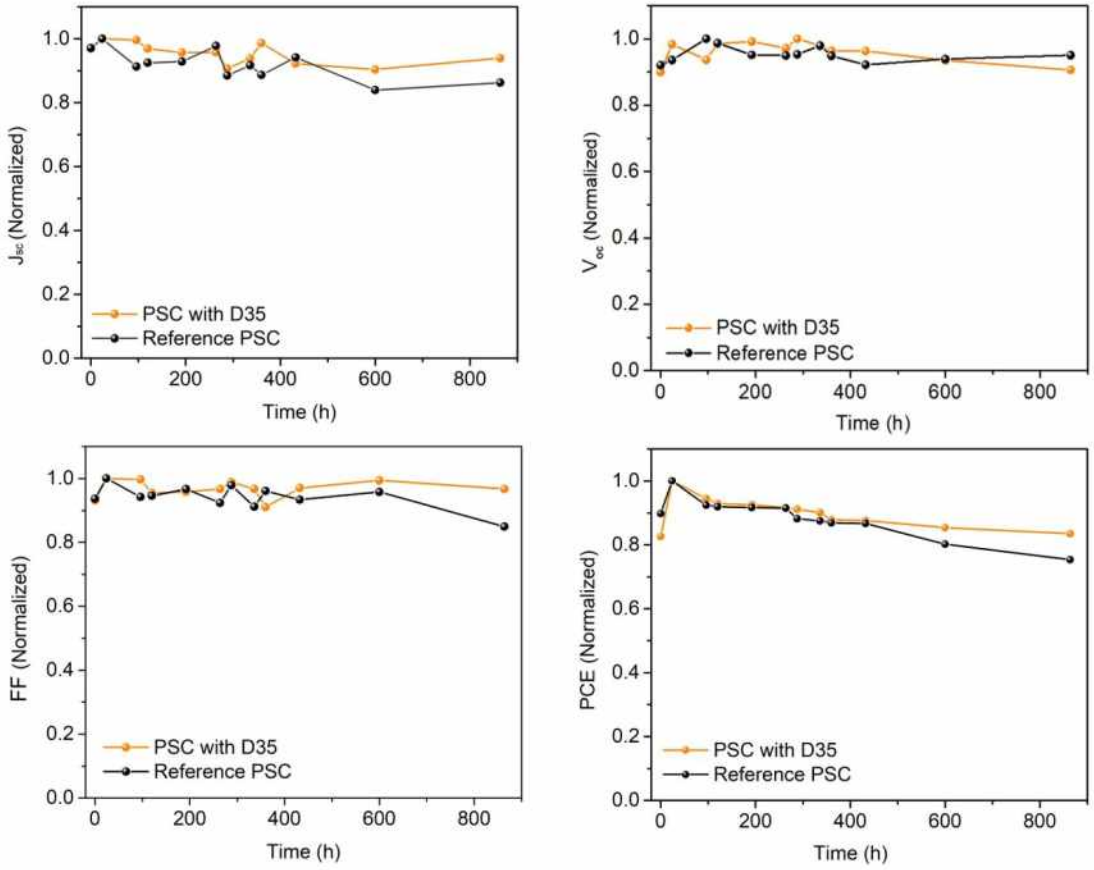

Figure 8-20: Evolution of the main photovoltaic parameters over time for PSCs with and without D35.

After 37 days, the PSCs with D35 has preserved 83% of their initial PCE. This is mainly attributed to the stabilization of FF which only declined by 2% compared to the initial value, and secondly to the evolution of J_{sc} which decreased by 5% compared to the starting point. Both values are improved in comparison with the reference PSC, which preserved 77% of its original PCE, a value lower by 11.5% than the modified device. On the contrary, the value of V_{oc} was practically unaffected by the presence of D35 since it is almost stable after 890h of storage.

CHAPTER (9)

Conclusions and perspective

Conclusions and perspective

This class of sulfonium-containing lead/tin halide perovskites has a high potential for semiconducting applications due to its high chemical stability in ambient conditions.

Below, I summarized the main finding of each chapter:

Chapter (3)

X-ray diffraction analysis shows that the solid solutions of a novel series of $(CH_3)_3SPbI_{3-x}Br_x$ (x = 0, 1, 2, 3) and $(CH_3)_3SPbI_{3-x}Cl_x$ (x = 0, 1, 2) crystallize in hexagonal symmetry (space group *P*6$_3$*mc*, No. 186) with 1D columns of face-sharing $[PbX_6]$ octahedra. $(CH_3)_3SPbCl_3$ crystallizes in orthorhombic symmetry (space group *Pnma*, No. 62) forming 3D network of vertex- and face-sharing $[PbCl_6]$ octahedra. The compounds show high chemical stability in ambient air at temperatures up to 80 °C and under solar simulator. There is an unusual effect of the halogen atom, as $(CH_3)_3SPbI_{3-x}Cl_x$ (x = 0, 1, 2) form solid solutions with 1D octahedral columns, whereas $(CH_3)_3SPbCl_3$ forms a 3D network of interconnected octahedra. Although the electronic band gaps are over 3 eV, and therefore not applicable as absorbers in solar cells, these perovskites are solution-processable and may be used as hole transporters in solar cells. Moreover, DFT and semiempirical extended Hückel calculations are proved to be efficient as a method for bandgap calculation in this class of materials.

Chapter (4)

The relative chemical stability of a novel $(CH_3)_3SSnI_3$ perovskite proves that the trimethylsulfonium cation undertakes indeed an important role in stabilizing the Sn^{2+} oxidation state in the 1D perovskite structure. UV-Vis spectroscopy indicates that the rate of irreversible oxidization upon exposure to air into $((CH_3)_3S)_2SnI_6$ is at least one order of magnitude lower than in hybrid tin(II) halide perovskites. Although $(CH_3)_3SSnI_3$ itself has relatively large band gap, which does not render it applicable as absorber in solar cells, the use of trimethylsulfonium as an additive to other perovskites, e.g. in $CsSnI_3$, may boost their stability. The wide band gap 1D layer can be introduced at the interface between the primary 3D perovskite absorber and the hole transport layer, in order to increase the stability of the corresponding perovskite devices. Such studies are currently in progress. Moreover, this study marks the contribution of Raman spectroscopy in the structural

analysis of compounds where traditional crystallography provides only limited information due to their diffuse scattering.

Chapter (5)

The new class, lead-free $((CH_3)_3S)_2SnX_6$ (X = Cl, Br, I) perovskite compounds has a high potential for semiconducting applications due to the low toxicity and high chemical stability in ambient conditions. The electronic bandgap of $((CH_3)_3S)_2SnI_6$ is at 1.38 eV, which is almost ideal for solar cells applications, whereas $((CH_3)_3S)_2SnX_6$ (X = Cl, Br) have E_g at 4.09 and 2.9 eV, respectively. I utilize $((CH_3)_3S)_2SnI_6$ as hole-transporting material in dye-sensitized solar cells, based on mesoporous titania electrodes sensitized with a Z907 organic dye. The solar cells performed a maximum power conversion efficiency of 5% which is higher than 4.23% found for the Cs_2SnI_6-based solar cell [153,298]. The higher performance of $((CH_3)_3S)_2SnI_6$ is attributed to efficient charge transport in the bulk material and hole extraction at the perovskite-Pt interface, as evidenced by electrochemical impedance spectroscopy. Our work underscores the possibility of developing third-generation solar cells with high performance and increased stability using tin-based perovskites working either as light absorbers or as HTMs or both.

Chapter (6)

Lead-free, air-stable, low toxic $((CH_3)_3S)_2SnI_{6-n}Cl_n$ and $((CH_3)_3S)_2SnI_{6-n}Br_n$ (n=1, 2) defect perovskites have high potential for solar cell applications. The photophysical characterization and DFT computational calculation confirm that the lattice vibrations modes and electronic bandgaps are between 1.38 and 1.5 eV and depend largely on the effect of mixing I and Cl/Br atoms. We successfully utilized the novel perovskite compounds as HTMs in electrolyte-free dye-sensitized solar cells, based on mesoporous titania electrodes sensitized by some transition metal complexes (Z907, N719) and organic (MK2, D35) dyes. A power conversion efficiency (PCE) of 4% under the standard illumination conditions of 100 mW/cm^2 (A.M. 1.5G) was achieved for the $((CH_3)_3S)_2SnI_5Br$ and $((CH_3)_3S)_2SnI_5Cl$ layer sandwiched between sensitizer metal-organic Z907 and Pt interface. Electrochemical impedance results confirm low hole extraction resistance of mono-substituted halogen at the perovskite-Pt electrode. Overall, our results promote trimethyl sulfonium tin-based perovskites as chemically stable hole-transport material in lead-free solar cells.

Chapter (7)

I successfully formed an interlayer of a wide bandgap air-stable 1D $(CH_3)_3SPbI_3$ perovskite through a cation exchange reaction between $(FA/MA/Cs)PbI_{3-x}Br_x$ and trimethyl sulfonium cations. Our results confirm that the interface layer of trimethyl sulfonium lead iodide has a critical role in improving the stability of the perovskite absorber degradation against light and humidity in excellent agreement with XRPD analysis of the 3D/1D bilayer (as we discussed in the corresponding section). The results showed a lower loss in the performance of (39.3%) of the modified PSCs compared to (70.5%) of the reference cells (relatively humidity 30% and dark conditions for 700 h), which also are a good agreement with the light stress results, that show a lower loss performance of (27.5%) of the modified cells compared to (83.7%) of the reference cells under continuous light stress for four hours. Our results underscore the possibility of developing a stable two layers perovskite which seems to be a very promising tool for developing high performing PSCs with improved stability.

Chapter (8)

An effective versatile strategy for enhancing perovskite device performance using the D35 donor-π-acceptor was introduced. The D35 treatment improves perovskite film crystallization, enhances light absorption and provokes an appropriate energy alignment that favors charge extraction to the anode and cathode electrodes. ESP analysis suggests that D35 possesses a carboxylate group with high electron density, which could coordinate/passivate with the undercoordinated Pb^{2+} cations of the perovskite crystals, thus retarding non-radiative recombination. At the other end of the D35 molecule, hydrophobic butoxy chains improve the moisture stability of the perovskite films. PSCs with the D35 interlayer showed the best PCE of 18.57% while unencapsulated modified devices retain 83% of their initial PCE after storage in a desiccator for 37days, while the PCE of the reference devices degraded to 77% after aging procedure. This work elaborates on a novel strategy to combine D-π-A organic dyes with perovskites to fabricate robust perovskite films for efficient and stable PSCs.

CHAPTER (10)

"References"

References

(1) Leonardo Maugeri. The Age of Oil: The Mythology, History, and Future of the World's Most Controversial Resource. *Choice Rev. Online* **2007**, *44* (05), 44–2726.

(2) IEA World Energy Balances 2019 Https://Www.Iea.Org/Subscribe-to-Data-Services/World-Energy-Balances-and-Statistics.

(3) Perez R. and Perez M. , IEA SHC Sol. Updat., 2009, 50, 2–3.

(4) Breidenich, C.; Magraw, D.; Rowley, A.; Rubin, J. W. The Kyoto Protocol to the United Nations Framework Convention on Climate Change. *Am. J. Int. Law* **1998**, *92* (2), 315–331.

(5) IEA (2015), "Energy and Climate Change", IEA, Paris Https://Www.Iea.Org/Reports/Energy-and-Climate-Change.

(6) Tress, W. Organic Solar Cells Theory, Experiment, and Device Simulation; Springer, 2014.

(7) Fraunhofer Institute for Solar Energy Systems, ISE with Support of PSE GmbH, Https://Www.Ise.Fraunhofer.de/Content/Dam/Ise/de/Documents/Publications /Studies/Photovoltaics-Report.Pdf. **2019**.

(8) Green, M. A.; Dunlop, E. D.; Hohl-Ebinger, J.; Yoshita, M.; Kopidakis, N.; Ho-Baillie, A. W. Y. Solar Cell Efficiency Tables (Version 55). *Prog. Photovoltaics Res. Appl.* **2020**, *28* (1), 3–15.

(9) National Renewable Energy Laboratory. Https://Www.Nrel.Gov/Pv/Cell-Efficiency.Html.

(10) Ranabhat, K.; Patrikeev, L.; Revina, A. A.; Andrianov, K.; Lapshinsky, V.; Sofronova, E. An Introduction to Solar Cell Technology. *J. Appl. Eng. Sci.* **2016**, *14* (4), 481–491.

(11) Roy, A.; Devi, P. S.; Karazhanov, S.; Mamedov, D.; Mallick, T. K.; Sundaram, S. A Review on Applications of Cu2ZnSnS4 as Alternative Counter Electrodes in Dye-Sensitized Solar Cells. *AIP Adv.* **2018**, *8* (7), 070701.

(12) https://www.wikiwand.com/en/Dye-sensitized_solar_cell.

(13) Weber, D. $CH_3NH_3PbX_3$, a Pb(II)-System with Cubic Perovskite Structure. *Z.*

Naturforsch. **1978**, No. 33b, 1443–1445.

(14) Weber, D. $CH_3NH_3SnBr_xI_{3-x}$, a Sn(II)-System with the Cubic Perovskite Structure. *Z. Naturforsch.* **1978**, *33b*, 862–865.

(15) Sun, Q.; Wang, J.; Yin, W. J.; Yan, Y. Bandgap Engineering of Stable Lead-Free Oxide Double Perovskites for Photovoltaics. *Adv. Mater.* **2018**, *30* (15), 1705901.

(16) Yin, W.-J. J.; Weng, B.; Ge, J.; Sun, Q.; Li, Z.; Yan, Y. Oxide Perovskites, Double Perovskites and Derivatives for Electrocatalysis, Photocatalysis, and Photovoltaics. *Energy Environ. Sci.* **2019**, *12* (2), 442–462.

(17) Weng, B.; Xiao, Z.; Meng, W.; Grice, C. R.; Poudel, T.; Deng, X.; Yan, Y. Bandgap Engineering of Barium Bismuth Niobate Double Perovskite for Photoelectrochemical Water Oxidation. *Adv. Energy Mater.* **2017**, *7* (9), 1602260.

(18) Weng, B.; Grice, C. R.; Ge, J.; Poudel, T.; Deng, X.; Yan, Y. Barium Bismuth Niobate Double Perovskite/Tungsten Oxide Nanosheet Photoanode for High-Performance Photoelectrochemical Water Splitting. *Adv. Energy Mater.* **2018**, *8* (10), 1701655.

(19) Pérez-Tomás, A.; Mingorance, A.; Tanenbaum, D.; Lira-Cantú, M. Metal Oxides in Photovoltaics: All-Oxide, Ferroic, and Perovskite Solar Cells. In *The Future of Semiconductor Oxides in Next-Generation Solar Cells*; 2018; pp 267–356.

(20) Grinberg, I.; West, D. V.; Torres, M.; Gou, G.; Stein, D. M.; Wu, L.; Chen, G.; Gallo, E. M.; Akbashev, A. R.; Davies, P. K.; Spanier, J. E.; Rappe, A. M. Perovskite Oxides for Visible-Light-Absorbing Ferroelectric and Photovoltaic Materials. *Nature* **2013**, *503* (7477), 509–512.

(21) Vasala, S.; Karppinen, M. $A_2B'B''O_6$ Perovskites: A Review. *Prog. Solid State Chem.* **2015**, *43* (1–2), 1–36.

(22) Glazer, A. M. The Classification of Tilted Octahedra in Perovskites. *Acta Crystallogr. Sect. B Struct. Crystallogr. Cryst. Chem.* **1972**, *28* (11), 3384–3392.

(23) Lufaso, M. W.; Barnes, P. W.; Woodward, P. M. Structure Prediction of Ordered and Disordered Multiple Octahedral Cation Perovskites Using SPuDS. *Acta Crystallogr. Sect. B Struct. Sci.* **2006**, *62* (3), 397–410.

(24) Shojaei, F.; Yin, W. J. Stability Trend of Tilted Perovskites. *J. Phys. Chem. C* **2018**, *122* (27), 15214–15219.

(25) Yoon, S. J.; Draguta, S.; Manser, J. S.; Sharia, O.; Schneider, W. F.; Kuno, M.; Kamat, P. V. Tracking Iodide and Bromide Ion Segregation in Mixed Halide Lead Perovskites during Photoirradiation. *ACS Energy Lett.* **2016**, *1* (1), 290–296.

(26) Hoefler, S. F.; Trimmel, G.; Rath, T. Progress on Lead-Free Metal Halide Perovskites for Photovoltaic Applications: A Review. *Monatshefte fur Chemie* **2017**, *148*, 795–826.

(27) Wehrenfennig, C.; Eperon, G. E.; Johnston, M. B.; Snaith, H. J.; Herz, L. M. High Charge Carrier Mobilities and Lifetimes in Organolead Trihalide Perovskites. *Adv. Mater.* **2014**, *26* (10), 1584–1589.

(28) Kojima, A.; Teshima, K.; Shirai, Y.; Miyasaka, T. Organometal Halide Perovskites as Visible-Light Sensitizers for Photovoltaic Cells. *J. Am. Chem. Soc.* **2009**, *131* (17), 6050–6051.

(29) Balis, N.; Dracopoulos, V.; Antoniadou, M.; Lianos, P. Solid-State Dye-Sensitized Solar Cells Made of Multilayer Nanocrystalline Titania and Poly(3-Hexylthiophene). *J. Photochem. Photobiol. A Chem.* **2010**, *214* (1), 69–73.

(30) Walsh, A. Principles of Chemical Bonding and Band Gap Engineering in Hybrid Organic-Inorganic Halide Perovskites. *J. Phys. Chem. C* **2015**, *119* (11), 5755–5760.

(31) Aleksandrov, K. S.; Bartolomé, J. Structural Distortions in Families of Perovskite-like Crystals. *Phase Transitions* **2001**, *74* (3), 255–335.

(32) Zeng, Z.; Calle-Vallejo, F.; Mogensen, M. B.; Rossmeisl, J. Generalized Trends in the Formation Energies of Perovskite Oxides. *Phys. Chem. Chem. Phys.* **2013**, *15* (20), 7526–7533.

(33) Johnsson, M.; Lemmens, P. Perovskites and Thin Films - Crystallography and Chemistry. *J. Phys. Condens. Matter* **2008**, *20* (26), 264001.

(34) Johnsson, M.; Lemmens, P. Crystallography and Chemistry of Perovskites. In *Handbook of Magnetism and Advanced Magnetic Materials*; 2007.

(35) Goldschmidt, V. M. Die Gesetze Der Krystallochemie. *Naturwissenschaften* **1926**, *14* (21), 477–485.

(36) Li, C.; Soh, K. C. K.; Wu, P. Formability of ABO_3 Perovskites. *J. Alloys Compd.* **2004**, *372* (1–2), 40–48.

(37) Li, C.; Lu, X.; Ding, W.; Feng, L.; Gao, Y.; Guo, Z. Formability of ABX 3 (X= F, Cl, Br, I) Halide Perovskites. *Acta Crystallogr. Sect. B Struct. Sci.* **2008**, *64* (6), 702–707.

(38) Kieslich, G.; Sun, S.; Cheetham, A. K. Solid-State Principles Applied to Organic–Inorganic Perovskites: New Tricks for an Old Dog. *Chem. Sci.* **2014**, *5* (12), 4712–4715.

(39) Kieslich, G.; Sun, S.; Cheetham, A. K. An Extended Tolerance Factor Approach for Organic-Inorganic Perovskites. *Chem. Sci.* **2015**, *6* (6), 3430–3433.

(40) Shannon, R. D. Revised Effective Ionic Radii and Systematic Studies of Interatomic Distances in Halides and Chalcogenides. *Acta Crystallogr. Sect. A* **1976**, *32* (5), 751–767.

(41) Chen, Q.; De Marco, N.; Yang, Y.; Song, T. Bin; Chen, C. C.; Zhao, H.; Hong, Z.; Zhou, H.; Yang, Y. Under the Spotlight: The Organic-Inorganic Hybrid Halide Perovskite for Optoelectronic Applications. *Nano Today* **2015**, *10* (3), 355–396.

(42) Kaltzoglou, A.; Stoumpos, C. C.; Kontos, A. G.; Manolis, G. K.; Papadopoulos, K.; Papadokostaki, K. G.; Psycharis, V.; Tang, C. C.; Jung, Y. K.; Walsh, A.; Kanatzidis, M. G.; Falaras, P. Trimethylsulfonium Lead Triiodide: An Air-Stable Hybrid Halide Perovskite. *Inorg. Chem.* **2017**, *56* (11), 6302–6309.

(43) Saparov, B.; Mitzi, D. B. Organic-Inorganic Perovskites: Structural Versatility for Functional Materials Design. *Chem. Rev.* **2016**, *116* (7), 4558–4596.

(44) Grancini, G.; Nazeeruddin, M. K. Dimensional Tailoring of Hybrid Perovskites for Photovoltaics. *Nature Reviews Materials*. Nature Publishing Group January 1, 2019, pp 4–22.

(45) Kim, H. S.; Lee, C. R.; Im, J. H.; Lee, K. B.; Moehl, T.; Marchioro, A.; Moon, S. J.; Humphry-Baker, R.; Yum, J. H.; Moser, J. E.; Grätzel, M.; Park, N. G. Lead Iodide Perovskite Sensitized All-Solid-State Submicron Thin Film Mesoscopic Solar Cell with Efficiency Exceeding 9%. *Sci. Rep.* **2012**, *2* (1), 1–7.

(46) Hao, F.; Stoumpos, C. C.; Chang, R. P. H.; Kanatzidis, M. G. Anomalous Band Gap Behavior in Mixed Sn and Pb Perovskites Enables Broadening of Absorption Spectrum in Solar Cells. *J. Am. Chem. Soc.* **2014**, *136* (22), 8094–8099.

(47) Eperon, G. E.; Burlakov, V. M.; Docampo, P.; Goriely, A.; Snaith, H. J. Morphological

Control for High Performance, Solution-Processed Planar Heterojunction Perovskite Solar Cells. *Adv. Funct. Mater.* **2014**, *24* (1), 151–157.

(48) Liang, P.-W.; Liao, C.-Y.; Chueh, C.-C.; Zuo, F.; Williams, S. T.; Xin, X.-K.; Lin, J.; Jen, A. K.-Y. Additive Enhanced Crystallization of Solution-Processed Perovskite for Highly Efficient Planar-Heterojunction Solar Cells. *Adv. Mater.* **2014**, *26* (22), 3748–3754.

(49) Jeon, N. J.; Noh, J. H.; Kim, Y. C.; Yang, W. S.; Ryu, S.; Seok, S. Il. Solvent Engineering for High-Performance Inorganic-Organic Hybrid Perovskite Solar Cells. *Nat. Mater.* **2014**, *13* (9), 897–903.

(50) Burschka, J.; Pellet, N.; Moon, S. J.; Humphry-Baker, R.; Gao, P.; Nazeeruddin, M. K.; Grätzel, M. Sequential Deposition as a Route to High-Performance Perovskite-Sensitized Solar Cells. *Nature* **2013**, *499* (7458), 316–319.

(51) Pang, S.; Hu, H.; Zhang, J.; Lv, S.; Yu, Y.; Wei, F.; Qin, T.; Xu, H.; Liu, Z.; Cui, G. $NH_2CH{=}NH_2PbI_3$: An Alternative Organolead Iodide Perovskite Sensitizer for Mesoscopic Solar Cells. *Chem. Mater.* **2014**, *26* (3), 1485–1491.

(52) Im, J. H.; Kim, H. S.; Park, N. G. Morphology-Photovoltaic Property Correlation in Perovskite Solar Cells: One-Step versus Two-Step Deposition of $CH_3NH_3PbI_3$. *APL Mater.* **2014**, *2* (8), 081510.

(53) Xiao, Z.; Bi, C.; Shao, Y.; Dong, Q.; Wang, Q.; Yuan, Y.; Wang, C.; Gao, Y.; Huang, J. Efficient, High Yield Perovskite Photovoltaic Devices Grown by Interdiffusion of Solution-Processed Precursor Stacking Layers. *Energy Environ. Sci.* **2014**, *7* (8), 2619–2623.

(54) Chen, Q.; Zhou, H.; Hong, Z.; Luo, S.; Duan, H. S.; Wang, H. H.; Liu, Y.; Li, G.; Yang, Y. Planar Heterojunction Perovskite Solar Cells via Vapor-Assisted Solution Process. *J. Am. Chem. Soc.* **2014**, *136* (2), 622–625.

(55) Niu, G.; Guo, X.; Wang, L. Review of Recent Progress in Chemical Stability of Perovskite Solar Cells. *J. Mater. Chem. A* **2015**, *3* (17), 8970–8980.

(56) Chung, I.; Song, J. H.; Im, J.; Androulakis, J.; Malliakas, C. D.; Li, H.; Freeman, A. J.; Kenney, J. T.; Kanatzidis, M. G. $CsSnI_3$: Semiconductor or Metal? High Electrical Conductivity and Strong near-Infrared Photoluminescence from a Single Material.

High Hole Mobility and Phase-Transitions. *J. Am. Chem. Soc.* **2012**, *134* (20), 8579–8587.

(57) Hao, F.; Stoumpos, C. C.; Cao, D. H.; Chang, R. P. H.; Kanatzidis, M. G. Lead-Free Solid-State Organic-Inorganic Halide Perovskite Solar Cells. *Nat. Photonics* **2014**, *8* (6), 489–494.

(58) World Bank. 2017. Global Solar Atlas. Https://Globalsolaratlas.Info/.

(59) Myers, D. R.; Emery, K.; Gueymard, C. Revising and Validating Spectral Irradiance Reference Standards for Photovoltaic Performance Evaluation. *J. Sol. Energy Eng. Trans. ASME* **2004**, *126* (1), 567–574.

(60) Luque, A.; Hegedus, S. *Handbook of Photovoltaic Science and Engineering*; 2011.

(61) Bouzidi, K.; Chegaar, M.; Bouhemadou, A. Solar Cells Parameters Evaluation Considering the Series and Shunt Resistance. *Sol. Energy Mater. Sol. Cells* **2007**, *91* (18), 1647–1651.

(62) Aberle, A. G.; Wenham, S. R.; Green, M. A. New Method for Accurate Measurements of the Lumped Series Resistance of Solar Cells. In *Conference Record of the IEEE Photovoltaic Specialists Conference*; 1993; pp 133–139.

(63) Nelson, C. A.; Monahan, N. R.; Zhu, X. Y. Exceeding the Shockley-Queisser Limit in Solar Energy Conversion. *Energy Environ. Sci.* **2013**, *6* (12), 3508–3519.

(64) Shockley, W.; Queisser, H. Detailed Balance Limit of Efficiency of Pn Junction Solar Cells. *J. Appl. Phys.* **1961**, *32*, 510.

(65) Stranks, S. D.; Burlakov, V. M.; Leijtens, T.; Ball, J. M.; Goriely, A.; Snaith, H. J. Recombination Kinetics in Organic-Inorganic Perovskites: Excitons, Free Charge, and Subgap States. *Phys. Rev. Appl.* **2014**, *2* (3), 034007.

(66) Shockley, W.; Read, W. T. Statistics of the Recombinations of Holes and Electrons. *Phys. Rev.* **1952**, *87* (5), 835–842.

(67) Taylor, W. E.; Odell, N. H.; Fan, H. Y. Grain Boundary Barriers in Germanium. *Phys. Rev.* **1952**, *88* (4), 867–875.

(68) Chowdhury, N. A.; Misra, D. Charge Trapping at Deep States in Hf–Silicate Based High-κ Gate Dielectrics. *J. Electrochem. Soc.* **2007**, *154* (2), G30.

(69) Grußmayer, K. S.; Steiner, F.; Lupton, J. M.; Herten, D. P.; Vogelsang, J. Differentiation between Shallow and Deep Charge Trap States on Single Poly(3-Hexylthiophene) Chains through Fluorescence Photon Statistics. *ChemPhysChem* **2015**, *16* (17), 3578–3583.

(70) Eades, W. D.; Swanson, R. M. Calculation of Surface Generation and Recombination Velocities at the Si-SiO2 Interface. *J. Appl. Phys.* **1985**, *58* (11), 4267–4276.

(71) Scheer, R.; Schock, H. W. *Chalcogenide Photovoltaics: Physics, Technologies, and Thin Film Devices*; 2011.

(72) McGehee, M. D. Perovskite Solar Cells: Continuing to Soar. *Nat. Mater.* **2014**, *13* (9), 845–846.

(73) Snaith, H. J.; Abate, A.; Ball, J. M.; Eperon, G. E.; Leijtens, T.; Noel, N. K.; Stranks, S. D.; Wang, J. T. W.; Wojciechowski, K.; Zhang, W. Anomalous Hysteresis in Perovskite Solar Cells. *J. Phys. Chem. Lett.* **2014**, *5* (9), 1511–1515.

(74) Chen, H. W.; Sakai, N.; Ikegami, M.; Miyasaka, T. Emergence of Hysteresis and Transient Ferroelectric Response in Organo-Lead Halide Perovskite Solar Cells. *J. Phys. Chem. Lett.* **2015**, *6* (1), 164–169.

(75) Wei, J.; Zhao, Y.; Li, H.; Li, G.; Pan, J.; Xu, D.; Zhao, Q.; Yu, D. Hysteresis Analysis Based on the Ferroelectric Effect in Hybrid Perovskite Solar Cells. *J. Phys. Chem. Lett.* **2014**, *5* (21), 3937–3945.

(76) Eames, C.; Frost, J. M.; Barnes, P. R. F.; O'Regan, B. C.; Walsh, A.; Islam, M. S. Ionic Transport in Hybrid Lead Iodide Perovskite Solar Cells. *Nat. Commun.* **2015**, *6* (1), 1–8.

(77) Li, C.; Tscheuschner, S.; Paulus, F.; Hopkinson, P. E.; Kießling, J.; Köhler, A.; Vaynzof, Y.; Huettner, S. Iodine Migration and Its Effect on Hysteresis in Perovskite Solar Cells. *Adv. Mater.* **2016**, *28* (12), 2446–2454.

(78) Unger, E. L.; Hoke, E. T.; Bailie, C. D.; Nguyen, W. H.; Bowring, A. R.; Heumüller, T.; Christoforo, M. G.; McGehee, M. D. Hysteresis and Transient Behavior in Current-Voltage Measurements of Hybrid-Perovskite Absorber Solar Cells. *Energy Environ. Sci.* **2014**, *7* (11), 3690–3698.

(79) Zhao, C.; Chen, B.; Qiao, X.; Luan, L.; Lu, K.; Hu, B. Revealing Underlying Processes

Involved in Light Soaking Effects and Hysteresis Phenomena in Perovskite Solar Cells. *Adv. Energy Mater.* **2015**, *5* (14), 1500279.

(80) Kim, H. S.; Park, N. G. Parameters Affecting I-V Hysteresis of $CH_3NH_3PbI_3$ Perovskite Solar Cells: Effects of Perovskite Crystal Size and Mesoporous TiO_2 Layer. *J. Phys. Chem. Lett.* **2014**, *5* (17), 2927–2934.

(81) Ono, L. K.; Raga, S. R.; Wang, S.; Kato, Y.; Qi, Y. Temperature-Dependent Hysteresis Effects in Perovskite-Based Solar Cells. *J. Mater. Chem. A* **2015**, *3* (17), 9074–9080.

(82) Sepalage, G. A.; Meyer, S.; Pascoe, A.; Scully, A. D.; Huang, F.; Bach, U.; Cheng, Y.-B.; Spiccia, L. Copper(I) Iodide as Hole-Conductor in Planar Perovskite Solar Cells: Probing the Origin of *J - V* Hysteresis. *Adv. Funct. Mater.* **2015**, *25* (35), 5650–5661.

(83) Corey, E. J.; Chaykovsky, M. Dimethyloxosulfonium Methylide ($(CH_3)_2SOCH_2$) and Dimethylsulfonium Methylide ($(CH_3)_2SCH_2$). Formation and Application to Organic Synthesis. *J. Am. Chem. Soc.* **1965**, *87* (6), 1353–1364.

(84) Koon, H. P.; Myung, S. S.; Yong, W. K. Facile Preparation of Trimethylsulfonium Bromide. *Bull. Korean Chem. Soc.* **2005**, *26* (10), 1491–1492.

(85) Byrne, B.; Lafleur Lawter, L. M. The Preparation of Trimethylsulfonium Chloride from Methyl Chloroformate and Dimethyl Sulfide. *Tetrahedron Lett.* **1986**, *27* (11), 1233–1236.

(86) Rigaku/MSC CrystalClear, R.M.I., The Woodlands, Texas, USA, 2005.

(87) Sheldrick, G. M. A Short History of SHELX. *Acta Crystallogr. Sect. A Found. Crystallogr.* **2008**, *64* (1), 112–122.

(88) Sheldrick, G. M. SHELXT - Integrated Space-Group and Crystal-Structure Determination. *Acta Crystallogr. Sect. A Found. Crystallogr.* **2015**, *71* (1), 3–8.

(89) Sheldrick, G. SHELXT: Integrating Space Group Determination and Structure Solution. *Acta Crystallogr. Sect. A Found. Adv.* **2014**, *70* (a1), C1437–C1437.

(90) T. Roisnel, J. R.-C. Fullprof, Version Sept. 2012.

(91) Carvajal, J. FULLPROF: A Program for Rietveld Refinement and Pattern Matching Analysis. *Abstracts of the Satellite Meeting on Powder Diffraction of the XV Congress of the IUCr*. 1990, p 127.

(92) Petrícek, V.; Dušek, M.; Palatinus, L. Crystallographic Computing System JANA2006: General Features. *Zeitschrift fur Krist.* **2014**, *229* (5), 345–352.

(93) Spackman, M. A.; Jayatilaka, D. Hirshfeld Surface Analysis. *CrystEngComm* **2009**, *11* (1), 19–32.

(94) Walrafen, G. E.; Hokmabadi, M. S.; Krishnan, P. N.; Guha, S.; Munro, R. G. Low-Frequency Raman Scattering from Vitreous and Molten B_2O_3. *J. Chem. Phys.* **1983**, *79* (8), 3609–3620.

(95) Kubelka, P.; Munk, F. An Article on Optics of Paint Layers (Engl. Übersetzung). *Z. Tech. Phys* **1931**, *12*, 593–601.

(96) Frisch, M. J. et al. Gaussian 09, Revision A.02. *Gaussian 09, Revision A.02*. 2009.

(97) Clark, S. J.; Segall, M. D.; Pickard, C. J.; Hasnip, P. J.; Probert, M. I. J.; Refson, K.; Payne, M. C. First Principles Methods Using CASTEP. *Zeitschrift fur Krist.* **2005**, *220* (5–6), 567–570.

(98) Segall, M. D.; Lindan, P. J. D.; Probert, M. J.; Pickard, C. J.; Hasnip, P. J.; Clark, S. J.; Payne, M. C. First-Principles Simulation: Ideas, Illustrations and the CASTEP Code. *J. Phys. Condens. Matter* **2002**, *14* (11), 2717–2744.

(99) Froyen, S. Brillouin-Zone Integration by Fourier Quadrature: Special Points for Superlattice and Supercell Calculations. *Phys. Rev. B* **1989**, *39* (5), 3168–3172.

(100) Hoffmann, R. An Extended Hückel Theory. I. Hydrocarbons. *J. Chem. Phys.* **1963**, *39* (6), 1397–1412.

(101) Manser, J. S.; Christians, J. A.; Kamat, P. V. Intriguing Optoelectronic Properties of Metal Halide Perovskites. *Chem. Rev.* **2016**, *116* (21), 12956–13008.

(102) Chen, J.; Žídek, K.; Chábera, P.; Liu, D.; Cheng, P.; Nuuttila, L.; Al-Marri, M. J.; Lehtivuori, H.; Messing, M. E.; Han, K.; Zheng, K.; Pullerits, T. Size-And Wavelength-Dependent Two-Photon Absorption Cross-Section of CsPbBr3 Perovskite Quantum Dots. *J. Phys. Chem. Lett.* **2017**, *8* (10), 2316–2321.

(103) Søndenå, R.; Stølen, S.; Ravindran, P.; Grande, T.; Allan, N. L. Corner- versus Face-Sharing Octahedra in $AMnO_3$ Perovskites (A=Ca, Sr, and Ba). *Phys. Rev. B - Condens. Matter Mater. Phys.* **2007**, *75* (18), 184105.

(104) Battle, P. D.; Gibb, T. C.; Jones, C. W. The Structural and Magnetic Properties of $SrMnO_3$: A Reinvestigation. *J. Solid State Chem.* **1988**, *74* (1), 60–66.

(105) Koutselas, I. B.; Ducasse, L.; Papavassiliou, G. C. Electronic Properties of Three- and Low-Dimensional Semiconducting Materials with Pb Halide and Sn Halide Units. *J. Phys. Condens. Matter* **1996**, *8* (9), 1217–1227.

(106) Smith, M. D.; Watson, B. L.; Dauskardt, R. H.; Karunadasa, H. I. Broadband Emission with a Massive Stokes Shift from Sulfonium Pb-Br Hybrids. *Chem. Mater.* **2017**, *29* (17), 7083–7087.

(107) Niemann, R. G.; Kontos, A. G.; Palles, D.; Kamitsos, E. I.; Kaltzoglou, A.; Brivio, F.; Falaras, P.; Cameron, P. J. Halogen Effects on Ordering and Bonding of $CH_3NH_3^+$ in $CH_3NH_3PbX_3$ (X = Cl, Br, I) Hybrid Perovskites: A Vibrational Spectroscopic Study. *J. Phys. Chem. C* **2016**, *120* (5), 2509–2519.

(108) Papavassiliou, G. C.; Mousdis, G. A.; Koutselas, I. B. Excitonic Bands in the Spectra of Some Organic-Inorganic Hybrid Compounds Based on Metal Halide Units. In *Monatshefte fur Chemie*; 2001; Vol. 132, pp 113–119.

(109) Papavassiliou, G. C.; Koutselas, I. B.; Terzis, A.; Raptopoulou, C. P. Some Natural Three-and Lower-Dimensional Semiconductor Systems with Metal-Halide Units. *MRS Proc.* **1994**, *358*, 283.

(110) Papavassiliou, G. C.; Mousdis, G. A.; Raptopoulou, C. P.; Terzis, A. Preparation and Characterization of $[C_6H_5CH_2NH_3]_2PbI_4$, $[C_6H_5CH_2CH_2SC(NH_2)_2]_3PbI_5$ and $[C_{10}H$. *Zeitschrift fur Naturforsch. - Sect. B J. Chem. Sci.* **1999**, *54* (11), 1405–1409.

(111) G.B. Gridunova, E.A. Ziger, V.M. Koshkin, S.V. Lindeman, I.T. Struchkov, V. E. S. A New Quasi-Unidimensional Semiconductor-Piperidinium Triiodoplumbate(II). *Dokl. Akad. Nuak* **1984**, *278*, 656.

(112) She, Y. J.; Zhao, S. P.; Tian, Z. F.; Ren, X. M. Inorganic-Organic Hybrid with One-Dimensional Face-Sharing Iodoplumbate Chain Showing Novel Dielectric Anomaly and Semiconductor Emission. *Inorg. Chem. Commun.* **2014**, *46*, 29–32.

(113) Tang, Z.; Guloy, A. M. A Methylviologen Lead(II) Iodide: Novel $[PbI_3^-]_\infty$ Chains with Mixed Octahedral and Trigonal Prismatic Coordination. *J. Am. Chem. Soc.* **1999**, *121* (2), 452–453.

(114) Krautscheid, H.; Vielsack, F. Synthese Und Kristallstrukturen Kettenförmiger Und Netzartiger Iodoplumbate. *Zeitschrift für Anorg. und Allg. Chemie* **1997**, *623* (1–6), 259–263.

(115) Alemany, P.; Alvarez, S. Bonding and Structure in $L_4M_2(\mu\text{-}XRn)_2$ Diamonds of Tetrahedral d^{10} Ions. Effect of Substituents on the M- -M Interaction. *Inorg. Chem.* **1992**, *31* (21), 4266–4275.

(116) Raptopoulou, C. P.; Terzis, A.; Mousdis, G. A.; Papavassiliou, G. C. $[CH_3SC(NH_2)_2]_3SnI_5$, $[CH_3SC(NH_2)_2][HSC(NH_2)_2]SnBr_4$, $(CH_3C_5H_4NCH_3)PbBr_3$,.. *Zeitschrift fur Naturforsch. - Sect. B J. Chem. Sci.* **2002**, *57* (6), 645–650.

(117) Papavassiliou, G. C. Three- and Low-Dimensional Inorganic Semiconductors. *Prog. Solid State Chem.* **1997**, *25* (3–4), 125–270.

(118) García-Rosell, M.; Bou, A.; Jiménez-Tejada, J. A.; Bisquert, J.; Lopez-Varo, P. Analysis of the Influence of Selective Contact Heterojunctions on the Performance of Perovskite Solar Cells. *J. Phys. Chem. C* **2018**, *122* (25), 13920–13925.

(119) Kim, H. B.; Yoon, Y. J.; Jeong, J.; Heo, J.; Jang, H.; Seo, J. H.; Walker, B.; Kim, J. Y. Peroptronic Devices: Perovskite-Based Light-Emitting Solar Cells. *Energy Environ. Sci.* **2017**, *10* (9), 1950–1957.

(120) Zhang, L.; Xu, L.; Li, Q.; Su, J.; Li, J. Double-Edged Sword Effects of Cation Rotation and Additive Passivation on Perovskite Solar Cell Performance: An Ab Initio Investigation. *Sol. Energy Mater. Sol. Cells* **2018**, *186*, 349–355.

(121) Cao, J.; Yin, J.; Yuan, S.; Zhao, Y.; Li, J.; Zheng, N. Thiols as Interfacial Modifiers to Enhance the Performance and Stability of Perovskite Solar Cells. *Nanoscale* **2015**, *7* (21), 9443–9447.

(122) Kaltzoglou, A.; Elsenety, M. M.; Koutselas, I.; Kontos, A. G.; Papadopoulos, K.; Psycharis, V.; Raptopoulou, C. P.; Perganti, D.; Stergiopoulos, T.; Falaras, P. Synthesis, Characterization and Optoelectronic Properties of Chemically Stable $(CH_3)_3SPbI_{3-x}Br_x$and $(CH_3)_3SPbI_{3-x}Cl_x$ (x = 0, 1, 2, 3) Perovskites. *Polyhedron* **2018**, *140*, 67–73.

(123) Elsenety, M. M.; Kaltzoglou, A.; Antoniadou, M.; Koutselas, I.; Kontos, A. G.; Falaras, P. Synthesis, Characterization and Use of Highly Stable Trimethyl Sulfonium

Tin(IV) Halide Defect Perovskites in Dye Sensitized Solar Cells. *Polyhedron* **2018**, *150*, 83–91.

(124) Kaltzoglou, A.; Antoniadou, M.; Perganti, D.; Siranidi, E.; Raptis, V.; Trohidou, K.; Psycharis, V.; Kontos, A. G.; Falaras, P. Mixed-Halide $Cs_2SnI_3Br_3$ Perovskite as Low Resistance Hole-Transporting Material in Dye-Sensitized Solar Cells. *Electrochim. Acta* **2015**, *184*, 466–474.

(125) Chung, I.; Lee, B.; He, J.; Chang, R. P. H.; Kanatzidis, M. G. All-Solid-State Dye-Sensitized Solar Cells with High Efficiency. *Nature* **2010**, *9* (7399), 486–489.

(126) Zhao, Z.; Gu, F.; Li, Y.; Sun, W.; Ye, S.; Rao, H.; Liu, Z.; Bian, Z.; Huang, C. Mixed-Organic-Cation Tin Iodide for Lead-Free Perovskite Solar Cells with an Efficiency of 8.12%. *Adv. Sci.* **2017**, *4* (11), 1700204.

(127) Nguyen-Tran, T.; An, N. M.; Nguyen, K. D.; Nguyen, T. D.; Truong, T. T. Synthesis of Organo Tin Halide Perovskites via Simple Aqueous Acidic Solution-Based Method. *J. Sci. Adv. Mater. Devices* **2018**, *3* (4), 471–477.

(128) Kontos, A. G.; Kaltzoglou, A.; Siranidi, E.; Palles, D.; Angeli, G. K.; Arfanis, M. K.; Psycharis, V.; Raptis, Y. S.; Kamitsos, E. I.; Trikalitis, P. N.; Stoumpos, C. C.; Kanatzidis, M. G.; Falaras, P. Structural Stability, Vibrational Properties, and Photoluminescence in $CsSnI_3$ Perovskite upon the Addition of SnF_2. *Inorg. Chem.* **2017**, *56* (1), 84–91.

(129) Gao, W.; Ran, C.; Li, J.; Dong, H.; Jiao, B.; Zhang, L.; Lan, X.; Hou, X.; Wu, Z. Robust Stability of Efficient Lead-Free Formamidinium Tin Iodide Perovskite Solar Cells Realized by Structural Regulation. *J. Phys. Chem. Lett.* **2018**, *9* (24), 6999–7006.

(130) Jokar, E.; Chien, C. H.; Fathi, A.; Rameez, M.; Chang, Y. H.; Diau, E. W. G. Slow Surface Passivation and Crystal Relaxation with Additives to Improve Device Performance and Durability for Tin-Based Perovskite Solar Cells. *Energy Environ. Sci.* **2018**, *11* (9), 2353–2362.

(131) Ke, W.; Priyanka, P.; Vegiraju, S.; Stoumpos, C. C.; Spanopoulos, I.; Soe, C. M. M.; Marks, T. J.; Chen, M. C.; Kanatzidis, M. G. Dopant-Free Tetrakis-Triphenylamine Hole Transporting Material for Efficient Tin-Based Perovskite Solar Cells. *J. Am. Chem. Soc.* **2018**, *140* (1), 388–393.

(132) Stoumpos, C. C.; Malliakas, C. D.; Kanatzidis, M. G. Semiconducting Tin and Lead Iodide Perovskites with Organic Cations: Phase Transitions, High Mobilities, and near-Infrared Photoluminescent Properties. *Inorg. Chem.* **2013**, *52* (15), 9019–9038.

(133) Fabini, D. H.; Stoumpos, C. C.; Laurita, G.; Kaltzoglou, A.; Kontos, A. G.; Falaras, P.; Kanatzidis, M. G.; Seshadri, R. Reentrant Structural and Optical Properties and Large Positive Thermal Expansion in Perovskite Formamidinium Lead Iodide. *Angew. Chemie Int. Ed.* **2016**, *55* (49), 15392–15396.

(134) Lode, C.; Krautscheid, H. Iodostannate(II) Mit Kettenförmigen $[SnI_3]^-$-Anionen – Der Übergang von Fünffach Zu Sechsfach Koordinierten SnII-Zentralatomen. *Zeitschrift für Anorg. und Allg. Chemie* **2001**, *627* (5), 841–846.

(135) Kumar, M. H.; Dharani, S.; Leong, W. L.; Boix, P. P.; Prabhakar, R. R.; Baikie, T.; Shi, C.; Ding, H.; Ramesh, R.; Asta, M.; Graetzel, M.; Mhaisalkar, S. G.; Mathews, N. Lead-Free Halide Perovskite Solar Cells with High Photocurrents Realized Through Vacancy Modulation. *Adv. Mater.* **2014**, *26* (41), 7122–7127.

(136) Khan, M. E.; Lee, J.; Byeon, S.; Kim, Y. Semimetallicity and Negative Differential Resistance from Hybrid Halide Perovskite Nanowires. *Adv. Funct. Mater.* **2019**, *29* (13), 1807620.

(137) Vassilakopoulou, A.; Papadatos, D.; Zakouras, I.; Koutselas, I. Mixtures of Quasi-Two and Three Dimensional Hybrid Organic-Inorganic Semiconducting Perovskites for Single Layer LED. *J. Alloys Compd.* **2017**, *692*, 589–598.

(138) Ypenburg, J. W.; van Der Leij-Van Wirdum, E.; Gerding, H. Vibrational Spectrum of Trimethylsulfonium Bromide. *Recl. des Trav. Chim. des Pays-Bas* **2010**, *90* (8), 896–900.

(139) Jain, P.; Dalal, N. S.; Toby, B. H.; Kroto, H. W.; Cheetham, A. K. Order-Disorder Antiferroelectric Phase Transition in a Hybrid Inorganic-Organic Framework with the Perovskite Architecture. *J. Am. Chem. Soc.* **2008**, *130* (32), 10450–10451.

(140) Jain, P.; Ramachandran, V.; Clark, R. J.; Hai, D. Z.; Toby, B. H.; Dalal, N. S.; Kroto, H. W.; Cheetham, A. K. Multiferroic Behavior Associated with an Order-Disorder Hydrogen Bonding Transition in Metal-Organic Frameworks (MOFs) with the Perovskite ABX_3 Architecture. *J. Am. Chem. Soc.* **2009**, *131* (38), 13625–13627.

(141) Besara, T.; Jain, P.; Dalal, N. S.; Kuhns, P. L.; Reyes, A. P.; Kroto, H. W.; Cheetham, A. K. Mechanism of the Order-Disorder Phase Transition, and Glassy Behavior in the Metal-Organic Framework $[(CH_3)_2NH_2]Zn(HCOO)_3$. *Proc. Natl. Acad. Sci. U. S. A.* **2011**, *108* (17), 6828–6832.

(142) Stranks, S. D.; Snaith, H. J. Metal-Halide Perovskites for Photovoltaic and Light-Emitting Devices. *Nat. Nanotechnol.* **2015**, *10* (5), 391–402.

(143) Brenner, T. M.; Egger, D. A.; Kronik, L.; Hodes, G.; Cahen, D. Hybrid Organic - Inorganic Perovskites: Low-Cost Semiconductors with Intriguing Charge-Transport Properties. *Nat. Rev. Mater.* **2016**, *1* (1), 15007.

(144) Antoniadou, M.; Siranidi, E.; Vaenas, N.; Kontos, A. G.; Stathatos, E.; Falaras, P. Photovoltaic Performance and Stability of $CH_3NH_3PbI_{3-x}Cl_x$ Perovskites. *J. Surfaces Interfaces Mater.* **2015**, *2* (4), 323–327.

(145) Balis, N.; Zaky, A. A.; Perganti, D.; Kaltzoglou, A.; Sygellou, L.; Katsaros, F.; Stergiopoulos, T.; Kontos, A. G.; Falaras, P. Dye Sensitization of Titania Compact Layer for Efficient and Stable Perovskite Solar Cells. *ACS Appl. Energy Mater.* **2018**, *1* (11), 6161–6171.

(146) Lee, M. M.; Teuscher, J.; Miyasaka, T.; Murakami, T. N.; Snaith, H. J. Efficient Hybrid Solar Cells Based on Meso-Superstructured Organometal Halide Perovskites. *Science (80-.).* **2012**, *338* (6107), 643–647.

(147) Saliba, M.; Orlandi, S.; Matsui, T.; Aghazada, S.; Cavazzini, M.; Correa-Baena, J.-P.; Gao, P.; Scopelliti, R.; Mosconi, E.; Dahmen, K.-H.; De Angelis, F.; Abate, A.; Hagfeldt, A.; Pozzi, G.; Graetzel, M.; Nazeeruddin, M. K. A Molecularly Engineered Hole-Transporting Material for Efficient Perovskite Solar Cells. *Nat. Energy* **2016**, *1* (2), 15017.

(148) Yi, C.; Li, X.; Luo, J.; Zakeeruddin, S. M.; GrÃ¤tzel, M. Perovskite Photovoltaics with Outstanding Performance Produced by Chemical Conversion of Bilayer Mesostructured Lead Halide/TiO_2 Films. *Adv. Mater.* **2016**, *28* (15), 2964–2970.

(149) Zhou, Y.; Garces, H. F.; Senturk, B. S.; Ortiz, A. L.; Padture, N. P. Room Temperature "One-Pot" Solution Synthesis of Nanoscale $CsSnI_3$ Orthorhombic Perovskite Thin Films and Particles. *Mater. Lett.* **2013**, *110*, 127–129.

(150) Fabini, D. H.; Laurita, G.; Bechtel, J. S.; Stoumpos, C. C.; Evans, H. A.; Kontos, A. G.; Raptis, Y. S.; Falaras, P.; Van Der Ven, A.; Kanatzidis, M. G.; Seshadri, R. Dynamic Stereochemical Activity of the Sn^{2+} Lone Pair in Perovskite $CsSnBr_3$. *J. Am. Chem. Soc.* **2016**, *138* (36), 11820–11832.

(151) Qiu, X.; Cao, B.; Yuan, S.; Chen, X.; Qiu, Z.; Jiang, Y.; Ye, Q.; Wang, H.; Zeng, H.; Liu, J.; Kanatzidis, M. G. From Unstable $CsSnI_3$ to Air-Stable Cs_2SnI_6: A Lead-Free Perovskite Solar Cell Light Absorber with Bandgap of 1.48 EV and High Absorption Coefficient. *Sol. Energy Mater. Sol. Cells* **2017**, *159*, 227–234.

(152) Lee, B.; Stoumpos, C. C.; Zhou, N.; Hao, F.; Malliakas, C.; Yeh, C. Y.; Marks, T. J.; Kanatzidis, M. G.; Chang, R. P. H. Air-Stable Molecular Semiconducting Iodosalts for Solar Cell Applications: Cs_2SnI_6 as a Hole Conductor. *J. Am. Chem. Soc.* **2014**, *136* (43), 15379–15385.

(153) Kaltzoglou, A.; Antoniadou, M.; Kontos, A. G.; Stoumpos, C. C.; Perganti, D.; Siranidi, E.; Raptis, V.; Trohidou, K.; Psycharis, V.; Kanatzidis, M. G.; Falaras, P. Optical-Vibrational Properties of the Cs_2SnX_6 (X = Cl, Br, I) Defect Perovskites and Hole-Transport Efficiency in Dye-Sensitized Solar Cells. *J. Phys. Chem. C* **2016**, *120* (22), 11777–11785.

(154) Frost, J. M.; Butler, K. T.; Brivio, F.; Hendon, C. H.; Van Schilfgaarde, M.; Walsh, A. Atomistic Origins of High-Performance in Hybrid Halide Perovskite Solar Cells. *Nano Lett.* **2014**, *14* (5), 2584–2590.

(155) Feng, J.; Xiao, B. Crystal Structures, Optical Properties, and Effective Mass Tensors of $CH_3NH_3PbX_3$ (X = I and Br) Phases Predicted from HSE06. *J. Phys. Chem. Lett.* **2014**, *5* (7), 1278–1282.

(156) Xu, P.; Chen, S.; Xiang, H.-J.; Gong, X.-G.; Wei, S.-H. Influence of Defects and Synthesis Conditions on the Photovoltaic Performance of Perovskite Semiconductor CsSnl(3). *Chem. Mater.* **2014**, *26* (20), 6068–6072.

(157) Ikeda, R.; Nakamura, D.; Kadel, R.; Weiss, A. The Trimethylsulfonium Ion, $[(CH_3)_3S]^{\oplus}$, in Hexachlorometallate(IV) Complexes, $[(CH_3)_3S]_2MCl_6$ (M = Pt, Se, Te, Sn). ^1H NMR, ^{35}Cl NQR, and X-Ray Diffraction S. *Berichte der Bunsengesellschaft für Phys. Chemie* **1983**, *87* (7), 570–574.

(158) Xiao, Z.; Meng, W.; Wang, J.; Mitzi, D. B.; Yan, Y. Searching for Promising New

Perovskite-Based Photovoltaic Absorbers: The Importance of Electronic Dimensionality. *Mater. Horizons* **2017**, *4* (2), 206–216.

(159) Etgar, L. The Merit of Perovskite's Dimensionality; Can This Replace the 3D Halide Perovskite? *Energy Environ. Sci.* **2018**, *11* (2), 234–242.

(160) Maughan, A. E.; Ganose, A. M.; Candia, A. M.; Granger, J. T.; Scanlon, D. O.; Neilson, J. R. Anharmonicity and Octahedral Tilting in Hybrid Vacancy-Ordered Double Perovskites. *Chem. Mater.* **2018**, *30* (2), 472–483.

(161) Hosseini, S. A.; Mahmoudi, G.; Garczarek, P.; Hazendonk, P.; Abedi, M.; Servati Gargari, M. Crystal Structures and Hirshfeld Surface Analysis Calculations of Mercury(II) Complexes with a Diiminopyridine Ligand. *J. Mol. Struct.* **2016**, *1105*, 159–168.

(162) Heß, D.; Gorlov, M.; Fischer, A.; Kloo, L. Syntheses and Crystal Structures of New Palladium(II) and Platinum(IV) Trialkylsulfonium Compounds. *Zeitschrift für Anorg. und Allg. Chemie* **2007**, *633* (4), 643–646.

(163) Shi, J. R.; Kume, Y.; Pelzl, J.; Xu, Y. C.; Wu, X. A Phase Transition in $(CH_3NH_3)_2SnCl_6$ Investigated by Raman Scattering. *J. Raman Spectrosc.* **1998**, *29* (2), 149–151.

(164) Pelzl, J.; Engels, P.; Florian, R. Raman Spectroscopic Study of the Structural Phase Transitions in K_2SnCl_6. *Phys. status solidi* **1977**, *82* (1), 145–148.

(165) Cai, Y.; Xie, W.; Ding, H.; Chen, Y.; Thirumal, K.; Wong, L. H.; Mathews, N.; Mhaisalkar, S. G.; Sherburne, M.; Asta, M. Computational Study of Halide Perovskite-Derived A_2BX_6 Inorganic Compounds: Chemical Trends in Electronic Structure and Structural Stability. *Chem. Mater.* **2017**, *29* (18), 7740–7749.

(166) Lippert, E. The Strengths of Chemical Bonds, von T. L. Cottrell. Butterworths Publications Ltd., London 1958. 2. Aufl., X, 317 S., Geb.t—/32/—. *Angew. Chemie* **1960**, *72* (16), 602.

(167) Anouti, M.; Timperman, L.; El Hilali, M.; Boisset, A.; Galiano, H. Sulfonium Bis(Trifluorosulfonimide) Plastic Crystal Ionic Liquid as an Electrolyte at Elevated Temperature for High-Energy Supercapacitors. *J. Phys. Chem. C* **2012**, *116* (17), 9412–9418.

(168) Perdew, J. P.; Burke, K.; Ernzerhof, M. Generalized Gradient Approximation Made

Simple. *Phys. Rev. Lett.* **1996**, *77* (18), 3865–3868.

(169) Perdew, J. P.; Ruzsinszky, A.; Csonka, G. I.; Vydrov, O. A.; Scuseria, G. E.; Constantin, L. A.; Zhou, X.; Burke, K. Restoring the Density-Gradient Expansion for Exchange in Solids and Surfaces. *Phys. Rev. Lett.* **2008**, *100* (13), 136406.

(170) Crowley, J. M.; Tahir-Kheli, J.; Goddard, W. A. Resolution of the Band Gap Prediction Problem for Materials Design. *J. Phys. Chem. Lett.* **2016**, *7* (7), 1198–1203.

(171) Wang, Y.; Gould, T.; Dobson, J. F.; Zhang, H.; Yang, H.; Yao, X.; Zhao, H. Density Functional Theory Analysis of Structural and Electronic Properties of Orthorhombic Perovskite $CH_3NH_3PbI_3$. *Phys. Chem. Chem. Phys.* **2014**, *16* (4), 1424–1429.

(172) Fabregat-Santiago, F.; Bisquert, J.; Cevey, L.; Chen, P.; Wang, M.; Zakeeruddin, S. M.; Grätzel, M. Electron Transport and Recombination in Solid-State Dye Solar Cell with Spiro-OMeTAD as Hole Conductor. *J. Am. Chem. Soc.* **2009**, *131* (2), 558–562.

(173) Seok, S. Il; Grätzel, M.; Park, N.-G. Methodologies toward Highly Efficient Perovskite Solar Cells. *Small* **2018**, *14* (20), 1704177.

(174) Egger, D. A.; Rappe, A. M.; Kronik, L. Hybrid Organic-Inorganic Perovskites on the Move. *Acc. Chem. Res.* **2016**, *49* (3), 573–581.

(175) Gao, P.; Graetzel, M.; Nazeeruddin, M. K.; Grätzel, M.; Nazeeruddin, M. K. Organohalide Lead Perovskites for Photovoltaic Applications. *Energy Environ. Sci.* **2014**, *7* (8), 2448–2463.

(176) Saliba, M.; Correa-Baena, J. P.; Wolff, C. M.; Stolterfoht, M.; Phung, N.; Albrecht, S.; Neher, D.; Abate, A. How to Make over 20% Efficient Perovskite Solar Cells in Regular (n-i-p) and Inverted (p-i-n) Architectures. *Chem. Mater.* **2018**, *30* (13), 4193–4201.

(177) Correa-Baena, J.-P.; Abate, A.; Saliba, M.; Tress, W.; Jesper Jacobsson, T.; Grätzel, M.; Hagfeldt, A. The Rapid Evolution of Highly Efficient Perovskite Solar Cells. *Energy Environ. Sci.* **2017**, *10* (3), 710–727.

(178) Green, M. A.; Ho-Baillie, A. Perovskite Solar Cells: The Birth of a New Era in Photovoltaics. *ACS Energy Lett.* **2017**, *2* (4), 822–830.

(179) Stranks, S. D.; Nayak, P. K.; Zhang, W.; Stergiopoulos, T.; Snaith, H. J. Formation of

Thin Films of Organic-Inorganic Perovskites for High-Efficiency Solar Cells. *Angew. Chemie - Int. Ed.* **2015**, *54* (11), 3240–3248.

(180) Jung, H. S.; Park, N. G. Perovskite Solar Cells: From Materials to Devices. *Small* **2015**, *11* (1), 10–25.

(181) Grätzel, M. The Light and Shade of Perovskite Solar Cells. *Nat. Mater.* **2014**, *13* (9), 838–842.

(182) Sanad, M. M. S.; Elseman, A. M.; Elsenety, M. M.; Rashad, M. M.; Elsayed, B. A. Facile Synthesis of Sulfide-Based Chalcogenide as Hole-Transporting Materials for Cost-Effective Efficient Perovskite Solar Cells. *J. Mater. Sci. Mater. Electron.* **2019**, *30* (7), 6868–6875.

(183) Perganti, D.; Giannouri, M.; Kontos, A. G.; Falaras, P. Cost-Efficient Platinum-Free DSCs Using Colloidal Graphite Counter Electrodes Combined with D35 Organic Dye and Cobalt$^{(II/III)}$ Redox Couple. *Electrochim. Acta* **2017**, *232*, 517–527.

(184) Stergiopoulos, T.; Konstantakou, M.; Falaras, P. Dye Solar Cells Combining a TiO_2 Surface-Blocking Organic Sensitizer and Solvent-Free Ionic Liquid-Based Redox Electrolyte. *RSC Adv.* **2013**, *3* (35), 15014–15021.

(185) Konstantakou, M.; Stergiopoulos, T.; Likodimos, V.; Vougioukalakis, G. C.; Sygellou, L.; Kontos, A. G.; Tserepi, A.; Falaras, P. Influence of Fluorine Plasma Treatment of TiO_2 Films on the Behavior of Dye Solar Cells Employing the Co$^{(II)/(III)}$ Redox Couple. *J. Phys. Chem. C* **2014**, *118* (30), 16760–16775.

(186) Konti, G.; Vougioukalakis, G. C.; Bidikoudi, M.; Kontos, A. G.; Methenitis, C.; Falaras, P. A Ru(II) Molecular Antenna Bearing a Novel Bipyridine–Acrylonitrile Ligand: Synthesis and Application in Dye Solar Cells. *Polyhedron* **2014**, *82*, 12–18.

(187) Kabanakis, A. N.; Bidikoudi, M.; Elsenety, M. M.; Vougioukalakis, G. C.; Falaras, P. Synthesis of Novel Semi-Squaraine Derivatives and Application in Efficient Dye-Sensitized Solar Cells. *Dye. Pigment.* **2019**, *165*, 308–318.

(188) Ledinský, M.; Löper, P.; Niesen, B.; Holovský, J.; Moon, S.-J.; Yum, J.-H.; De Wolf, S.; Fejfar, A.; Ballif, C. Raman Spectroscopy of Organic–Inorganic Halide Perovskites. *J. Phys. Chem. Lett.* **2015**, *6* (3), 401–406.

(189) Vanderbilt, D. Soft Self-Consistent Pseudopotentials in a Generalized Eigenvalue

Formalism. *Phys. Rev. B* **1990**, *41* (11), 7892–7895.

(190) Hernández-Haro, N.; Ortega-Castro, J.; Martynov, Y. B.; Nazmitdinov, R. G.; Frontera, A. DFT Prediction of Band Gap in Organic-Inorganic Metal Halide Perovskites: An Exchange-Correlation Functional Benchmark Study. *Chem. Phys.* **2019**, *516*, 225–231.

(191) Krüger, J.; Plass, R.; Cevey, L.; Piccirelli, M.; Grätzel, M.; Bach, U. High Efficiency Solid-State Photovoltaic Device Due to Inhibition of Interface Charge Recombination. *Appl. Phys. Lett.* **2001**, *79* (13), 2085–2087.

(192) Boschloo, G.; Häggman, L.; Hagfeldt, A. Quantification of the Effect of 4-Tert-Butylpyridine Addition to I^-/I_3^- Redox Electrolytes in Dye-Sensitized Nanostructured TiO_2 Solar Cells. *J. Phys. Chem. B* **2006**, *110* (26), 13144–13150.

(193) Kiermasch, D.; Rieder, P.; Tvingstedt, K.; Baumann, A.; Dyakonov, V.; Kiermasch, D. Improved Charge Carrier Lifetime in Planar Perovskite Solar Cells by Bromine Doping. *Sci. Rep.* **2016**, *6* (1), 39333.

(194) Wehrenfennig, C.; Liu, M.; Snaith, H. J.; Johnston, M. B.; Herz, L. M. Charge-Carrier Dynamics in Vapour-Deposited Films of the Organolead Halide Perovskite $CH_3NH_3PbI_{3-x}Cl_x$. *Energy Environ. Sci.* **2014**, *7* (7), 2269–2275.

(195) Renewables Global Status Report. *https://www.ren21.net/reports/global-status-report/*.

(196) Gao, P.; Grätzel, M.; Nazeeruddin, M. K. Organohalide Lead Perovskites for Photovoltaic Applications. *Energy Environ. Sci.* **2014**, *7* (8), 2448–2463.

(197) Balis, N.; Verykios, A.; Soultati, A.; Constantoudis, V.; Papadakis, M.; Kournoutas, F.; Drivas, C.; Skoulikidou, M. C.; Gardelis, S.; Fakis, M.; Kennou, S.; Kontos, A. G.; Coutsolelos, A. G.; Falaras, P.; Vasilopoulou, M. Triazine-Substituted Zinc Porphyrin as an Electron Transport Interfacial Material for Efficiency Enhancement and Degradation Retardation in Planar Perovskite Solar Cells. *ACS Appl. Energy Mater.* **2018**, *1* (7), 3216–3229.

(198) Bush, K. A. et al. 23.6%-Efficient Monolithic Perovskite/Silicon Tandem Solar Cells With Improved Stability. *Nat. Energy* **2017**, *2* (4), 17009.

(199) Chen, J.; Lee, D.; Park, N. G. Stabilizing the Ag Electrode and Reducing J-V Hysteresis

through Suppression of Iodide Migration in Perovskite Solar Cells. *ACS Appl. Mater. Interfaces* **2017**, *9* (41), 36338–36349.

(200) Valles-Pelarda, M.; Hames, B. C.; García-Benito, I.; Almora, O.; Molina-Ontoria, A.; Sánchez, R. S.; Garcia-Belmonte, G.; Martín, N.; Mora-Sero, I. Analysis of the Hysteresis Behavior of Perovskite Solar Cells with Interfacial Fullerene Self-Assembled Monolayers. *J. Phys. Chem. Lett.* **2016**, *7* (22), 4622–4628.

(201) Li, M.; Yan, X.; Kang, Z.; Huan, Y.; Li, Y.; Zhang, R.; Zhang, Y. Hydrophobic Polystyrene Passivation Layer for Simultaneously Improved Efficiency and Stability in Perovskite Solar Cells. *ACS Appl. Mater. Interfaces* **2018**, *10* (22), 18787–18795.

(202) Ke, W.; Kanatzidis, M. G. Prospects for Low-Toxicity Lead-Free Perovskite Solar Cells. *Nat. Commun.* **2019**, *10* (1), 965.

(203) Yoon, S. J.; Kuno, M.; Kamat, P. V. Shift Happens. How Halide Ion Defects Influence Photoinduced Segregation in Mixed Halide Perovskites. *ACS Energy Lett.* **2017**, *2* (7), 1507–1514.

(204) Balakrishna, R. G.; Kobosko, S. M.; Kamat, P. V. Mixed Halide Perovskite Solar Cells. Consequence of Iodide Treatment on Phase Segregation Recovery. *ACS Energy Lett.* **2018**, *3* (9), 2267–2272.

(205) Fu, Q.; Tang, X.; Huang, B.; Hu, T.; Tan, L.; Chen, L.; Chen, Y. Recent Progress on the Long-Term Stability of Perovskite Solar Cells. *Adv. Sci.* **2018**, *5* (5), 1700387.

(206) Schloemer, T. H.; Christians, J. A.; Luther, J. M.; Sellinger, A. Doping Strategies for Small Molecule Organic Hole-Transport Materials: Impacts on Perovskite Solar Cell Performance and Stability. *Chem. Sci.* **2019**, *10* (7), 1904–1935.

(207) Song, Z.; Abate, A.; Watthage, S. C.; Liyanage, G. K.; Phillips, A. B.; Steiner, U.; Graetzel, M.; Heben, M. J. Perovskite Solar Cell Stability in Humid Air: Partially Reversible Phase Transitions in the PbI,$_2$-CH_3NH_3I-H_2O System. *Adv. Energy Mater.* **2016**, *6* (19), 1600846.

(208) Zhao, J.; Cai, B.; Luo, Z.; Dong, Y.; Zhang, Y.; Xu, H.; Hong, B.; Yang, Y.; Li, L.; Zhang, W.; Gao, C. Investigation of the Hydrolysis of Perovskite Organometallic Halide $CH_3NH_3PbI_3$ in Humidity Environment. *Sci. Rep.* **2016**, *6*, 21976.

(209) Tong, C. J.; Geng, W.; Tang, Z. K.; Yam, C. Y.; Fan, X. L.; Liu, J.; Lau, W. M.; Liu, L. M.

Uncovering the Veil of the Degradation in Perovskite CH3NH3PbI3 upon Humidity Exposure: A First-Principles Study. *J. Phys. Chem. Lett.* **2015**, *6* (16), 3289–3295.

(210) Shirayama, M.; Kato, M.; Miyadera, T.; Sugita, T.; Fujiseki, T.; Hara, S.; Kadowaki, H.; Murata, D.; Chikamatsu, M.; Fujiwara, H. Degradation Mechanism of $CH_3NH_3PbI_3$ Perovskite Materials upon Exposure to Humid Air. *J. Appl. Phys.* **2016**, *119* (11), 115501.

(211) Saliba, M.; Matsui, T.; Seo, J. Y.; Domanski, K.; Correa-Baena, J. P.; Nazeeruddin, M. K.; Zakeeruddin, S. M.; Tress, W.; Abate, A.; Hagfeldt, A.; Grätzel, M. Cesium-Containing Triple Cation Perovskite Solar Cells: Improved Stability, Reproducibility and High Efficiency. *Energy Environ. Sci.* **2016**, *9* (6), 1989–1997.

(212) Singh, T.; Miyasaka, T. Stabilizing the Efficiency Beyond 20% with a Mixed Cation Perovskite Solar Cell Fabricated in Ambient Air under Controlled Humidity. *Adv. Energy Mater.* **2018**, *8* (3), 1700677.

(213) Prochowicz, D.; Tavakoli, M. M.; Kalam, A.; Chavan, R. D.; Trivedi, S.; Kumar, M.; Yadav, P. Influence of A-Site Cations on the Open-Circuit Voltage of Efficient Perovskite Solar Cells: A Case of Rubidium and Guanidinium Additives. *J. Mater. Chem. A* **2019**, *7*, 8218–8225.

(214) Chen, J.; Kim, S. G.; Park, N. G. $FA_{0.88}Cs_{0.12}PbI_{3-x}(PF_6)_x$ Interlayer Formed by Ion Exchange Reaction between Perovskite and Hole Transporting Layer for Improving Photovoltaic Performance and Stability. *Adv. Mater.* **2018**, *30* (40), 1801948.

(215) Li, Y.; Wang, Z.; Ren, D.; Liu, Y.; Zheng, A.; Zakeeruddin, S. M.; Dong, X.; Hagfeldt, A.; Grätzel, M.; Wang, P. SnS Quantum Dots as Hole Transporter of Perovskite Solar Cells. *ACS Appl. Energy Mater.* **2019**, *2* (5), 3822–3829.

(216) Min, H.; Kim, G.; Paik, M. J.; Lee, S.; Yang, W. S.; Jung, M.; Seok, S. Il. Stabilization of Precursor Solution and Perovskite Layer by Addition of Sulfur. *Adv. Energy Mater.* **2019**, *9* (17), 1803476.

(217) Kaltzoglou, A.; Manolis, G. K.; Elsenety, M. M.; Koutselas, I.; Psycharis, V.; Kontos, A. G.; Falaras, P. Synthesis and Characterization of Lead-Free $(CH_3)_3SSnI_3$ 1-D Perovskite. *J. Electron. Mater.* **2019**, *48* (11), 7533–7538.

(218) Elsenety, M. M.; Antoniadou, M.; Kaltzoglou, A.; Kontos, A. G.; Philippopoulos, A. I.; Mitsopoulou, C. A.; Falaras, P. Synthesis, Characterization of $((CH_3)_3S)_2SnI_{6-n}Cl_n$ and $((CH_3)_3S)_2SnI_{6-n}Br_n$ (N=1, 2) Perovskites and Use in Dye-Sensitized Solar Cells. *Mater. Chem. Phys.* **2020**, *239*, 122310.

(219) Zhou, C.; Lin, H.; Tian, Y.; Yuan, Z.; Clark, R.; Chen, B.; van de Burgt, L. J.; Wang, J. C.; Zhou, Y.; Hanson, K.; Meisner, Q. J.; Neu, J.; Besara, T.; Siegrist, T.; Lambers, E.; Djurovich, P.; Ma, B. Luminescent Zero-Dimensional Organic Metal Halide Hybrids with near-Unity Quantum Efficiency. *Chem. Sci.* **2018**, *9* (3), 586–593.

(220) Fan, J.; Ma, Y.; Zhang, C.; Liu, C.; Li, W.; Schropp, R. E. I.; Mai, Y. Thermodynamically Self-Healing 1D–3D Hybrid Perovskite Solar Cells. *Adv. Energy Mater.* **2018**, *8* (16), 1703421.

(221) Ma, C.; Shen, D.; Huang, B.; Li, X.; Chen, W.-C.; Lo, M.-F.; Wang, P.; Hon-Wah Lam, M.; Lu, Y.; Ma, B.; Lee, C.-S. High Performance Low-Dimensional Perovskite Solar Cells Based on a One Dimensional Lead Iodide Perovskite. *J. Mater. Chem. A* **2019**, *7* (15), 8811–8817.

(222) Zhou, C.; Tian, Y.; Wang, M.; Rose, A.; Besara, T.; Doyle, N. K.; Yuan, Z.; Wang, J. C.; Clark, R.; Hu, Y.; Siegrist, T.; Lin, S.; Ma, B. Low-Dimensional Organic Tin Bromide Perovskites and Their Photoinduced Structural Transformation. *Angew. Chemie - Int. Ed.* **2017**, *56* (31), 9018–9022.

(223) Yang, S.; Wang, Y.; Liu, P.; Cheng, Y. B.; Zhao, H. J.; Yang, H. G. Functionalization of Perovskite Thin Films with Moisture-Tolerant Molecules. *Nat. Energy* **2016**, *1*, 15016.

(224) Wang, F.; Geng, W.; Zhou, Y.; Fang, H. H.; Tong, C. J.; Loi, M. A.; Liu, L. M.; Zhao, N. Phenylalkylamine Passivation of Organolead Halide Perovskites Enabling High-Efficiency and Air-Stable Photovoltaic Cells. *Adv. Mater.* **2016**, *28* (45), 9986–9992.

(225) Gao, L.; Spanopoulos, I.; Ke, W.; Huang, S.; Hadar, I.; Chen, L.; Li, X.; Yang, G.; Kanatzidis, M. G. Improved Environmental Stability and Solar Cell Efficiency of (MA,FA)PbI_3 Perovskite Using a Wide-Band-Gap 1D Thiazolium Lead Iodide Capping Layer Strategy. *ACS Energy Lett.* **2019**, *4* (7), 1763–1769.

(226) Paulsson, H.; Berggrund, M.; Svantesson, E.; Hagfeldt, A.; Kloo, L. Molten and Solid Metal-Iodide-Doped Trialkylsulphonium Iodides and Polyiodides as Electrolytes in

Dye-Sensitized Nanocrystalline Solar Cells. *Sol. Energy Mater. Sol. Cells* **2004**, *82* (3), 345–360.

(227) Wang, P.; Wenger, B.; Humphry-Baker, R.; Moser, J. E.; Teuscher, J.; Kantlehner, W.; Mezger, J.; Stoyanov, E. V.; Zakeeruddin, S. M.; Grätzel, M. Charge Separation and Efficient Light Energy Conversion in Sensitized Mesoscopic Solar Cells Based on Binary Ionic Liquids. *J. Am. Chem. Soc.* **2005**, *127* (18), 6850–6856.

(228) Kim, B.; Kim, M.; Lee, J. H.; Seok, S. Il. Enhanced Moisture Stability by Butyldimethylsulfonium Cation in Perovskite Solar Cells. *Adv. Sci.* **2020**, *7* (3), 1901840.

(229) Tavakoli, M. M.; Saliba, M.; Yadav, P.; Holzhey, P.; Hagfeldt, A.; Zakeeruddin, S. M.; Grätzel, M. Synergistic Crystal and Interface Engineering for Efficient and Stable Perovskite Photovoltaics. *Adv. Energy Mater.* **2019**, *9* (1), 1802646.

(230) Gomez, A.; Sanchez, S.; Campoy-Quiles, M.; Abate, A. Topological Distribution of Reversible and Non-Reversible Degradation in Perovskite Solar Cells. *Nano Energy* **2018**, *45*, 94–100.

(231) Shao, Y.; Xiao, Z.; Bi, C.; Yuan, Y.; Huang, J. Origin and Elimination of Photocurrent Hysteresis by Fullerene Passivation in $CH_3NH_3PbI_3$ Planar Heterojunction Solar Cells. *Nat. Commun.* **2014**, *5* (1), 1–7.

(232) Gharibzadeh, S.; Abdollahi Nejand, B.; Jakoby, M.; Abzieher, T.; Hauschild, D.; Moghadamzadeh, S.; Schwenzer, J. A.; Brenner, P.; Schmager, R.; Haghighirad, A. A.; Weinhardt, L.; Lemmer, U.; Richards, B. S.; Howard, I. A.; Paetzold, U. W. Record Open-Circuit Voltage Wide-Bandgap Perovskite Solar Cells Utilizing 2D/3D Perovskite Heterostructure. *Adv. Energy Mater.* **2019**, *9*, 1803699.

(233) Wright, A. D.; Verdi, C.; Milot, R. L.; Eperon, G. E.; Pérez-Osorio, M. A.; Snaith, H. J.; Giustino, F.; Johnston, M. B.; Herz, L. M. Electron-Phonon Coupling in Hybrid Lead Halide Perovskites. *Nat. Commun.* **2016**, *7*, 11755.

(234) Zhu, C. et al. Strain Engineering in Perovskite Solar Cells and Its Impacts on Carrier Dynamics. *Nat. Commun.* **2019**, *10* (1), 815.

(235) DeQuilettes, D. W.; Vorpahl, S. M.; Stranks, S. D.; Nagaoka, H.; Eperon, G. E.; Ziffer, M. E.; Snaith, H. J.; Ginger, D. S. Impact of Microstructure on Local Carrier Lifetime

in Perovskite Solar Cells. *Science (80-.).* **2015**, *348* (6235), 683–686.

(236) Jiang, Q.; Zhao, Y.; Zhang, X.; Yang, X.; Chen, Y.; Chu, Z.; Ye, Q.; Li, X.; Yin, Z.; You, J. Surface Passivation of Perovskite Film for Efficient Solar Cells. *Nat. Photonics* **2019**, *13* (7), 460–466.

(237) Liu, Y.; Akin, S.; Pan, L.; Uchida, R.; Arora, N.; Milić, J. V.; Hinderhofer, A.; Schreiber, F.; Uhl, A. R.; Zakeeruddin, S. M.; Hagfeldt, A.; Ibrahim Dar, M.; Grätzel, M. Ultrahydrophobic 3D/2D Fluoroarene Bilayer-Based Water-Resistant Perovskite Solar Cells with Efficiencies Exceeding 22%. *Sci. Adv.* **2019**, *5* (6), 2543.

(238) Snaith, H. J.; Abate, A.; Ball, J. M.; Eperon, G. E.; Leijtens, T.; Nakita, K.; Stranks, S. D.; Wang, J. T. W.; Wojciechowski, K.; Zhang, W.; Noel, N. K.; Stranks, S. D.; Wang, J. T. W.; Wojciechowski, K.; Zhang, W. Anomalous Hysteresis in Perovskite Solar Cells-Supporting Information. *J. Phys. Chem. Lett.* **2014**, *5* (9), 1511–1515.

(239) Ravishankar, S.; Gharibzadeh, S.; Roldán-Carmona, C.; Grancini, G.; Lee, Y.; Ralaiarisoa, M.; Asiri, A. M.; Koch, N.; Bisquert, J.; Nazeeruddin, M. K. Influence of Charge Transport Layers on Open-Circuit Voltage and Hysteresis in Perovskite Solar Cells. *Joule* **2018**, *2* (4), 788–798.

(240) Cho, A. N.; Jang, I. H.; Seo, J. Y.; Park, N. G. Dependence of Hysteresis on the Perovskite Film Thickness: Inverse Behavior between TiO2 and PCBM in a Normal Planar Structure. *J. Mater. Chem. A* **2018**, *6* (37), 18206–18215.

(241) Sanchez, R. S.; Gonzalez-Pedro, V.; Lee, J. W.; Park, N. G.; Kang, Y. S.; Mora-Sero, I.; Bisquert, J. Slow Dynamic Processes in Lead Halide Perovskite Solar Cells. Characteristic Times and Hysteresis. *J. Phys. Chem. Lett.* **2014**, *5* (13), 2357–2363.

(242) Mesquita, I.; Andrade, L.; Mendes, A. Temperature Impact on Perovskite Solar Cells Under Operation. *ChemSusChem* **2019**, *12* (10), 2186–2194.

(243) Tang, Z.; Bessho, T.; Awai, F.; Kinoshita, T.; Maitani, M. M.; Jono, R.; Murakami, T. N.; Wang, H.; Kubo, T.; Uchida, S.; Segawa, H. Hysteresis-Free Perovskite Solar Cells Made of Potassium-Doped Organometal Halide Perovskite. *Sci. Rep.* **2017**, *7* (1), 12183.

(244) Li, Z.; Tinkham, J.; Schulz, P.; Yang, M.; Kim, D. H.; Berry, J.; Sellinger, A.; Zhu, K. Acid Additives Enhancing the Conductivity of Spiro-OMeTAD Toward High-Efficiency

and Hysteresis-Less Planar Perovskite Solar Cells. *Adv. Energy Mater.* **2017**, *7* (4), 1601451.

(245) Chen, H. W.; Huang, T. Y.; Chang, T. H.; Sanehira, Y.; Kung, C. W.; Chu, C. W.; Ikegami, M.; Miyasaka, T.; Ho, K. C. Efficiency Enhancement of Hybrid Perovskite Solar Cells with MEH-PPV Hole-Transporting Layers. *Sci. Rep.* **2016**, *6*, 34319.

(246) Dong, X.; Fang, X.; Lv, M.; Lin, B.; Zhang, S.; Ding, J.; Yuan, N. Improvement of the Humidity Stability of Organic–Inorganic Perovskite Solar Cells Using Ultrathin Al2O3 Layers Prepared by Atomic Layer Deposition. *J. Mater. Chem. A* **2015**, *3* (10), 5360–5367.

(247) Li, N.; Zhu, Z.; Li, J.; Jen, A. K.-Y.; Wang, L. Inorganic $CsPb_{1-x}Sn_xIBr_2$ for Efficient Wide-Bandgap Perovskite Solar Cells. *Adv. Energy Mater.* **2018**, *8* (22), 1800525.

(248) Akbulatov, A. F.; Frolova, L. A.; Dremova, N. N.; Zhidkov, I.; Martynenko, V. M.; Tsarev, S. A.; Luchkin, S. Y.; Kurmaev, E. Z.; Aldoshin, S. M.; Stevenson, K. J.; Troshin, P. A. Light or Heat: What Is Killing Lead Halide Perovskites under Solar Cell Operation Conditions? *J. Phys. Chem. Lett.* **2019**, *11* (1), 333–339.

(249) Bi, E.; Chen, H.; Xie, F.; Wu, Y.; Chen, W.; Su, Y.; Islam, A.; Grätzel, M.; Yang, X.; Han, L. Diffusion Engineering of Ions and Charge Carriers for Stable Efficient Perovskite Solar Cells. *Nat. Commun.* **2017**, *8*, 15330.

(250) Lee, J. W.; Dai, Z.; Han, T. H.; Choi, C.; Chang, S. Y.; Lee, S. J.; De Marco, N.; Zhao, H.; Sun, P.; Huang, Y.; Yang, Y. 2D Perovskite Stabilized Phase-Pure Formamidinium Perovskite Solar Cells. *Nat. Commun.* **2018**, *9* (1), 3021.

(251) Shlenskaya, N. N.; Belich, N. A.; Grätzel, M.; Goodilin, E. A.; Tarasov, A. B. Light-Induced Reactivity of Gold and Hybrid Perovskite as a New Possible Degradation Mechanism in Perovskite Solar Cells. *J. Mater. Chem. A* **2018**, *6* (4), 1780–1786.

(252) Yun, J. S.; Seidel, J.; Kim, J.; Soufiani, A. M.; Huang, S.; Lau, J.; Jeon, N. J.; Seok, S. Il; Green, M. A.; Ho-Baillie, A. Critical Role of Grain Boundaries for Ion Migration in Formamidinium and Methylammonium Lead Halide Perovskite Solar Cells. *Adv. Energy Mater.* **2016**, *6* (13), 1600330.

(253) Stranks, S. D.; Eperon, G. E.; Grancini, G.; Menelaou, C.; Alcocer, M. J. P.; Leijtens, T.; Herz, L. M.; Petrozza, A.; Snaith, H. J. Electron-Hole Diffusion Lengths Exceeding 1

Micrometer in an Organometal Trihalide Perovskite Absorber. *Science (80-.).* **2013**, *342* (6156), 341–344.

(254) Wang, R.; Xue, J.; Meng, L.; Lee, J. W.; Zhao, Z.; Sun, P.; Cai, L.; Huang, T.; Wang, Z.; Wang, Z. K.; Duan, Y.; Yang, J. L.; Tan, S.; Yuan, Y.; Huang, Y.; Yang, Y. Caffeine Improves the Performance and Thermal Stability of Perovskite Solar Cells. *Joule* **2019**, *3* (6), 1464–1477.

(255) Chen, F.; Xu, C.; Xu, Q.; Zhu, Y.; Qin, F.; Zhang, W.; Zhu, Z.; Liu, W.; Shi, Z. Self-Assembled Growth of Ultrastable $CH_3NH_3PbBr_3$ Perovskite Milliwires for Photodetectors. *ACS Appl. Mater. Interfaces* **2018**, *10* (30), 25763–25769.

(256) Cho, K. T.; Paek, S.; Grancini, G.; Roldán-Carmona, C.; Gao, P.; Lee, Y.; Nazeeruddin, M. K. Highly Efficient Perovskite Solar Cells with a Compositionally Engineered Perovskite/Hole Transporting Material Interface. *Energy Environ. Sci.* **2017**, *10* (2), 621–627.

(257) Said, A. A.; Xie, J.; Wang, Y.; Wang, Z.; Zhou, Y.; Zhao, K.; Gao, W.; Michinobu, T.; Zhang, Q. Efficient Inverted Perovskite Solar Cells by Employing N-Type ($D–A_1–D–A_2$) Polymers as Electron Transporting Layer. *Small* **2019**, *15* (29), 1803339.

(258) Said, A. A.; Xie, J.; Zhang, Q. Recent Progress in Organic Electron Transport Materials in Inverted Perovskite Solar Cells. *Small* **2019**, *15* (27), 1900854.

(259) Wang, N.; Zhao, K.; Ding, T.; Liu, W.; Ahmed, A. S.; Wang, Z.; Tian, M.; Sun, X. W.; Zhang, Q. Improving Interfacial Charge Recombination in Planar Heterojunction Perovskite Photovoltaics with Small Molecule as Electron Transport Layer. *Adv. Energy Mater.* **2017**, *7* (18).

(260) Gu, P. Y.; Wang, N.; Wang, C.; Zhou, Y.; Long, G.; Tian, M.; Chen, W.; Sun, X. W.; Kanatzidis, M. G.; Zhang, Q. Pushing up the Efficiency of Planar Perovskite Solar Cells to 18.2% with Organic Small Molecules as the Electron Transport Layer. *J. Mater. Chem. A* **2017**, *5* (16), 7339–7344.

(261) Faheem, M. B.; Khan, B.; Feng, C.; Farooq, M. U.; Raziq, F.; Xiao, Y.; Li, Y. All-Inorganic Perovskite Solar Cells: Energetics, Key Challenges, and Strategies toward Commercialization. *ACS Energy Lett.* **2020**, *5* (1), 290–320.

(262) Yin, W. J.; Shi, T.; Yan, Y. Unusual Defect Physics in $CH_3NH_3PbI_3$ Perovskite Solar Cell

Absorber. *Appl. Phys. Lett.* **2014**, *104* (6), 063903.

(263) Lin, Y.; Shen, L.; Dai, J.; Deng, Y.; Wu, Y.; Bai, Y.; Zheng, X.; Wang, J.; Fang, Y.; Wei, H.; Ma, W.; Zeng, X. C.; Zhan, X.; Huang, J. π-Conjugated Lewis Base: Efficient Trap-Passivation and Charge-Extraction for Hybrid Perovskite Solar Cells. *Adv. Mater.* **2017**, *29* (7), 1604545.

(264) Wu, Z.; Raga, S. R.; Juarez-Perez, E. J.; Yao, X.; Jiang, Y.; Ono, L. K.; Ning, Z.; Tian, H.; Qi, Y. Improved Efficiency and Stability of Perovskite Solar Cells Induced by C=O Functionalized Hydrophobic Ammonium-Based Additives. *Adv. Mater.* **2018**, *30* (3), 1703670.

(265) Kim, W.; Park, J. B.; Kim, H.; Kim, K.; Park, J.; Cho, S.; Lee, H.; Pak, Y.; Jung, G. Y. Enhanced Long-Term Stability of Perovskite Solar Cells by Passivating Grain Boundary with Polydimethylsiloxane (PDMS). *J. Mater. Chem. A* **2019**, *7* (36), 20832–20839.

(266) Gong, X.; Guan, L.; Pan, H.; Sun, Q.; Zhao, X.; Li, H.; Pan, H.; Shen, Y.; Shao, Y.; Sun, L.; Cui, Z.; Ding, L.; Wang, M. Highly Efficient Perovskite Solar Cells via Nickel Passivation. *Adv. Funct. Mater.* **2018**, *28* (50), 1804286.

(267) Feng, X.; Chen, R.; Nan, Z.-A.; Lv, X.; Meng, R.; Cao, J.; Tang, Y. Perfection of Perovskite Grain Boundary Passivation by Eu-Porphyrin Complex for Overall-Stable Perovskite Solar Cells. *Adv. Sci.* **2019**, *6* (5), 1802040.

(268) Zhao, X.; Yao, C.; Liu, T.; Hamill, J. C.; Ngongang Ndjawa, G. O.; Cheng, G.; Yao, N.; Meng, H.; Loo, Y. Extending the Photovoltaic Response of Perovskite Solar Cells into the Near-Infrared with a Narrow-Bandgap Organic Semiconductor. *Adv. Mater.* **2019**, 1904494.

(269) Wang, Y.; Wu, Y.; Fu, S.; Song, C.; Wan, L.; Zhang, W.; Li, X.; Yang, W.; Song, W.; Fang, J. Barium Acetate as an Additive for High Performance Perovskite Solar Cells. *J. Mater. Chem. C* **2019**, *7* (37), 11411–11418.

(270) Li, N.; Xu, F.; Qiu, Z.; Liu, J.; Wan, X.; Zhu, X.; Yu, H.; Li, C.; Liu, Y.; Cao, B. Sealing the Domain Boundaries and Defects Passivation by Poly(Acrylic Acid) for Scalable Blading of Efficient Perovskite Solar Cells. *J. Power Sources* **2019**, *426*, 188–196.

(271) Wang, Z.; Pradhan, A.; Kamarudin, M. A.; Pandey, M.; Pandey, S. S.; Zhang, P.; Ng, C.

H.; Tripathi, A. S. M.; Ma, T.; Hayase, S. Passivation of Grain Boundary by Squaraine Zwitterions for Defect Passivation and Efficient Perovskite Solar Cells. *ACS Appl. Mater. Interfaces* **2019**, *11* (10), 10012–10020.

(272) Zhou, Y.; Zhong, H.; Han, J.; Tai, M.; Yin, X.; Zhang, M.; Wu, Z.; Lin, H. Synergistic Effect of Charge Separation and Defect Passivation Using Zinc Porphyrin Dye Incorporation for Efficient and Stable Perovskite Solar Cells. *J. Mater. Chem. A* **2019**, *7* (46), 26334–26341.

(273) Zhang, S.; Hu, Z.; Zhang, J.; Jia, X.; Jiang, J.; Chen, Y.; Lin, B.; Jiang, H.; Fang, B.; Yuan, N.; Ding, J. Interface Engineering via Phthalocyanine Decoration of Perovskite Solar Cells with High Efficiency and Stability. *J. Power Sources* **2019**, *438*, 226987.

(274) Cao, J.; Li, C.; Lv, X.; Feng, X.; Meng, R.; Wu, Y.; Tang, Y. Efficient Grain Boundary Suture by Low-Cost Tetra-Ammonium Zinc Phthalocyanine for Stable Perovskite Solar Cells with Expanded Photoresponse. *J. Am. Chem. Soc.* **2018**, *140* (37), 11577–11580.

(275) Zhang, S.; Islam, A.; Yang, X.; Qin, C.; Zhang, K.; Numata, Y.; Chen, H.; Han, L. Improvement of Spectral Response by Co-Sensitizers for High Efficiency Dye-Sensitized Solar Cells. *J. Mater. Chem. A* **2013**, *1* (15), 4812–4819.

(276) Tavakoli, M. M.; Yadav, P.; Prochowicz, D.; Sponseller, M.; Osherov, A.; Bulović, V.; Kong, J. Controllable Perovskite Crystallization via Antisolvent Technique Using Chloride Additives for Highly Efficient Planar Perovskite Solar Cells. *Adv. Energy Mater.* **2019**, *9* (17), 1803587.

(277) Chang, J.; Chen, H.; Wang, G.; Wang, B.; Chen, X.; Yuan, H. Electronic and Optical Properties of Perovskite Compounds $MA_{1-\alpha}FA_{\alpha}PbI_{3-\beta}X_{\beta}$ (X = Cl, Br) Explored for Photovoltaic Applications. *RSC Adv.* **2019**, *9* (12), 7015–7024.

(278) Yang, L.; Cappel, U. B.; Unger, E. L.; Karlsson, M.; Karlsson, K. M.; Gabrielsson, E.; Sun, L.; Boschloo, G.; Hagfeldt, A.; Johansson, E. M. J. Comparing Spiro-OMeTAD and P3HT Hole Conductors in Efficient Solid State Dye-Sensitized Solar Cells. *Phys. Chem. Chem. Phys.* **2012**, *14* (2), 779–789.

(279) Li, Y.; Sun, C.; Song, P.; Ma, F.; Kungwan, N.; Sun, M. Physical Insight on Mechanism of Photoinduced Charge Transfer in Multipolar Photoactive Molecules. *Sci. Rep.* **2018**, *8* (1), 1–18.

(280) Wu, Y.; Zhu, W. Organic Sensitizers from D–π–A to D–A–π–A: Effect of the Internal Electron-Withdrawing Units on Molecular Absorption, Energy Levels and Photovoltaic Performances. *Chem. Soc. Rev.* **2013**, *42* (5), 2039–2058.

(281) Yang, W. S.; Noh, J. H.; Jeon, N. J.; Kim, Y. C.; Ryu, S.; Seo, J.; Seok, S. Il. High-Performance Photovoltaic Perovskite Layers Fabricated through Intramolecular Exchange. *Science (80-.).* **2015**, *348* (6240), 1234–1237.

(282) Jeon, N. J.; Noh, J. H.; Yang, W. S.; Kim, Y. C.; Ryu, S.; Seo, J.; Seok, S. Il. Compositional Engineering of Perovskite Materials for High-Performance Solar Cells. *Nature* **2015**, *517* (7535), 476–480.

(283) Zhang, W.; Saliba, M.; Moore, D. T.; Pathak, S. K.; Hörantner, M. T.; Stergiopoulos, T.; Stranks, S. D.; Eperon, G. E.; Alexander-Webber, J. A.; Abate, A.; Sadhanala, A.; Yao, S.; Chen, Y.; Friend, R. H.; Estroff, L. A.; Wiesner, U.; Snaith, H. J. Ultrasmooth Organic-Inorganic Perovskite Thin-Film Formation and Crystallization for Efficient Planar Heterojunction Solar Cells. *Nat. Commun.* **2015**, *6* (1), 1–10.

(284) Dryza, V.; Bieske, E. J. Does the Triphenylamine-Based D35 Dye Sensitizer Form Aggregates on Metal-Oxide Surfaces? *J. Photochem. Photobiol. A Chem.* **2015**, *302*, 35–41.

(285) Dong, H.; Yue, M.; Pang, S.; Zhu, W.; Chen, D.; Xi, H.; Lin, Z.; Chang, J.; Zhang, J.; Hao, Y.; Zhang, C. A Modulated Double-Passivation Strategy Toward Highly Efficient Perovskite Solar Cells with Efficiency Over 21%. *Sol. RRL* **2019**, *3* (12), 1900291.

(286) Bi, D.; Yi, C.; Luo, J.; Décoppet, J. D.; Zhang, F.; Zakeeruddin, S. M.; Li, X.; Hagfeldt, A.; Grätzel, M. Polymer-Templated Nucleation and Crystal Growth of Perovskite Films for Solar Cells with Efficiency Greater than 21%. *Nat. Energy* **2016**, *1* (10), 1–5.

(287) Al-Zahrani, F. A. M.; El-Shishtawy, R. M.; Asiri, A. M.; Al-Soliemy, A. M.; Mellah, K. A.; Ahmed, N. S. E.; Jedidi, A. A New Phenothiazine-Based Selective Visual and Fluorescent Sensor for Cyanide. *BMC Chem.* **2020**, *14* (1), 1–11.

(288) Niu, T.; Lu, J.; Munir, R.; Li, J.; Barrit, D.; Zhang, X.; Hu, H.; Yang, Z.; Amassian, A.; Zhao, K.; Liu, S. F. Stable High-Performance Perovskite Solar Cells via Grain Boundary Passivation. *Adv. Mater.* **2018**, *30* (16), 1706576.

(289) Yum, J.-H.; Hagberg, D. P.; Moon, S.-J.; Karlsson, K. M.; Marinado, T.; Sun, L.; Hagfeldt,

A.; Nazeeruddin, M. K.; Grätzel, M. A Light-Resistant Organic Sensitizer for Solar-Cell Applications. *Angew. Chemie* **2009**, *121* (9), 1604–1608.

(290) Yum, J.-H.; Hardin, B. E.; Moon, S.-J.; Baranoff, E.; Nüesch, F.; McGehee, M. D.; Grätzel, M.; Nazeeruddin, M. K. Panchromatic Response in Solid-State Dye-Sensitized Solar Cells Containing Phosphorescent Energy Relay Dyes. *Angew. Chemie* **2009**, *121* (49), 9441–9444.

(291) Hagberg, D. P.; Jiang, X.; Gabrielsson, E.; Linder, M.; Marinado, T.; Brinck, T.; Hagfeldt, A.; Sun, L. Symmetric and Unsymmetric Donor Functionalization. Comparing Structural and Spectral Benefits of Chromophores for Dye-Sensitized Solar Cells. *J. Mater. Chem.* **2009**, *19* (39), 7232–7238.

(292) Peddapuram, A.; Cheema, H.; Adams, R. E.; Schmehl, R. H.; Delcamp, J. H. A Stable Panchromatic Green Dual Acceptor, Dual Donor Organic Dye for Dye-Sensitized Solar Cells. *J. Phys. Chem. C* **2017**, *121* (16), 8770–8780.

(293) Manser, J. S.; Kamat, P. V. Band Filling with Free Charge Carriers in Organometal Halide Perovskites. *Nat. Photonics* **2014**, *8* (9), 737–743.

(294) Adinolfi, V.; Yuan, M.; Comin, R.; Thibau, E. S.; Shi, D.; Saidaminov, M. I.; Kanjanaboos, P.; Kopilovic, D.; Hoogland, S.; Lu, Z.-H.; Bakr, O. M.; Sargent, E. H. The In-Gap Electronic State Spectrum of Methylammonium Lead Iodide Single-Crystal Perovskites. *Adv. Mater.* **2016**, *28* (17), 3406–3410.

(295) Tan, H.; Jain, A.; Voznyy, O.; Lan, X.; De Arquer, F. P. G.; Fan, J. Z.; Quintero-Bermudez, R.; Yuan, M.; Zhang, B.; Zhao, Y.; Fan, F.; Li, P.; Quan, L. N.; Zhao, Y.; Lu, Z. H.; Yang, Z.; Hoogland, S.; Sargent, E. H. Efficient and Stable Solution-Processed Planar Perovskite Solar Cells via Contact Passivation. *Science (80-.).* **2017**, *355* (6326), 722–726.

(296) Heo, J. H.; You, M. S.; Chang, M. H.; Yin, W.; Ahn, T. K.; Lee, S. J.; Sung, S. J.; Kim, D. H.; Im, S. H. Hysteresis-Less Mesoscopic $CH_3NH_3PbI_3$ Perovskite Hybrid Solar Cells by Introduction of Li-Treated TiO_2 Electrode. *Nano Energy* **2015**, *15*, 530–539.

(297) Yang, D.; Yang, R.; Ren, X.; Zhu, X.; Yang, Z.; Li, C.; Liu, S. F. Hysteresis-Suppressed High-Efficiency Flexible Perovskite Solar Cells Using Solid-State Ionic-Liquids for Effective Electron Transport. *Adv. Mater.* **2016**, *28* (26), 5206–5213.

(298) Kaltzoglou, A.; Perganti, D.; Antoniadou, M.; Kontos, A. G.; Falaras, P. Stress Tests on Dye-Sensitized Solar Cells with the Cs_2SnI_6 Defect Perovskite as Hole-Transporting Material. *Energy Procedia* **2016**, *102*, 49–55.